

# Investigation of Quantum Spin Systems with Auxiliary Particles

## Dissertation

zur Erlangung des Grades eines Doktors der Naturwissenschaften  
am Fachbereich Physik  
der Freien Universität Berlin  
vorgelegt von

Nils F. Niggemann

Berlin, 2024

## **Gutachter**

Erstgutachter: Prof. Dr. Johannes Reuther (*Freie Universität Berlin*)

Zweitgutachter: Prof. Dr. Piet Brouwer (*Freie Universität Berlin*)

Tag der Disputation: 16 Dezember, 2024

# Selbständigkeitserklärung

Name: Niggemann

Vorname: Nils

Ich erkläre gegenüber der Freien Universität Berlin, dass ich die vorliegende Dissertation selbstständig und ohne Benutzung anderer als der angegebenen Quellen und Hilfsmittel angefertigt habe. Die vorliegende Arbeit ist frei von Plagiaten. Alle Ausführungen, die wörtlich oder inhaltlich aus anderen Schriften entnommen sind, habe ich als solche kenntlich gemacht. Diese Dissertation wurde in gleicher oder ähnlicher Form noch in keinem früheren Promotionsverfahren eingereicht.

Mit einer Prüfung meiner Arbeit durch ein Plagiatsprüfungsprogramm erkläre ich mich einverstanden.

Berlin, 10 Januar, 2024

---

Ort, Datum

---

Unterschrift



# Contents

<b>List of Publications</b>	<b>8</b>
<b>Kurzfassung</b>	<b>10</b>
<b>Abstract</b>	<b>11</b>
<b>1. Introduction</b>	<b>13</b>
1.1. Introduction to quantum magnetism . . . . .	14
1.2. Different types of order . . . . .	15
1.3. The self-consistent gaussian approximation . . . . .	19
1.4. Emergent gauge theories and quantum spin liquids . . . . .	23
1.5. Fractons and higher-rank gauge theories . . . . .	29
1.6. Basic concepts of the PFFRG . . . . .	31
1.7. Outline of the thesis . . . . .	37
<b>2. The Pseudo Majorana functional renormalization group</b>	<b>39</b>
2.1. $SO(3)$ Majorana Representation . . . . .	42
2.2. General Majorana FRG Flow Equations . . . . .	44
2.3. Symmetry-Based Vertex Parametrization . . . . .	48
2.4. Pseudo-Majorana FRG Flow Equations . . . . .	53
2.5. Observables . . . . .	57
2.6. Application: Small Spin Clusters . . . . .	58
<b>3. Extensions of the formalism</b>	<b>65</b>
3.1. Parquet formalism and the multiloop expansion . . . . .	65
3.2. Temperature flow . . . . .	66
3.3. Finite spin . . . . .	77
<b>4. Magnetic phases of the <math>J_1 - J_2</math> simple cubic Heisenberg model</b>	<b>81</b>
4.1. Nearest-neighbor antiferromagnet . . . . .	82
4.2. Phase diagram in temperature flow . . . . .	88
4.3. Discussion of the stripe phase transition . . . . .	90
<b>5. The Heisenberg Pyrochlore Model</b>	<b>95</b>
5.1. Quantitative Benchmarks . . . . .	95
5.2. Finite-width pinch points . . . . .	96
5.3. Spin 1 model . . . . .	101
5.4. Effect of the $J_2$ coupling . . . . .	104

5.5. Discussion of previous PFFRG results . . . . .	106
<b>6. Quantum Effects on Unconventional Pinch Point Singularities</b>	<b>111</b>
6.1. Introduction . . . . .	111
6.2. Unconventional gauge theories from an octochlore model. . . . .	112
6.3. Emergent gauge theories . . . . .	115
6.4. Twofold pinch points . . . . .	116
6.5. Multifold pinch points . . . . .	118
6.6. Quadratic pinch points . . . . .	120
6.7. Pinch-lines . . . . .	123
6.8. Discussion . . . . .	125
<b>7. Fracton phase in a square lattice model</b>	<b>129</b>
7.1. Construction of a classical fracton model . . . . .	129
7.2. Gaussian approximation of the classical model . . . . .	132
7.3. Classical Ising model . . . . .	135
7.4. Fluctuator and symmetry properties . . . . .	137
7.5. Spin-1/2 spiderweb model . . . . .	139
7.6. Spin-1 spiderweb model . . . . .	141
7.7. Discussion . . . . .	147
<b>8. Conclusion</b>	<b>151</b>
<b>9. Acknowledgements</b>	<b>155</b>
<b>Appendix A. Inclusion of the RPA</b>	<b>157</b>
<b>Appendix B. Two-loop contributions within PMFRG</b>	<b>161</b>
B.1. Parametrization . . . . .	164
B.2. Symmetries . . . . .	165
<b>Appendix C. Parquet formalism for Majorana fermions</b>	<b>169</b>
C.1. Schwinger-Dyson equation . . . . .	170
C.2. Multiloop Flow equations . . . . .	175
C.3. Benchmarks . . . . .	185
<b>Appendix D. Spin-S flow equations and correlation functions</b>	<b>189</b>
<b>Appendix E. Details on the numerical PMFRG implementation</b>	<b>193</b>
<b>Appendix F. Implementation details regarding the spiderweb model</b>	<b>195</b>
F.1. Exact diagonalization in block diagonal Hilbert space . . . . .	195

---

F.2. Green function Monte Carlo . . . . .	196
F.3. Details on the rank-2 U(1) field theory . . . . .	200

---

## List of publications

This thesis is based on and uses material published in the following publications, with one further work in preparation.

- [1] **Niggemann, N.**, Sbierski, B., Reuther, J.  
“*Frustrated quantum spins at finite temperature: Pseudo-Majorana functional renormalization group approach*”  
**Phys Rev. B 103(10), 104431 (2021)**  
<https://doi.org/10.1103/PhysRevB.103.104431>  
Chapter 2 and Section 1.6 include part of this work. <sup>(1)</sup>
- [2] **Niggemann, N.**, Reuther, J., Sbierski, B.  
“*Quantitative functional renormalization for three-dimensional quantum Heisenberg models*”  
**SciPost Phys. 12, 156 (2022)**  
<https://doi.org/10.21468/SciPostPhys.12.5.156>  
Chapters 4 and 5 and Appendices A, B and E include part of this work. <sup>(1)</sup>
- [3] **Niggemann, N.**, Reuther, J., and Iqbal, Y.  
“*Quantum effects on unconventional pinch point singularities*”  
**Physical Review Letters 130 (19), 196601 (2023)**  
<https://doi.org/10.1103/PhysRevLett.130.196601>  
Chapter 6 includes part of this work. <sup>(2)</sup>
- [4] Hagymási, I., **Niggemann, N.**, Reuther, J.  
“*Phase diagram of the antiferromagnetic  $J_1 - J_2$  spin-1 pyrochlore Heisenberg model*”  
**Phys Rev. B 110, 224416 (2024)**  
<https://doi.org/10.1103/PhysRevB.110.224416>  
Section 3.3 and Chapter 5 include part of this work. <sup>(3)</sup>
- [5] Schneider, B., Reuther, J., Gonzalez, M.G., Sbierski, B., **Niggemann, N.**  
“*Temperature flow in pseudo-Majorana functional renormalization for quantum spins*”  
**Phys. Rev. B 109, 195109 (2024)**  
<https://link.aps.org/doi/10.1103/PhysRevB.109.195109>  
Section 3.2 includes part of this work. <sup>(3)</sup>
- [6] **Niggemann, N.**, Adhikary, M., Schaden, Y., Reuther, J.  
“*Exact fracton quantum spin liquid in a spin-1 square lattice model*”  
**in preparation**  
Chapter 7 includes part of this work.



---

(1) Article licensed under the Creative Commons Attribution 4.0 International License: <https://creativecommons.org/licenses/by/4.0/>.

(2) © 2023 by The American Physical Society. Permissions to use the article on free access e-print servers are granted by the APS copyright transfer agreement <https://journals.aps.org/authors/transfer-of-copyright-agreement>.

(3) © 2024 by The American Physical Society. Permissions to use the article on free access e-print servers are granted by the APS copyright transfer agreement <https://journals.aps.org/authors/transfer-of-copyright-agreement>.

The author was also involved in the following works not included in this dissertation:

- [7] **Niggemann, N.**, Hering, M., Reuther, J.  
“Classical spiral spin liquids as a possible route to quantum spin liquids”  
**J. Phys.: Condens. Matter** **32** 024001 (2019)  
<https://dx.doi.org/10.1088/1361-648X/ab4480>  
This work has been completed before the start of this thesis.
- [8] Astrakhantsev, N., Ferrari, F., **Niggemann, N.**, Müller, T., Chauhan, A., Kshetri-mayum, A., Ghosh, P., Regnault, N., Thomale, R., Reuther, J., Neupert, T., Iqbal, Y.  
“Pinwheel valence bond crystal ground state of the spin- Heisenberg antiferromagnet on the shuriken lattice”  
**Phys. Rev. B.** **104**, L220408 (2021) (Editor’s Suggestion)  
<https://doi.org/10.1103/PhysRevB.104.L220408>.
- [9] Kiese, D., Ferrari, F., Astrakhantsev, N., **Niggemann, N.**, Ghosh, P., Müller, T., Thomale, R., Neupert, T., Reuther, J., J. M. P. Gingras, Trebst, S., and Iqbal, Y.  
“Pinch-points to half-moons and up in the stars: The kagome skymap”  
**Phys. Rev. Research** **5**, L012025 (2023)  
<https://doi.org/10.1103/PhysRevResearch.5.L012025>
- [10] Müller, T., Kiese, D., **Niggemann, N.**, Sbierski, B., Reuther, J., Trebst, S., Thomale, R., Iqbal, Y.  
“Pseudo-fermion functional renormalization group for spin models”  
**Rep. Prog. Phys.** **87** 036501 (2023)  
<https://dx.doi.org/10.1088/1361-6633/ad208c>
- [11] **Niggemann, N.**, Astrakhantsev, N., Ralko, A., Ferrari, F., Maity, A., Müller, T., Richter, J., Thomale, R., Neupert, T., Reuther, J., Iqbal, Y., Jeschke H. O.  
“Quantum paramagnetism in the decorated square-kagome antiferromagnet  $\text{Na}_6\text{Cu}_7\text{BiO}_4(\text{PO}_4)_4\text{Cl}_3$ ”  
**Phys. Rev. B** **108**, L241117 (2023)  
<https://link.aps.org/doi/10.1103/PhysRevB.108.L241117>

Data and code for the evaluation of numerical results are made available online via Zenodo at <https://zenodo.org/communities/crc183/records>.

The work presented in this thesis has led to the development of several open-source software packages available on Github at <https://github.com/NilsNiggemann/>.

---

## Kurzfassung

In dieser Dissertation werden Fortschritte bei der Beschreibung von Quantenmagneten vorgestellt, vor allem durch die Entwicklung einer neuen Methode, der so genannten *pseudo-Majorana* functional renormalization group (PMFRG). Die PMFRG ist in der Lage, stark wechselwirkende Quantenmagnete in schwierigen Szenarien genau zu beschreiben, in denen die meisten anderen Methoden versagen.

Grundlegend für den Formalismus der PMFRG ist eine Resummation von Feynman-Diagrammen, die eine direkte Behandlung des Vielkörperproblems im thermodynamischen Limit von unendlich vielen Teilchen ermöglicht. Während exakte Resummationsschemata unmöglich sind, nutzt die PMFRG den Rahmen der Renormierungsgruppe, um eine numerische Summation mehrerer Klassen von Diagrammen bis zu unendlicher Ordnung durchzuführen. Bemerkenswerte Beispiele für solche Diagramme stehen im Zusammenhang mit weit verbreiteten Phänomenen wie der magnetischen Ordnung, aber auch mit exotischeren Quantenspinflüssigkeiten, die durch emergente Eichtheorien und Fraktionalisierung beschriebene Phasen sind. Um diesen Vorteil auszunutzen, werden Spin-Operatoren, für die diagrammatische Techniken nur begrenzt verfügbar sind, auf Majorana-Fermionen abgebildet. Diese Abbildung erweist sich als vorteilhaft im Vergleich zu den üblicherweise verwendeten komplexen Fermionen. Nach der Etablierung des Formalismus wird die PMFRG auf paradigmatische Probleme im Bereich des frustrierten Magnetismus bei endlicher Temperatur angewendet. Die mit dem PMFRG erzielten Ergebnisse erweisen sich als quantitativ genau, typischerweise mit Abweichungen zu exakten Lösungen von weniger als 10%. Insbesondere ist die PMFRG auch auf allgemeinere frustrierter dreidimensionaler Magneten anwendbar, für welche keine exakten Lösungen existieren und auf welche andere Methoden oft nicht anwendbar sind.

Desweiteren betrachtet diese Arbeit emergente Eichtheorien höheren Ranges mit unbeweglichen Quasiteilchenanregungen, bekannt als *Fraktonen*. Zunächst wird die Physik verschiedener Pinch-Point-Merkmale, die mit diesen Eichtheorien einher gehen, analysiert. Unter Verwendung der PMFRG wird eine Instabilität dieser Phasen unter Quantenfluktuationen festgestellt. Schließlich wird ein neues Frakton-Modell konstruiert, welches einen analytisch lösbaren Punkt mit einer Spinflüssigkeit aufweist. Die Stabilität dieser Phase wird durch den Vergleich von numerisch exakten Quanten-Monte-Carlo-Simulationen und der analytischen Lösung der emergenten Rang-2-Gittereichtheorie verifiziert, womit es zum ersten Zweikörper-Spinmodell mit einer emergenten Frakton-Quanten-Spinflüssigkeit wird. In den folgenden Kapiteln werden daher wesentliche Fortschritte in zwei wichtigen Gebieten der Physik vorgestellt: numerische Lösungen des Quantenvielteilchenproblems und die Untersuchung emergenter Eichtheorien in Spinsystemen.

---

## Abstract

This thesis presents advances in the description of quantum magnets, primarily through the development of a new method called the *pseudo-Majorana* functional renormalization group (PMFRG). The PMFRG is capable of accurately describing strongly interacting quantum magnets in challenging scenarios where most other methods fail.

Fundamental to the formalism of the PMFRG is a resummation of Feynman diagrams, which allows direct treatment of the many-body problem in the thermodynamic limit of infinitely many particles. While exact resummation schemes are impossible, the PMFRG uses the framework of the renormalization group to perform a numerical summation of several classes of diagrams to infinite order. Notable examples of such diagrams are associated with common phenomena such as magnetic order, as well as more exotic quantum spin liquids, which are phases described by emergent gauge theories and fractionalization. To exploit this advantage, spin operators for which diagrammatic techniques are limited are mapped to auxiliary Majorana fermions. This mapping proves to be advantageous compared to the more commonly used complex fermions. After establishing its formalism, the PMFRG is applied to paradigmatic problems in the field of frustrated magnetism at finite temperature. The numerical results obtained with the PMFRG are shown to be quantitatively accurate, typically providing errors of less than 10% compared to exact solutions. In particular, the PMFRG remains applicable to more general scenarios of frustrated three-dimensional magnets where exact solutions are unavailable, and where most other methods are infeasible.

In addition, this thesis investigates emergent higher-rank gauge theories with immobile quasiparticle excitations known as *fractons*. The physics of several pinch point features associated with these gauge theories is then analyzed. Using the PMFRG, it is found that these phases are very fragile under the inclusion of quantum fluctuations. Finally, a new fracton spin model is constructed that exhibits an exactly soluble point with a spin liquid phase. The stability of this phase is then verified by numerically exact quantum Monte Carlo simulations of the spin model compared to the analytical solution of the emergent rank-2 lattice gauge theory, making it the first two-body spin model with an emergent fracton quantum spin liquid. The following chapters therefore present substantial progress in two important areas: numerical solutions of the quantum many-body problem and the study of emergent gauge theories in spin systems.



## Introduction

The overwhelming majority of contemporary condensed matter physics considers simple systems consisting of elementary particles such as electrons interacting via standard electromagnetic forces. Although both the particles and the forces have been well-known for several centuries now, the laws of quantum mechanics allow for an astonishing number of phenomena. Many of these effects occur at extremely low temperatures, where quantum effects are predominant and the huge number of electronic degrees of freedom is drastically reduced to a still vast number of energetically favorable quantum states. Depending on microscopic details, the physics described by these accessible states can be of drastically different nature than the original system of interest. Such observations often motivate a reductionist approach, deriving simpler descriptions in terms of effective models that can be used to gain a better understanding of the complex behavior of interacting quantum particles. Quantum spin systems encapsulate a broad class of such problems, describing the interactions between immobile particles with intrinsic quantum mechanical angular momenta, commonly referred to as *quantum spins*. This simplified description has been immensely productive in identifying and characterizing new physical phenomena, often establishing spin models as the initial instructive example when establishing a new, much broader framework of physics, such as in the case of finite-temperature phase transitions, quantum entanglement, and the more recent field of emergent gauge theories. On the other hand, the challenges of directly solving a system of interacting quantum spins are still notoriously difficult, owing to the fact that the Hilbert space dimension grows exponentially with the number of particles. For instance, solving the Hamiltonian of just 100 interacting spins - arguably still far away from the physically interesting thermodynamic limit - requires diagonalizing a  $2^{100} \approx 10^{30}$  dimensional matrix. Storing only a single eigenvector alone would require about  $6 \times 10^{20}$  terabytes of memory, easily exceeding the limits of anything that could be built by modern technology.

The latter, in particular, will be one of the driving forces that motivate the developments presented within this thesis. Presently, nearly all of the fundamental theories found in physics are expressed as gauge theories, from the theory of electrodynamics over the theory of relativity and the standard model. In quantum magnets with an emergent gauge theory, it is possible to observe physics in an artificial universe, where different laws of physics apply. In such cases, the spin

degrees of freedom may *fractionalize*, meaning that the flip of a single spin creates two or more well-defined excitations, which may differ from all fundamental particles found in nature. These *quasiparticles* can fully separate, moving independently of each other and thus give rise to an entirely new description of physics, such as a full theory of quantum electromagnetism with a different fine-structure constant [12] or particles that are neither bosons nor fermions [13]. These properties, along with their technological prospects offered in the field of quantum information, make physical systems with emergent gauge theories of immense interest.

While the complexity of quantum many-body physics enables such fascinating effects, it simultaneously poses severe challenges that need to be overcome in order to correctly predict the physics of interacting systems. Toy models with the desired properties are often challenging to realize in experiments due to limitations in the control of microscopic interactions in real materials. It thus becomes necessary to devise new methods capable of handling these less perfect scenarios where exact solutions are unattainable. It can be easily checked that the mean-field descriptions of spin systems are fundamentally incapable of describing magnetically disordered states, let alone those with fractionalized particles and emergent gauge theories. In this context, auxiliary particle representations have become useful, as they provide a natural way for spins to fractionalize into fermionic or bosonic degrees of freedom [14]. Of course, solving the original problem of many interacting spins beyond the mean-field approximation remains severely challenging. This chapter will serve as a guide for important concepts and methods that will be used in the following chapters.

## 1.1. Introduction to quantum magnetism

It was in 1924, precisely one hundred years ago, that Ernst Ising's first attempt at explaining the origin of ferromagnetism was made using a simple classical model which has since become famous under the name *Ising model*. In this description, a magnet is thought to consist of a collection of binary microscopic magnets which are strictly localized on the sites of a lattice. While such discrete microscopic magnetic moments, so-called *spins*, indeed exist as inherent properties of most fundamental particles such as electrons, protons, and neutrons they are fundamentally of quantum mechanical nature. By contrast, in Ising's original description, they are treated as classical variables  $s_i = \pm 1$  that interact via a phenomenological

coupling  $J_{ij}$  such that the total energy of the system is given by

$$H = \frac{1}{2} \sum_{i,j} s_i J_{ij} s_j. \quad (1.1)$$

While Ising's original solution in one dimension was unable to find a phase transition at any finite temperature, follow-up works such as Lars Onsager's exact prediction of a finite temperature phase transition in two dimensions have paved the way for our modern understanding of magnetism [15, 16]. Astonishingly, even in more modern times, the Ising model remains a topic of interest, for instance in the study of spin glasses which culminated in the award of the 2021 physics Nobel prize to Giorgio Parisi [17] and can emerge from Eq. (1.1) by randomizing the couplings  $J_{ij}$ . However, it is easily argued that the description of spins as simple integers is ill-motivated in the general case and is thus blind to a vast number of exciting phases and phenomena. To treat spins faithfully in their full quantum mechanical nature, one must instead consider spin operators  $S^\alpha = \frac{\hbar}{2} \sigma^\alpha$ , where  $\hbar$  is the reduced Planck constant and. For spin-1/2, spin operators can be represented by the Pauli matrices

$$\sigma^x = \begin{pmatrix} 0 & 1 \\ 1 & 0 \end{pmatrix}, \quad \sigma^y = \begin{pmatrix} 0 & -i \\ i & 0 \end{pmatrix}, \quad \sigma^z = \begin{pmatrix} 1 & 0 \\ 0 & -1 \end{pmatrix}. \quad (1.2)$$

In the following, we shall thus consider a generalization of Eq. (1.1), for which we may define a Hamiltonian as

$$H = \frac{1}{2} \sum_{i,j} \sum_{\alpha\beta} S_i^\alpha J_{ij}^{\alpha\beta} S_j^\beta. \quad (1.3)$$

Note that the Ising limit is recovered for  $J_{ij}^{\alpha\beta} = J_{ij} \delta^{\alpha z} \delta^{\beta z}$ . In this case, the Hamiltonian only contains  $\sigma^z$  terms which mutually commute and can be replaced by their eigenvalues  $\pm 1$ . Usually, the limit of classical spins, represented as vectors, is recovered in the limit of large spin quantum numbers  $S$  [18, 19]. Another notable limit is the isotropic Heisenberg model  $J_{ij}^{\alpha\beta} = J_{ij} \delta^{\alpha\beta}$ , which itself can be seen as a special case of the Hubbard model at half filling [20]. In the following chapters, a system of natural units will be considered where  $\hbar = k_B = 1$ , where  $k_B$  is the Boltzmann constant.

## 1.2. Different types of order

Equation (1.3) encapsulates a vast spectrum of observable phenomena, ranging from simple paramagnets to thermal or quantum phase transitions into mag-

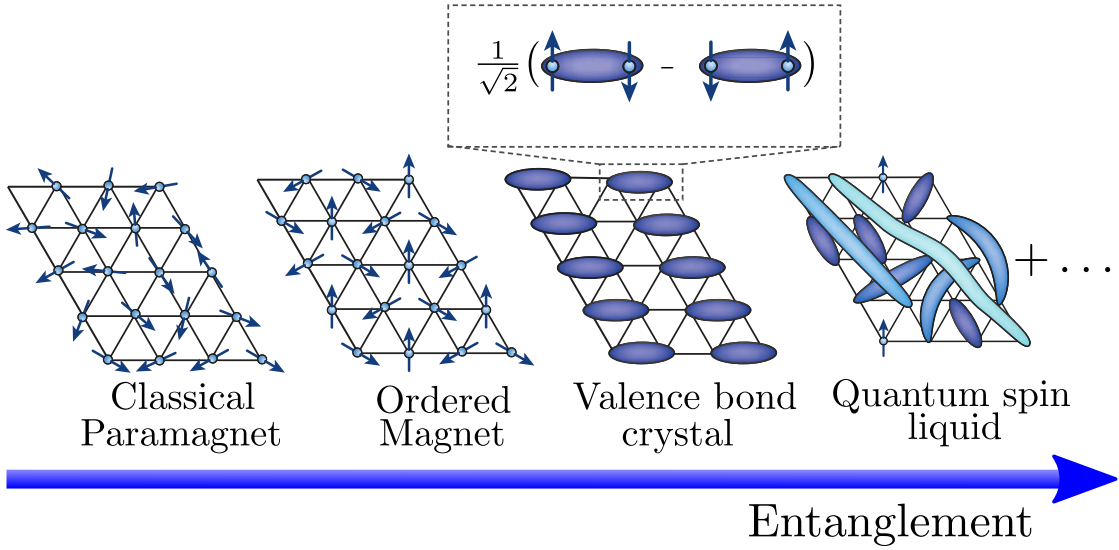


Figure 1.1.: Magnetic phases of quantum spin systems. Partially adapted from Ref. [29].

netically ordered phases, peculiar effects such as order-by-disorder phase transitions [21, 22] or magnetically disordered low-temperature phases [23–28]. These spin systems can also exhibit more rare quantum phases of matter such as *valence bond solids*, which instead break translational or rotational symmetries [8, 27] or even highly exotic *quantum spin liquid* phases which do not break any conventional order at all, see Fig. 1.1. Ordered phases are typically well understood in the Landau paradigm, i.e., by defining a local *order parameter*  $\langle \mathcal{O} \rangle$  which is nonzero only in the ordered phase. By contrast, any local order parameter has to vanish for a quantum spin liquid. To distinguish such an exotic state from a trivial paramagnet (which likewise does not break any symmetry of the Hamiltonian) the framework of Landau theory becomes obsolete and must be replaced by a more sophisticated description using gauge theories which are to be introduced later in Section 1.4. Nonetheless, the concepts of conventional order prove quintessential in the study of magnetic phases of Eq. (1.3) and will be briefly reviewed here. As an example, let us first consider the case of magnetic order in which spins align in a regular pattern. The most prominent case of this is, of course, ferromagnets, where spins are all aligned along one direction allowing us to define a magnetization

$$M^\alpha = \frac{1}{N_{\text{sites}}} \sum_i^{N_{\text{sites}}} \langle S_i^\alpha \rangle. \quad (1.4)$$

It should be clear that this quantity can be used to distinguish between a ferromagnetic state, which has a finite value of  $M$ , and a paramagnetic phase, which has



$M = 0$  if one does not apply an external magnetic field. Note that in the case of antiferromagnetic order, i.e., an anti-alignment of spins on neighboring sites, Eq. (1.4) needs to be replaced by a staggered magnetization  $M_s^\alpha = \frac{1}{N_{\text{sites}}} \sum_i^{N_{\text{sites}}} (-1)^i \langle S_i^\alpha \rangle$ . There is, however, a subtlety: It is evident from Eq. (1.3) that states with  $M^\alpha$  have the same energy as states with a magnetization of  $-M^\alpha$ . Even an exact solution of Eq. (1.3) will thus never predict a finite magnetization upon averaging over degenerate ground states. While nature provides perturbations that are able to lift this degeneracy and allow for a spontaneous breaking of symmetry, in a theoretical calculation such a perturbation has to be introduced by hand, for instance by a magnetic field  $\mathbf{h}$  that is to be taken to zero at the end of the calculation. We can then quantify a system's tendency to form magnetic order by defining the so-called *magnetic susceptibility*

$$\chi^{\alpha\beta} \equiv \left. \frac{\partial M^\alpha}{\partial h^\beta} \right|_{\mathbf{h}=0}. \quad (1.5)$$

A system that exhibits ferromagnetic order will have a diverging susceptibility in the thermodynamic limit, as any infinitesimal change in the magnetic field will yield a drastic response of the magnetization, making the magnetic susceptibility a powerful tool to study phase transitions. Moreover, by making use of linear response theory, one can show that the susceptibility can also be computed from a spin-spin correlation function. Generalizing Eq. (1.5), this may be written as

$$\begin{aligned} \delta M^\alpha(t) &= \sum_\beta \sum_{ij} \int_{-\infty}^{\infty} dt' \chi_{ij}^{\alpha\beta}(t, t') h_\beta(t') \\ \chi_{ij}^{\alpha\beta}(t, t') &= i\theta(t - t') \langle [S_i^\alpha(t), S_j^\beta(t')] \rangle. \end{aligned} \quad (1.6)$$

where  $\delta M^\alpha$  is the response in magnetization,  $\theta$  the Heaviside step-function  $[A, B] = AB - BA$  the commutator of two operators  $A$  and  $B$ , and  $S_i^\alpha(t)$  the time-dependent spin operator in the Heisenberg picture. The average  $\langle \mathcal{O} \rangle$  of an operator  $\mathcal{O}$  at temperature  $T$  is performed as usual as  $\frac{1}{\mathcal{Z}} \text{Tr} [e^{-H/T} \mathcal{O}]$ , where  $\mathcal{Z} = \text{Tr} [e^{-H/T}]$  is the *partition function*. Note that energy conservation implies that  $\chi_{ij}^{\alpha\beta}(t, t')$  is a function of  $t - t'$  only, so that we may consider  $\chi_{ij}^{\alpha\beta}(t) \equiv \chi_{ij}^{\alpha\beta}(t, 0)$  without loss of generality.

Instead of considering the correlations between all sites  $i, j$ , for translation-invariant systems, it is more convenient to consider the Fourier transform of the susceptibility

$$\chi(\mathbf{q}, t) = \frac{1}{N_{\text{sites}}} \sum_{ij} e^{-i\mathbf{q}(\mathbf{r}_i - \mathbf{r}_j)} \chi_{ij}(t), \quad (1.7)$$

While it has been argued that a divergent susceptibility signals a magnetic phase transition, much can be learned from the precise nature of this divergence. First and foremost, the momentum  $\mathbf{q}$  at which this divergence occurs characterizes the type of magnetic order, for instance, a ferromagnet will have a divergence at  $\mathbf{q} = (0, 0, 0)$ , while an antiferromagnet will have a divergence at  $\mathbf{q} = (\pi, \pi, \pi)$ . A profound observation is the scaling behavior of  $\chi(\mathbf{q}) \sim (T - T_c)^\gamma$  near second-order phase transitions at a critical temperature  $T_c$ . This scaling is universal, meaning that the dimensionless constant  $\gamma$  does not depend on microscopic details of the system but instead on the universality class of the phase transition. For instance, in the Heisenberg universality class, it is found as  $\gamma \approx 1.39$  [30]. In later parts of this thesis, we shall see how this knowledge can be used to correctly determine the critical temperature of a phase transition, even in the presence of finite-size effects.

### Related quantities

Next to the magnetic susceptibility defined here, related and often mathematically equivalent quantities can also be found in the literature. For instance, the *dynamic spin structure factor*  $S(\mathbf{q}, \omega)$  is defined as

$$S^{\alpha\beta}(\mathbf{q}, \omega) = \frac{1}{N_{\text{sites}}} \sum_{ij} e^{-i\mathbf{q}(\mathbf{r}_i - \mathbf{r}_j)} \int_{-\infty}^{\infty} dt e^{i\omega t} \langle S_i^\alpha(t) S_j^\beta(0) \rangle. \quad (1.8)$$

It is a quantity that can be measured in inelastic neutron scattering experiments and its frequency dependence  $\omega$  contains information about spectrum of excitations. By the *fluctuation-dissipation theorem* the dynamic structure factor is related to the susceptibility as [31]

$$\text{Im}\chi(\mathbf{q}, \omega) = \frac{1 - e^{-\omega/T}}{2} S(\mathbf{q}, \omega). \quad (1.9)$$

Note that in many cases, determining dynamic correlators a technically challenging problem. A powerful approach is the *imaginary time formalism*, where one replaces the time variable  $t$  by an imaginary time  $\tau = it$ , such that time evolution  $e^{iHt}$  becomes equivalent to the density matrix  $e^{-H/T}$ .

The imaginary time susceptibility  $\chi^{\alpha\beta}(\mathbf{q}, i\omega_n)$  can be used to compute the dynamic structure factor, if the former is known analytically. An infamous problem arises if this is not the case, as the numerical analytic continuation from imaginary to real frequencies is an ill-defined problem, as small errors in the numerical result can cause drastically different results.

In numerical solutions which are often limited to finite system sizes  $L$ , phase transitions between magnetically ordered and paramagnetic phases are typically identified via a finite size scaling of the susceptibility, or, alternatively, the correlation length  $\xi$  which can be obtained from the equal-time spin structure factor  $S(\mathbf{q})$  [32] via

$$\xi = \frac{L}{2\pi} \sqrt{\frac{S(\mathbf{q}^*)}{S(\mathbf{q}^* + \frac{2\pi}{L}\mathbf{e}_{\mathbf{q}^*})} - 1}. \quad (1.10)$$

Here,  $L$  is the maximal distance beyond which spin correlations are set to zero (for example the system size) and  $\mathbf{q}^*$  is the point in reciprocal space where  $S(\mathbf{q})$  is maximal which corresponds to the wave vector of the magnetic order to be probed. Furthermore,  $\mathbf{e}_{\mathbf{q}^*}$  is a unit vector in reciprocal space that points towards the direction of deepest descend away from  $\mathbf{q}^*$ . Crucially, a finite  $L$  has a similar effect than a finite system size such that precisely at the critical temperature the correlation length behaves as  $\xi \sim L$ . This criterion is used to detect critical ordering temperatures in numerical runs with varying  $T$  and  $L$ .

### 1.3. The self-consistent gaussian approximation

The Hamiltonian in Eq. (1.3) poses a formidable challenge and is typically devoid of exact solutions in almost all cases. The underlying difficulty is the exponential growth of the Hilbert space, for example, for spin-1/2, as the dimension grows as  $2^N$ , making any attempt at diagonalizing the exponentially large Hamiltonian matrix only possible for very small systems of about 30-40 sites. On the other hand, most emergent phenomena are inherent many-body effects, requiring us to study large, ideally infinite, systems.

Nonetheless, there are ways to extract some information even in such cases, which shall be reviewed in the following. One of the simplest approximations is to disregard quantum effects entirely and instead work with classical variables. It should be clear that this approximation is of a rather qualitative nature. Nonetheless, a good understanding of a model is often obtained by considering the effect of small quantum fluctuations around a classical ground state, as we shall see in Section 1.4. The Ising model in Eq. (1.1) is an example of this since the spin operators  $s_i = \sigma_i^z/2$  all mutually commute and may thus be replaced by their eigenvalues  $\pm 1/2$ , yielding a fully classical Hamiltonian. The goal then becomes to minimize the quantity  $H$ , a real number, as a function of all the spin variables  $s_i$ . While this may appear simple at first, the catch is that the solution must obey the constraint

that all spins must have values of either  $-1/2$  or  $1/2$ . This makes it impossible to find the minimum as  $\frac{d}{ds_i}H = 0$ . One may appreciate just how difficult solving the quantum many-body problem truly is: Even under the drastic simplification of disregarding quantum effects, the Ising model is one of *Karp's 21 NP-complete problems* [33, 34], and thus equivalent to the most difficult problems known to humanity. While approximate solutions can usually be found numerically to high precision with Monte Carlo approaches [35], here we discuss an analytical technique called the self-consistent Gaussian approximation, or sometimes the large- $\mathcal{N}$  method, which is ubiquitous in the study of classical frustrated magnets due to its simplicity [36–47].

We consider a general spin Hamiltonian as in Eq. (1.3). Ultimately, our strategy will be to simplify the problem at hand by relaxing the spin constraint  $|\mathbf{S}_i| = 1/2$  [48]. A symmetric crystal lattice can be expressed by a unit cell with a finite number of (sublattice) sites as well as lattice vectors. Translating any site by such a vector will result in the position of another site of the same sublattice. To make use of this translational symmetry, the Hamiltonian is first rewritten in terms of the Fourier transform of spin components on each sublattice, which are indicated by roman letters, a, b:

$$S_a^\alpha(\mathbf{q}) = \frac{1}{\sqrt{N_{\text{cells}}}} \sum_{i \in a} e^{-i\mathbf{q}\mathbf{r}_i} S_i^\alpha, \quad S_i^\alpha = \frac{1}{\sqrt{N_{\text{cells}}}} \sum_{\mathbf{q}} e^{i\mathbf{q}\mathbf{r}_i} S_a^\alpha(\mathbf{q}). \quad (1.11)$$

We may identify  $\frac{1}{N_{\text{cells}}} \sum_{i \in a} \sum_{j \in b} J_{ij}^{\alpha\beta} e^{-i\mathbf{q}(\mathbf{r}_i - \mathbf{r}_j)} \equiv J_{ab}^{\alpha\beta}(\mathbf{q})$  as the Fourier transform of the couplings, which we assume only depend on the separation vector between the two sites  $i, j$ . To simplify notation, we group sublattice and spin components together and define *superlabels*:

$$\mathbf{a} \equiv (\alpha, a), \quad \mathbf{b} \equiv (\beta, b) \quad (1.12)$$

and finally arrive at

$$H = \frac{1}{2} \sum_{\mathbf{q}} \sum_{\mathbf{ab}} S^{\mathbf{a}}(\mathbf{q}) J_{\mathbf{ab}}(\mathbf{q}) S^{\mathbf{b}}(-\mathbf{q}). \quad (1.13)$$

As an example, consider a Heisenberg model ( $N = 3$ ) on a honeycomb lattice, which features 2 sites per unit cell.  $J_{\mathbf{ab}}$  becomes a  $(6 \times 6)$  matrix. Due to the highly symmetric Heisenberg interactions  $J_{\mathbf{ab}} \equiv J_{\mathbf{ab}}^{\alpha\beta} = J_{\mathbf{ab}} \delta^{\alpha\beta}$ , this matrix can be decomposed into 3 independent  $2 \times 2$  blocks.

Ground states of Eq. (1.13) can be found by diagonalizing  $J_{\mathbf{ab}}(\mathbf{q})$  and minimizing its eigenvalues  $E^{\mathbf{a}}(\mathbf{q})$ . In the generic case, this minimum will be at a unique

ordering wave vector  $\mathbf{q}$  up to point group symmetries of the Hamiltonian, such as rotations and reflections. Here, one may reasonably expect magnetic order in the ground state despite the approximations made, as there is typically a valid spin configuration of similar energy that can be described by such a wave vector, such as, for instance, a spin spiral  $\mathbf{S}(\mathbf{q}) \sim (\cos \mathbf{q} \cdot \mathbf{r}, \sin \mathbf{q} \cdot \mathbf{r}, 0)$ . On the other hand, a large degeneracy in the spectrum  $E^{\mathbf{a}}(\mathbf{q})$  can be an indicator of more complex behavior that motivates closer inspection.

Beyond identifying ground states, observables can be computed at arbitrary temperature from the partition function:

$$\mathcal{Z} = \int D\lambda \int \mathcal{D}\mathbf{S} e^{-H/T + \sum_a \sum_{i \in a} \lambda_{ia} (\sum_\alpha S_{ia}^\alpha S_{ia}^\alpha - 1)}. \quad (1.14)$$

Here, the  $\lambda_{ia}$  correspond to Lagrange multipliers, which exactly enforce the spin constraint  $|\mathbf{S}_i|^2 = 1$  on *each site*<sup>1</sup>, and the path integrals over the classical fields  $S_i^{\mathbf{a}}, \lambda_i$  are defined by integrating over all configurations of each field, for example,  $\int \mathcal{D}S \equiv \int \prod_i \prod_{\mathbf{a}} dS_i^{\mathbf{a}}$  [30, 49]. By inserting the Fourier transform from Eq. (1.11), we may also write this using an equivalent transform for  $\lambda_{i,a}$  as in Eq. (1.11)

$$\mathcal{Z} = \int D\lambda \int \mathcal{D}\mathbf{S} e^{-\sum_{\mathbf{ab}} \sum_{\mathbf{qq}'} S^{\mathbf{a}}(\mathbf{q}) (\frac{1}{T} J_{\mathbf{ab}}(\mathbf{q}) \delta(\mathbf{q} + \mathbf{q}') - \lambda_a(\mathbf{q} - \mathbf{q}') \delta_{\mathbf{ab}}) S^{\mathbf{b}}(\mathbf{q}') - \sum_{\mathbf{aq}} \lambda_a(\mathbf{q})} \quad (1.15)$$

$$\equiv \int D\lambda \int \mathcal{D}\mathbf{S} e^{-\sum_{\mathbf{ab}} \sum_{\mathbf{qq}'} S^{\mathbf{a}}(\mathbf{q}) M_{\mathbf{ab}}(\mathbf{q}, \mathbf{q}') S^{\mathbf{b}}(\mathbf{q}') - \sum_{\mathbf{aq}} \lambda_a(\mathbf{q})}, \quad (1.16)$$

where  $M_{\mathbf{ab}}(\mathbf{q}, \mathbf{q}') = \frac{1}{T} J_{\mathbf{ab}}(\mathbf{q}) \delta(\mathbf{q} + \mathbf{q}') - \lambda_a(\mathbf{q} - \mathbf{q}') \delta_{\mathbf{ab}}$ . For any generic two-body Hamiltonian  $H$ , we can verify that the spin-dependent part in the exponent is quadratic in  $S$ , taking the abstract form of a generalized matrix product  $S_n M_{nm} S_m$ , and thus allowing us to perform the Gaussian integral analytically [36, 38, 41, 43, 45, 47], yielding:

$$\mathcal{Z} = \int D\lambda \exp \left\{ -\frac{1}{2} \text{Tr} \{ \log M \} - \sum_{\mathbf{aq}} \lambda_a(\mathbf{q}) \right\}. \quad (1.17)$$

Note that any constant prefactors of  $\mathcal{Z}$  are neglected here and in the following since they do not contribute to observables.

In order to solve the final integration, one has to rely on the saddle-point approximation, assuming that the exponent is a function with a single well-defined minimum around which it may be expanded as a function of  $\lambda^2$ . To simplify

<sup>1</sup>Since observables do not depend on constant prefactors of  $\mathcal{Z}$  but rather its derivatives, we can freely define rescaled Lagrange multipliers, where here a factor of  $1/i$  is chosen.

<sup>2</sup>In most derivations found in literature, this approximation is motivated by assuming isotropic exchange couplings such that the trace over spin components yields a simple factor  $\mathcal{N}$  of the number of spin components. Subsequently, this number is taken to the limit  $\mathcal{N} \rightarrow \infty$ , such that the exponential function becomes an infinitely sharp peak centered.

this part even further, one usually makes the approximation of neglecting spatial fluctuations by setting  $\lambda_a(\mathbf{q}) \rightarrow \lambda\delta(\mathbf{q})$ .

$$\mathcal{Z} = \exp\left\{-\frac{1}{2} \text{Tr}\{\log M(\lambda_0)\} - N_{\text{sites}}\mathcal{N}\lambda_0\right\}. \quad (1.18)$$

The minimum of the exponent is given by taking the derivative with respect to the single remaining variable  $\lambda$

$$\begin{aligned} N_{\text{sites}} &= -\frac{1}{2} \text{Tr}\left[M^{-1}\right] \\ 1 &= -\frac{1}{2N_{\text{sites}}} \sum_q \sum_{\mathbf{a}} [J(\mathbf{q})/T - \lambda\mathbb{1}]^{-1}_{\mathbf{aa}}. \end{aligned} \quad (1.19)$$

Once the Lagrange multiplier  $\lambda$  is determined by solving Eq. (1.19), observables are determined by taking functional derivatives of the partition function. For example, it is easily verified by using Eqs. (1.15) and (1.18) that the spin structure factor is given by

$$\mathcal{S}^{\mathbf{ab}}(\mathbf{q}) = \langle S^{\mathbf{a}}(\mathbf{q})S^{\mathbf{b}}(-\mathbf{q}) \rangle = \frac{1}{\mathcal{Z}} \frac{\delta \mathcal{Z}}{\delta J(\mathbf{q})_{\mathbf{ab}}} = \frac{\delta \log \mathcal{Z}}{\delta J(\mathbf{q})_{\mathbf{ab}}}. \quad (1.20)$$

Using this with our result Eq. (1.18), we find

$$\begin{aligned} \mathcal{S}^{\mathbf{ab}}(\mathbf{q}) &= -\frac{1}{2} \sum_{\mathbf{q}'} \sum_{\mathbf{a}'} \frac{\delta}{\delta J_{\mathbf{ab}}(\mathbf{q})} [\log J(\mathbf{q}')/T - \lambda\mathbb{1}]_{\mathbf{a}'\mathbf{a}'} \\ &= -\frac{1}{2} \sum_{\mathbf{q}'} \sum_{\mathbf{a}'} \frac{\delta J(\mathbf{q}')}{\delta J_{\mathbf{ab}}(\mathbf{q})} [J(\mathbf{q}')/T - \lambda\mathbb{1}]_{\mathbf{a}'\mathbf{a}'}^{-1} \\ &= -\frac{1}{2T} M_{\mathbf{ba}}^{-1}(\mathbf{q}). \end{aligned} \quad (1.21)$$

This result also allows for a particularly simple interpretation of Eq. (1.19), namely that the correct choice of  $\lambda$  implies the fulfillment of the sum rule:

$$\sum_{\mathbf{a}} \sum_i \langle |S_i|^2 \rangle = \sum_{\mathbf{a}} \sum_{\mathbf{q}} \langle S^{\mathbf{a}}(\mathbf{q})S^{\mathbf{a}}(-\mathbf{q}) \rangle = N_{\text{sites}}, \quad (1.22)$$

or in other words, the spin length constraint is fulfilled on average [48]. Clearly, this approximation is not quantitatively reliable, particularly when a system features more than one inequivalent site per unit cell. Corrections, including spatial fluctuations of  $\lambda_a(\mathbf{q})$ , can be obtained within the so-called *nematic bond theory* [37, 46]. However, the Gaussian approximation remains a very popular tool in the study of classical spin models due to its simplicity. In particular, for some models at zero

temperature, instead of solving Eq. (1.19), the spin structure factor in Gaussian approximation can be obtained by projecting out certain spin components [50, 51], making this approximation a practical starting point for several classifications of classical spin liquids [52–54]. This will be discussed in more detail in Sections 6.3 and 7.2.

## 1.4. Emergent gauge theories and quantum spin liquids

Depending on the context, the definition of what a quantum spin liquid is often changes. One of the simplest and thus widespread definitions is that a quantum spin liquid is a phase of matter that lacks any type of ordering down to zero temperature [14, 29, 55–58]. While this definition captures many essential qualities, it clearly includes some phases of matter that do not display any inherently interesting phenomena. For instance, a trivial system consisting of a number of  $N$  fully free, non-interacting spins will clearly never display any ordering. This example might sound contrived (in any realistic setting, small couplings will generally be generated one way or another), but it nonetheless shows that a rigorous definition of a material beyond conventional order needs to go beyond conventional ordering concepts itself. It is also practically impossible to verify the absence of any possible type of order, since one would need to check increasingly complex order parameters.

Perhaps a better definition of a quantum spin liquid is a phase that can be described by an *emergent gauge theory* [56], a theory in which a subset of the original spin degrees of freedom (typically those states that are accessible at low energies) form new, effective degrees of freedom that can be analogous to excitations of quasiparticles with fascinating properties that may be rare or even impossible to find in nature. Most famously, a single spin-flip excitation may *fractionalize*, i.e., form a pair of quasiparticles with fractional charges or spin moments that can separate and move independently of each other. While interesting on its own, feasible realizations of fractionalized particles can serve as a stable form of quantum memory or even be used as a platform to achieve topological error correction in quantum computers. We will now begin by reviewing a famous example of how a particularly well-known gauge theory,  $U(1)$  electrodynamics, can emerge from simple spin degrees of freedom in real materials.

In cases where the spectrum has a subextensive degeneracy, i.e., the minima of  $E^{\mathbf{a}}(\mathbf{q})$  form lines or surfaces with a dimension less than the dimension of the lattice, the ground state may be disordered, or selected entirely from entropic fluctuations via a mechanism known as thermal *order by disorder*. In some special cases, the degeneracy may even be extensive, i.e., one band  $E^{\mathbf{a}}(\mathbf{q})$  is completely flat. Even thermal fluctuations are then usually insufficient to select a unique ground state, giving rise to a *classical spin liquid*. Probably the most illustrious example of this can be found in the *pyrochlore lattice*, which features a four-site unit cell ( $\mathbf{b}_0 = 0$ ,  $\mathbf{b}_i = \frac{1}{2}\mathbf{a}_i$ ), within a face-centered cubic (fcc) basis

$$\mathbf{a}_1 = \frac{1}{2}(1, 1, 0)^T, \quad \mathbf{a}_2 = \frac{1}{2}(1, 0, 1)^T, \quad \mathbf{a}_3 = \frac{1}{2}(0, 1, 1)^T. \quad (1.23)$$

This way, the sites are arranged on the vertices of corner-sharing tetrahedra as depicted in Fig. 1.2. An extensive ground state degeneracy emerges in the case of antiferromagnetic nearest-neighbor interactions, where for now we only consider Ising interactions.

$$\begin{aligned} H &= J \sum_{\langle ij \rangle} S_i^z S_j^z \\ &= \frac{J}{2} \sum_{\blacktriangle} \left( \sum_{i \in \blacktriangle} S_i^z \right)^2 + \text{const.}, \end{aligned} \quad (1.24)$$

where the second line, featuring a sum over all tetrahedra  $\blacktriangle$  in the system, is readily verified upon expanding the square. It can now be seen that any spin configuration in which the total magnetization of each tetrahedron is zero, i.e.,

$$\sum_{i \in \blacktriangle} S_i^z = 0 \quad \forall \blacktriangle \quad (1.25)$$

realizes an exact ground state with an energy of 0. Such a rule is known as an *ice rule*, and the corresponding state is *spin ice*, in analogy to observations in water ice where the proton configurations of  $\text{H}_2\text{O}$  molecules remain fluctuating down to arbitrarily low temperatures, leading to a highly unusual residual entropy at zero temperature [59]. Although such a phase was already predicted by Anderson in 1956 [60], an experimental realization was only found much later in 1997 in the material  $\text{Ho}_2\text{Ti}_2\text{O}_7$  [61–64] and shortly after in  $\text{Dy}_2\text{Ti}_2\text{O}_7$  [65–67], featuring a local, ferromagnetic Ising anisotropy instead of an antiferromagnetic one as in Eq. (1.24). Such an anisotropy causes spins to either point inside a tetrahedron or outside, as depicted in Fig. 1.2. Note that the ground state constraint  $\sum_{i \in \blacktriangle} S_i^z = 0$  translates to a “two-in, two-out” rule, however, otherwise not much changes in its mathematical description. We may now identify the ground state constraint 1.25 in terms



of classical electrostatics, a  $U(1)$  gauge theory. To this end, one may perform a coarse-graining of the spins to a continuous field  $\mathbf{E}(\mathbf{r})$ , which points in the direction of the spins and thus has no sources and no drains, as dictated by the “two-in, two-out” rule. In other words, the electric field satisfies a charge-free Gauss law.

$$\nabla \cdot \mathbf{E}(\mathbf{r}) = 0 \Leftrightarrow \mathbf{q} \cdot \mathbf{E}(\mathbf{q}) = 0. \quad (1.26)$$

Instead of coarse-graining, one may formulate a discrete version of electrodynamics by defining an electric field on a dual lattice as a linear combination of spins on each sublattice and identifying Eq. (1.25) as a discretized gradient [52, 68]. Indeed, this slightly more involved description will be necessary for the description of quantum spin ice.

The existence of an extensive degeneracy can be easily seen in the Gaussian approximation by diagonalizing  $H$  in momentum space, but can also be verified exactly in the Ising case by considering the effect of elementary excitations. As shown in Fig. 1.2, a single spin flip acting on a ground state creates two defect tetrahedra which can be seen as electric charges  $\sum_{i \in \triangle} S_i^z = \pm 2|S_i^z|$  since they are given by the divergence of the electric field<sup>3</sup>.

In a system, charges are always conserved: This may be proved using Gauss’ law in the same way as in conventional electromagnetism by integrating the charge density  $\rho(\mathbf{r}) = \nabla \cdot \mathbf{E}(\mathbf{r})$  over some volume  $V$  with boundary  $S$ .

$$\int_V d^3r \rho(\mathbf{r}) = \int_{S=\partial V} d\mathbf{A} \cdot \mathbf{E}(\mathbf{r}) = Q_{\text{enclosed}}. \quad (1.27)$$

Any change in the total charge  $Q_{\text{enclosed}}$  must thus be due to transport across the boundary  $S$ , and the total charge, integrating over all space, is always zero. While charges must always be created in pairs as a result, they are free to propagate through the lattice by consecutive spin flips, as visible in Fig. 1.2. In particular, positive and negative charges can recombine into the vacuum state, leaving behind only a closed loop of flipped spins, a so-called *Dirac string*. This string is not a physical object as it corresponds to a gauge transformation  $\mathbf{E} \rightarrow \mathbf{E} + \nabla \times \chi$ , however, it illustrates the extensive ground state degeneracy since it consists only of a finite number of spins, with the smallest possible loop consisting of six spins. Interestingly, this phase comes with an easily measurable smoking gun signature,

---

<sup>3</sup>Since the emergent field is given by spins which have an intrinsic magnetic field, the emergent field is sometimes referred to as a magnetic field instead. The charges of this theory are then referred to as magnetic monopoles in a seeming violation of the laws of electrodynamics. While there is some arbitrariness in defining the electric and magnetic field, quantum fluctuations will guarantee the emergence of the respective other field with corresponding charges. Generally, magnetic monopoles can arise on a discrete version of the gauge theory since the vector potential is only defined up to a phase  $2\pi$  in contrast to continuum theories.

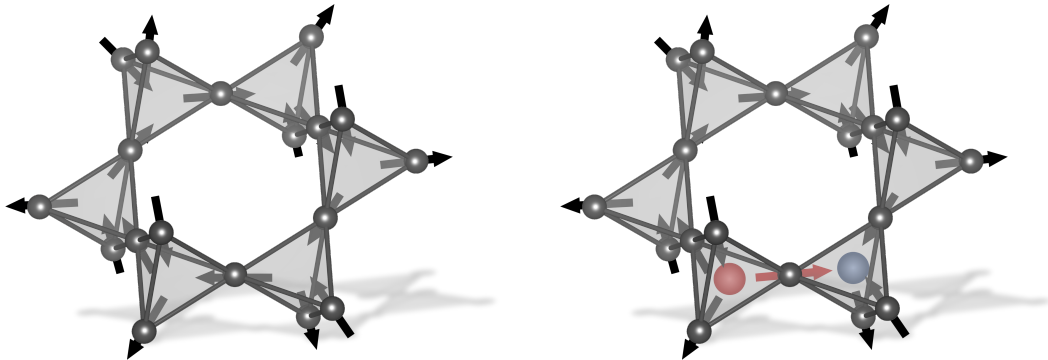


Figure 1.2.: Spin fractionalization

a rare property for spin liquids [29, 55, 57, 69], so-called *pinch point* features in the spin structure factor [36, 41, 42, 70]. While the structure factor is commonly used to study magnetic order, the presence of a local ice-rule constraint results in non-analyticities in the structure factor that are experimentally observable [71]. As outlined further in Chapter 5 and Chapter 6, thermal and quantum fluctuations have predictable effects on these pinch points, which may be used as a diagnostic tool to distinguish between different types of spin liquids.

Clearly, the presence of such a large degeneracy is highly artificial. Realistically, small perturbations to the model in Eq. (1.24) will lift this degeneracy and select a unique ground state leading to a vanishing entropy at zero temperature. However, this ground state does not necessarily have to be magnetically ordered and indeed may be highly exotic if this perturbation introduces quantum fluctuations. The most natural step to investigate this is to include small terms that allow for spin flip processes

$$H = \frac{J}{2} \sum_{\langle ij \rangle} S_i^z S_j^z + J_{\perp} \sum_{\langle ij \rangle} S_i^+ S_j^- + \text{h.c.} \quad (1.28)$$

and perform a degenerate perturbation theory in  $J_{\perp}/J$  [40, 72]. We may think of the Ising model as a trivial quantum model, in which the Hamiltonian consists of  $1 \times 1$  blocks, corresponding to the choice of the eigenvalues  $\sigma_i^z \rightarrow \pm 1$ . It can be seen that the first order in perturbation theory vanishes since  $\langle \mathbf{x}' | S_i^+ S_j^- | \mathbf{x} \rangle = 0$  for any two classical spin configurations  $\mathbf{x}, \mathbf{x}'$ , with  $\mathbf{x} = (\uparrow_1, \downarrow_2, \dots, \uparrow_{N_{\text{sites}}})$  in the ground state manifold. The lowest order non-diagonal process that tunnels between two classical ground states are third order terms that flip an entire hexagonal plaquette of spins, see Fig. 1.2. The effective low-energy description is thus given by plaquette moves that flip a counterclockwise alignment of six spins to a clockwise one and

vice versa <sup>4</sup>:

$$H_{\text{eff}} = - \sum_{\square} S_{\square_1}^+ S_{\square_2}^- S_{\square_3}^+ S_{\square_4}^- S_{\square_5}^+ S_{\square_6}^- + \text{h.c.} \quad (1.29)$$

$$\equiv - \sum_{\square} |\circ\rangle\langle\circ| + |\circ\rangle\langle\circ|. \quad (1.30)$$

While sign-problem free and thus numerically solvable by quantum Monte Carlo [74, 75], some analytical understanding can be gained by interpreting this Hamiltonian as a variant of a quantum dimer model [76, 77].

$$H_{\text{RK}} = - \sum_{\square} |\circ\rangle\langle\circ| + |\circ\rangle\langle\circ| + \mu(|\circ\rangle\langle\circ| + |\circ\rangle\langle\circ|). \quad (1.31)$$

This model features an exactly soluble point at the *Rokhsar Kivelson* point  $\mu = 1$ , where the Hamiltonian takes the form of a projector

$$H_{\text{RK}}|_{\mu=1} = \sum_{\square} (|\circ\rangle - |\circ\rangle)(\langle\circ| - \langle\circ|). \quad (1.32)$$

The lowest energy of such a projector, 0, can only be reached by the state that is annihilated by it. This state is an equal weight superposition of all possible classical configurations (up to a normalization constant)

$$|\psi_{\text{RK}}\rangle = \sum_{\{\mathbf{x}\}} |\mathbf{x}\rangle. \quad (1.33)$$

This state features massive entanglement and is a realization of the resonating valence bond state originally proposed by Anderson [78], in other words, a *quantum spin liquid*.

The effective theory of this ground state and its low-lying excitations is a theory of lattice quantum electrodynamics, a compact  $U(1)$  lattice gauge theory<sup>5</sup>, meaning that it is characterized by canonically conjugate fields  $[A_i^\alpha, E_j^\beta] = i\hbar\delta_{ij}\delta^{\alpha\beta}$ , where  $A$  is the corresponding *vector potential*. In this context, compactness refers to the fact that the magnetic field, given by a discrete form of the curl  $\mathbf{B} = \nabla_{\square} \times \mathbf{A}$ , is

---

<sup>4</sup>Note that the sign of this Hamiltonian does not affect the low energy properties as it can be accounted for in a unitary transformation [73]

<sup>5</sup>Strictly speaking, this gauge theory is also *frustrated* as the mapping to a  $U(1)$  theory is not exact. This is due to the subtlety that the electric field is expected to take integer values  $\dots, -1, 0, 1, \dots$ , while spins quantum numbers are half-integers which exclude a value of 0. This has important consequences, as otherwise, the gauge theory would always be confined, meaning quasiparticle excitations are not free to move and would quickly decay. See Ref. [68] for more details.

only uniquely determined up to a multiplicity of  $2\pi$  [55, 68]. Being a realization of quantum electrodynamics, this theory predicts the excitation of linearly dispersing photons as well as electric and magnetic monopoles, also referred to as *spinons* and *visons*, respectively [79, 80]. Finally, recent discoveries in the compounds of dipolar-octupolar pyrochlores such as  $\text{Ce}_2\text{Zr}_2\text{O}_7$  pose promising candidate systems to realize quantum spin liquids and observe artificial photons in real materials [80–87].

### Other types of spin liquids

Quantum spin ice is a particularly instructive example of how a gauge theory can emerge from simple spin degrees of freedom. However, there are many other classes of spin liquids that can emerge. One of the most prominent examples is the so-called  $\mathbb{Z}_2$  spin liquid found as an exact ground state in Kitaev’s Toric code and Honeycomb models [13, 88]. Instead of an emergent  $U(1)$  degree of freedom (i.e., the gauge field can change by a phase  $e^{i\phi}$ ), this gauge field has only a discrete degree of freedom  $\pm 1$ , and thus has vastly different properties. Most importantly, while the aforementioned  $U(1)$  liquids come with gapless quasiparticle excitations (photons, in the previous case),  $\mathbb{Z}_2$  liquids typically have a topologically degenerate ground state with a finite excitation gap, making them highly stable against small and local perturbations [13, 88, 89]. Being a very active field of experimental investigation, there are several candidate materials with suitable interactions for hosting a  $\mathbb{Z}_2$  quantum spin liquid, although no consensus has been reached so far on the existence of this spin liquid phase.

Recently, significant advancements in the field of cold atoms have led to promising results in realizing  $\mathbb{Z}_2$  spin liquids via Rydberg atom arrays [90–93]. There are numerous other types of spin liquids, for instance, the gapless Dirac spin liquids believed to be found as the ground state of the Heisenberg model on the Kagome and triangular lattices [94–97], which also exhibit an emergent  $U(1)$  gauge field, or chiral spin liquids [98–100], which have a chiral order parameter and thus break time-reversal symmetry but do not order magnetically.

In Chapter 6, the even more exotic case of so-called *fracton spin liquids* will be investigated. As we will see, fracton models can be constructed classically, following local rules in close analogy to spin ice [51, 101]. However, it is still an ongoing topic of research to determine if and how the effect of quantum fluctuations can be used to install quantum fracton order.

## 1.5. Fractons and higher-rank gauge theories

We shall now investigate a new type of spin liquid, which, surprisingly, has a close connection to the pyrochlore model. Fractons, particles with restricted or fully absent mobility [102–113], have also been studied in a different context, particularly in the realm of high-energy physics with connections to gravity [114], elasticity theory [115], as well as glassy states of matter [116, 117]. Generally one distinguishes two types of fractons: type-I fractons, appear on the corners of membrane operators. As a result, moving a fracton amounts to moving the entire membrane which requires an infinite number of spin flips in the thermodynamic limit. In nature, such a process is virtually impossible to occur due to thermal or quantum fluctuations. This also implies that in such a theory there must be sub-dimensional particles, so-called lineons, which consists of groups of fractons and can be moved along a line. Type-II fractons, on the other hand, are found at the corners of *fractal* operators. More generally, in a type-II fracton theory, there are no mobile excitations [102]. However, it remains uncertain whether such a particle can be found in nature. While there are spin models that exhibit exact gapped fracton ground states, such as the X-cube model that realizes type-I fractons [89] and Haah’s code that features type-II fractons [118], these models rely on artificial multi-spin interactions that are challenging to implement in experimental platforms. In addition to these models, significant insights have been gained through Pretko’s formulation of fractons using higher rank gauge theories. These gauge theories resemble  $U(1)$  electrodynamics, but with the crucial distinction that the emergent gauge field, the electric field, is no longer a vector field but rather a tensor [103–105]. For instance, a rank-2  $U(1)$  gauge theory can be expressed as

$$\partial_\mu \partial_\nu E^{\mu\nu}(\mathbf{r}) = \rho(\mathbf{r}) \quad (1.34)$$

where  $\rho(\mathbf{r})$  is a scalar field corresponding to a charge density. In full analogy to Eq. (1.27), we can verify that this theory once more has well-defined and conserved charge excitations by simply noticing that we can again derive a standard rank 1 Gauss law by defining a current vector field  $J^\mu \equiv \partial_\nu E^{\mu\nu}$ . However, the rank 2 theory has another conservation law: By integrating the dipole moment over some volume, we find that the dipole moment is also a conserved quantity which, in a closed volume, can only escape via the boundary [105, 106]

$$\int_V d^3r x^\mu \rho = \int_V d^3r x^\mu \partial_\nu \partial_\sigma E^{\nu\sigma} = \int_{S=\partial V} dn_\sigma (x^\mu \partial_\nu E^{\nu\sigma} - E^{\mu\sigma}). \quad (1.35)$$

Here, the unit vector  $n_\sigma$  is perpendicular to the surface  $S$ . This additional conservation law has profound consequences regarding the mobility of charge excitations. We have seen in Fig. 1.2 that moving a charge corresponds to a local creation of a

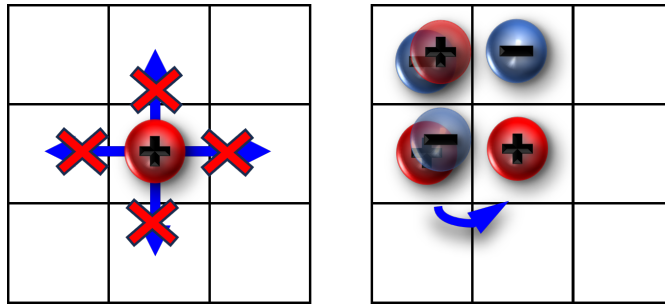


Figure 1.3.: An isolated, immobile fracton (left) and a lineon, which can be moved along a one-dimensional line by quadrupole excitations.

dipole moment, canceling one pair of opposite charges. As any local operator can no longer change the dipole moment, an isolated charge thus becomes impossible to move - the defining property of a type-I fracton phase. Similarly, a type-II fracton phase may also be realized by a gauge theory featuring mixed derivatives of the electric field which can imply infinitely many conservation laws and thus fully immobile particles [52, 53, 113]. We may also use this argument to identify another peculiar type of quasiparticle in such a higher-rank  $U(1)$  theory: The next-lowest local excitation that is allowed by conservation laws is a quadrupole. Clearly, acting such an operator on a single charge will result in an energy cost since it increases the total number of charges. On the other hand, a pair of charges, a dipole, *can* be moved. This is depicted in Fig. 1.3. If a quadrupole of fractons has been created, i.e., by flipping a single spin, it can be separated into two dipoles which are deconfined and can be separated to arbitrary distances, as long as they are only moved along one dimension. Such one-dimensional particles are referred to as *lineons*. Similar to its rank-1 counterpart, a higher rank  $U(1)$  comes with clear signatures, multifold pinchpoints in the spin structure factor [117]. In Chapter 6, we will identify additional signatures found in spin models with emergent higher rank gauge fields. Recently, within the Gaussian approximation featured in Section 1.3, comprehensive classifications of various types of classical spin liquids were done, see for example [52–54].

While a higher-rank  $U(1)$  gauge theory is thus certainly capable of describing the peculiar behavior of these fracton phases, it seems highly unlikely that such an artificial gauge field could exist in nature. In condensed matter systems, however, it is certainly possible that such a phase could emerge as an effective theory. Recently, it was found that an emergent higher-rank gauge field can emerge in a *classical* spin Hamiltonian, following a similar construction to spin ice [51]. On the other hand, this construction is valid purely at a classical level. The question of whether such a phase becomes destabilized or enhanced under quantum fluctuations will

be the subject of the later chapters of this thesis.

## 1.6. Basic concepts of the PFFRG

As the following chapters will review methodological advancements made in the pseudo-Majorana functional renormalization group (PMFRG), we first briefly review basic concepts and properties of the *pseudofermion*-FRG approach without being exhaustive on all methodological details. A more detailed and self-contained description can be found in Refs. [10, 119–122]. For a more general introduction, see Ref. [123].

### Motivation

The classical approximation neglects many important effects and will thus provide an incorrect description of a quantum spin system. Due to the immense difficulty in solving the quantum many-body problem, there exist a vast number of numerical techniques, each with their distinct advantages and disadvantages. Generally, methods can be categorized into sampling-based methods such as quantum Monte Carlo (QMC), wavefunction compression methods such as the density matrix renormalization group (DMRG), diagrammatic approaches such as mean-field theory, or the functional renormalization group (FRG).

While most quantum Monte Carlo methods can deliver exact results (up to quantifiable and numerically controllable standard uncertainties), their application requires strictly positive statistical probabilities. These so-called sign-problem free methods require the Hamiltonian to have a well-behaved sign structure, such as strictly negative matrix elements. Unfortunately, this is only rarely the case, most importantly not for almost all frustrated antiferromagnets [124, 125]. The compression-based approaches, such as DMRG and tensor network methods, have shown great promise in one and two dimensions. Their error is also numerically controllable. However, their divide-and-conquer approach requires the system being studied to have only a small amount of entanglement between the two parts that are separated. Crucially, they lack convergence if the amount of entanglement in the system exceeds the *area law*, i.e., if the two parts of a system are entangled only via their respective boundaries. These methods are difficult to apply in three dimensions since the size of the boundary grows quadratically with the dimension [126], in stark contrast to the constant boundary size in one dimension. For most two- and virtually all three-dimensional frustrated magnets, this leaves us with approximate solutions, which often do not have a controllable way of min-

imizing the error of the approximation.

Other common techniques are variational approaches [127, 128], which make use of the fact that the mean energy  $E_{\mathbf{v}} = \langle \psi_{\mathbf{v}} | H | \psi_{\mathbf{v}} \rangle$  of any state  $|\psi_{\mathbf{v}}\rangle$  depending on a set of variational parameters  $\mathbf{v}$  is bounded from below by the true ground state energy  $E_0$ . Moreover, minimizing  $E_{\mathbf{v}}$  with respect to the variational parameters  $\mathbf{v}$  will maximize the overlap of  $|\psi_{\mathbf{v}}\rangle$  with the true ground state, at least for finite, gapped systems [129]. Certainly, a well-chosen variational wavefunction can give fantastic results [127]. However, a bias is certainly introduced by this choice. A notable method is the *variational Monte Carlo* approach, in which the energy is minimized by a stochastic optimization algorithm [130–133]. Recent developments in the usage of neural networks as variational wavefunctions have shown great promise in overcoming the limitations of traditional variational wavefunctions [134–139]. However, even variational states with many parameters may suffer from their limited expressibility, and in many cases, it can be that the required number of neural network parameters exceeds the number of parameters that can be trained in a feasible amount of time, especially if the system size becomes large.

These shortcomings of other methods have motivated the search for new approaches, particularly in two and three dimensions, which are of particular importance for experimental materials. Computing the many-body wavefunction is typically only the means to an end, while the real goal is the computation of observables, or even just the characterization of a phase diagram. In such cases, diagrammatic many-body theory is a viable alternative. Within this approach, a system's many-body Green functions, which are the amplitudes of a quantum transition from one state to another, are determined. As a concrete example, the single-particle Green function determined as a thermal expectation value of fermionic annihilation  $c_k(\tau)$  and creation  $c_k^\dagger(\tau)$  operators, satisfying canonical anticommutation relations  $\{c_k(\tau), c_{k'}^\dagger(\tau')\} = \delta_{kk'}\delta(\tau - \tau')$ . The Green function is then given by

$$G(k, \tau | k', \tau') \equiv \langle \mathcal{T}_\tau c_{k'}^\dagger(\tau') c_k(\tau) \rangle, \quad (1.36)$$

corresponds to the amplitude of the propagation of a fermion with momentum  $k$  at time  $\tau$  to a state with momentum  $k'$  at time  $\tau'$ , where  $\mathcal{T}_\tau$  is the time-ordering operator [30, 49, 140]. This concept is readily extended to the two-particle Green function

$$G^{(2)}(k_1, k_2, \tau_1, \tau_2 | k'_1, k'_2, \tau'_1, \tau'_2) \equiv \langle \mathcal{T} c_{k'_1}^\dagger(\tau'_1) c_{k'_2}^\dagger(\tau'_2) c_{k_2}(\tau_2) c_{k_1}(\tau_1) \rangle, \quad (1.37)$$

which in turn can be used to compute relevant two-body observables, i.e., any operator that can be expressed in terms of two fermionic creation and annihilation



operators.

Many-particle Green functions may be computed perturbatively, accurate up to some finite order in the interaction strength relative to some other non-interacting energy scale. However, often times this approach suffers from infrared divergences of individual terms at finite order. The *renormalization group* (RG) was designed to circumvent this by summing up contributions to infinite order in a regularized fashion. This regularization separates contributions by their energy scale, first summing up the high-energy degrees of freedom, then continuously summing up smaller energy scales, allowing individually divergent contributions to cancel each other [141–144]. On the other hand, while formally exact and conceptually elegant, the procedure of renormalization is in practice challenging and requires further approximations. In the following, we will give a quick overview of the main concepts of the so-called functional renormalization group (FRG) [123, 145–148], whereas the subsequent chapters 2 and 3 will introduce the formalism in more detail and outline their application to spin systems.

The FRG’s fundamental building blocks are the so-called one-particle irreducible *vertex functions*. Diagrammatically, the  $n$ -particle vertex function is defined by taking the  $n$ -particle propagator, or Green function (i.e., Eq. (1.37)) and removing all diagrams that can be completely separated by cutting a single fermionic propagator, as shown in Fig. 1.4. Inversely, the Green function can also be determined from the irreducible vertex. For instance, the one-particle Green function is given by the *Dyson equation* [49, 123].

$$G(k, i\omega_n) = G_0(k, i\omega_n) + G_0(k, i\omega_n)\Sigma(k, i\omega_n)G(k, i\omega_n), \quad (1.38)$$

where  $G_0$  is the non-interacting Green function and  $\Sigma$  is the one-particle vertex, most commonly referred to as the self-energy. The first step of the renormalization procedure is then to introduce an infrared cutoff that modifies the bare Green function as  $\mathbf{G}_0 \rightarrow \Theta^\Lambda \mathbf{G}_0$ . This is shown in Fig. 1.4 where the modified propagators are highlighted in red. While there is considerable freedom in choosing a regulator,  $\Theta^\Lambda$  is often chosen to be zero for  $\Lambda \rightarrow \infty$  and one for  $\Lambda \rightarrow 0$ . The most relevant property is that it interpolates between an exactly solvable (though unphysical) limit and the physical theory of interest. Formally exact flow equations, ordinary differential equations, for vertex functions can be derived by taking a derivative of the vertices with respect to the RG scale  $\Lambda$ . This is sketched in Fig. 1.4, for the full derivative via the many-body path integral formalism, see [123]. Unfortunately, this system of equations is infinitely large due to the fact that the derivative of each vertex contains terms with higher-order vertices. In order to go to high orders in this hierarchy, it requires solving an exponentially large number of differential

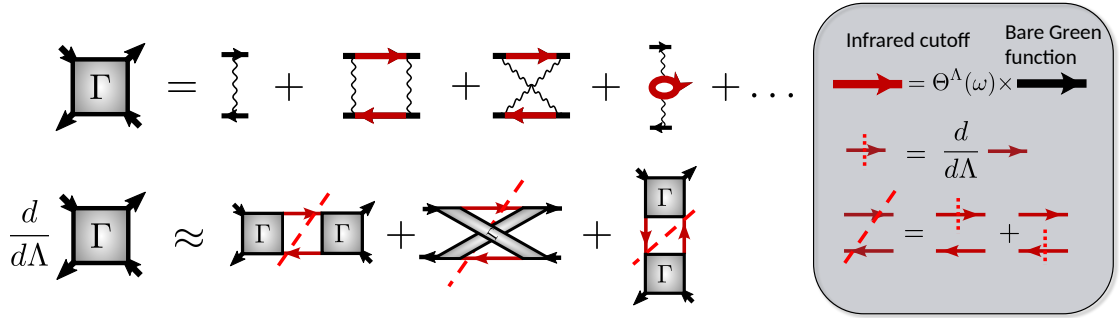


Figure 1.4.: Perturbative expansion of the two-particle vertex to second order. Propagators are indicated by red arrows, which are affected by the cutoff. Interaction lines are displayed as wavy lines. (Approximate) FRG vertex flow equation can be derived by taking derivatives with respect to the cutoff and grouping diagrams into three channels by re-inserting the full vertex. Diagrams, which cannot be expressed this way, i.e. corresponding to contractions of three-body interactions, are discarded.

equations, which quickly becomes unfeasible. A well-established approximation is to neglect all terms containing the six-point or three-particle vertex [123, 145–147, 149]. The resulting set of equations is shown in Fig. 1.4, where internal propagators are colored in red. If the Hamiltonian of interest does not feature any three-body interactions, this vertex is zero at the initial scale. However, as the renormalization procedure allows for the generation of effective couplings, a finite six-point vertex can be generated from two-particle interactions. As a result, we can expect this approximation to hold as long as the two-particle vertex does not grow too large. For strongly coupled systems, this limitation becomes by far the most severe, as we shall explore in later chapters.

The pseudo-fermion functional renormalization group (PFFRG), first introduced by Reuther and Wölfle in 2010 [119], has since been established as a capable tool for tackling these most challenging cases [9, 10, 82, 150–154]. Due to its inclusion of important mean-field contributions, such as the random phase approximation (RPA) and the ladder series diagrams to infinite order, it is particularly suited to higher dimensions. These full inclusion of the RPA and ladder-type diagrams are particularly powerful: Magnetically ordered systems are known to be well described by the RPA series, while quantum spin liquids are always obtained in the limit  $N \rightarrow \infty$  of an  $SU(N)$  expansion in the number of fermionic flavors, a limit equivalent to the ladder series [120, 155]. Individually, both series are biased towards their respective effect; for instance, the RPA is incapable of describing any

magnetically disordered state and predicts a divergent magnetic susceptibility at a mean-field critical temperature. The PFFRG, on the other hand, can be used to approximate both the disordered and the ordered state, making it extremely flexible. At its core, there are only two fundamental challenges that limit the predictive power of the PFFRG: The first is the truncation of the infinite series of diagrams in the vertex expansion, ignoring the contributions of the six-point vertex which includes many three-body terms. Although some three-body diagrams are generated in the course of the FRG flow, this approximation is inherently uncontrolled and may lead to significant errors, which we shall explore more in the following chapters. The other limitation comes from the fact that there is no exact representation of spins in terms of bosons or complex fermions, which are the foundation of the path integral formulation and thus most diagrammatic techniques.

### Auxiliary particle representation of spins

In order to apply the FRG to spin systems, one must first overcome a significant obstacle: while the FRG is derived in terms of general fermionic or bosonic degrees of freedom, spin operators have more complicated commutation relations. Crucially, the path integral formalism, from which the FRG is usually derived, is inapplicable to spins as a result. Recently, there have been promising attempts to formulate an alternative description of spin diagrammatics and FRG in terms of pure spin operators [156–158].

The most common representation of spins through fermions by far is the Abrikosov representation [159]:

$$S_i^\alpha = \frac{1}{2\hbar} \sum_{\sigma, \sigma' \in \{\uparrow, \downarrow\}} f_{i\sigma}^\dagger \sigma_{\sigma\sigma'}^\alpha f_{i\sigma'}. \quad (1.39)$$

For each lattice site, this corresponds to placing a spin-up or spin-down fermion, which is capable of representing the degrees of freedom of a single spin-1/2. However, by explicitly computing the product of two spin operators expressed via Abrikosov fermions, we acquire an additional contribution:

$$S^\alpha S^\beta = \frac{i\hbar}{2} \varepsilon^{\alpha\beta\rho} S^\rho + \frac{\hbar^2}{4} \delta^{\alpha\beta} + \frac{\hbar^2}{4} \delta^{\alpha\beta} \left( (n_\uparrow - n_\downarrow)^2 - 1 \right). \quad (1.40)$$

From Eq. (1.40), we can see that the unphysical contribution arises if a site is either empty or doubly occupied, in which case we have  $(S^\alpha)^2 = 0$ . As a result, any approach that aims to employ such a representation needs a mechanism to project out these extra *unphysical* degrees of freedom. In the context of the FRG, this would mean including a fluctuating gauge field to enforce the single fermion occupation constraint.

Unfortunately, incorporating such a term is technically extremely challenging and thus usually omitted. While the severity of this problem is somewhat limited at zero temperature, as it can be argued that sites with an effective spin-0 moment cannot contribute to the energy and thus come at a cost  $\sim J$ , counterexamples to this argument can be constructed. In either case, at finite temperature, there will inevitably be a contribution from unphysical states, rendering PFFRG inapplicable [1, 160]. It can be argued that the *pseudo Majorana functional renormalization group* (PMFRG) introduced within this thesis effectively tackles both of the problems outlined above by switching to a spin representation in terms of Majorana operators  $\eta^\alpha$  instead. Majoranas are defined via their properties

$$\{\eta^\alpha, \eta^\beta\} = \delta^{\alpha,\beta}, \quad (\eta^\alpha)^\dagger = \eta^\alpha, \quad (1.41)$$

where spin operators are written by a product of two Majoranas [161–163]

$$S_i^x = -i\eta_i^y \eta_i^z, \quad S_i^y = -i\eta_i^z \eta_i^x, \quad S_i^z = -i\eta_i^x \eta_i^y. \quad (1.42)$$

It should be noted that this representation differs from the much better-known representation used in Kitaev’s original solution of the Kitaev-Honeycomb model [13], which features four Majoranas per site and, crucially, also unphysical states that need to be projected out. We will see in the following that this representation does not suffer from unphysical states despite also enlarging the Hilbert space. Furthermore, as we will see in Chapter 4, the possibility of working at a finite temperature  $T$  allows us to use the temperature  $T$  as a control parameter: At large temperatures, the error introduced by neglecting higher vertices vanishes, which allows for quantitatively accurate results in this regime, something which is not possible in PFFRG. With more recent improvements to the formalism, such as the temperature flow scheme which uses the physical temperature as a cutoff and was shown to be capable of detecting phase transitions down to extremely low temperatures [5], the PMFRG significantly improves upon the drawbacks of the PFFRG while retaining its advantages of efficiency and flexibility [10].

The key benefit of the representation in Eq. (1.39) and, as we shall see, Eq. (1.42), is that the resulting model becomes amenable to fermionic many-body techniques such as the FRG, which is formulated in terms of irreducible fermionic vertex functions (“essential parts of correlation functions”). The PFFRG is capable of treating general two-body spin Hamiltonians as in Eq. (1.3) however, in the following, we consider only the special case of Heisenberg models:

$$H = \sum_{(i,j)} J_{ij} \sum_{\alpha} S_i^{\alpha} S_j^{\alpha} \quad (1.43)$$

, where  $(i, j)$  refers to all possible pairings of sites. The centerpiece of the PFFRG method is given by a hierarchy of flow equations reminiscent of one-loop diagrammatic perturbation theory, which describe the change of vertex functions when a

Matsubara-frequency cutoff parameter  $\Lambda$ , introduced in the bare Green function  $G^{0,\Lambda}(i\omega) = G^0(i\omega)\Theta(|\omega| - \Lambda)$ , is varied. The basic idea is that at the starting point  $\Lambda = \infty$ , the bare propagator vanishes and all vertex functions are trivially known. For a numerical solution of the flow equations down to  $\Lambda = 0$  (the cutoff-free physical case), a truncation of the formally exact hierarchy of flow equations, usually at the level of the four-point vertex, is necessary.

The four-point vertex is directly related to the (momentum-resolved) static spin susceptibility, which represents the central outcome of the PFFRG approach. The onset of magnetic ordering is signaled by a divergence of the susceptibility along the RG flow (which in a finite system typically reduces to a finite peak or a kink). Accordingly, non-magnetic (and possibly quantum spin liquid) phases are characterized by an RG flow that remains smooth down to the lowest accessible  $\Lambda$  scales. Due to the lack of a small parameter in the purely interacting pseudo-fermion Hamiltonian, the truncation of the flow equations is an - a priori - uncontrolled procedure. It can be shown, however, that within the usual truncation on the level of the four-point vertex, both quantum fluctuations and classical ordering tendencies are correctly described in leading orders of  $1/N$  and  $1/S$ , respectively [120, 121]. Here,  $N$  and  $S$  describe the artificial enlargement of the spin's symmetry group ( $SU(2) \rightarrow SU(N)$ ) and the spin length ( $1/2 \rightarrow S$ ), respectively. In two very recent works, certain contributions of the six-point vertex have been taken into account using a multiloop extension [164, 165], equivalent to a solution of the parquet self-consistency equations [166, 167]. The quantitative robustness of the results with respect to increasing loop orders was interpreted as further evidence for the accuracy of the PFFRG.

## 1.7. Outline of the thesis

The preceding sections have highlighted specific areas motivating the investigation of quantum spin systems, provided an overview of the notorious challenge that they pose, and the existing methodology. The following Chapter 2 will begin with a detailed description of the pseudo Majorana functional renormalization group (PMFRG). Subsequently, methodological advancements to this method are discussed in Chapter 3. The PMFRG's applicability then used in more complex cases such as the paradigmatic Cubic lattice (Chapter 4) and Heisenberg Pyrochlore model (Chapter 5). These chapters will show how the PMFRG at finite temperatures can be used to obtain quantitatively accurate results for frustrated and non-frustrated systems alike. The final chapters will cover the intriguing cases

of spin systems with emergent higher-rank spin gauge theories. In particular, the PMFRG will be employed in Chapter 6, to investigate a recently found classical construction of several different types of higher-rank  $U(1)$  spin liquids in the presence of quantum fluctuations. Then, the particular case of an emergent rank-2  $U(1)$  gauge theory is considered in Chapter 7, where a new model is constructed with the goal to realize a quantum fracton spin liquid. Finally, in Chapter 8, the major findings shall be summarized and contextualized in the broader scope of ongoing and future research in many-body method development, the study of emergent gauge theories.

## The Pseudo Majorana functional renormalization group

Finding numerical solutions of quantum many-body problems is one of the core disciplines in modern condensed matter theory. In a wide range of physical settings the problem amounts to analyze ground-state and finite-temperature phases of a system of interacting spins on a lattice. Even though the corresponding microscopic models are often conceptually simple, such as two-body Heisenberg spin Hamiltonians, they may harbor a colorful range of physical phenomena including exotic types of long-range orders [168], quantum phase transitions [31, 169] or quantum spin liquids [29, 55, 78]. While quantum spin phases are traditionally described in terms of broken or unbroken symmetries, a more modern understanding also includes concepts such as long-range entanglement or topological order [170] and reaches out to applications in the context of quantum information processing [171].

Despite the shifts of focus which the field has gone through in the recent decades, the accurate numerical treatment of interacting quantum spin systems remains a highly challenging and longstanding problem. In fact, none of the currently available numerical methods is able to ultimately determine the eigenstates of a generic spin model. For example, quantum Monte Carlo methods [172, 173] which enjoy the invaluable advantage that numerical errors are, in principle, only of statistical nature, suffer from the infamous sign problem when applied to frustrated spin systems. Similarly, density matrix renormalization group, matrix product, and tensor network approaches [174–178] have made tremendous progress in recent years and are the undisputed method of choice for a variety of spin systems (particularly in one dimension). On the other hand, the scaling of the entanglement entropy poses a serious challenge for such techniques in higher dimensions.

An alternative approach is based on functional renormalization group (FRG) concepts [123, 179, 180] which are, in principle, oblivious to the system's dimensionality. In its standard fermionic formulation this technique has first been applied in the context of electronic Hubbard-like models [145, 181, 182] where it has become an established tool to describe competing types of long-range orders. In addition, a more recently developed variant of the FRG [119] specifically targets quantum spin systems. The key conceptual step of this latter technique is

to express the spin operators in terms of auxiliary fermions [183], justifying the name pseudofermion functional renormalization group (PFFRG). Within the last decade the PFFRG has been successfully applied to a wide range of spin systems [7, 119–122, 150, 154, 155, 164, 165, 184–212] and has constantly been extended and generalized. Today, the PFFRG is, hence, remarkably flexible with a scope of applicability comprising two dimensional [7, 119, 120, 122, 153, 155, 164, 165, 184–186, 188–191, 193–198, 200, 202, 207–212] and three dimensional [7, 150, 187, 190, 192, 194, 196, 199, 201, 202, 204, 206] quantum spin systems on arbitrary lattices, including complex frustrated and longer-range coupled networks [154, 197] with general isotropic or anisotropic [122] two-body spin interactions. Further recent developments concern the generalization to arbitrary spin magnitudes  $S$  [120] or higher spin symmetry groups  $SU(N)$  [121, 155, 206] and, on a more technical level, the implementation of multi-loop schemes [164, 165, 195].

Despite its success in accurately determining ground state spin correlations, the PFFRG comes along with a well-known obstacle. The aforementioned pseudofermionic description introduces an enlargement of the Hilbert space associated with states that do not correspond to states of the physical spin system. These unphysical states typically appear at energies above the ground state energy of the spin system. Thus, on the level of zero-temperature investigations, this problem has been argued to be rather mild and can be treated by shifting unphysical states to higher energies [120]. In a recent investigation of this problem, on the other hand, the average spin magnitude within the PFFRG was found to differ from the theoretically expected result even for higher loop orders [164]. More importantly, the enlarged Hilbert space has so far prohibited an application to finite temperatures.

This chapter aims at resolving issues due to unphysical spin states by modifying the PFFRG on a very fundamental level. Instead of using a complex fermionic spin representation, we employ a certain, so-called  $SO(3)$  Majorana fermion rewriting of spin operators [161, 162] which does not generate unphysical states but only introduces redundant Hilbert space sectors. This property distinguishes it from other Majorana representations [163] and as such makes it attractive as a first candidate for a Majorana-based spin FRG. We, accordingly, dub this approach pseudo Majorana functional renormalization group (PMFRG) method. This modification opens up various directions of investigation: (i) Most importantly, the PMFRG becomes applicable to finite temperatures which only requires small methodological adjustments presented below. (ii) As a side product, we discuss how to calculate thermodynamic quantities such as the free energy, energy and heat capacity which have so far not been studied within the PFFRG. (iii). The developments below are



---

formulated in a general way such that they are applicable to arbitrary Majorana models also outside the realm of quantum magnetism. (*iv*) Certain spin models, most prominently the Kitaev honeycomb model [13], are exactly solvable when expressed in terms of Majorana fermions. Although Kitaev's spin representation differs from the one employed here, the exact solution is also obtainable within the  $SO(3)$  Majorana representation [163] used here. Even though not the focus of this work, one may thus expect that the PMFRG performs better for Kitaev-type spin models and perturbations thereof as compared to the PFFRG.

This chapter also features applications of the PMFRG to simple quantum spin models allowing us to assess its accuracy. As a first benchmark test small clusters of up to six interacting spins are treated where the results can be straightforwardly compared with exact diagonalization. An overall finding is that the thermodynamic behavior of the spin correlations from PMFRG are surprisingly accurate and reproduce the exact result significantly better than PFFRG. It should be emphasized that despite the finite Hilbert space of small spin clusters, their treatment within PMFRG is still highly non-trivial and poses the same challenges as for infinite lattice systems. Indeed, due to the incorporation of various mean-field limits, one can expect that the FRG unfolds its full strength only in infinite spin systems of two and higher dimensions. Later chapters will then discuss the application of the PMFRG to frustrated lattice models. A persistent technical issue, however, occurs in the low temperature limit where PMFRG detects spurious divergencies of spin correlations. Although such divergences are not uncommon in the context of zero temperature FRG [10] it is argued that this behavior can be an artifact of the redundant Hilbert space sectors in the Majorana representation. While such subtleties remain to be further studied the developments introduced here lay the groundwork for various future directions of research and significantly enlarge the scope of applicability of FRG approaches.

## 2.1. $SO(3)$ Majorana Representation

In this section we discuss the  $SO(3)$  Majorana representation [161, 162] for spin-1/2 in detail. For each spin  $S_i^\alpha$  at site  $i$ , three different flavors  $\alpha \in \{x, y, z\}$  of Majorana fermions  $\eta_i^{\alpha\dagger} = \eta_i^\alpha$  are introduced. They fulfill the anticommutation relations  $\{\eta_i^\alpha, \eta_j^\beta\} = \delta_{ij}\delta^{\alpha\beta}$  which imply  $(\eta_i^\alpha)^2 = 1/2$ . The formal Hilbert space dimension per Majorana is  $\sqrt{2}$  as appropriate for half a (complex) fermion. The spin operators  $S_i^\alpha = -\frac{i}{2} \sum_{\beta\gamma} \varepsilon^{\alpha\beta\gamma} \eta_i^\beta \eta_i^\gamma$ , more explicitly written as

$$S_i^x = -i\eta_i^y \eta_i^z, \quad S_i^y = -i\eta_i^z \eta_i^x, \quad S_i^z = -i\eta_i^x \eta_i^y, \quad (2.1)$$

can be easily checked to fulfill the spin-1/2 algebra

$$S_i^\alpha S_i^\beta = \frac{1}{4} \delta^{\alpha\beta} + \frac{i}{2} \sum_{\alpha\beta\gamma} \varepsilon^{\alpha\beta\gamma} S_i^\gamma. \quad (2.2)$$

As an example, a Heisenberg coupling term from Hamiltonian Eq. (4.1) is represented as

$$\sum_\alpha S_i^\alpha S_j^\alpha = -(\eta_i^y \eta_i^z \eta_j^y \eta_j^z + \eta_i^x \eta_i^z \eta_j^x \eta_j^z + \eta_i^x \eta_i^y \eta_j^x \eta_j^y). \quad (2.3)$$

As usual for auxiliary particle representations, the  $SO(3)$  Majorana representation comes with a gauge freedom. The local  $\mathbb{Z}_2$  gauge transformation  $\eta_i^\alpha \rightarrow \varepsilon_i \eta_i^\alpha$  with  $\varepsilon_i = \pm 1$  leaves spin operators invariant since each spin consists of a product of exactly two Majoranas with equal lattice index. This gauge freedom is also relevant to understand the structure of the Majorana Hilbert space. To see this, define the Majorana operator

$$\tau_i = -2i\eta_i^x \eta_i^y \eta_i^z, \quad (2.4)$$

which anticommutes with any  $\tau_j$  from a different site  $j \neq i$  and fulfills

$$\tau_i \eta_j^\alpha = \begin{cases} \eta_i^\alpha \tau_i & \text{if } i = j \\ -\eta_j^\alpha \tau_i & \text{if } i \neq j \end{cases}. \quad (2.5)$$

Consequently,  $\tau_i$  commutes with all spin operators and thus with any spin Hamiltonian. To construct a set of mutually commuting operators one needs to pair  $\tau_i$  with another conserved Majorana operator.

One choice [213] is to define an additional Majorana  $\eta_i^0$  per site, so that the parity  $p_i = 2i\tau_i \eta_i^0$  with eigenvalues  $\pm 1$  is a constant of motion. These eigenvalues

split the local Majorana Hilbert space of dimension four into two dynamically decoupled two-dimensional parts each of which are in one-to-one correspondence to the original local spin Hilbert space. To invoke  $\eta_i^0$  in the Hamiltonian, parity projection schemes are required that eventually lead to one of two alternative four-Majorana spin representations [163]. However, as stated above, we will avoid this additional complication in the remainder of this work.

An alternative, non-local pairing scheme which does not introduce additional degrees of freedom requires an even number of sites  $N$  [214]. Given an arbitrary but fixed pairing of sites  $(i, j)$ , we can define the  $N/2$  parities  $p_{(i,j)} = 2i\tau_i\tau_j = \pm 1$ . Similar to above, each eigenstate of a spin Hamiltonian is  $2^{N/2}$ -fold degenerate, each copy labeled by the above parities. In other words, the total Majorana Hilbert space dimension of  $2^{3N/2}$  is organized into the usual  $2^N$  physical spin configurations, each with an artificial degeneracy of  $2^{N/2}$ . Choosing a different pairing of sites corresponds to a unitary rotation of the  $2^{N/2}$  basis vectors for the artificial part of the Hilbert space. Note that since Eq. (2.1) fully reproduces the correct spin algebra without the need for an additional constraint, this Hilbert-space enlargement introduces no unphysical states, but only exact copies of the physical spin states [163]. This degeneracy is closely connected to the aforementioned local  $\mathbb{Z}_2$  gauge symmetry: As the transformation  $\tau_i \rightarrow -\tau_i$  flips the parity  $p_{(i,j)}$ , it switches between degenerate states of different parities.

For thermodynamic properties, the above degeneracy leads to the relation  $\mathcal{Z}_{pm} = 2^{N/2}\mathcal{Z}$  between the exact partition functions defined in spin and  $SO(3)$  pseudo-Majorana (pm) Hilbert space. Thus, we have for the physical free energy per site,  $f = -T \log(\mathcal{Z})/N$ ,

$$f = f_{pm} + \frac{T}{2} \log(2) \quad (2.6)$$

where the first term  $f_{pm} \equiv -\frac{T}{N} \log(\mathcal{Z}_{pm})$  will be computed via PMFRG and the second term accounts for the redundancy inherent in the  $SO(3)$  Majorana representation.

Any expectation values for spin operators (or correlators)  $\mathcal{O}_s$  are easily computed in the Majorana representation as well. This follows from the observation that the Majorana version of such an operator,  $\mathcal{O}_{pm}$ , is diagonal in the parity sector and the same is true for any physical density matrix  $\rho_{pm}$ , like for example the Boltzmann factor  $\rho_{pm} \sim e^{-\beta H_{pm}}$ . Then the degeneracy factor  $2^{N/2}$  simply cancels [215] and we have

$$\langle \mathcal{O}_s \rangle \equiv \frac{\text{tr } \mathcal{O}_s \rho_s}{\text{tr } \rho_s} = \frac{\text{tr } \mathcal{O}_{pm} \rho_{pm}}{\text{tr } \rho_{pm}} \equiv \langle \mathcal{O}_{pm} \rangle. \quad (2.7)$$

Finally, we discuss the role of rotations in spin space. In order to employ the global  $SO(3)$  symmetry of the Heisenberg Hamiltonian in Eq. (1.43) later on, we demonstrate here that the three Majoranas transform under  $SO(3)$  rotations like the coordinates of a physical vector. Using  $\tau_i$ , the spin operators can be re-expressed as

$$S_i^\alpha = \tau_i \eta_i^\alpha. \quad (2.8)$$

We may now consider the general  $SO(3)$  transformation  $\eta_i^\alpha \rightarrow \sum_\beta R_{\alpha\beta} \eta_i^\beta$  with  $R_{\alpha\beta} \in SO(3)$  being a three dimensional rotation matrix. As  $\tau_i$  is invariant under this transformation [163], spin operators must transform as

$$R_{\alpha\beta} S_i^\beta = \tau_i \sum_\beta R_{\alpha\beta} \eta_i^\beta. \quad (2.9)$$

It follows that physical  $SO(3)$  rotations of a spin  $i$  are equivalent to rotations of the Majorana vector  $(\eta_i^x, \eta_i^y, \eta_i^z)$ .

## 2.2. General Majorana FRG Flow Equations

As a basis for the FRG treatment of spin systems in pseudo-Majorana representation, we first introduce flow equations that are valid for general interacting Majorana Hamiltonians. We consider

$$H = \frac{i}{2} \sum_{\mu_1, \mu_2} A_{\mu_1 \mu_2} \eta_{\mu_1} \eta_{\mu_2} + \frac{1}{4!} \sum_{\mu_1, \mu_2, \mu_3, \mu_4} V_{\mu_1 \mu_2 \mu_3 \mu_4} \eta_{\mu_1} \eta_{\mu_2} \eta_{\mu_3} \eta_{\mu_4}, \quad (2.10)$$

where  $\{\mu_i\}$  is an arbitrary set of single-particle indices. As above, we use the convention  $\{\eta_{\mu_i}, \eta_{\mu_j}\} = \delta_{\mu_i \mu_j}$ . Majorana exchange statistics require the antisymmetry of  $A$  and  $V$  under exchange of any two indices, hermiticity mandates that both couplings must be real.

Assuming thermal equilibrium, we move on to an imaginary time path integral formulation [215, 216] defined in terms of Grassmann fields  $\eta_\mu(\tau)$ . The action reads

$$S = \int_0^\beta d\tau \left( \sum_\mu \frac{1}{2} \eta_\mu(\tau) \partial_\tau \eta_\mu(\tau) + H(\{\eta_\mu(\tau)\}) \right), \quad (2.11)$$

where  $\partial_\tau$  denotes a derivative with respect to imaginary time and  $\beta = 1/T$ . We define the Fourier transform  $\eta_\mu(\tau) = T \sum_n e^{i\omega_n \tau} \eta_\mu(i\omega_n)$  where the fermionic Matsubara frequencies are given by  $i\omega_n = \pi T(2n + 1)$ , with  $n \in \mathbb{Z}$ . In slight abuse

of notation, in the following, we will denote  $\omega_{n_1}$  by  $\omega_1$  and equivalently for other frequencies. The non-interacting part of the action may then be written as

$$S_0 = -\frac{1}{2} \frac{1}{\beta^2} \sum_{\omega_1, \omega_2} \sum_{\mu_1, \mu_2} \eta_{\mu_1}(\omega_1) [\mathbf{G}_0^{-1}]_{\mu_1\omega_1, \mu_2\omega_2} \eta_{\mu_2}(\omega_2). \quad (2.12)$$

with the bare Majorana Green function

$$[\mathbf{G}_0^{-1}]_{\mu_1\omega_1, \mu_2\omega_2} = (i\omega_1\delta_{\mu_1\mu_2} - iA_{\mu_1\mu_2})\beta\delta_{\omega_1, -\omega_2}. \quad (2.13)$$

This definition is analogous to the complex fermionic bare Green function except for the opposing signs of the two frequencies in the Kronecker delta related to the absence of an independent Grassmann partner field  $\bar{\eta}$  with a relative sign in the Fourier transform.

We are now ready to apply the general FRG scheme from Ref. [123], derived for an action of a superfield vector  $\Psi$  containing an arbitrary number of bosonic or Grassmann fields labeled by the composite index  $l = (\omega_l, \mu_l)$ ,

$$\begin{aligned} S[\Psi] &= S_0[\Psi] + S_{\text{int}}[\Psi] \\ &= -\frac{1}{2} \int_l \int_{l'} \Psi_l [\mathbf{G}_0^{-1}]_{l, l'} \Psi_{l'} + S_{\text{int}}[\Psi]. \end{aligned} \quad (2.14)$$

where  $\int_l = \beta^{-1} \sum_{\omega_l} \sum_{\mu_l}$ . A comparison of Eq. (2.14) and Eq. (2.12) yields the direct correspondence  $\Psi_{l=(\mu_l, \omega_l)} = \eta_{\mu_l}(\omega_l)$ . The difference to the superfield vectors of complex fermions or bosons is emphasized, which require an additional but independent superfield label, i.e.  $\Psi = (\bar{\psi}, \psi)$ .

The starting point of the FRG scheme is the introduction of a cutoff scale  $\Lambda$  in the bare Green function  $\mathbf{G}_0 \rightarrow \mathbf{G}_0^\Lambda$  such that  $\mathbf{G}_0^{\Lambda=\infty} = 0$  and  $\mathbf{G}_0^{\Lambda=0} = \mathbf{G}_0$ . Although the flow equations describing the evolution of irreducible vertices with  $\Lambda$  [123] below are general, in the rest of this work, we will consider a multiplicative Matsubara frequency cutoff  $\Theta^\Lambda(\omega_1)$  to the bare Green function

$$[\mathbf{G}_0^\Lambda]_{\mu_1\omega_1, \mu_2\omega_2} = \Theta^\Lambda(|\omega_1|) [\mathbf{G}_0]_{\mu_1\omega_1, \mu_2\omega_2}. \quad (2.15)$$

At zero temperature, this cutoff is often chosen to be a Heaviside function  $\Theta^\Lambda(|\omega|) = \theta(|\omega| - \Lambda)$ , at finite temperatures a smooth cutoff must be chosen instead. While a momentum based cutoff is also used in some works, we will not consider such schemes here, as the main focus lies on pseudo-Majoranas without kinetic energy.

As a consequence of the cutoff, the self-energy  $\Sigma$  and the four-point vertex  $\Gamma$  acquire implicit dependence on  $\Lambda$ . These quantities are defined via the Dyson

equation in a superspace spanned by  $(\omega_i, \mu_i)$

$$\mathbf{G} = [\mathbf{G}_0^{-1} - \mathbf{\Sigma}]^{-1} \quad (2.16)$$

and the tree-expansion for the connected Green functions

$$G_{l_1, l_2, l_3, l_4}^{4,c} = - \int_{l_1', 2', 3', 4'} \mathbf{G}_{l_1 l_1'} \mathbf{G}_{l_2 l_2'} \mathbf{G}_{l_3 l_3'} \mathbf{G}_{l_4 l_4'} \times \Gamma_{l_1' l_2' l_3' l_4'} \quad (2.17)$$

respectively. This  $\Lambda$ -dependence is given by coupled differential equations, referred to as *flow equations*. Physical results can be extracted from the solution at  $\Lambda = 0$ . Since the action for Majorana systems was rephrased in superfield notation, we can employ the associated general flow equations [123] for the interaction correction to the free energy,  $F_{\text{int}}^\Lambda$ ,  $\Sigma^\Lambda$  and  $\Gamma^\Lambda$

$$\frac{d}{d\Lambda} F_{\text{int}}^\Lambda = \frac{1}{2} \text{Tr} \left[ \dot{G}^\Lambda G^{0,\Lambda} [G^\Lambda]^{-1} \Sigma^\Lambda \right], \quad (2.18a)$$

$$\frac{d}{d\Lambda} \Sigma_{1,2}^\Lambda = -\frac{1}{2} \sum_{1',2'} \dot{G}_{1',2'}^\Lambda \Gamma_{1',2',1,2}^\Lambda, \quad (2.18b)$$

$$\frac{d}{d\Lambda} \Gamma_{1,2,3,4}^\Lambda = X_{1,2|3,4}^\Lambda - X_{1,3|2,4}^\Lambda + X_{1,4|2,3}^\Lambda, \quad (2.18c)$$

$$X_{1,2|3,4}^\Lambda = \sum_{1', \dots, 4'} \dot{G}_{1',2'}^\Lambda G_{3',4'}^\Lambda \Gamma_{1,2,1',3'}^\Lambda \Gamma_{2',4',3,4}^\Lambda. \quad (2.18d)$$

As appropriate in thermal equilibrium, and to simplify notation, we employ a modified version of the Green function and vertices with the frequency conserving delta-function explicitly spelled out,

$$\mathbf{G}_{\mu_1 \omega_1, \mu_2 \omega_2} = G_{\mu_1 \mu_2}(\omega_2) \beta \delta_{\omega_1, -\omega_2} \quad (2.19a)$$

$$\mathbf{\Sigma}_{\mu_1 \omega_1, \mu_2 \omega_2} = \Sigma_{\mu_1 \mu_2}(\omega_1) \beta \delta_{\omega_1, -\omega_2} \quad (2.19b)$$

$$\Gamma_{\mu_1 \omega_1, \mu_2 \omega_2, \mu_3 \omega_3, \mu_4 \omega_4} \equiv \Gamma_{\mu_1 \mu_2 \mu_3 \mu_4}(\omega_1, \omega_2, \omega_3, \omega_4) \times \beta \delta_{\omega_1 + \omega_2 + \omega_3 + \omega_4, 0}. \quad (2.19c)$$

With the above definition, the Dyson equation for fixed frequency indices,  $\mathbf{G}_{-\omega, \omega} = \left[ [\mathbf{G}_0^{-1}]_{\omega, -\omega} - \mathbf{\Sigma}_{\omega, -\omega} \right]^{-1}$ , can be written as

$$G(\omega) = [i\omega - iA - \Sigma(\omega)]^{-1}. \quad (2.20)$$

The Green function and self-energy defined in Eq. (2.19a) and (2.19b) fulfill  $G(\omega) = G^T(-\omega)$  and  $\Sigma(\omega) = \Sigma^T(-\omega)$ , respectively.

We also restrict ourselves to the absence of parity symmetry breaking (expectation values of odd numbers of Majorana operators vanish) and neglect the contribution from the six-point vertex. The flow equation for the four-point vertex then separates into three distinct channels, each of which is characterized by one of the three bosonic transfer frequencies defined as

$$\begin{aligned} s &= \omega_1 + \omega_2 = -\omega_3 - \omega_4, \\ t &= \omega_1 + \omega_3 = -\omega_2 - \omega_4, \\ u &= \omega_1 + \omega_4 = -\omega_2 - \omega_3. \end{aligned} \quad (2.21)$$

The Majorana flow equations for the interaction correction to the free energy, self energy and the four-point vertex read [123]

$$\frac{d}{d\Lambda} F_{\text{int}}^\Lambda = \frac{1}{2} \int_{\nu_{1,2,3,4}} T \sum_{\omega'} S_{\nu_1\nu_2}^\Lambda(\omega') G_{\nu_2\nu_3}^{0,\Lambda}(-\omega') [G^\Lambda]_{\nu_3\nu_4}^{-1}(-\omega') \Sigma_{\nu_4,\nu_1}^\Lambda(\omega') \quad (2.22a)$$

$$\frac{d}{d\Lambda} \Sigma_{\mu_1,\mu_2}^\Lambda(\omega) = -\frac{1}{2} \int_{\nu_{1,2}} T \sum_{\omega'} S_{\nu_1\nu_2}^\Lambda(\omega') \Gamma_{\nu_1\nu_2\mu_1\mu_2}^\Lambda(-\omega', \omega', \omega, -\omega) \quad (2.22b)$$

$$\begin{aligned} \frac{d}{d\Lambda} \Gamma_{\mu_1,\mu_2,\mu_3,\mu_4}^\Lambda(\omega_1, \omega_2, \omega_3, \omega_4) &= \int_{\nu_{1,2,3,4}} T \sum_{\omega} S_{\nu_1\nu_2}^\Lambda(\omega) \\ &\times \left[ \Gamma_{\mu_1\mu_2\nu_4\nu_1}^\Lambda(\omega_1, \omega_2, \omega - s, -\omega) \Gamma_{\nu_2\nu_3\mu_3\mu_4}^\Lambda(\omega, -\omega + s, \omega_3, \omega_4) G_{\nu_3\nu_4}^\Lambda(\omega - s) \right. \\ &+ \Gamma_{\mu_1\nu_1\mu_3\nu_4}^\Lambda(\omega_1, -\omega, \omega_3, \omega - t) \Gamma_{\nu_2\nu_2\nu_3\mu_4}^\Lambda(\omega, \omega_2, -\omega + t, \omega_4) G_{\nu_3\nu_4}^\Lambda(\omega - t) \\ &\left. - \Gamma_{\mu_1\nu_4\nu_1\mu_4}^\Lambda(\omega_1, \omega - u, -\omega, \omega_4) \Gamma_{\nu_3\nu_2\mu_3\nu_2}^\Lambda(-\omega + u, \omega_2, \omega_3, \omega) G_{\nu_3\nu_4}^\Lambda(\omega - u) \right]. \end{aligned} \quad (2.22c)$$

As the free energy does not feed back into the other flow equations it is usually not considered within FRG schemes. In this chapter, we use its solution to derive further thermodynamic quantities. In these expressions, we have introduced the single-scale propagator which is defined as a matrix product of Green functions

$$\begin{aligned} \mathbf{S}^\Lambda &= -\mathbf{G}^\Lambda \left[ \frac{d}{d\Lambda} [\mathbf{G}_0^\Lambda]^{-1} \right] \mathbf{G}^\Lambda \\ S^\Lambda(\omega_2) &= -G^\Lambda(\omega_2) \left[ \frac{d}{d\Lambda} [G_0^\Lambda]^{-1}(\omega_2) \right] G^\Lambda(\omega_2). \end{aligned} \quad (2.23)$$

In order to solve the flow equations, initial conditions for self-energy and the four-point vertex are required. As the bare propagator vanishes in this limit, we

immediately see that

$$\begin{aligned}
 F_{\text{int}}^{\Lambda \rightarrow \infty} &= 0, \\
 \Sigma_{\mu_1, \mu_2}^{\Lambda \rightarrow \infty}(\omega) &= 0, \\
 \Gamma_{\mu_1, \mu_2, \mu_3, \mu_4}^{\Lambda \rightarrow \infty}(\omega_1, \omega_2, \omega_3, \omega_4) &= V_{\mu_1, \mu_2, \mu_3, \mu_4}.
 \end{aligned} \tag{2.24}$$

## 2.3. Symmetry-Based Vertex Parametrization

We now specialize the general Majorana FRG of this section to treat the interacting system of pseudo-Majoranas ensuing from the application of the representation (2.1) to the Heisenberg spin-1/2 Hamiltonian (1.43),

$$H = - \sum_{(i,j)} J_{ij} \left( \eta_i^y \eta_j^y \eta_i^z \eta_j^z + \eta_i^z \eta_j^z \eta_i^x \eta_j^x + \eta_i^x \eta_j^x \eta_i^y \eta_j^y \right). \tag{2.25}$$

As a first step, we proceed with a detailed discussion of the parametrization of vertices and propagators using the symmetries of Eq. (2.25). Following the approach of Ref. [122], we will first derive symmetry relations for the Green functions defined as

$$\begin{aligned}
 G(1, 2) &= \int_0^\beta d\tau_1 d\tau_2 e^{i\omega_1 \tau_1} e^{i\omega_2 \tau_2} \langle \eta_{\mu_1}(\tau_1) \eta_{\mu_2}(\tau_2) \rangle \\
 &= G_{\mu_1, \mu_2}(\omega_2) \beta \delta_{\omega_1, -\omega_2}
 \end{aligned} \tag{2.26}$$

$$\begin{aligned}
 G^4(1, 2, 3, 4) &= \int_0^\beta d\tau_1 d\tau_2 d\tau_3 d\tau_4 e^{i(\omega_1 \tau_1 + \omega_2 \tau_2 + \omega_3 \tau_3 + \omega_4 \tau_4)} \\
 &\quad \times \langle \eta_{\mu_1}(\tau_1) \eta_{\mu_2}(\tau_2) \eta_{\mu_3}(\tau_3) \eta_{\mu_4}(\tau_4) \rangle
 \end{aligned} \tag{2.27}$$

$$= G_{\mu_1, \mu_2, \mu_3, \mu_4}^4(s, t, u) \beta \delta_{\omega_1 + \omega_2 + \omega_3 + \omega_4, 0}. \tag{2.28}$$

where the labels (1, 2, 3, 4) contain all arguments that are not *explicitly* specified, i.e.  $1 = (\mu_1, \omega_1)$  in this case. Matsubara frequency conservation follows from the fact that thermal expectation values only depend on imaginary time differences. The time-ordering operator is suppressed since it is included in the path integral formalism by default. The properties derived in the following will then carry over to  $\Sigma$  and  $\Gamma$  due to their relations via Eqs. (2.16) and (2.17).

### Hermiticity

The Hamiltonian is a hermitian operator, satisfying  $H = H^\dagger$ . Due to  $\langle \mathcal{O} \rangle^* = \langle \mathcal{O}^\dagger \rangle$  and  $\eta(\tau)^\dagger = e^{-H\tau} \eta e^{H\tau} = \eta(-\tau)$  in the Heisenberg picture, one can find the complex



conjugate of the two-point Green functions as

$$\begin{aligned} G(1, 2)^* &= \int d\tau_1 d\tau_2 e^{-i\omega_1\tau_1 - i\omega_2\tau_2} \langle \eta_{\mu_2}(-\tau_2) \eta_{\mu_1}(-\tau_1) \rangle \\ &= -G(1, 2). \end{aligned} \quad (2.29)$$

As a consequence, the two-point Green function in Matsubara frequency space is purely imaginary and from an analogous argument, the four-point Green function must be real

$$\begin{aligned} G(1, 2) &\in i\mathbb{R}, \\ G^4(1, 2, 3, 4) &\in \mathbb{R}. \end{aligned} \quad (2.30)$$

### Time reversal symmetry

Time reversal  $T$  is an anti-unitary operation ( $\langle \psi | \psi' \rangle^* = \langle T\psi | T\psi' \rangle$ ) which in the present case can be defined by performing a complex conjugation while leaving Majorana operators invariant [217]:

$$TiT^{-1} = -i, \quad T\eta_\mu T^{-1} = \eta_\mu. \quad (2.31)$$

This flips the sign of the spin operators (2.1) as required. Time reversal symmetry is violated by an external magnetic field or, more generally, any Majorana bilinear in the Hamiltonian. For a  $T$ -symmetric Hamiltonian  $THT^{-1} = H$ , thermal expectation values obey  $\langle \mathcal{O} \rangle = \langle T\mathcal{O}T^{-1} \rangle^*$ . From this, we have  $\langle \eta_{\mu_1}(\tau_1) \eta_{\mu_2}(\tau_2) \rangle = \langle \eta_{\mu_1}(\tau_1) \eta_{\mu_2}(\tau_2) \rangle^*$  and with Eq. (2.26), it follows that

$$G_{\mu_1\mu_2}(\omega_1, \omega_2) = G_{\mu_1\mu_2}(-\omega_1, -\omega_2)^*. \quad (2.32)$$

Similarly, the four-point correlator has the property

$$G^4(1, 2, 3, 4) = G_{\mu_1\mu_2\mu_3\mu_4}^4(-\omega_1, -\omega_2, -\omega_3, -\omega_4)^*. \quad (2.33)$$

### Local $\mathbb{Z}_2$ gauge redundancy

Since our considerations from here on require the explicit specification of site indices, we will now separate the previously used superlabel  $\mu$  into a site-index and a Majorana flavor  $\mu \rightarrow (i, \alpha)$ . In the  $SO(3)$  Majorana representation spins are invariant under the gauge transformation  $\eta_i^\alpha \rightarrow \varepsilon_i \eta_i^\alpha$  for all  $\alpha = x, y, z$  with  $\varepsilon_i = \pm 1$  for an arbitrary lattice site  $i$ . Since expectation values must be invariant under gauge transformations as well, we may write

$$\langle \eta_{i_1}^{\alpha_1}(\tau_1) \eta_{i_2}^{\alpha_2}(\tau_2) \rangle = \varepsilon_{i_1} \varepsilon_{i_2} \langle \eta_{i_1}^{\alpha_1}(\tau_1) \eta_{i_2}^{\alpha_2}(\tau_2) \rangle, \quad (2.34)$$

where  $\varepsilon_{i_1}\varepsilon_{i_2} = -1$  may always be chosen for two different sites. As a consequence, non-zero propagators must contain an even number of Majorana operators from each site, so that

$$G_{i_1i_2}(1, 2) \equiv \delta_{i_1i_2}G_{i_1}(1, 2). \quad (2.35)$$

Likewise, the four-point correlator can only depend on up to two distinct sites only, so we choose

$$G_{i,i,j,j}^4(1, 2, 3, 4) \equiv G_{ij}^4(1, 2; 3, 4). \quad (2.36)$$

Correlators of the form  $ijij$  and  $ijji$  need to be brought to the standard form Eq. (2.36) using fermionic anticommutation rules, which restricts the number of allowed permutations in  $G_{ij}^4(1, 2; 3, 4)$  to exchanges of the first and last two indices only. As a consequence of the (bi-)local nature of propagators (four-point vertices), the site summations in the flow equations can be simplified. The special case  $i = j$  for the four-point vertex needs to be considered separately. The corresponding flow equations can then be expressed diagrammatically as shown in Fig. 2.1. The bubble-diagram corresponding to the  $s$ -channel of the non-local vertex  $\Gamma_{ij}$  shown in Fig. 2.1 (d) is of particular interest. As in the PFFRG this diagram includes the random-phase approximation which is responsible for the emergence of long-range magnetic order [120].


### Lattice symmetries


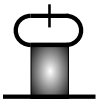
For simplicity, the systems that are considered in the following consist of equivalent sites. Correlators can then always be computed with one arbitrary reference site fixed. Combining this with local  $\mathbb{Z}_2$  gauge redundancy eliminates all site indices of the two-point correlator. Similarly, four-point correlators depend only on the distance vector between the two sites. Although this means that the order of site indices in  $\Gamma_{ij}$  is irrelevant for systems with equivalent sites, we will not make use of this property. As a result, the pseudo-Majorana flow equations presented here are easily generalized towards non-Bravais lattices by adding an additional sublattice-index. Most lattice systems further exhibit point-group symmetries, such as the  $C_4$  rotation symmetry and mirror planes of the square lattice, which can straightforwardly be used to reduce the numerical effort and are not further discussed in the following due to their lattice-specific nature.

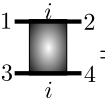
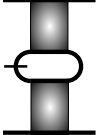
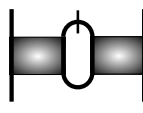
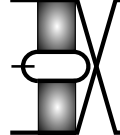
### Global $SO(3)$ rotation symmetry

The global  $SO(3)$  spin-rotation symmetry of the Heisenberg model can easily be translated to vertex functions. As discussed in Sec. 2.1, global spin rotations specified by a  $3 \times 3$  rotation matrix  $R_{\alpha\mu}(\phi)$  act on the Majorana fermions as

$$\eta_i^\alpha \rightarrow \sum_{\beta} R_{\alpha\beta}(\phi)\eta_i^\beta \quad \forall i. \quad (2.37)$$

a)  $\frac{d}{d\Lambda} F_{\text{int}}^{\Lambda} = \frac{1}{2}$  

b)  $\frac{d}{d\Lambda}$    $= \frac{1}{2}$  

c)  $\frac{d}{d\Lambda}$    $= -$    $-$    $+$  

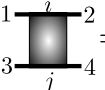
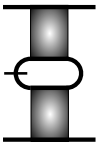




d)  $\frac{d}{d\Lambda}$    $= -$    $-$    $-$    
 $-$    $-$  

Figure 2.1.:  $\mathbb{Z}_2$ -invariant Majorana FRG flow equations for the interaction correction to the free energy (a), the self-energy (b), and the local (c) and nonlocal (d) four-point vertices. The order of labels  $1 = (\alpha_1, \omega_1)$  always corresponds to that on the left hand side of the vertex flow equations such that the site index is conserved along solid lines. In these equations, internal lines correspond to fully dressed Green functions  $G_i(1, 2)$ , while the single scale propagator  $S_i(1, 2)$  is represented by a slashed line. Similarly, the crossed line in (a) corresponds to the local propagator  $[SG^0G^{-1}]_i(1, 2)$ .

Angle	x	y	z
$\pi/2$	$\eta^y \rightarrow -\eta^z$ $\eta^z \rightarrow \eta^y$	$\eta^x \rightarrow \eta^z$ $\eta^z \rightarrow -\eta^x$	$\eta^x \rightarrow -\eta^y$ $\eta^y \rightarrow \eta^x$
$\pi$	$\eta^y \rightarrow -\eta^y$ $\eta^z \rightarrow -\eta^z$	$\eta^x \rightarrow -\eta^x$ $\eta^z \rightarrow -\eta^z$	$\eta^x \rightarrow -\eta^x$ $\eta^y \rightarrow -\eta^y$

Table 2.1.: Symmetry transformations corresponding to specific spin rotations along the  $x, y$  and  $z$  axes.

The Heisenberg Hamiltonian is invariant under spin rotations due to the isotropic nature of its couplings.

We will now apply this symmetry to restrict the types of vertices and find relations between vertices with different flavor indices. Of particular interest are the specific rotations along the  $x, y$  and  $z$ -axes as displayed in Table 2.1. The combination  $R_x(\pi/2) \circ R_z(\pi/2) \equiv \mathcal{P}$  realizes an anti-cyclic permutation of the flavors. We apply these symmetries to correlators, using the convention  $\gamma \neq \alpha \neq \beta \neq \gamma$  to refer to fixed, pairwise different flavors. In this way, we find that the two-point Green function does not depend on any flavor labels.

$$\begin{aligned} \langle \eta_1^\alpha \eta_2^\beta \rangle &\stackrel{R_\alpha(\pi)}{=} -\langle \eta_1^\alpha \eta_2^\beta \rangle = 0, \\ \Rightarrow G_{\alpha_1, \alpha_2}(1, 2) &= G_{\alpha_1}(1, 2) \delta_{\alpha_1, \alpha_2} \stackrel{\mathcal{P}}{=} G(1, 2) \delta_{\alpha_1, \alpha_2}. \end{aligned} \quad (2.38)$$

Because the four-point correlator has four flavor indices, at least two of them must be equal. An argument analogous to above shows that only vertices with an even number of flavors can be nonzero. Furthermore, rotations by  $\pi/2$  transform different flavor combinations into each other, for instance

$$\langle \eta_1^\alpha \eta_2^\alpha \eta_3^\beta \eta_4^\beta \rangle \stackrel{R_\alpha(\pi/2)}{=} \langle \eta_1^\alpha \eta_2^\alpha \eta_3^\gamma \eta_4^\gamma \rangle. \quad (2.39)$$

These arguments identify four independent flavor configurations for the four-point correlator,  $G_{xxxx}^4(1, 2, 3, 4)$ ,  $G_{xxyy}^4(1, 2, 3, 4)$ ,  $G_{xyxy}^4(1, 2, 3, 4)$  and  $G_{xyyx}^4(1, 2, 3, 4)$ , all other types are either zero or related by Eq. (2.39).

After these simplifications, we consider a general rotation to find a relation between those four different correlators. Since they are now parametrized in terms of  $x$  and  $y$ , we only need to consider rotations along the  $z$ -axis. The  $\eta^x$  Majoranas then transform as  $\eta_i^x \rightarrow \cos \theta \eta_i^x - \sin \theta \eta_i^y$  so that

$$G_{xxxx}^4 \stackrel{R_z(\theta)}{=} \langle (\cos \theta \eta_1^x - \sin \theta \eta_1^y) \dots (\cos \theta \eta_4^x - \sin \theta \eta_4^y) \rangle. \quad (2.40)$$

Expanding the product and using the above symmetries, we obtain a relation independent of  $\theta$

$$G_{xxxx}^4 = G_{xxyy}^4 + G_{xyxy}^4 + G_{yyyx}^4, \quad (2.41)$$

where the argument  $(1, 2, 3, 4)$  has been suppressed. Since we considered an arbitrary rotation, our last consideration further serves as a proof that no other symmetries than the ones already shown may be found from  $SO(3)$  rotations. Indeed, one arrives at the same identity regardless of which type of correlator one transforms (i.e. transforming  $G_{xyxy}^4$  yields the same result). Rotations along the  $x$  or  $y$  direction also generate no further information as a result of the permutation symmetry  $\mathcal{P}$  and rotations around an arbitrary axis may always be decomposed as a product of  $x, y$  and  $z$  rotations.

## 2.4. Pseudo-Majorana FRG Flow Equations

The symmetries of the last section imply the following parametrization of the pseudo-Majorana propagator,

$$G(1, 2) = \mathcal{G}(-\omega_1) \delta_{i_1, i_2} \delta_{\alpha_1, \alpha_2} \delta_{\omega_1, -\omega_2} \beta, \quad (2.42)$$

where the imaginary and antisymmetric self-energy, abbreviated as  $\Sigma(\omega) = -i\gamma(\omega)$ , enters via the Dyson equation (2.16),

$$\mathcal{G}(\omega) = \frac{1}{i\omega + i\gamma(\omega)} \equiv -ig(\omega). \quad (2.43)$$

In analogy to the real functions  $\gamma(\omega)$  and  $g(\omega)$  we also replace the imaginary single scale propagator via  $S^\Lambda(\omega) = -i\dot{g}^\Lambda(\omega)$ . Due to the diagonal structure of the propagators, the symmetries for the four-point Green functions then carry over to vertex functions [cf. Eq. (2.17)] whose frequency dependence is parametrized by the three bosonic frequencies introduced in Eq. (2.21). The three independent four-point vertices are

$$\begin{aligned} \Gamma_a \, ij(s, t, u) &\equiv \Gamma_{xi, xi, xj, xj}(s, t, u), \\ \Gamma_b \, ij(s, t, u) &\equiv \Gamma_{xi, xi, yj, yj}(s, t, u), \\ \Gamma_c \, ij(s, t, u) &\equiv \Gamma_{xi, yi, xj, yj}(s, t, u). \end{aligned} \quad (2.44)$$

In the special case  $i = j$ , there are only two independent vertices since

$$\Gamma_c \, ii(s, t, u) = -\Gamma_b \, ii(t, s, u). \quad (2.45)$$

Operation	Symmetry for $\Gamma_{\mu ij}(s, t, u)$	valid $\mu$
$1 \leftrightarrow 2$	$t \leftrightarrow u$ and $\Gamma_{\mu} \leftrightarrow -\Gamma_{\mu}$	$a, b$
$T \circ (1, 3) \leftrightarrow (2, 4)$	$s \leftrightarrow -s$	$a, b, c$
$T \circ (1, 2) \leftrightarrow (3, 4)$	$t \leftrightarrow -t$ and $i \leftrightarrow j$	$a, b, c$
$T \circ (1, 2) \leftrightarrow (4, 3)$	$u \leftrightarrow -u$ and $i \leftrightarrow j$	$a, b, c$

Table 2.2.: Transformations of the frequency arguments under time reversal  $T$  and specific permutations of indices in  $\Gamma_{ij}(1, 2; 3, 4)$ . The latter three rows apply to all three types of vertices and allow for a parametrization using positive frequencies only. Note that the final two permutations also exchange the order of  $i$  and  $j$  which is of importance for non-Bravais lattices. The remaining  $t \leftrightarrow u$  symmetry for  $\Gamma_c$  can be established by the exchange  $1 \leftrightarrow 2$ , which changes the vertex to the form  $\Gamma_{xyyx}$ . Using Eq. (2.41) to express  $\Gamma_{xyyx}(s, t, u) = -\Gamma_c(s, u, t)$  in terms of the other vertices used in the parametrization, we obtain  $\Gamma_c ij(s, u, t) = (-\Gamma_a ij + \Gamma_b ij + \Gamma_c ij)(s, t, u)$ .

Vertices with negative bosonic frequencies are symmetry related to positive frequencies by time-reversal and a symmetry  $t \leftrightarrow u$  further allows to reduce the numerical effort. Details are given in Table 2.2. In the above parametrization, the flow equations for the interaction correction to the free energy per spin and the self-energy may be simplified. Specifying the external flavor and site indices on the left hand side of the flow equations, we directly perform flavor sums to obtain

$$\frac{d}{d\Lambda} f_{\text{int}}^{\Lambda} = -\frac{3T}{2} \sum_{\omega} \dot{g}^{\Lambda}(\omega) \frac{g^{0,\Lambda}(\omega)}{g^{\Lambda}(\omega)} \gamma^{\Lambda}(\omega), \quad (2.46)$$

$$\begin{aligned} \frac{d}{d\Lambda} \gamma^{\Lambda}(\omega_1) = \frac{T}{2} \sum_{\omega} \sum_j \dot{g}^{\Lambda}(\omega) \left\{ \Gamma_a^{\Lambda} ij(0, \omega_1 + \omega, \omega_1 - \omega) \right. \\ \left. + 2\Gamma_b^{\Lambda} ij(0, \omega_1 + \omega, \omega_1 - \omega) \right\}. \end{aligned} \quad (2.47)$$

Similarly, we may now express the flow equations for four-point vertices in the same way. For conciseness of notation, both the initial fermionic frequencies as well as the exchange frequencies  $s, t$  and  $u$  will be used on the right hand side which are defined by Eq. (2.21), or inversely,

$$\begin{aligned} \omega_1 = \frac{s+t+u}{2}, \quad \omega_2 = \frac{s-t-u}{2} \\ \omega_3 = \frac{-s+t-u}{2}, \quad \omega_4 = \frac{-s-t+u}{2}. \end{aligned} \quad (2.48)$$

$$\frac{d}{d\Lambda} \Gamma_{a\ ij}^\Lambda(s, t, u) = X_{a\ ij}^\Lambda(s, t, u) - \tilde{X}_{a\ ij}^\Lambda(t, s, u) + \tilde{X}_{a\ ij}^\Lambda(u, s, t) \quad (2.49a)$$

$$\frac{d}{d\Lambda} \Gamma_{b\ ij}^\Lambda(s, t, u) = X_{b\ ij}^\Lambda(s, t, u) - \tilde{X}_{c\ ij}^\Lambda(t, s, u) + \tilde{X}_{c\ ij}^\Lambda(u, s, t) \quad (2.49b)$$

$$\frac{d}{d\Lambda} \Gamma_{c\ i,j\neq i}^\Lambda(s, t, u) = X_{c\ ij}^\Lambda(s, t, u) - \tilde{X}_{b\ ij}^\Lambda(t, s, u) + \tilde{X}_{d\ ij}^\Lambda(u, s, t) \quad (2.49c)$$

$$X_{a,ij}^\Lambda(s, t, u) = T \sum_{\omega, k} P^\Lambda(\omega, s) \left[ \Gamma_{a,ki}^\Lambda(s, \omega + \omega_1, \omega + \omega_2) \Gamma_{a,kj}^\Lambda(s, \omega - \omega_3, \omega - \omega_4) + 2(a \rightarrow b) \right] \quad (2.50a)$$

$$X_{b,ij}^\Lambda(s, t, u) = T \sum_{\omega, k} P^\Lambda(\omega, s) \left[ \Gamma_{a,ki}^\Lambda(s, \omega + \omega_1, \omega + \omega_2) \Gamma_{b,kj}^\Lambda(s, \omega - \omega_3, \omega - \omega_4) + (a \rightarrow b) + (a \leftrightarrow b) \right] \quad (2.50b)$$

$$X_{c,ij}^\Lambda(s, t, u) = T \sum_{\omega, k} P^\Lambda(\omega, s) \left[ \Gamma_{c,ki}^\Lambda(s, \omega + \omega_1, \omega + \omega_2) \Gamma_{c,kj}^\Lambda(s, \omega - \omega_3, \omega - \omega_4) + (\omega_1 \leftrightarrow \omega_2, \omega_3 \leftrightarrow \omega_4) \right] \quad (2.50c)$$

$$\tilde{X}_{a\ i,j\neq i}^\Lambda(s, t, u) = T \sum_{\omega} P^\Lambda(\omega, s) \left\{ \left[ \Gamma_{a,ij}^\Lambda(\omega + \omega_2, s, \omega + \omega_1) \Gamma_{a,ij}^\Lambda(\omega - \omega_4, s, \omega - \omega_3) + (\omega_1 \leftrightarrow \omega_2, \omega_3 \leftrightarrow \omega_4, i \leftrightarrow j) \right] + 2(a \rightarrow c) \right\} \quad (2.51a)$$

$$\tilde{X}_{b\ i,j\neq i}^\Lambda(s, t, u) = T \sum_{\omega} P^\Lambda(\omega, s) \left\{ \left[ \Gamma_{a,ij}^\Lambda(\omega + \omega_2, s, \omega + \omega_1) \Gamma_{c,ij}^\Lambda(\omega - \omega_4, s, \omega - \omega_3) + (\omega_1 \leftrightarrow \omega_2, \omega_3 \leftrightarrow \omega_4, i \leftrightarrow j) \right] + (a \rightarrow c) + (a \leftrightarrow c) \right\} \quad (2.51b)$$

$$\tilde{X}_{c\ i,j\neq i}^\Lambda(s, t, u) = T \sum_{\omega} P^\Lambda(\omega, s) \left\{ \left[ \Gamma_{b,ij}^\Lambda(\omega + \omega_2, \omega + \omega_1, s) \Gamma_{b,ij}^\Lambda(\omega - \omega_4, \omega - \omega_3, s) + (\omega_1 \leftrightarrow \omega_2, \omega_3 \leftrightarrow \omega_4, i \leftrightarrow j) \right] + (b \rightarrow c) \right\} \quad (2.51c)$$

$$\tilde{X}_{d\ i,j\neq i}^\Lambda(s, t, u) = T \sum_{\omega} P^\Lambda(\omega, s) \left\{ \left[ \Gamma_{b,ij}^\Lambda(\omega + \omega_2, \omega + \omega_1, s) \Gamma_{c,ij}^\Lambda(\omega - \omega_4, \omega - \omega_3, s) + (\omega_1 \leftrightarrow \omega_2, \omega_3 \leftrightarrow \omega_4, i \leftrightarrow j) \right] + (b \leftrightarrow c) \right\} \quad (2.51d)$$

To reduce the length of expressions, the bubble propagator  $P^\Lambda = \dot{g}^\Lambda(\omega)g^\Lambda(\omega + s)$  and single-channel contributions  $X_{a,b,c\ ij}^\Lambda$  and  $\tilde{X}_{a,b,c,d\ ij}^\Lambda$  were defined in Eqs. (2.50) and (2.51) [195]. The flow equations of local vertices are obtained noting that  $\tilde{X}_{a,b,c\ ii}^\Lambda(s, t, u) \equiv X_{a,b,c\ ii}^\Lambda(s, t, u)$ . It is further stressed that no flow equation for

$\Gamma_{c\ ii}$  is required in Eq. (2.49), as this vertex is equivalent to  $\Gamma_{b\ ii}$  by virtue of Eq. (2.45).

In the PFFRG, the Katanin truncation scheme [149] was instrumental in providing sufficient feedback of the self-energy flow into the vertex flow equations [119]. It amounts to promoting the single-scale propagator in the flow equations of four-point vertices to a full derivative of the Green function

$$\begin{aligned} S^\Lambda(\omega) &\rightarrow \frac{d}{d\Lambda} \mathcal{G}^\Lambda(\omega) \equiv S_{\text{conv.}}(\omega) + S_{\text{Kat}}(\omega) \\ &= -\mathcal{G}(\omega)^2 \frac{d}{d\Lambda} [\mathcal{G}^{0\Lambda}(\omega)]^{-1} + \mathcal{G}(\omega)^2 \frac{d}{d\Lambda} \Sigma^\Lambda(\omega). \end{aligned} \quad (2.52)$$

At zero temperature, frequencies become continuous and  $T \sum_\omega \rightarrow (2\pi)^{-1} \int d\omega$ . Using the sharp frequency cutoff  $\mathcal{G}^{0\Lambda}(\omega) = \mathcal{G}^0(\omega) \theta(|\omega| - \Lambda)$ , we thus obtain in the usual way using Morris's Lemma [218]

$$\dot{g}_{T=0}^\Lambda(\omega) = -\frac{\delta(|\omega| - \Lambda)}{\omega + \gamma^\Lambda(\omega)} + \dot{g}_{\text{Kat}}^\Lambda(\omega). \quad (2.53)$$

At finite temperatures, a sharp cutoff of frequencies is no longer possible due to ambiguities that arise if  $|\omega| - \Lambda$  lies between two discrete Matsubara frequencies. Noting that there is still freedom in the choice of a smooth cutoff [203, 219], here we choose a Lorentzian cutoff function

$$\Theta^\Lambda(\omega_n) = \frac{\omega_n^2}{\omega_n^2 + \Lambda^2}. \quad (2.54)$$

Using Eqs. (2.15), (2.16) and (2.52) the expressions for the Green function and the single-scale propagator become

$$\begin{aligned} g^\Lambda(i\omega_n) &= \frac{\omega_n}{\omega_n^2 + \omega_n \gamma(\omega_n) + \Lambda^2} \\ \dot{g}^\Lambda(i\omega_n) &= -g^2(i\omega_n) \left( \frac{2\Lambda}{\omega_n} + \frac{d\gamma^\Lambda(i\omega_n)}{d\Lambda} \right). \end{aligned} \quad (2.55)$$

Finally, we need to specify the initial conditions for the newly defined vertices. After re-expressing the Heisenberg Hamiltonian (1.43) by insertion of Eq. (2.1) for the spin operators, a comparison of coefficients yields

$$\begin{aligned} f_{\text{int}}^{\Lambda \rightarrow \infty} &= 0, \\ \Sigma^{\Lambda \rightarrow \infty} &= 0, \\ \Gamma_{a\ ij}^{\Lambda \rightarrow \infty} &= \Gamma_{b\ ij}^{\Lambda \rightarrow \infty} = 0, \\ \Gamma_{c\ ij}^{\Lambda \rightarrow \infty} &= -J_{ij}. \end{aligned} \quad (2.56)$$



To summarize, in the PMFRG scheme the flow equations for the free energy (2.46), self-energy (2.47) and the vertex functions (2.49), are solved numerically starting from large but finite  $\Lambda \gg J$  down to  $\Lambda \simeq 0$ , approximating the initial conditions with the  $\Lambda \rightarrow \infty$  values presented above. The flow of the free energy correction is integrated along the way but does not feed back into the other flow equations. The next section describes how to extract observables along the flow and, most importantly, at the physical endpoint  $\Lambda = 0$ .

## 2.5. Observables

In this section, we discuss the observables for Heisenberg spin-1/2 systems that will be studied in the following sections. These are the free energy, internal energy, heat capacity and static susceptibility. We explain how these observables are calculated from the eigenstates and -energies of the spin Hamiltonian (1.43), its exact representation with  $SO(3)$  Majorana fermions and from the (approximate) solution of the PMFRG flow equations.

From the partition function of a  $N$ -spin system with eigenenergies  $E_n$ ,  $\mathcal{Z} = \sum_n e^{-\beta E_n}$ , the free energy per spin is given by

$$F/N = f = -\frac{T}{N} \log(\mathcal{Z}) = -\frac{T}{N} \log \sum_n e^{-\beta E_n}. \quad (2.57)$$

The energy per spin is

$$E/N = -\frac{\partial \log(\mathcal{Z})}{N \partial \beta} = \frac{\partial(f\beta)}{\partial \beta} = \frac{1}{N\mathcal{Z}} \sum_n E_n e^{-\beta E_n}, \quad (2.58)$$

which as a function of  $T$  also determines the heat capacity

$$C/N = \frac{\partial}{\partial T} E/N = \frac{1}{NT^2} \left( \frac{1}{\mathcal{Z}} \sum_n E_n^2 e^{-\beta E_n} - E^2 \right). \quad (2.59)$$

For small systems amenable to exact diagonalization, the rightmost expressions are most convenient. From the solution of the PMFRG flow equation (2.46) for the interaction correction to the pseudo-Majorana free energy per site, we find  $f_{pm} = f_{pm,0} + f_{\text{int}}^{\Lambda=0}$ . The non-interacting free energy for three pseudo-Majoranas per site is  $f_{pm,0} = -3T \log(2)/2$ . Using the relation between  $f_{pm}$  and  $f$ , Eq. (2.6), we finally obtain

$$f = -T \log(2) + f_{\text{int}}^{\Lambda=0}. \quad (2.60)$$

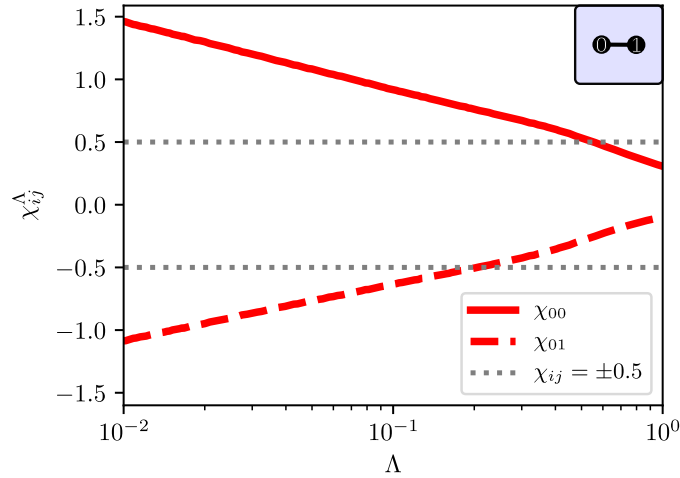


Figure 2.2.: Zero temperature PMFRG flow of the static local and nonlocal susceptibilities  $\chi_{ij}$  for the antiferromagnetic Heisenberg dimer. The grey dotted line represents the exact physical ( $\Lambda = 0$ ) result.

The static spin-spin correlator can be computed from

$$\chi_{ij} = \int_0^\beta d\tau \langle S_i^z(\tau) S_j^z(0) \rangle. \quad (2.61)$$

Note that  $\chi_{ij}$  can also be interpreted as a static (zero-field) susceptibility as it measures the response of a spin at site  $i$  when a magnetic field is exerted at site  $j$ . We represent the spin operators by Majorana fermions and obtain from the vertices of the PMFRG at cutoff scale  $\Lambda$ ,

$$\begin{aligned} \chi_{ij}^\Lambda = & + T^2 \sum_{\omega_1 \omega_2} g^\Lambda(\omega_1)^2 g^\Lambda(\omega_2)^2 \Gamma_{c\ ij}^\Lambda(0, \omega_1 + \omega_2, \omega_1 - \omega_2) \\ & + T \sum_{\omega_1} g^\Lambda(\omega_1)^2 \delta_{ij}. \end{aligned} \quad (2.62)$$

## 2.6. Application: Small Spin Clusters

### Spin dimer and the fermion parity issue

Small spin clusters constitute an ideal testbed for probing the accuracy of numerical approaches as they already represent non-trivial problems within the PMFRG (and PFFRG) but are still exactly solvable. We first investigate the simple case of two spins,  $i = 0, 1$  coupled with an antiferromagnetic Heisenberg interaction  $J = 1$ . Due to the small Hilbert space, this dimer model  $H_{N=2} = \sum_\alpha S_0^\alpha S_1^\alpha$  is

analytically solvable. While the free energy Eq. (2.57) is straightforwardly found, some care is required for the calculation of the susceptibility from the Lehmann representation where the term contributing in the case  $i\nu + E_n - E_m = 0$  is often neglected in textbook derivations. We obtain

$$\begin{aligned}\chi_{00} &= \frac{e^\beta - 1 + \beta}{2(e^\beta + 3)}, \\ \chi_{01} &= -\frac{e^\beta - 1 - \beta}{2(e^\beta + 3)}.\end{aligned}\tag{2.63}$$

The PMFRG results for the static susceptibility in the case  $T = 0$  are shown in Fig. 2.2 as a function of the cutoff. We find that  $\chi_{ij}^\Lambda$  flows smoothly without any feature, surpasses the exact results  $\chi_{ij} = \pm 0.5$  and diverges at  $\Lambda = 0$ . This unphysical divergence is not restricted to the Heisenberg dimer but appears in all other models considered here. However, the dimer allows for the most simple discussion of the origin of this divergence, which equally plagues the flow of the nonlocal vertices of type  $\Gamma_{a,01} = \Gamma_{x_0,x_0,x_1,x_1}$  and  $\Gamma_{c,01} = \Gamma_{x_0,y_0,x_1,y_1}$ .

To explain the origin of this divergence, consider the Heisenberg dimer which can be exactly solved in the  $SO(3)$  Majorana representation,

$$H_{N=2} = -\frac{1}{4}p^x p^y p^z (p^x + p^y + p^z).\tag{2.64}$$

Here,  $p^\alpha \equiv 2i\eta_0^\alpha \eta_1^\alpha$  are the three flavor parities related to the non-local parity introduced in Sec. 2.1 via  $p_{(0,1)} = 2i\tau_0\tau_1 = -p^x p^y p^z$ . While  $p_{(i,j)} = \pm 1$  is always conserved for generic spin systems,  $p^\alpha = \pm 1$  are additional constants of motion only for the dimer, Eq. (2.64). As any state, the ground state is  $2^{N/2} = 2$  fold degenerate and identified in this case by  $p^\alpha = 1$  or  $p^\alpha = -1$  for all  $\alpha$ . Now consider the effect of a small perturbation,  $H_{N=2} \rightarrow H_{N=2} + vp^x$ . This does not correspond to any physical perturbation in terms of spin operators but lifts the ground state degeneracy. From this point of view, the ground state expectation value  $\langle p^\alpha \rangle = 0$  is fragile, any finite perturbation violating the conservation of  $\tau_i$  as defined in Eq. (2.4) with  $i = 0, 1$  generically causes  $\langle p^\alpha \rangle = \pm 1$ . This effect is of course alleviated at finite temperature, where the relative population difference of the two lowest states split by  $\sim v$  is controlled by the ratio  $v/T$ . Kubo's formula allows to formalize the above considerations for the linear response of  $\langle p^\alpha \rangle$  with respect to  $vp^x$ ,

$$\langle p^\alpha \rangle = -vG_{p^\alpha p^x}^R(i\omega_k = 0).\tag{2.65}$$

In Matsubara frequency space, the retarded Green function above may be obtained in the Lehmann representation noting that the parities are diagonal in the eigen-

basis of the unperturbed Hamiltonian  $\langle n|p^\alpha|m\rangle = p_n^\alpha \delta_{nm}$ ,

$$G_{p^\alpha p^x}(i\omega_k = 0) = \frac{\beta}{\mathcal{Z}} \sum_n e^{-\beta E_n} p_n^\alpha p_n^x. \quad (2.66)$$

At low temperatures this yields  $\beta = \frac{1}{T}$ , similar to the Curie-like  $1/T$  behaviour of the spin susceptibility of a free spin  $1/2$  which also features a degenerate ground state in the field-free case. In complete analogy to the spin susceptibility in Eq. (2.62), we can now find the tree expansion of the parity susceptibility  $G_{p^\alpha p^x}(i\omega_k = 0)$  in terms of the non-local vertices of type  $\Gamma_a$  (for  $\alpha = x$ ) or  $\Gamma_c$  ( $\alpha = y, z$ ). The expressions are similar to Eq. (2.62) but crucially probe different frequency combinations of the vertices ( $t = 0$  instead of  $s = 0$ ). In other words, non-local vertex components of order  $\sim 1/T$  are inherently expected in the  $\text{SO}(3)$  Majorana representation. In an exact calculation, these components are responsible for the  $1/T$  parity susceptibility of Eq. (2.66), but do not affect the spin susceptibility. However, the PMFRG is not an exact method and the unphysical behavior of  $\chi_{ij}^\Lambda$  at  $T = 0$  must be a consequence of truncating the PMFRG flow equations which apparently causes this divergence to spill over to the spin susceptibility. It is an interesting question if an improved two-loop truncation scheme (correct to order  $\mathcal{O}(J^3)$ ) [195] or a recently developed but numerically demanding multi-loop generalizations of the (PF)FRG [164, 165], can be a possible cure to this problem.

Fortunately, as the unphysical divergence in the PMFRG flow only occurs at  $\Lambda = 0$  and for  $T = 0$ , there are other options to extract physically meaningful results without going beyond the flow equations presented above. First, it is still possible to detect magnetic phases, heralded by divergences at finite  $\Lambda$  as we have tested for the  $J_1 - J_2$  square lattice Heisenberg model (data not shown).

The rest of the discussion is devoted to a second option, which is the restriction to finite temperatures. As explained above, this can be expected to suppresses the unphysical divergence and we indeed find all vertices and flowing susceptibilities converge towards  $\Lambda \rightarrow 0$ , see lower inset of Fig. 2.3 for  $T = 0.1$ .

### Dimer and hexamer at finite temperature

Results for the physical finite- $T$  susceptibility of the dimer at  $\Lambda = 0$  are shown in Fig. 2.3. For  $T \gtrsim 0.2$ , we find a very close agreement between the susceptibility obtained via PMFRG and the exact result (solid lines) from Eq. (2.63). The difference between the exact result and the PMFRG increases with decreasing temperature, in agreement with the discussion in the previous subsection. We also show analogous results of the PFFRG, where the presence of unphysical states

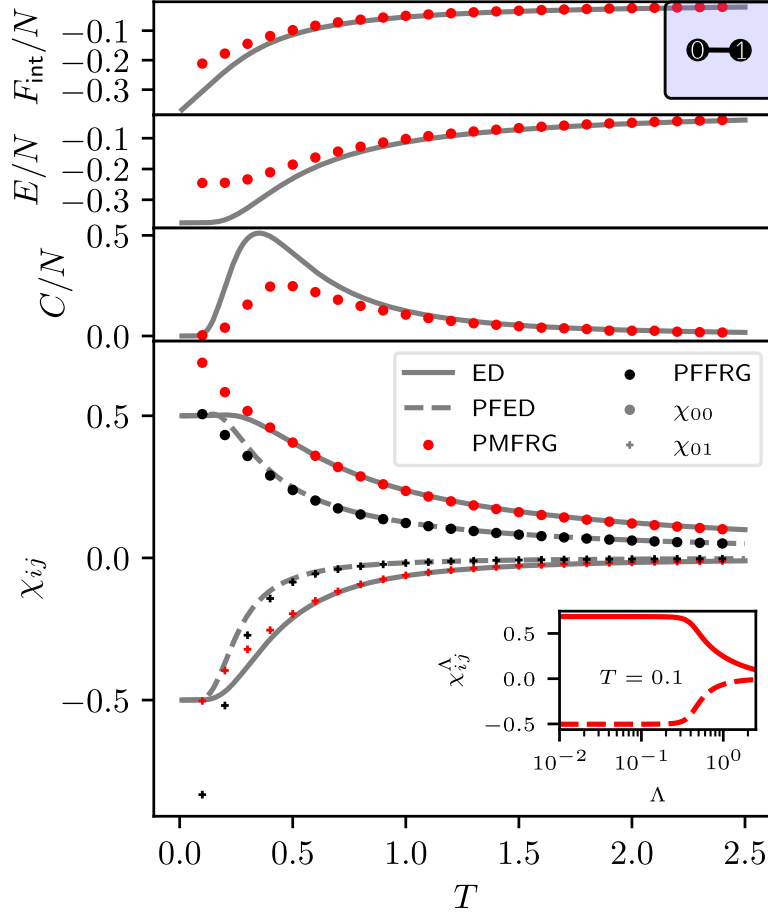


Figure 2.3.: (Free) energy, heat capacity per spin and static susceptibilities of the Heisenberg dimer with  $J = 1$  obtained via PMFRG (red symbols) at  $\Lambda = 0$  as a function of temperature. Displayed in solid (dashed) grey lines are the results obtained by (pseudo-fermion) exact diagonalization, as well as the finite temperature spin susceptibilities of the PFFRG in black symbols. Each data point corresponds to a fully converged flow with respect to  $\Lambda$  as demonstrated in the exemplary plot at  $T = 0.1$  (cf. Fig. 2.2).

seriously compromises the accuracy of the results at any finite temperature scale. To support this interpretation, we have also included the results of an exact diagonalization scheme of the pseudo-fermionic Hamiltonian without projecting out unphysical states, further referred to as PFED. The close agreement between PFFRG and PFED demonstrates the problematic impact of unphysical states at finite temperatures which so far has no known resolution. One approach, the Popov-Fedotov projection scheme, suppresses unphysical states in exact calculations of observables upon the introduction of an imaginary chemical potential. Producing a quarter-period shift of Matsubara frequencies [203, 220], this option can be integrated in the PFFRG, however, numerical results show that the spin constraint  $|\langle S^z \rangle|^2 = 1/4$  is violated at any temperature due to truncation effects, much in contrast to the PMFRG, where the constraint is always fulfilled by construction [160].

Besides the magnetic susceptibility, the solution of the free energy flow equation enables us to compute a variety of related thermodynamic observables, such as the energy per spin and the heat capacity, also displayed in Fig. 2.3. We observe good agreement at large enough temperatures. At intermediate scales  $T \simeq 0.5$ , the quality of the thermodynamic quantities from the PMFRG decreases as can be seen most clearly from the overestimation of the energy per spin or the underestimation of the peak in the heat capacity. These inaccuracies likely stem from the underestimation of the Majorana self-energy at small frequencies, a known problem in pseudo-fermion FRG approaches to spin systems of small dimensionality [184].

Analogous results are obtained for larger spin clusters such as the Heisenberg hexamer, a hexagon of six equivalent spins with nearest and next-nearest neighbor interactions,  $J_1 = 1$  and  $J_2 = 0.5$  respectively. As shown in Fig. 2.4, the PMFRG results are in good agreement with ED at not too small temperatures. The susceptibilities are generally more accurate than the thermodynamic properties. The susceptibility obtained via PFFRG shows large deviations from ED results at all temperatures. It is emphasized again that small spin clusters are particularly challenging within the FRG framework since its built-in mean-field limits are generally not expected to describe such systems accurately. On the other hand, mean-field approaches perform better in higher-dimensional systems. The FRG is, hence, expected to reach its full potential for larger or even infinite systems to which we move on in the later chapters Chapters 4 to 6.

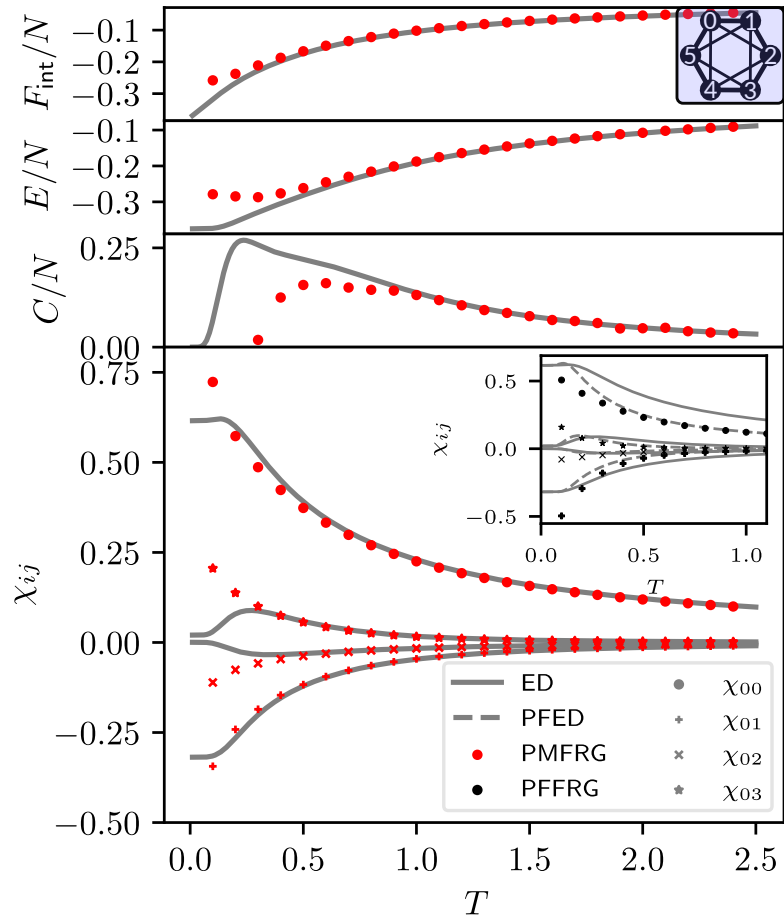


Figure 2.4.: PMFRG results for the Heisenberg hexamer in analogy to Fig. 2.3. The corresponding PFFRG and PFED results of the spin susceptibility are included in the inset.





## Extensions of the formalism

### 3.1. Parquet formalism and the multiloop expansion

Recently, a very active direction of research in the context of FRG method development has been the multiloop expansion [164, 165, 167, 221–226]. Aiming to improve upon the accuracy of the one-loop formalism, the goal is to systematically increase the number of diagrams included in the flow equations by recursively inserting loop diagrams into themselves. Eberlein’s initial inclusion of two-loop corrections were motivated from diagrams that are included in the three-particle vertex but can be expressed using a combination of two-particle diagrams, shown in Fig. 3.1, similar in spirit to the inclusion of Katanin’s correction [149]. A detailed derivation of the two-loop corrections for Majorana fermions is detailed in Chapter B. In Chapter 5, we shall see the effect of these contributions on the nearest neighbor pyrochlore ferro- and antiferromagnets.

Soon after this, Kugler and von Delft derived the iterative procedure to include higher-loop corrections mentioned above [167]. More importantly, they showed that this procedure converges at infinite loop order to the so-called *Parquet approximation* [227, 228], a self-consistent equation based upon the formally exact *Bethe-Salpeter equation* [229] shown in Fig. 3.2.

The implementation of these corrections within the PFFRG, while ultimately successful, were initially met with technical challenges that required significant improvements to the numerical accuracy of Matsubara frequency discretization and numerical integration [164, 165]. On the other hand, the PMFRG does not

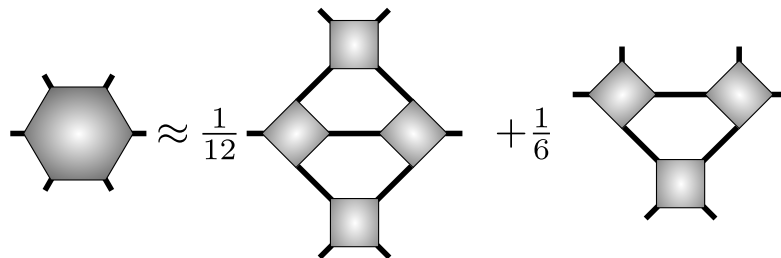


Figure 3.1.: Two-loop approximation for the six-point vertex.

$$\begin{aligned}
 (a) \quad & \text{---} \Sigma \text{---} = \frac{1}{2} \text{---} \Gamma_0 \text{---} + \frac{1}{6} \text{---} \Gamma_0 \text{---} \Gamma \text{---} \\
 (b) \quad & \begin{array}{c} 1 \\ \text{---} \Gamma \text{---} \\ 2 \quad 3 \end{array} \begin{array}{c} 4 \\ \text{---} \\ \end{array} = \begin{array}{c} 1 \\ \text{---} R \text{---} \\ 2 \quad 3 \end{array} \begin{array}{c} 4 \\ \text{---} \\ \end{array} + \begin{array}{c} 1 \\ \text{---} \gamma \text{---} \\ 2 \quad 3 \end{array} \begin{array}{c} 4 \\ \text{---} \\ \end{array} + \begin{array}{c} 1 \\ \text{---} \bar{\gamma} \text{---} \\ 2 \quad 3 \end{array} \begin{array}{c} 4 \\ \text{---} \\ \end{array} \\
 (c) \quad & \begin{array}{c} \text{---} \gamma \text{---} \\ \text{---} \end{array} = \frac{1}{2} \text{---} \Gamma_0 \text{---} \Gamma \text{---} + \begin{array}{c} \text{---} \gamma \text{---} \\ \text{---} \end{array} \Gamma \text{---}
 \end{aligned}$$

Figure 3.2.: **Diagrammatic Majorana parquet equations.** (a) Self-consistent Schwinger-Dyson equation for the self-energy  $\Sigma$ . (b) Decomposition of the Majorana four-point vertex  $\Gamma$  into the fully irreducible vertex  $R$ , two-particle reducible contributions in the  $s$ -channel,  $\gamma$ , and  $\bar{\gamma}_{1,2|3,4} = -\gamma_{1,3|2,4} + \gamma_{1,4|2,3}$  and (c) Bethe-Salpeter equation for  $\gamma$ .

require such efforts due to its application at finite temperature where the Matsubara frequencies are naturally discretized. To reduce the technical complexity of this chapter, the reader is referred to Chapter C for details regarding the so-far unpublished derivation of the Bethe-Salpeter and Schwinger-Dyson equations for Majorana fermions, as well as the derivation of the one- and two-loop approximations from this formalism in Section C.2.

Indeed, at finite temperature it is possible to iteratively converge to a solution of the parquet equations, without resorting to the multiloop expansion. On the other hand, its benchmark applications to toy-models so-far have been of limited success, yielding either no substantial improvement or even strictly worse [160], see also Section C.3.

## 3.2. Temperature flow

While the parquet formalism surprisingly did not yield substantial improvements to the one-loop PMFRG, we now turn to a formalism which exploits the existing strengths of the one-loop formalism and was found to improve the detection of magnetic phase transitions at much lower temperatures. While PMFRG simula-

tions at finite temperature represent an important method extension and become even perturbatively error-controlled at large temperature, the cost of this improvement is significant, as it requires a separate solution of the numerically expensive FRG flow equations at each temperature. The renormalization group parameter is typically implemented through an artificial infrared cutoff  $\Lambda$  in the single particle Green function, suppressing fermionic propagation with Matsubara frequencies  $|\omega_n| \ll \Lambda$ . An alternative formulation was first demonstrated by Honerkamp and Salmhofer in Ref. [230] for systems of itinerant fermions where *temperature* was employed as a flow parameter instead. In this approach, a single FRG flow along the physical temperature provides a whole slice through a finite-temperature phase diagram at once. On the other hand, however, the usual notion of RG as a successive integration of UV degrees of freedom is lost [181, 231].

### Action and field rescaling

We shall assume a general spin-1/2 Hamiltonian

$$H = \sum_{i,\alpha} h_i^\alpha S_i^\alpha + \frac{1}{2} \sum_{i,j,\alpha_1,\alpha_2} S_i^{\alpha_1} J_{ij}^{\alpha_1\alpha_2} S_j^{\alpha_2}, \quad (3.1)$$

where  $S_i^\alpha$  with  $\alpha = x, y, z$  are the components of a spin-1/2 operator on site  $i$ ,  $J_{ij}^{\alpha\beta}$  are general anisotropic spin interactions and  $h_i^\alpha$  is a site-dependent magnetic field. We map  $H$  onto a pseudo-Majorana Hamiltonian using the  $SO(3)$  representation in Eq. (2.1)

We again consider a general system of interacting Majoranas with the action written in imaginary time as in Eq. (2.11)  $\tau$  [1], where we now write the interaction part explicitly

$$S = \frac{1}{2} \int_0^\beta d\tau \eta_{\alpha_1}(\tau) (\delta_{\alpha_1\alpha_2} \partial_\tau + iA_{\alpha_1\alpha_2}) \eta_{\alpha_2}(\tau) + \frac{1}{4!} \int_0^\beta d\tau V_{\alpha_1\alpha_2\alpha_3\alpha_4} \eta_{\alpha_1}(\tau) \eta_{\alpha_2}(\tau) \eta_{\alpha_3}(\tau) \eta_{\alpha_4}(\tau). \quad (3.2)$$

Here, Einstein summation is assumed,  $\beta = 1/T$  is the inverse temperature and  $\eta_\alpha(\tau)$  are real and antisymmetric Majorana fields satisfying  $\{\eta_\alpha, \eta_\beta\} = \delta_{\alpha\beta}$  and  $\eta_\alpha(\tau)^\dagger = \eta_\alpha(-\tau)$ , while  $\alpha$  refers to indices labeling an arbitrary set of single-particle quantum numbers. The key step in the derivation of a temperature flow FRG scheme is to gather all temperature dependence in the non-interacting part of the Hamiltonian. Here, we do this by introducing a modified Fourier transform

$$\eta(\omega) = T^{\frac{1}{4}} \int_0^1 d\tau e^{-i\omega\tau} \eta\left(\frac{\tau}{T}\right), \quad \eta\left(\frac{\tau}{T}\right) = T^{-\frac{1}{4}} \sum_\omega e^{i\omega\tau} \eta(\omega), \quad (3.3)$$

with the dimensionless Matsubara frequencies  $\omega = \pi(2n + 1)$  and  $n \in \mathbb{Z}$ , which is more convenient but otherwise equivalent to the rescaling of fields as done by Honerkamp and Salmhofer [230]. In the case of  $A_{\alpha_1\alpha_2} = 0$  it is also equivalent to the rescaling introduced in the interaction-flow scheme of Honerkamp et al. [231]. Crucially, the transformation is chosen in such a way that no implicit temperature dependencies enter through frequencies and the interacting part of the rescaled action. This way, we may express Eq. (3.2) as

$$S = -\frac{1}{2} \sum_{\substack{\omega_1, \omega_2 \\ \alpha_1 \alpha_2}} \eta_{\alpha_1}(\omega_1) G_{0; \alpha_1 \alpha_2}^{-1, T}(\omega_1, \omega_2) \eta_{\alpha_2}(\omega_2) \\ + \frac{1}{4!} \sum_{\substack{\omega_1, \dots, \omega_4 \\ \alpha_1 \dots \alpha_4}} V_{\alpha_1 \alpha_2 \alpha_3 \alpha_4} \eta_{\alpha_1}(i\omega_1) \eta_{\alpha_2}(i\omega_2) \eta_{\alpha_3}(i\omega_3) \eta_{\alpha_4}(i\omega_4) \delta_{\omega_1 + \omega_2 + \omega_3 + \omega_4, 0} \quad (3.4)$$

where we defined

$$G_{0; \alpha_1 \alpha_2}^{-1, T}(\omega_1, \omega_2) = \frac{i}{\theta(T)} [\omega_1 \delta_{\alpha_1, \alpha_2} - \theta(T)^2 A_{\alpha_1 \alpha_2}] \delta_{\omega_1, -\omega_2} \quad (3.5)$$

as the bare Green function. The crucial insight is that  $\theta(T) = T^{-\frac{1}{2}}$  can be seen as a regulator function since it implies a vanishing propagator  $G_0^T \rightarrow 0$  for  $T \rightarrow \infty$ . In the usual FRG formalism this is achieved by a regulator  $G_0 \rightarrow \Theta^\Lambda G_0$  where the function  $\Theta^\Lambda$  vanishes at the start of the flow at  $\Lambda \rightarrow \infty$ . It is noted that, while this suppression does not by itself act as an infrared cutoff of the Matsubara frequencies, the finite temperature has a similar effect of regularizing infrared divergencies as it shifts the smallest Matsubara frequency away from zero. In Eq. (3.4), the temperature dependence is fully contained in the regulator  $\theta(T)$ , which trivially generates the same hierarchy of flow equations as in the standard FRG formalism (see, for example Ref. [123]), upon simply replacing all derivatives with respect to the artificial cutoff  $\Lambda$  by derivatives with respect to  $T$ .

### Flow Equations and observables

The FRG flow equations are derived from the action [Eq. (3.4)] in full analogy to the standard PMFRG formalism [1]. In this fermionic language, Majorana Green functions are defined as the bare propagator  $G_0^T$ , full propagator  $G^T$  and connected two particle Green function  $G_c^{4, T}$

$$G_{1,2}^T = \langle \eta_2 \eta_1 \rangle, \quad (3.6)$$

$$G_{c; 1,2,3,4}^{4, T} = \langle \eta_4 \eta_3 \eta_2 \eta_1 \rangle - \langle \eta_4 \eta_3 \rangle \langle \eta_2 \eta_1 \rangle \\ + \langle \eta_4 \eta_2 \rangle \langle \eta_3 \eta_1 \rangle - \langle \eta_3 \eta_2 \rangle \langle \eta_4 \eta_1 \rangle, \quad (3.7)$$

---

<sup>2</sup>This can be seen by setting the interaction-flow parameter  $g = T^{3/2}$  which results in the same bare Greensfunction as in Eq. (3.5)

where we have introduced the superlabels  $1 = (i_1, \mu_1, \omega_1)$  that collectively describe site, spin and frequency index where the latter emerges after Fourier transforming the associated imaginary-time ordered correlation functions.

In the FRG formalism, the objects of interest are the self-energy  $\Sigma_{1,2}$  and the four-point vertex  $\Gamma_{1,2,3,4}$  which are related to Green functions via the Dyson equation and the tree expansion [123]

$$\Sigma_{1,2}^T = G_{0;1,2}^{-1,T} - G_{1,2}^{-1,T}, \quad (3.8)$$

$$\Gamma_{1,2,3,4}^T = - \sum_{1', \dots, 4'} G_{1,1'}^{-1,T} G_{2,2'}^{-1,T} G_{3,3'}^{-1,T} G_{4,4'}^{-1,T} G_{c;1',2',3',4'}^{4,T}. \quad (3.9)$$

As outlined in Chapter 2 in thermal equilibrium the Green functions and vertices are frequency conserving while due to a local  $\mathbb{Z}_2$  gauge symmetry in the Majorana representation [Eq. (2.1)] the propagator and self energy are local and the vertex is bi-local,

$$G_{1,2}^T = G_{i_1; \alpha_1 \alpha_2}^T(\omega_2) \delta_{i_1, i_2} \delta_{\omega_1, -\omega_2}, \quad (3.10)$$

$$G_{0;1,2}^{-1,T} = G_{0; i_1; \alpha_1 \alpha_2}^{-1,T}(\omega_1) \delta_{i_1, i_2} \delta_{\omega_1, -\omega_2}, \quad (3.11)$$

$$\Sigma_{1,2}^T = \Sigma_{i_1; \alpha_1 \alpha_2}^T(\omega_1) \delta_{i_1, i_2} \delta_{\omega_1, -\omega_2}, \quad (3.12)$$

$$\Gamma_{1,2,3,4}^T = \delta_{\omega_1 + \omega_2 + \omega_3 + \omega_4, 0} [ \quad (3.13)$$

$$\begin{aligned} & \Gamma_{i_1 i_3; \alpha_1 \alpha_2 \alpha_3 \alpha_4}^T(\omega_1, \omega_2, \omega_3, \omega_4) \delta_{i_1, i_2} \delta_{i_3, i_4} \\ & - \Gamma_{i_1 i_2; \alpha_1 \alpha_3 \alpha_2 \alpha_4}^T(\omega_1, \omega_3, \omega_2, \omega_4) \delta_{i_1, i_3} \delta_{i_2, i_4} \\ & + \Gamma_{i_1 i_2; \alpha_1 \alpha_4 \alpha_2 \alpha_3}^T(\omega_1, \omega_4, \omega_2, \omega_3) \delta_{i_1, i_4} \delta_{i_2, i_3} ]. \end{aligned}$$

In the following, we provide the flow equations for the interacting free-energy  $f_{\text{int}} = F_{\text{int}}/N = -T \log\left(\frac{Z}{Z_0}\right)$ , where  $N$  is the number of sites, the self-energy  $\Sigma_{i_1; \alpha_1, \alpha_2}^T(\omega_1)$  and vertex  $\Gamma_{i_1 i_3; \alpha_1 \alpha_2 \alpha_3 \alpha_4}^T(\omega_1, \omega_2, \omega_3, \omega_4)$  that can be derived analogously to Eqs. (2.46), (3.14) and (3.16). With the transfer frequencies in Eq. (2.21) these

flow equations are given by

$$\frac{d}{dT} \frac{f_{\text{int}}}{T} = \frac{1}{2N} \sum_{\substack{k,\omega \\ \beta_1 \dots \beta_4}} \Sigma_{k;\beta_2\beta_3}^T(\omega) G_{k;\beta_3\beta_4}^T(\omega) G_{0;k;\beta_4\beta_1}^{-1,T}(\omega) \frac{\partial}{\partial T} G_{0;k;\beta_1\beta_2}^T(\omega) \quad (3.14)$$

$$\frac{d}{dT} \Sigma_{i;\alpha_1\alpha_2}^T(\omega) = \frac{1}{2} \sum_{\substack{k,\omega' \\ \beta_1,\beta_2}} \Gamma_{ki;\beta_2\beta_1\alpha_1\alpha_2}^T(-\omega', \omega', \omega, -\omega) \frac{\partial}{\partial T} G_{k;\beta_1\beta_2}^T(\omega') \quad (3.15)$$

$$\begin{aligned} \frac{d}{dT} \Gamma_{ij;\alpha_1\alpha_2\alpha_3\alpha_4}^T(s, t, u) &= X_{ij;\alpha_1,\alpha_2;\alpha_3,\alpha_4}(s, t, u) - \tilde{X}_{ij;\alpha_1,\alpha_3;\alpha_2,\alpha_4}(t, s, u) \\ &\quad + \tilde{X}_{ij;\alpha_1,\alpha_4;\alpha_2,\alpha_3}(u, s, t) \end{aligned} \quad (3.16)$$

$$\begin{aligned} X_{ij;\alpha_1,\alpha_2;\alpha_3,\alpha_4} &= \frac{1}{2} \sum_{k,\omega} \sum_{\beta_1 \dots \beta_4} \Gamma_{ik;\alpha_1\alpha_2\beta_1\beta_2}^T(\omega_1, \omega_2, \omega - s, -\omega) \Gamma_{kj;\beta_3\beta_4\alpha_3\alpha_4}^T(\omega, s - \omega, \omega_3, \omega_4) \\ &\quad \times P_{kk;\beta_2\beta_3;\beta_4\beta_1}^T(\omega, \omega - s), \end{aligned} \quad (3.17)$$

$$\begin{aligned} \tilde{X}_{ij;\alpha_1,\alpha_2;\alpha_3,\alpha_4} &= \sum_{\omega} \sum_{\beta_1 \dots \beta_4} \Gamma_{ij;\alpha_1\beta_1\alpha_3\beta_3}^T(\omega_1, -\omega, \omega_2, \omega - s) \Gamma_{ij;\beta_2\alpha_2\beta_4\alpha_4}^T(\omega, \omega_3, s - \omega, \omega_4) \\ &\quad \times P_{ij;\beta_1\beta_2;\beta_4\beta_3}^T(\omega, \omega - s), \end{aligned} \quad (3.18)$$

where we define the single-scale propagator as

$$\frac{\partial}{\partial T} G_{k;\alpha_1\alpha_2}^T(\omega) = - \sum_{\beta_1\beta_2} G_{k;\alpha_1\beta_1}^T(\omega) G_{k;\beta_2\alpha_2}^T(\omega) \frac{\partial}{\partial T} G_{0;k;\beta_1\beta_2}^{-1,T}(\omega), \quad (3.19)$$

and the bubble propagator as

$$P_{ij;\alpha_1\alpha_2;\alpha_3\alpha_4}^T(\omega, \omega - s) = \frac{\partial}{\partial T} \left[ G_{i;\alpha_1\alpha_2}^T(\omega) G_{j;\alpha_3\alpha_4}^T(\omega - s) \right]. \quad (3.20)$$

The main differences between the flow equations presented here and those of Eqs. (2.22a) to (2.22c) are the definition of the propagator and the absence of factors  $T$  associated with the frequency sums. The initial conditions follow immediately from the fact that the bare propagator  $G_0^T$  vanishes at  $T = \infty$  so that the only nonzero vertex at the beginning of the flow is the bare spin interaction:

$$\lim_{T \rightarrow \infty} \frac{f_{\text{int}}}{T} = 0, \quad (3.21)$$

$$\Sigma_{i;\alpha_1\alpha_2}^{T \rightarrow \infty}(\omega) = 0, \quad (3.22)$$

$$\Gamma_{ij;\alpha_1\alpha_2\alpha_3\alpha_4}^{T \rightarrow \infty}(s, t, u) = - \sum_{\beta_1\beta_2} \epsilon_{\alpha_1\alpha_2\beta_1} J_{ij}^{\beta_1\beta_2} \epsilon_{\beta_2\alpha_1\alpha_2}, \quad (3.23)$$

where  $\epsilon_{\alpha_1\alpha_2\alpha_4}$  is the fully antisymmetric tensor. Note that by convention the magnetic field is implemented in the off-diagonal elements of the bare inverse Green function in Eq. (3.5) instead of in the self-energy with  $A_{\alpha_1\alpha_2}$  given by

$$A_{\alpha_1\alpha_2} = - \sum_{\beta} \epsilon_{\alpha_1\alpha_2\beta} h^{\beta}. \quad (3.24)$$

In the Katanin truncation scheme [149] that we use for all calculations below, the partial derivative in Eq. (3.20) is changed to a total derivative, thus including a feedback of the self-energy derivative into the vertex flow equation. This approximation is originally motivated by its inclusion of contributions from the six-point vertex.

It is emphasized that the self-energy defined above is related to the  $\Lambda$ -flow self-energy as  $\Sigma^{\Lambda=0}(\omega) = T^{1/2}\Sigma^T(\omega)$ , while the vertex is unchanged  $\Gamma_{ij}^{\Lambda=0}(s, t, u) = \Gamma_{ij}^T(s, t, u)$ <sup>1</sup>. In practice, one can further reduce the number of independent vertex components by considering the spin and lattice symmetries of the model of interest [1].

### Observables

A feature of the temperature flow is that we have direct access to the differentiated vertices with respect to temperature. Therefore, we have direct access to the free energy  $f$  and mean energy  $U = \langle H \rangle$  while the heat capacity  $C = \frac{dU}{dT}$  can be obtained by numerical differentiation. By using the known result for the partition function of free spins-1/2 in a magnetic field  $\mathbf{h}_i$

$$\log(Z_0) = \sum_i \log \left( 2 \cosh \left( \frac{|\mathbf{h}_i|}{T} \right) \right) \quad (3.25)$$

we can write them as

$$f = f_{\text{int}} - T \log(Z_0), \quad (3.26)$$

$$\frac{U}{N} = -T^2 \frac{d}{dT} \left( \frac{f_{\text{int}}}{T} - \log(Z_0) \right), \quad (3.27)$$

$$C = \frac{dU}{dT}. \quad (3.28)$$

Other observables are the magnetization  $M_i^{\alpha} = \langle S_i^{\alpha} \rangle$ , magnetic susceptibility

---

<sup>1</sup>Note that the full vertex function  $\Gamma^{\Lambda}(\omega_1, \omega_2, \omega_3, \omega_4) \equiv \Gamma^{\Lambda}(s, t, u) \beta \delta_{\omega_1 + \omega_2 + \omega_3 + \omega_4, 0}$  has a relative factor of  $\beta = 1/T$ .

$\chi_{ij}^{\alpha_1\alpha_2}(\omega) = \int_0^\beta e^{i\omega\tau} \langle S_i^{\alpha_2}(\tau) S_j^{\alpha_1}(0) \rangle$  and the equal time spin-spin correlator  $\langle S_i^{\alpha_2} S_j^{\alpha_1} \rangle$ :

$$M_j^\alpha = -iT^{\frac{1}{2}} \sum_\omega \sum_{\beta_1\beta_2} \frac{\epsilon_{\alpha\beta_1\beta_2}}{2} G_{j;\beta_2\beta_1}^T(\omega), \quad (3.29)$$

$$\langle S_i^{\alpha_1} S_j^{\alpha_2} \rangle = \frac{1}{\beta} \sum_\omega \chi_{ij}^{\alpha_2\alpha_1}(\omega), \quad (3.30)$$

$$\begin{aligned} \chi_{ij}^{\alpha_1\alpha_2}(\omega) &= \beta \delta_{0,\omega} M_i^{\alpha_1} M_j^{\alpha_2} + \delta_{ij} \sum_{\substack{\omega_1 \\ \alpha\beta\gamma\delta}} \frac{\epsilon_{\alpha_2\beta_1\beta_2} \epsilon_{\alpha_1\beta_3\beta_4}}{4} \\ &\times \left[ G_{i;\beta_4\beta_1}^T(\omega_1) G_{i;\beta_2\beta_3}^T(\omega_1 + \omega) - G_{i;\beta_3\beta_1}^T(\omega_1) G_{i;\beta_2\beta_4}^T(\omega_1 + \omega) \right] \\ &+ \sum_{\substack{\omega_1\omega_2 \\ \beta_1\dots\beta_4 \\ \gamma_1\dots\gamma_4}} \frac{\epsilon_{\alpha_2\beta_1\beta_2} \epsilon_{\alpha_1\beta_3\beta_4}}{4} \Gamma_{ij;\gamma_4\gamma_3\gamma_2\gamma_1}^T(-\nu, -\omega_1 - \omega_2, \omega_2 + \nu - \omega_1) \\ &\times G_{\beta_4\gamma_4}^T(\omega_1 - \nu) G_{\gamma_3\beta_3}^T(\omega_1) G_{\beta_2\gamma_2}^T(\omega_2 + \nu) G_{\gamma_1\beta_1}^T(\omega_2) \end{aligned} \quad (3.31)$$

To verify the correctness of this implementation, in Section 3.2, we consider a simple, exactly solvable model of two interacting spins. Note that this model poses the same methodological challenge to the PMFRG as infinite systems and thus provides an excellent benchmark. Overall, we observe similar or better results as compared to the  $\Lambda$ -flow method. Note that as detailed in the Section 3.2, other checks via exact relations between vertices are also possible, but less reliable as they check only for conservations of specific constants of motions which may be unrelated to quantities of interest.

### Heisenberg dimer as benchmark model for $T$ -flow PMFRG

To benchmark the temperature flow PMFRG, we investigate the Heisenberg dimer  $H = \sum_\alpha S_1^\alpha S_2^\alpha$ . Despite its apparent simplicity, this model provides a formidable challenge to diagrammatic approaches such as the PMFRG which are oblivious to the size of the Hilbert space. As the low dimensionality renders several crucial mean-field contributions which are fully included in the FRG such as the RPA and ladder-type series insufficient [10], one may consider it as a worst-case benchmark: Generally speaking, the higher-dimensional systems treated in this work, are much better described by mean-field contributions and are thus expected to be better behaved. Due to its simple implementation and the availability of exact results, the same dimer system has been studied previously for similar purpose [1, 160].

Here, we consider the static spin-spin correlators  $\chi_{11}(\omega = 0)$  and  $\chi_{12}(\omega = 0)$  as well as the interaction correction to the free energy  $f_{\text{int}}$ , the energy per site  $U$



and the heat capacity  $C$  obtained by Eqs. (3.26)-(3.28). Alternatively, the internal energy can also be obtained via  $U = \langle H \rangle$  which for the general Hamiltonian in Eq. (3.1) reads as

$$U = \sum_{i,\alpha} h_i^\alpha M_i^\alpha + \frac{1}{2} \sum_{\substack{i,j \\ \alpha\beta}} J_{ij}^{\alpha,\beta} \langle S_i^\alpha S_j^\beta \rangle, \quad (3.32)$$

where  $M_i^\alpha = 0$  in the present case, since no magnetic field  $h_i^\alpha$  is considered. These quantities are compared against the exact solution in Fig. 3.3 shown as black lines: The interaction correction to the free energy  $f_{\text{int}}$ , shown in red in panel (a), is obtained from the zero-point vertex in Eq. (3.14). We observe the temperature flow (solid line) to be closer to the exact result than the  $\Lambda$ -flow result (square markers). From  $f_{\text{int}}$ , the energy per site  $U/N$  may be obtained using Eq. (3.27) via a numerical derivative with respect to  $T$ . Again, we observe the  $T$ -flow curve to be closer to the exact result than in  $\Lambda$ -flow in panel (b). In the  $T$ -flow scheme, we may avoid inaccuracies from numerical derivatives by inserting the right hand side of the flow equation in Eq. (3.14) for  $\frac{df_{\text{int}}}{dT}$  in Eq. (3.27). The result is shown by the blue dashed line. As the numerical accuracy of the solution is rather high with a tolerance of  $\sim 10^{-7}$ , the result is identical to the one obtained via numerical derivatives. Further shown in orange is the  $T$ -flow result obtained from spin-spin correlations as defined in Eq. (3.32). For intermediate to large temperatures, this quantity is the most accurate but becomes unphysical around  $T \sim 0.25$ , showing an increase as the temperature decreases. By taking a numerical derivative, we may also obtain an estimate for the heat capacity  $C$  from all these results, shown in panel (c). While the  $T$ -flow peak height of the heat capacity is closer to the exact result than the  $\Lambda$ -flow result, its peak location is shifted. We conclude that the energy per site and the heat capacity are strongly affected by truncation errors, since already small errors introduced by neglecting the six-point vertex propagate through the four- and two-point vertex to the zero-point vertex and are then magnified even further upon taking derivatives.

On the other hand, the static spin-spin correlations  $\chi_{11}(\omega = 0)$  and  $\chi_{12}(\omega = 0)$  are significantly less affected by this problem as they are obtained directly from the four-point vertex via Eq. (3.31). At large temperatures  $T \gg J$ , where both PMFRG flow approaches are well controlled, they agree well with each other and the exact result. At low temperatures, deviations from the exact result become visible within both the  $T$ -flow and standard  $\Lambda$ -flow PMFRG. Somewhat surprisingly, we observe that the local spin correlator  $\chi_{11}(\omega = 0)$  appears much more accurate in the temperature flow formalism, while the non-local one deviates from the exact result in the same way as in the  $\Lambda$ -flow scheme. It is noted that this improvement in accuracy may be incidental. In conclusion, we find that both FRG approaches correctly describe correlations in the Heisenberg dimer at high

and intermediate temperatures. This holds despite the challenges that the dimer presents to diagrammatic approaches due to its low dimensionality. On the other hand, thermodynamic observables such as the specific heat suffer considerably from error propagation introduced in the derivatives and are thus much less reliable. As a result, in this work we have only relied on results obtained from spin-spin correlators.

### Internal consistency checks for PMFRG

The truncation of the flow equation hierarchy by neglecting the six point vertex is an inherently uncontrolled approximation at low temperatures, making estimates of the exact error bars impossible. Instead, we can rely upon the fulfillment of a Ward identity as a qualitative measure of the truncation error to indicate challenging parameter regimes: All pseudo-Majorana Hamiltonians feature a set of local constants of motion,

$$\theta_j = -2i\eta_j^x\eta_j^y\eta_j^z. \quad (3.33)$$

This allows us to derive an exact relation between fully local two- and four-point Majorana correlators [1, 213, 215]. Hence we may express the static local spin-spin correlator which is usually computed from the four-point Majorana vertex [see Eq. (3.31)] alternatively through the two-point Green function, here shown for the static part at  $\omega = 0$ ,

$$\chi_{jj}^{\alpha_1\alpha_2}(\omega = 0) = \sum_{\omega'} \frac{i}{\omega'\sqrt{T}} G_{j;\alpha_1\alpha_2}^T(\omega'). \quad (3.34)$$

This relation must be satisfied for any exact calculation. For the approximate PMFRG, we can use the degree of violation as an internal consistency check and define the quantity

$$\Delta = \left| \frac{\chi_{jj}^{\alpha_1\alpha_2}(0)_1 - \chi_{jj}^{\alpha_1\alpha_2}(0)_2}{\chi_{jj}^{\alpha_1\alpha_2}(0)_1 + \chi_{jj}^{\alpha_1\alpha_2}(0)_2} \right|, \quad (3.35)$$

where the subscripts 1 and 2 refer to the two different methods of computing  $\chi_{jj}^{\alpha_1\alpha_2}(\omega = 0)$ , via Eq. (3.34) and Eq. (3.31), respectively.

Figure 3.4 shows the violation of the consistency condition  $\Delta = 0$  for the Heisenberg dimer from Section 3.2 in the  $\Lambda$  and  $T$ -flow schemes. We notice that  $\Delta$  is larger in the temperature flow scheme, compared to the  $\Lambda$ -flow PMFRG, despite the overall better agreement of the temperature flow with the exact result.

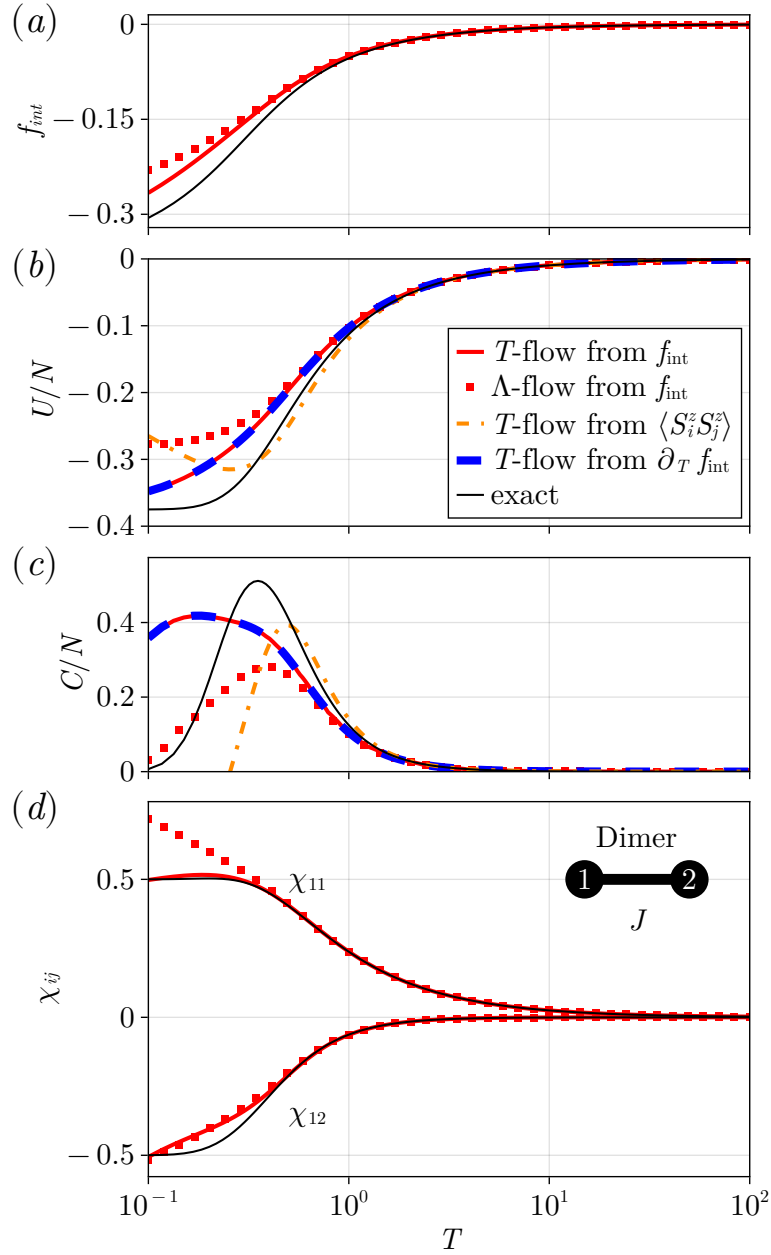


Figure 3.3.: Thermodynamic quantities for the temperature flow PMFRG on the Heisenberg dimer in comparison to the exact result (black) and the standard  $\Lambda$ -flow PMFRG (squares). (a): interaction correction to the free energy  $f_{\text{int}}$  from Eq. (3.14). For the energy per site  $U/N$  (b) and the specific heat  $C/N$  (c), the darkred dash-dotted line represents the value obtained via Eq. (3.32). The solid red line represents the value obtained via Eq. (3.28). The same quantity can be obtained directly via the flow equation Eq. (3.14) shown in blue dashed lines without the need to perform numerical derivatives. (d) shows the two inequivalent static spin-spin correlators  $\chi_{11}$  and  $\chi_{12}$  obtained via Eq. (3.31).

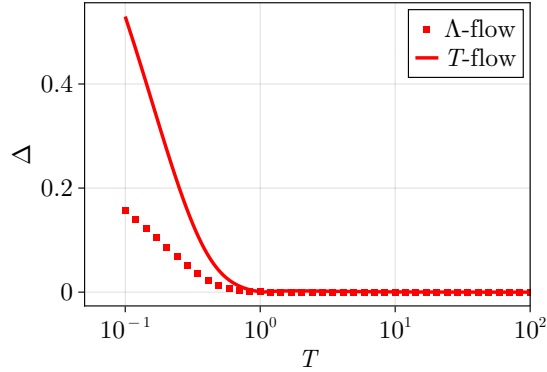


Figure 3.4.: Violation of the consistency check [Eq. (3.35)] for the Heisenberg dimer in the  $\Lambda$ -flow and  $T$ -flow PMFRG schemes.

Although  $\Delta$  can not replace a real error bar since it only contains information about the violation of the conservation law for the constant of motion  $\theta_j$ , a small value of  $\Delta$  in the few-percent range is an indicator that the truncation of flow equations is still in the well-controlled limit. However, it should be noted that even with a large  $\Delta$  the method can produce qualitatively and in principle even quantitatively accurate data for quantities which are not directly linked to the conservation of  $\theta_j$  which is violated. This is visible in the case of the dimer shown in Fig. 3.4 where  $\Delta$  is larger in the temperature flow scheme as compared to the  $\Lambda$ -flow result even though the quantities of interest, primarily the susceptibility, lie closer to the exact result in  $T$ -flow.

### Detection of magnetic phase transitions

When studying spin systems at finite temperatures one is commonly interested in phase transitions or the lack thereof. Historically, magnetic phase transitions in the pseudoparticle-FRG context have been detected as instabilities in the flow equations, where a divergence is often detected as a sharp feature, i.e. “kink” in the corresponding susceptibility. This approach has the disadvantage that the exact point of the feature can heavily depend on numerical parameters such as the maximum correlation length, the frequency discretization or the accuracy of the ODE solver. Moreover, the distinction a weak “kink” from a disordered state is subject to interpretation and thus often of more qualitative nature. As outlined in previous works [2, 160, 232], finite-size scaling can instead be used as an unbiased and reliable method to extract quantitatively accurate critical temperatures from pseudo-particle-FRG calculations. We approximate the rescaled correlation length

by fitting a Lorentz curve with width  $\frac{1}{\xi}$  to the largest peak located at wavevector  $\mathbf{Q}$  of the Fourier transformed susceptibility  $\chi^{\alpha_1\alpha_2}(\mathbf{k})$  [32]

$$\frac{\xi}{L} = \frac{1}{2\pi} \max_{\delta} \left( \sqrt{\frac{\chi_{\max}(\mathbf{Q})}{\chi_{\max}(\mathbf{Q} + \frac{2\pi}{L}\delta)} - 1} \right) \quad (3.36)$$

$$\chi_{\max}(\mathbf{Q}) = \max_{\alpha_1\alpha_2} (\chi^{\alpha_1\alpha_2}(\mathbf{Q})). \quad (3.37)$$

Here,  $\delta$  is a vector of unit length and  $L$  is a measure of system size, and therefore, the maximum correlation length. In translationally invariant systems we need only consider sites  $i$  in  $\Sigma_i$  and  $\Gamma_{ij}$  that lie in the first unit cell and set  $\Gamma_{ij} = 0$  if the sites  $i$  and  $j$  are separated by more than  $L$  nearest neighbor bonds. We detect a phase transition by calculating  $\frac{\xi}{L}$  for multiple  $L$ . In a paramagnetic regime  $\frac{\xi}{L}$  decreases with  $L$  while in a magnetic regime  $\frac{\xi}{L}$  increases with  $L$ . The critical temperature is the temperature at which  $\frac{\xi}{L}$  is independent of  $L$ .

### 3.3. Finite spin

Although the implementation of higher spin magnitudes  $S$  was previously shown in the context of PFFRG [120], the present case requires further considerations which we now discuss in detail. The  $SO(3)$  Majorana representation employed in PMFRG is applicable only for spin-1/2 operators. Ideally, the solution for  $S > 1/2$  would be to find a representation of spin- $S$  operators in terms of Majorana fermions, which does not introduce any unphysical states. However, such a representation exists only for  $S = 1/2$  and  $S = 3/2$ , whereas for all other spin magnitudes unphysical sectors cannot be avoided [233]. Thus, in the present  $S = 1$  case we follow the approach of Ref. [120] that introduces various copies (replicas) of spin-1/2 degrees of freedom on each site but that also inevitably involves unphysical states that need to be dealt with.

Specifically, our approach of implementing an effective spin quantum number  $S_{\text{eff}}$  amounts to introducing  $2S_{\text{eff}}$  spin-1/2 operators  $\mathbf{S}_{i_\mu}$  on each site  $i$  such that

$$\mathbf{S}_{i,\text{eff}} = \sum_{\mu=1}^{2S_{\text{eff}}} \mathbf{S}_{i_\mu}, \quad (3.38)$$

where  $\mu \in \{1, 2, \dots, 2S_{\text{eff}}\}$  is the additional replica index. Here and in the following, we use the convention that  $\mathbf{S}_{i_\mu}$  refers to a spin-1/2 operator, corresponding

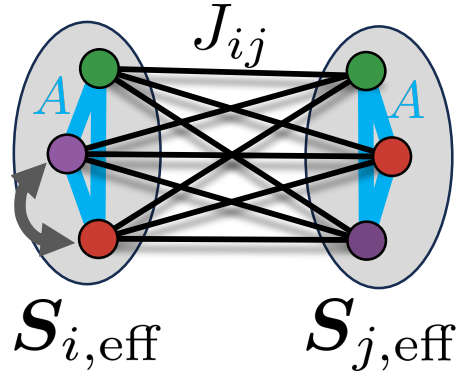


Figure 3.5.: Illustration of two effective spin-3/2 degrees of freedom, each composed of three spin-1/2 replicas, interacting with each other. The spin replicas  $S_{i_1}, S_{i_2}, S_{i_3}$  are fully equivalent and colored differently only for visual clarity. The grey arrow indicates an exemplary permutation of replicas which leaves the model invariant.

to the  $\mu$ -th replica spin located on site  $i$  whereas operators that implement higher spins  $S_{\text{eff}}$  are denoted  $\mathbf{S}_{i,\text{eff}}$ .

Thus, the effective model treated in PMFRG model results from replacing spin operators by  $\mathbf{S}_{i,\text{eff}}$  according to Eq. (3.38) giving rise to a Hamiltonian in terms of spin-1/2 operators,

$$\begin{aligned}
 H &= \sum_{(i,j)} \sum_{\mu,\nu} J_{ij} \mathbf{S}_{i_\mu} \cdot \mathbf{S}_{j_\nu} + A \sum_i \left( \sum_\mu \mathbf{S}_{i_\mu} \right)^2 \\
 &\equiv \sum_{(i,j)} \sum_{\mu,\nu} J_{i_\mu;j_\nu} \mathbf{S}_{i_\mu} \cdot \mathbf{S}_{j_\nu},
 \end{aligned} \tag{3.39}$$

where  $(i, j)$  denotes pairs of sites  $i \neq j$  (summed over only once). To tune the energy of unphysical states, we add a level repulsion term  $\sim A$  on the right hand side of the first line of Eq. (3.39): For  $A < 0$ , the Hilbert space sector where the addition of angular momenta realizes the largest spin quantum number  $S_{\text{eff}}$  is energetically favored over (unphysical) states with smaller spin quantum numbers  $S < S_{\text{eff}}$ . Furthermore, in the second line of Eq. (3.39) we combine the original couplings  $J_{ij}$  and the level repulsion  $A$  into a joint interaction constant  $J_{i_\mu;j_\nu}$  which now depends on site indices  $i, j$  and replica indices  $\mu, \nu$ .

The replica construction is depicted in Fig. 3.5 for the case of two interacting  $S_{\text{eff}} = 3/2$  spins. Colored circles correspond to  $S = 1/2$  replicas which are coupled to each other locally with the ferromagnetic coupling  $A$  and non-locally via the

exchange interaction  $J_{ij}$ . Strictly speaking, this mapping is only exact in the limit  $A \rightarrow -\infty$ , which, however, cannot be treated within PMFRG. This is due to the fact that the approximation of neglecting higher vertices in PMFRG breaks down if the effective interaction becomes too large compared to the temperature. In practice, it is sufficient to choose  $A$  to be proportional to the temperature,

$$A = -\gamma T, \quad (3.40)$$

such that unphysical states are always gapped out, while  $A$  is still small enough to avoid methodological challenges. Below, we will determine the best parameter  $\gamma$  in the present  $S = 1$  case.

The Hamiltonian of this system treated via replicas  $\mu = 1, 2, 3$  is

$$H = J \sum_{\mu=1}^3 \sum_{\nu=1}^3 \mathbf{S}_{1\mu} \cdot \mathbf{S}_{2\nu} + A \sum_{i=1}^2 \left( \sum_{\mu=1}^3 \mathbf{S}_{i\mu} \right)^2, \quad (3.41)$$

where we set  $J = 1$  in the following. In Fig. 3.6 we present results for the static local spin correlator  $\chi_{11}(i\nu = 0)$  and the static non-local spin correlator  $\chi_{12}(i\nu = 0)$ . Shown in Fig. 3.6 are three different choices of the level repulsion  $A$ . For small level repulsion  $|A| = 0.1 \ll J \equiv 1$ , we observe good agreement between the exact results for the spin-3/2 dimer before and after the introduction of replicas (i.e., without and with unphysical  $S = 1/2$  states) at low temperatures. This is expected since the ground state of an unfrustrated spin system typically lies in the sector with maximal (effective) spin as the interaction energy  $\sim \mathbf{S}_{1,\text{eff}} \cdot \mathbf{S}_{2,\text{eff}}$  is largest in this case. It can be seen that PMFRG agrees remarkably well with the exact result of the replica system in Eq. (3.41) (dashed line). At higher temperatures, the effect of unphysical states becomes visible since the excitation gap to such states, determined by  $A$ , is too small to suppress their impact on physical observables. Conversely, for a larger level repulsion of  $A = -2$ , we observe good agreement between PMFRG and the exact result at higher temperatures as the unphysical states are further shifted to higher energies. However, at low temperatures, methodological difficulties arise because the dominant energy scale in the Hamiltonian (now given by  $A$ ), also sets the temperature scale  $T \sim |A|$  below which results can become inaccurate. The solution to this problem is to introduce a level repulsion  $A = -\gamma T$  that scales linearly in temperature, as shown in the bottom panel of Fig. 3.6. There we find that the value  $\gamma = 1.5$  maximizes the agreement between PMFRG and the exact result both at high and low temperatures.

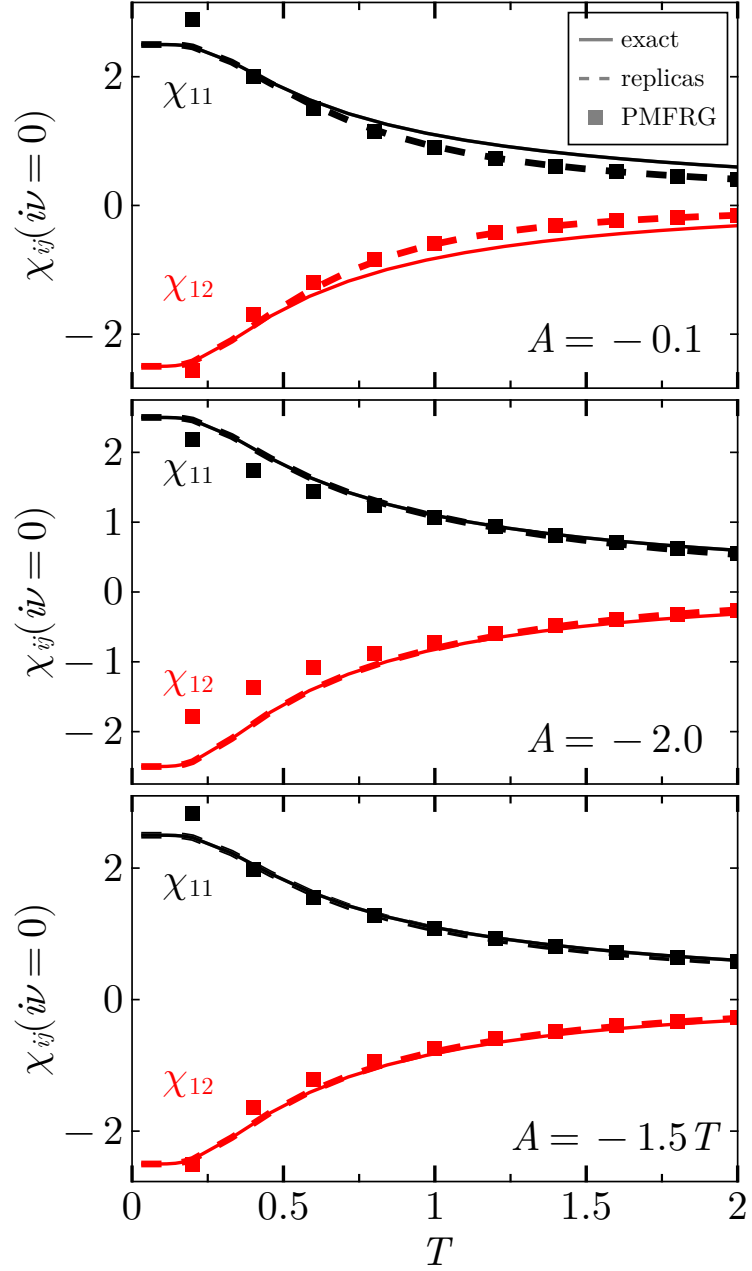


Figure 3.6.: Spin correlations of the  $S = 3/2$  Heisenberg dimer for different choices of the level repulsion,  $A = -0.1$ ,  $A = -2$ ,  $A = -1.5T$ , from top to bottom. The solid black (red) line indicates the exact solution of the local correlator  $\chi_{11}$  (non-local correlator  $\chi_{12}$ ). The dashed lines correspond to the exact solution after the introduction of replica spins [see Fig. 3.5], i.e., in the presence of unphysical  $S = 1/2$  spin states. Squares indicate results from PMFRG.



## Magnetic phases of the $J_1 - J_2$ simple cubic Heisenberg model

A wide spectrum of magnetic phenomena occurs in systems described by a Heisenberg model [234] in which spin-1/2 operators  $\mathbf{S}_i$  located on lattice sites  $i$  are coupled via isotropic exchange interactions  $J_{ij}$ ,

$$H = \sum_{i<j} J_{ij} \mathbf{S}_i \mathbf{S}_j. \quad (4.1)$$

In spite of the apparent simplicity of Eq. (4.1), the calculation of measurable quantities remains a notoriously difficult problem, particularly in the most realistic case of three spatial dimensions. Numerical methods, while indispensable and of steadily increasing power, either suffer from an intrinsic bias, are limited in the quantitative accuracy of their predictions or are unfeasible for the treatment of generic three-dimensional (3D) systems.

Besides more established approaches such as quantum Monte Carlo (QMC) [235], exact diagonalization [32], and density-matrix renormalization group (DMRG) [176], new concepts like the functional renormalization group [123, 145] are currently on the rise for spin systems, owing to their flexibility and applicability to even complex coupling scenarios. While it is now possible to directly treat the RG flow of spin-vertex functions [236], more established variants represent spin operators in terms of auxiliary fermions. The pseudofermion functional renormalization group (PFFRG) method [119, 120, 153, 155, 188] is particularly strong in calculating ground state spin correlations. On the other hand, these methods are sometimes associated with the weaknesses that (*i*) they are in no simple way endowed with a parameter that systematically controls the accuracy and (*ii*) rigorous benchmark tests with other methods are rarely possible. The recent application of multiloop FRG extension [167] to the PFFRG [164, 165] has made an important step forward concerning (*i*) by systematically increasing the loop order  $\ell$  of diagrammatic contributions to the vertex flow.

In this chapter, (*ii*) will be tackled by exploiting the PMFRG's capability of treating finite temperatures which opens up a plethora of further applications and opportunities for benchmarking. The PMFRG in the conventional  $\Lambda$ -flow scheme as introduced in Chapter 2 is applied to two types of models; the first ones are

unfrustrated 3D systems such as the nearest-neighbor simple cubic lattice antiferromagnet where one expects a finite temperature transition to a magnetically ordered state. Details of these second-order phase transitions such as the critical temperature and -exponents are well studied from QMC [173] which treats unfrustrated models in a completely unbiased and error-controlled way. For the PMFRG, probing universal finite-size scaling [237] behaviors provides an optimal testbed and allows us to demonstrate its beyond-mean-field character in a quantitative and rigorous way. Overall, the QMC results are very well reproduced, which concerns the values of critical temperatures  $T_c$ , the critical exponent for the correlation length  $\nu$  which we confirm via a scaling collapse, and the anomalous dimension  $\eta$ . An interesting byproduct of these results is the insight that the system size parameter  $L$  which in PMFRG limits the range of spin-correlations can be used for finite-size scalings in a similar way as the box-size in QMC.

## 4.1. Nearest-neighbor antiferromagnet

We start by investigating the capability of the one-loop PMFRG in systems with well established magnetic long-range order. To this end, we study the Heisenberg model [Eq. (4.1)] on the simple cubic lattice and set the nearest-neighbor antiferromagnetic coupling to  $J_1 = 1$ . With no further-neighbor couplings present, this model is unfrustrated and can be treated with the quantum Monte-Carlo method (QMC). Sandvik [173] found magnetic Néel order with an ordering wavevector  $\mathbf{q}_N = (\pi, \pi, \pi)$  below a critical temperature  $T_c^{\text{QMC}} = 0.946(1)$ . Finite-size scaling of the static Néel susceptibility  $\chi_N$  computed for a cubic-box geometry with a linear size of up to  $L_{\text{box}}^{\text{QMC}} \leq 16$  and periodic boundary conditions confirmed that the transition is in the classical 3D Heisenberg universality class with correlation length critical exponent  $\nu = 0.71$  and anomalous dimension  $\eta = 0.035$  known from Monte-Carlo simulations of numerically less demanding classical systems [238] or the conformal bootstrap method, see e.g. [239]. The same critical exponents can also be accessed within a FRG treatment of a classical bosonic order parameter field theory [240, 241].

In the following, the one-loop PMFRG will be benchmarked against well-controlled QMC results. In contrast to QMC, the PMFRG treats formally infinite (translational invariant) systems but introduces a cutoff-length  $L$ . Correlations between lattice sites with a distance larger than  $L$  are neglected by setting the associated irreducible vertices  $\Gamma$  to zero. Consequently, convergence in  $L$  cannot be expected if the system features large or even divergent correlation length scales

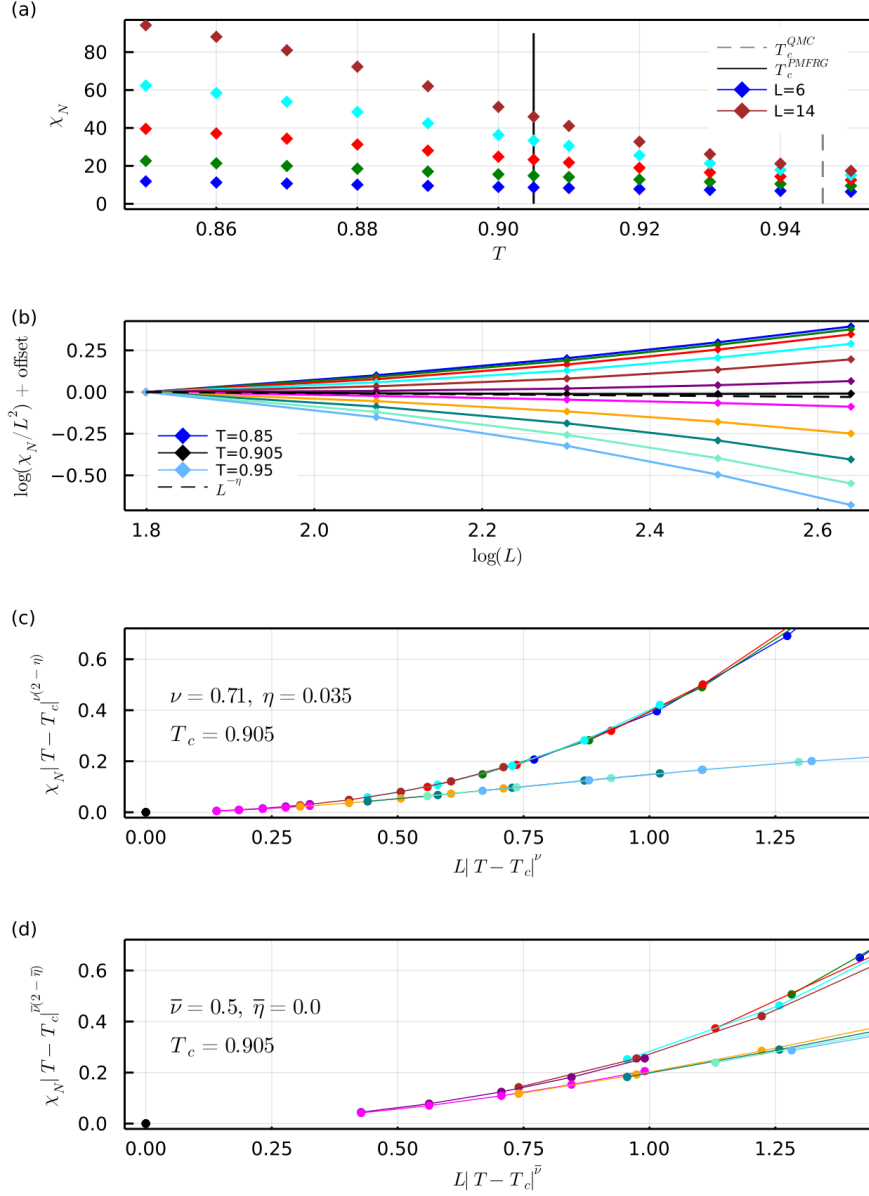


Figure 4.1.: (a) Néel susceptibility from one-loop PMFRG in the antiferromagnetic nearest-neighbor Heisenberg model on the simple cubic lattice for temperatures around  $T = 0.9$  and varying cutoff length  $L = 6, 8, 10, 12, 14$ . The number of positive Matsubara frequencies is  $N_w = 32$ . (b) Length-dependence of the susceptibility from (a); the critical temperature can be identified from a pure power-law behavior (no curvature in log-log plot). Adjacent curves have a temperature difference of  $\Delta T = 0.01$ , except of the black curve which has additionally been inserted for  $T = 0.905$ . (c) Scaling collapse for the data using the established critical exponents  $\nu$  and  $\eta$  from the classical 3D Heisenberg universality class, the same with mean-field exponents is shown in (d).

as, for example, close to a phase transition. While this effect has never been systematically studied in the context of PFFRG, here we turn it into an advantage and demonstrate that in the spin-FRG context  $L$  can be used for finite-size scaling, just as the box size  $L_{\text{box}}^{\text{QMC}}$  in the context of QMC.

The PMFRG results for the static (end-of-flow) Néel-susceptibility  $\chi_N$  around  $T = 0.9$  and cutoff-lengths  $L = 6, 8, 10, 12, 14$  are shown in Fig. 4.1(a). As expected, the missing convergence of  $\chi_N$  with  $L$  (except possibly at the largest  $T$ ) indicates the presence of a correlation length larger than  $L_{\text{max}} = 14$ . Although this number seems modest we are treating about  $4/3\pi L_{\text{max}}^3 \simeq 11494$  sites correlated to a reference site, almost three times the maximal number of sites considered in the QMC analysis of Ref. [173].

In Fig. 4.1(b), the critical temperature is determined from the expected behavior  $\chi_N(T = T_c, L)/L^2 \propto L^{-\eta}$ , which singles out the data trace for the critical temperature  $T = T_c$  from the condition of vanishing curvature<sup>1</sup>. This way, one finds  $T_c = 0.905(5)$ , about 5% smaller than the QMC reference value  $T_c^{\text{QMC}} = 0.946(1)$ . In principle  $\eta$  could be estimated independently from the slope of the  $T_c$ -data trace. In practice, this is difficult due to the limited system sizes in a quantum simulation and the numerically small value of  $\eta = 0.035$ , so that we are content with showing consistency between the measured and predicted slope (dashed line). In contrast, the value of the correlation length exponent  $\nu$  is easier to confirm. In Fig. 4.1(c) the anticipated finite-size scaling behavior is checked for temperatures  $T$  in the vicinity of  $T_c$  [173],

$$\chi_N(L, T) \propto |T - T_c|^{-\nu(2-\eta)} g_{\pm}(L|T - T_c|^{\nu}). \quad (4.2)$$

Using  $T_c$  as obtained above, the PMFRG data collapses into two branches of the scaling function  $g_{\pm}$  for  $T \gtrless T_c$ . Importantly, the quality of this collapse decreases when mean-field exponents are used, see Fig. 4.1(d). This indicates the beyond mean-field nature of the PMFRG, despite the fact that fluctuations of the order parameter are not fully included due to the truncation of the six-point and higher vertices. In more detail, the  $\phi^4$  term in the effective field theory is related to coarse-grained (connected) four-spin correlations, which naively would require the eight-point Majorana correlators not included in this treatment which is limited to Majorana four-point functions. However, we observe  $S_i^{\alpha}(\tau_1)S_i^{\beta}(\tau_2) \sim \eta_i^{\alpha}(\tau_1)\eta_i^{\beta}(\tau_2)$  due to a presence of a constant of motion as explained in Ref. [242].

---

<sup>1</sup>For all scaling plots, we re-define  $L = [3/(4\pi n)N]^{1/3}$  using the number  $N$  of sites correlated to the reference site. The number of sites in unit volume is denoted by  $n$ ,  $n = 1$  for cubic- and  $n = 16$  for the pyrochlore lattice. This smoothens edge-effects for small  $L$  and yields better scaling plots.

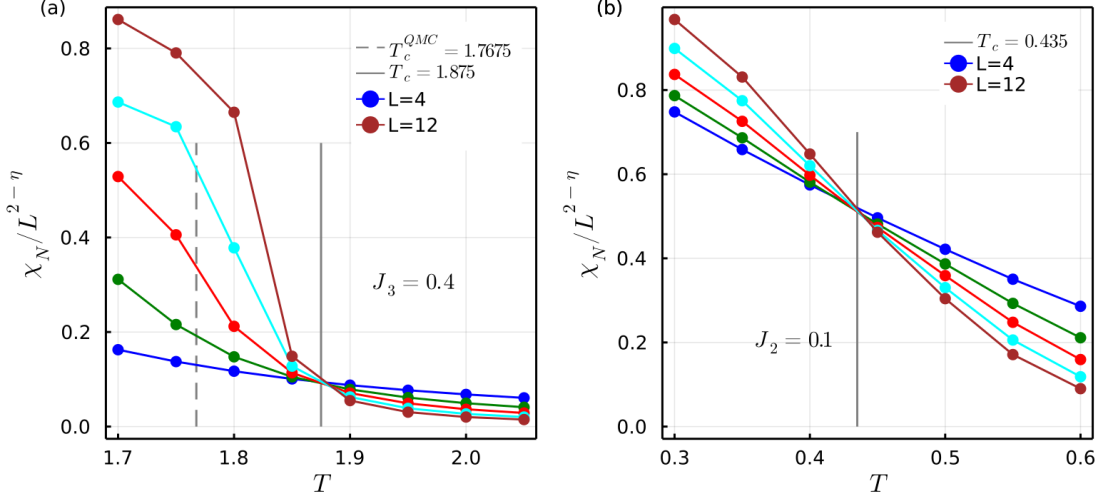


Figure 4.2.: Scaling plot of the cubic lattice susceptibility similar to Fig. 4.1, but for the  $J_1$ - $J_3$  model with  $J_3 = 0.4$  (a) and the frustrated  $J_1$ - $J_2$  model with  $J_2 = 0.1$  (b). PMFRG estimates for the critical temperatures follow from the unique crossing points of the data traces.

As a consequence, the PMFRG's four-Majorana correlators connect to four-spin correlators if the latter are bilocal, i.e.  $\langle S_i S_i S_j S_j \rangle$ . Despite these considerations, it should be emphasized, however, that the strength of the PMFRG lies within its capability to treat microscopic models of frustrated quantum magnets, and is not meant to compete with established high-precision methods to extract critical exponents from effective field theories, see the discussion above.

In this spirit, we proceed by involving additional couplings between next-nearest and next-next-nearest neighbouring sites,  $J_{2,3}$ . Here,  $J_2$  ( $J_3$ ) is a coupling between sites separated along the face (body) diagonal of an elementary cube. The  $J_1$ - $J_3$  Heisenberg model is unfrustrated and can again be studied with QMC [243]. The PMFRG susceptibility for the case  $J_3 = 0.4$  known to enter a Néel ordered phase, is shown in Fig. 4.2(a) and indicates a critical temperature  $T_c = 1.875$ , again about 5% different from the QMC value  $T_c^{\text{QMC}} = 1.7675$ .

Finally, the system is frustrated by a next-nearest neighbor coupling  $J_2$ . In the classical case, Monte-Carlo simulations [244] (with unit spin length) have found the phase diagram in Fig. 4.3, see blue symbols. Increasing  $J_2$  from zero, the ordering temperature for Néel order decreases until it reaches  $T_c \simeq 0.3$  at  $J_2 = 0.25$  from where on a striped antiferromagnetic order with wave vector  $(0, \pi, \pi)$  and equivalent types take over and the ordering temperature increases again. In the quantum

case of  $S = 1/2$  spins, where QMC suffers from the sign problem, the phase diagram has been studied with a variety of methods like spin-wave theory [245, 246], spherically symmetric Green function approximation [247], differential operator technique [248], coupled cluster method [249] and the PFFRG [243]. Despite all these efforts, no consistent picture of the phase diagram has emerged. The qualitative question is if quantum fluctuations suppress the classical magnetic order around  $J_2 = 0.25$  in favor of an intervening paramagnetic phase at  $T = 0$ . The PFFRG, for example, qualitatively reproduces the classical result with a finite break-down scale of the flow (see below) for all  $J_2$ , see brown curve in Fig. 4.3<sup>2</sup>. The coupled cluster method, which infers ground state properties from extrapolation of observables found for finite-size clusters, shows some indication for a tiny paramagnetic phase around  $J_2 \simeq 0.275$ .

In this challenging setting, the capabilities of the PMFRG to tackle frustrated systems are now demonstrated by studying small  $J_2 = 0.1$ , for which, according to the scaling plot in Fig. 4.2(b), Néel order is detected below  $T_c = 0.435$ . This surprisingly small value of  $T_c$  (at half the temperature estimated from the break-down scale of the PFFRG flow in Ref. [243]) might hint towards a larger paramagnetic region in the  $J_2/J_1$ -phase diagram of the model than previously thought. Indeed, repeating the calculation of  $T_c$  for various  $J_2$  between zero and 0.1, we extrapolate the observed linear-in- $J_2$  behavior of  $T_c$  to find it vanishing around  $J_{2,c} \simeq 0.19$  (red dots and red dashed line). Although this extrapolation has to be taken cautiously, it seems to indicate the onset of a quantum disordered phase significantly below the estimated value  $J_{2,c} \simeq 0.275$  from the coupled cluster method of Ref. [243, 249]. Interestingly, the scaling approach of the PMFRG susceptibility fails for larger  $J_2$  where no line-crossings could be observed for the expected ordering wave vectors, despite the susceptibilities growing significantly with decreasing temperature. This will be further explored in the next section, by first considering the temperature flow as an alternative method.

To summarize this section, these results indicate that one-loop PMFRG is suitable to study finite-temperature magnetic phase transitions in 3D frustrated and unfrustrated Heisenberg systems. Although critical temperatures are a few percent off from QMC reference values, the susceptibility data shows the expected scaling behavior at second-order phase transitions, a strong indication for the beyond-mean-field nature of the PMFRG. In particular, there is no breakdown of the flow or any divergence in the susceptibility at any temperature treated. This is expected in the exact (or at least beyond-mean-field/RPA) treatment of an effectively finite-sized system which should not show any spontaneous symmetry breaking.

---

<sup>2</sup>In PFFRG, a paramagnetic phase is found by adding a finite  $J_3 > 0$ , see Ref. [243]

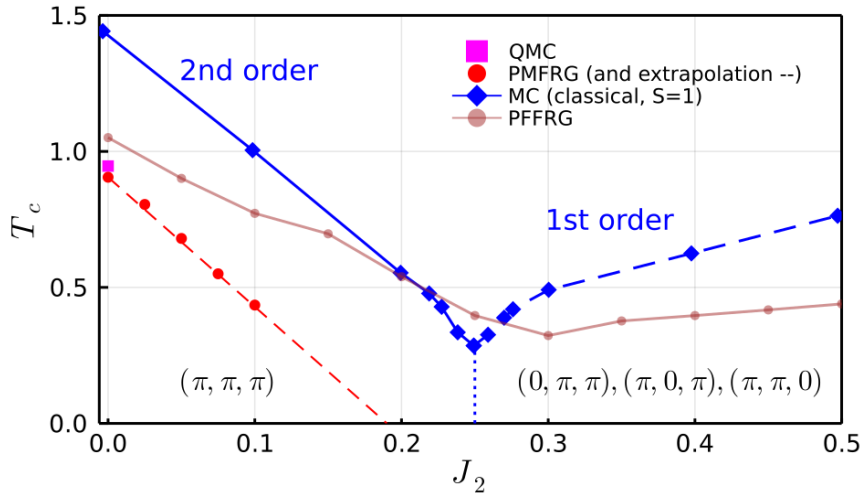


Figure 4.3.: Finite temperature phase diagram of the simple cubic  $J_1$ - $J_2$  Heisenberg antiferromagnet. The data for the classical model with unit spin length is reproduced from Ref. [244] (blue), the transition to the Néel phase for  $J_2 < 0.25$  is second order, while the striped phase for  $J_2 > 0.25$  is reached via a first order transition. The PFFRG result reproduced from Ref. [243] is shown in brown. The one-loop PMFRG results (red dots) for ordering temperatures are only available for the second-order transition and at not too small temperatures; extrapolation to larger  $J_2$  (red dashed line) yields  $J_{2,c} \simeq 0.19$  at  $T = 0$ .

The observed scaling behavior provides a significantly more accurate and rigorous approach to detect magnetic phase transitions than previous PFFRG works where kinks in the renormalization group flow have been used as a signature for ordering. Furthermore, estimates for critical temperatures within PFFRG are complicated by the presence of unphysical states. Instead, critical temperatures were previously based on the approximate (i.e. mean-field-like) relation  $T_c = \pi\Lambda_c/2$  between critical temperature and the divergence in the cutoff scale which may introduce errors, particularly in the presence of strong quantum fluctuations. These results show that it is advantageous to obtain finite ordering temperatures for frustrated models from PMFRG which operates explicitly at finite temperatures instead.

## 4.2. Phase diagram in temperature flow

We now turn to the same model treated with the temperature flow description. It should be noted that due to the truncation of flow equations, different flow schemes are generally inequivalent and may lead to different results, particularly in the limit of strong correlations.

Figure 4.4(a) displays a critical scaling of the correlation length as indicated by the line crossings of  $\xi/L$ , where  $L$  is the spatial cutoff distance beyond which vertices are approximated as zero. While this does not yield different results compared to the scaling of  $\chi \sim L^{2-\eta}$  used in the previous section, this more self-contained approach does not require any external knowledge regarding the system's universality class. The critical temperature is detected as  $T_c \approx 0.97$ . This result is in good agreement to quantum Monte Carlo ( $T_c = 0.946$ ). Incidentally, and perhaps accidentally, it is marginally better compared to the previous  $\Lambda$ -flow result shown in Fig. 4.1.

In the frustrated regime at finite  $J_2 > 0$ , Monte Carlo simulations for classical spins ( $|\mathbf{S}| = 1$ ) [244] find order at finite temperatures throughout the phase diagram, with a continuous phase transition to Néel order for  $J_2 < 0.25$ . For  $J_2 > 0.25$  antiferromagnetic stripe order with wave vector  $\mathbf{k} = (\pi, \pi, 0)$  (and symmetry related wave vectors) is reached via a first order phase transition, see Fig. 4.4(c).

In the quantum spin-1/2 case, the possible presence of a small nonmagnetic region around  $J_2 = 0.25$  is still debated. At  $T = 0$ , linear spin wave theory [250] and the coupled cluster method [249] predict antiferromagnetic order from  $J_2 = 0$  that transitions into a small paramagnetic phase at  $J_2 \approx 0.25$  before undergoing a



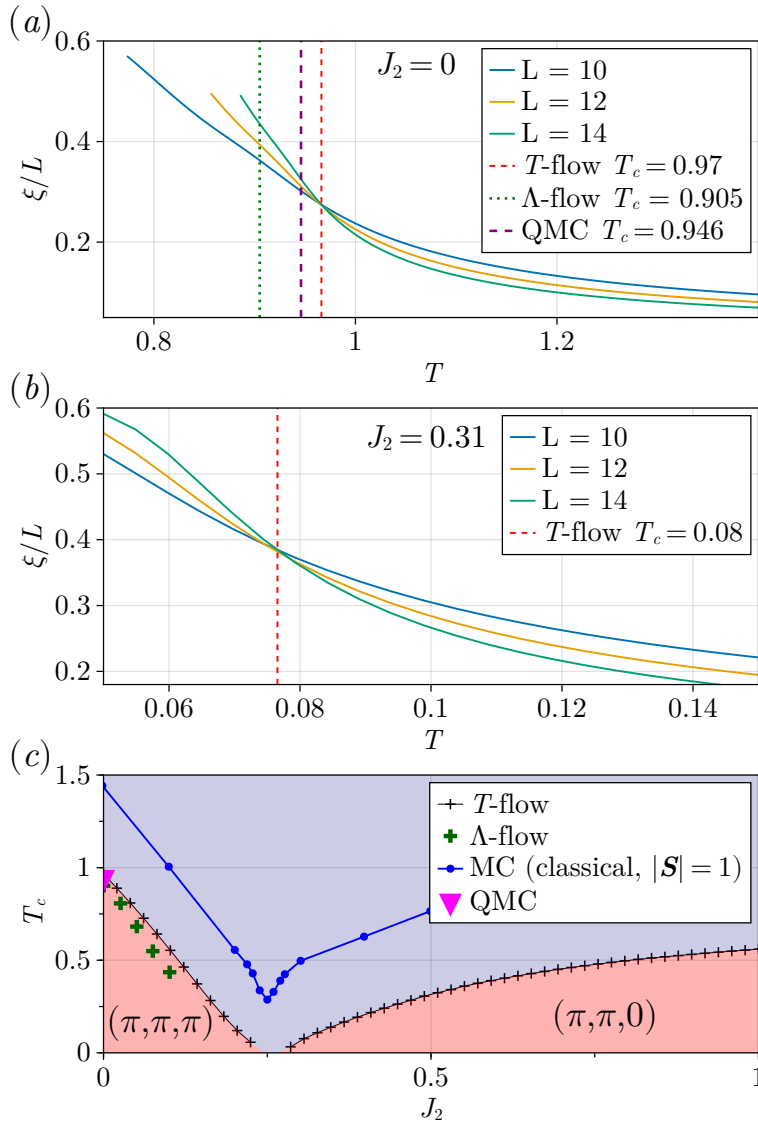


Figure 4.4.: PMFRG results for the  $J_1$ - $J_2$  Heisenberg model on the cubic lattice. (a) Finite-size scaling of the correlation length using  $T$ -flow PMFRG for the simple cubic Heisenberg antiferromagnet at  $J_2 = 0$  in comparison to the standard  $\Lambda$ -flow PMFRG from Fig. 4.1 and quantum Monte Carlo (QMC) [173]. (b) Finite-size scaling of the correlation length using  $T$ -flow PMFRG for the simple cubic Heisenberg antiferromagnet at  $J_2 = 0.31$ . (c) Phase diagram: The transition temperature for the classical model with unit spin length is reproduced from Ref. [244] (blue). The critical temperatures obtained from  $T$ -flow (black crosses) predicts slightly larger transition temperatures than the standard  $\Lambda$ -flow PMFRG (green) in the Néel ordered regime. At  $J_2 \gtrsim 0.25$  the  $T$ -flow scheme detects critical scaling towards a stripe-ordered phase in qualitative agreement to the classical model. This critical temperature is not detected in the  $\Lambda$ -flow scheme.

second phase transition into the antiferromagnetic stripe phase for  $J_1/J_2 > 0.25$ . On the other hand, nonlinear corrections [250] to spin wave theory as well as a variational cluster approach [251], predict no paramagnetic phase between the two ordered phases. Using the  $T$ -flow PMFRG as outlined above, we determine the finite temperature phase diagram, detecting critical temperatures down to a minimum simulation temperature of  $T \sim 0.05$ , with the case  $J_2 = 0.31$  shown in Fig. 4.4(b). The full phase diagram obtained this way is shown in Fig. 4.4(c). In agreement with other methods, we find a phase transition to antiferromagnetic Néel order for  $J_2 \lesssim 0.25$  and to antiferromagnetic stripe order for  $J_2 \gtrsim 0.25$ . Due to the observed critical scaling in system size, all phase transitions are of second order. In between, we observe a small regime without any sign of magnetic order. Although intrinsic consistency checks seem to indicate less accurate results at lower temperatures (see Section 3.2), these findings support claims that there might be a small region with a paramagnetic phase in between the antiferromagnetic Néel and stripe ordered phases.

### 4.3. Discussion of the stripe phase transition

As discussed above, the temperature formalism detects a second order phase transition towards stripe order in the regime  $J_2 \gtrsim 0.25$ . Although expected from other methods, this result initially appears incompatible with the previous findings in the  $\Lambda$ -flow scheme, which, despite observing large dominant stripe correlations could not detect a critical scaling. We will now see that this apparent discrepancy has a simple explanation by further including this artificial infrared cutoff  $\Lambda$  into the temperature flow scheme and interpreting it as an auxiliary parameter.

To compare differences between the two flow schemes we dress the temperature flow propagator with the usual cutoff of the  $\Lambda$ -flow [1],  $\Theta^\Lambda(\omega) = \frac{T^2\omega^2}{T^2\omega^2 + \Lambda^2}$  so that

$$G_{i;\alpha_1\alpha_2}^{-1,T}(\omega_1) = \frac{1}{\Theta^\Lambda(\omega_1)} G_{0;i;\alpha_1\alpha_2}^{-1,T}(\omega_1) - \Sigma_{i;\alpha_1\alpha_2}^T(\omega_1). \quad (4.3)$$

By construction, in the limit  $\Lambda = 0$ , Eq. (4.3) reduces to the propagator of the standard temperature flow scheme. Additionally, this propagator is now equal to the  $\Lambda$ -flow propagator in the entire  $T, \Lambda$  parameter space (aside from the trivial prefactors of  $T^{1/2}$  due to the rescaling of Majorana fields). Hence, physical observables at large  $T$  or  $\Lambda$  will be equal in both approaches. If both  $T \lesssim 1$  and

$\Lambda \lesssim 1$ , however, the approximation of neglecting higher order vertices becomes uncontrolled, generally allowing for different results between the two methods. Figure 4.5 shows a comparison of the  $T$ -flow scheme (dressed with a  $\Lambda$  cutoff) and the  $\Lambda$ -flow scheme as a function of  $T$  and  $\Lambda$  both at  $J_2 = 0$  (Néel order) and  $J_2 = 1$  (stripe order). As both  $T$  and  $\Lambda$  suppress spin correlations, magnetic order can only be stabilized in a finite region around  $T = \Lambda = 0$  as indicated schematically in Fig. 4.5(a,b). As displayed further, the conventional  $\Lambda$ -flow scheme approaches the ordered phase along lines of constant  $T$  while the  $T$ -flow approaches it along constant  $\Lambda$ .

The remaining panels (c-f) display the difference of the rescaled correlation length for the dominant susceptibility

$$\Delta\tilde{\xi}_{1,2} = \frac{\xi(L_1)}{L_1} - \frac{\xi(L_2)}{L_2} \quad (4.4)$$

for two different spatial cutoff distances  $L_1 > L_2$ . At the phase transition, we have  $\xi(L) \propto L$  and thus  $\Delta\tilde{\xi} = 0$ . Consequently, for large enough  $L_{1,2}$ , we can identify the region with  $\Delta\tilde{\xi} > 0$  ( $\Delta\tilde{\xi} < 0$ ) as the ordered (disordered) phase.

For  $J_2 = 0$  [see Fig. 4.5(c) and (d)] both  $\Lambda$  and  $T$ -flows find magnetic order at  $\Lambda = 0$  for  $T \approx 0.9$ . Although RG flows can become unphysical below the critical scale of a phase transition, in the  $\Lambda$ -flow the susceptibility and correlation lengths converge to a large but finite plateau value. For small temperatures of  $T < 0.3$ , on the other hand, we observe a very different behavior of the correlation length which displays a peak as a function of  $\Lambda$  at a finite  $\Lambda \sim 1.25$  indicated by the white circle in Fig 4.5(c). This sharp feature, also referred to as a *flow breakdown*, originates from a peak of the maximum susceptibility (see Section 3.2) in the renormalization flow. In zero-temperature approaches it is an established signature of a phase transition [10, 150, 243, 252], whose detection, however, can be ambiguous in practice. Below the critical temperature, the  $T$ -flow correlations grow rapidly. Numerically, this requires increasingly smaller steps when solving the flow equations, which we eventually terminate as seen for  $J_2 = 0$  in Fig. 4.5(d). Strikingly, at a finite value of  $\Lambda$  in Fig. 4.5(d), the scaling collapse is no longer obtained, leaving the right boundary of the magnetic phase seemingly absent, with similar flow breakdown features as found in the  $\Lambda$ -flow scheme, also indicated via a white circle.

We now move on discussing the  $T$ - $\Lambda$  phase diagrams at  $J_2 = 1$  for both, the  $\Lambda$ -flow and  $T$ -flow schemes in Fig. 4.5(e) and (f), respectively. The  $T$ -flow result in Fig. 4.5(f) resembles the observation in Fig. 4.5(d) in that a critical scaling is only found at small  $\Lambda$  but disappears as  $\Lambda$  increases. The  $\Lambda$ -flow behavior at

$J_2 = 1$  in Fig. 4.5(e) also resembles Fig. 4.5(d) and (f) *but with the roles of  $T$  and  $\Lambda$  reversed*: While Fig. 4.5(e) only displays a phase transition at finite  $\Lambda \sim 1$  and small  $T \lesssim 0.3$ , critical scaling is never found in the physically relevant limit  $\Lambda = 0$ . This makes it impossible to extract a critical temperature in the  $J_2 > 0.25$  parameter regime within the  $\Lambda$ -flow scheme.

These results can be interpreted as follows: Clearly, both,  $\Lambda$ -flow and  $T$ -flow PMFRG methods are sensitive to ordering tendencies. However, each approach is better suited to detect phase boundaries that do not require a long flow through a critical region close to a magnetic phase. For example, such situations occur when a magnetically ordered phase is only grazed during the renormalization group flow in either  $\Lambda$  or  $T$ , shown by green arrows in panels (a) and (b) of Fig. 4.5. In these critical regions, vertices grow large and the approximation of neglecting higher-order vertices is no longer accurate. Concretely, this means that the  $\Lambda$ -flow scheme is more sensitive to phase boundaries found at finite  $\Lambda$ , while the  $T$ -flow is better at detecting the opposite boundary at finite  $T$  and small values of  $\Lambda$ . Indeed, one can approximate the shape of the full magnetic phase in the  $T$ - $\Lambda$  space by the complement of both methods. This is visualized by the yellow dashed line in Fig. 4.5(d) and (f).

We see that for  $J_1 = 1$  the challenge to resolve magnetic order in the  $\Lambda$ -flow scheme is especially pronounced as the top phase boundary in  $T$ - $\Lambda$  space is particularly flat [see Fig. 4.5(f)], and the ordering temperature much smaller. To extract physical quantities, the FRG in the  $\Lambda$ -flow scheme needs to be solved all the way down to  $\Lambda = 0$ , possibly flowing through an ordering transition, where the truncation of flow equations is known to break down. The temperature flow on the other hand needs to be followed only slightly beyond the boundary of the phase transition. We can therefore conclude that the  $T$ -flow scheme is the favorable method as it approaches the phase boundary from the physically relevant direction.

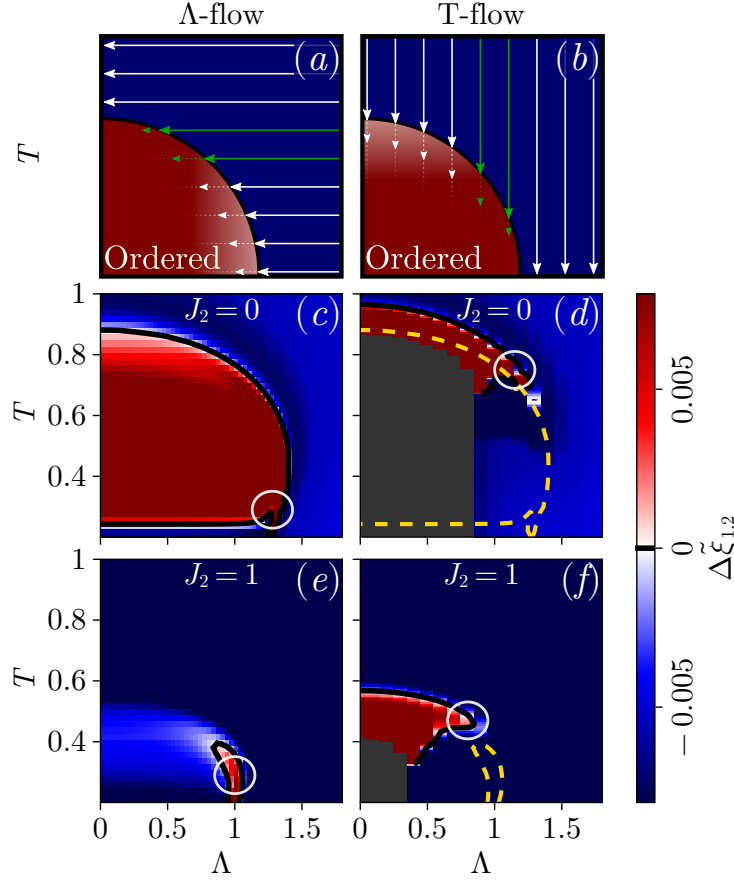


Figure 4.5.: Magnetic phase diagram for the  $\Lambda$ -flow scheme (left) and the  $T$ -flow scheme (right) both as functions of physical temperature  $T$  and the artificial infrared cutoff  $\Lambda$ . (a,b): Schematic picture of the phase diagram and the direction of the flow (arrows) for both schemes. Each arrow represents an independent FRG run. Green arrows indicate problematic flow paths along the circumference of the ordered dome close to the phase boundary. (c-f): The ordered (paramagnetic) phase is determined by a positive (negative) difference of the rescaled correlation length in Eq. (4.4) between two runs for  $L_1 = 14$  and  $L_2 = 12$ . Additionally, the phase boundaries given by the contour  $\Delta\tilde{\xi} = 0$  are indicated by black lines. In (d) and (f), the phase boundary from the  $\Lambda$ -flow scheme is displayed in yellow. White circles highlight exemplary positions of breakdowns of the PMFRG flow. For better visibility, the color range is limited to a small region around  $\Delta\tilde{\xi} = 0$ .



## The Heisenberg Pyrochlore Model

While the previous chapter demonstrated the PMFRG’s applicability to systems ordering magnetically, strongly frustrated and magnetically disordered models are also treatable. A prominent example of a geometrically frustrated lattice is the pyrochlore network [253], defined by a four-site basis arranged within an fcc lattice. Here, as shown in Fig. 1.2, each site is placed at the vertex of an arrangement of corner-sharing tetrahedra where the edges are given by nearest-neighbor bonds [254]. The classical nearest-neighbor antiferromagnetic Heisenberg model features an extensive ground state degeneracy as the lowest energy can be achieved by any state fulfilling the constraint of a vanishing magnetization within each individual tetrahedron, often referred to as a *spin-ice rule* [29, 61, 255]. The quantum versions of models with such a degeneracy are often believed to evade magnetic long-range ordering at low temperatures and, as such, are promising candidates as hosts for quantum spin liquids. Recent studies confirm the non-magnetic ground state of the nearest neighbor spin-1/2 pyrochlore antiferromagnet but suggest a spontaneous breaking of  $C_3$  and inversion symmetry [8, 256, 257] possibly indicating a valence-bond solid. Yet, the predictions of magnetic monopole and emergent photon excitations resulting from an underlying  $U(1)$  gauge structure remain a fascinating research perspective for related models [73]. Arising from the local nature of the ground state constraint, an interesting feature is the observation of non-analytical points in the classical spin structure factor, so-called “pinch points” (also referred to as “bow-ties”), at  $T = 0$  within the  $hhl$ -plane [41–43].

### 5.1. Quantitative Benchmarks

Being well-suited to treat quantum systems at finite temperatures, we now investigate the performance of the PMFRG in the case of the nearest-neighbor quantum spin-1/2 pyrochlore antiferromagnet. In order to verify the quantitative reliability of these results, we start comparing the static component of the spin susceptibility  $\chi \equiv \chi(\mathbf{q} = 0)$  against DMRG [257] and diagrammatic Monte-Carlo [258] as well as the Padé approximant of the high-temperature series expansion (HTSE) in Fig. 5.1 [259, 260]. On the one-loop level the results differ from other methods by  $\sim 10\%$  at  $T \sim J_1$  with further increasing differences for lower temperatures,

indicating a smaller accuracy than the one-loop results in Sec. 4. However, under the additional inclusion of two-loop ( $\ell = 2$ ) contributions the results are found to be in perfect agreement with all other methods, remaining consistent with DMC even at temperatures as low as  $T \simeq 0.2$ . Figure 5.2 shows the energy per site  $e$  and the specific heat capacity  $c = \frac{de}{dT}$  as functions of the temperature. The energy per site  $e$  can be alternatively found from the expectation value of the Hamiltonian, which can be written in terms of equal time spin-spin correlators [164]

$$\langle H \rangle = \sum_{i < j} J_{ij} \langle S_i(0) S_j(0) \rangle \quad (5.1)$$

with  $\langle S_i(0) S_j(0) \rangle = \sum_n \chi_{ij}(i\nu_n)$ .

It can be seen that the energy computed from the PMFRG susceptibility via Eq. (5.1) is generally consistent with the one derived from the PMFRG free-energy and HTSE, although acquiring an unphysical negative slope (i.e. negative heat capacity) around  $T \lesssim 0.3$ . This is likely a first indicator of the aforementioned low-temperature divergence in the PMFRG flow discussed above and in Ref. [1]. The energies obtained via the free energy, by contrast, retain a positive slope down to lower temperatures but will ultimately behave similar due to the free energy's indirect coupling to the four-point vertex. Despite this observation, it is stressed that the energy is not to be understood as a measure of accuracy in the variational sense and as such is not bounded from below by the true energy. While a temperature below  $T \simeq 0.2J_1$  is currently not accessible, the finite temperature energy compares well with a recent many-variable Monte Carlo (mVMC) study at  $T = 0$  (dashed black line).

## 5.2. Finite-width pinch points

The spin susceptibility of the pyrochlore features bow-tie patterns in the  $hhl$ -plane, connected to the existence of the classical ground state ice rule [43]. Figure 5.3 shows the static susceptibility [Eq. (2.61)] obtained from two-loop PMFRG at  $T = 0.2$  in the  $hhl$ -plane, which features a pronounced peak structure around  $\mathbf{q} = (0, 0, 4\pi)$  (and symmetry-related points) where one would classically expect the pinch points. In the classical case, the width of these peaks along the  $[00l]$ -direction is known to vanish analytically in the  $T \rightarrow 0$  limit whereas thermal fluctuations at  $T > 0$  lift the non-analyticity of the pinch points. The associated finite width  $\sigma \sim \sqrt{T}$  of the broadened peaks is a measure for how much the ice rule is violated at finite temperatures [261–263].



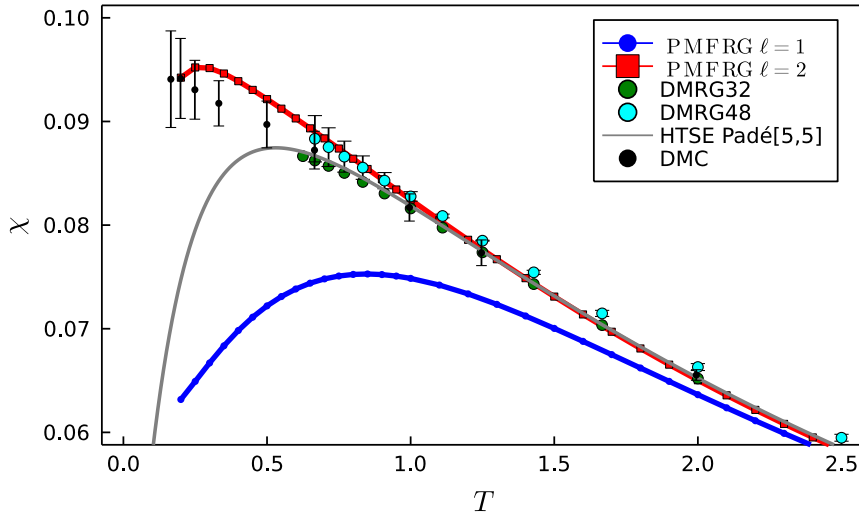


Figure 5.1.: Uniform ( $\mathbf{q} = 0$ ) susceptibility for the pyrochlore antiferromagnet from PMFRG as a function of temperature in comparison with diagrammatic Monte Carlo (DMC) [258], density-matrix renormalization group [257] (DMRG, cluster sizes 32 and 48) and the Padé approximant of the high temperature series expansion [259].

In a quantum system, thermal- and quantum fluctuations compete. Using the PMFRG, the full-width at half maximum (FWHM) of the peak is measured along the  $[00l]$ -direction, see Fig. 5.3(b). Although at low temperatures, we observe a straight line in a plot over  $\sqrt{T}$ , an extrapolation to  $T = 0$  results in a finite width at  $T = 0$  where two-loop PMFRG predicts a slightly smaller value than one-loop. It can be concluded that while the qualitative applicability of the classical ice rule remains visible in the overall structure of the susceptibility, a full  $\sqrt{T}$ -law without a constant offset is only correct for the classical model. Quantum effects not only broaden the peak at  $T = 0$  [150], but remain strong enough at finite temperatures to increase deviations from the classical ice rule ground state. As discussed above, deviations from exact results at low temperatures stem from the truncation of the flow equations. In an attempt to partially correct the introduced errors, the two-loop corrections represent certain contributions from the neglected six-point vertex, and the full multiloop expansion can be more generally understood as a systematic way to iteratively recover all diagrams contained in the parquet approximation [164, 165, 167, 221, 224, 264]. However, the effects of each additional loop order and the overall properties of loop-convergence are highly nontrivial for a purely interacting model such as the Heisenberg Hamiltonian and require a careful case-based numerical analysis.

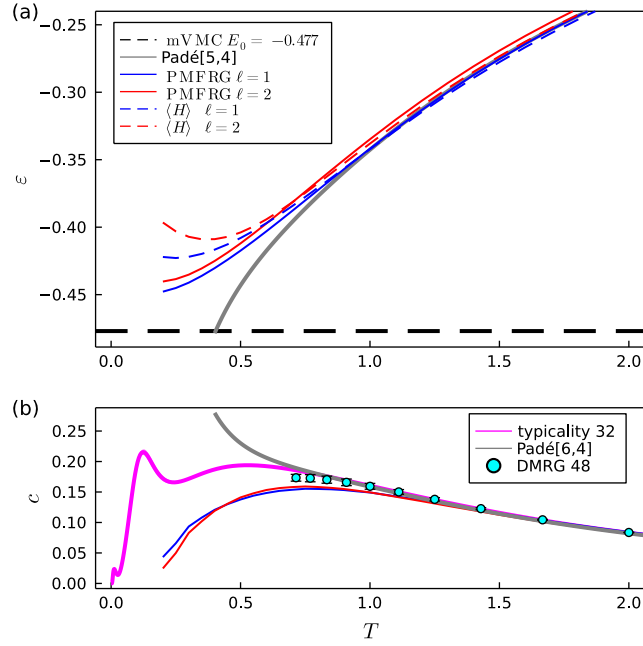


Figure 5.2.: Energy per site (a) and specific heat capacity (b) as a function of temperature for one-loop ( $\ell = 1$ ) in blue and two-loop ( $\ell = 2$ ) in red. An estimate of the energy per site within PMFRG is accessible either from a derivative of the free energy (solid), Eq. (2.22a), or through the expectation value of  $H$  in terms of equal time spin-correlators (dashed) Eq. (5.1). Additionally shown is the ground state energy estimate from mVMC [8, 257] and the specific heat capacity from DMRG and canonical typicality on a 48- and 32-site cluster, respectively [257].

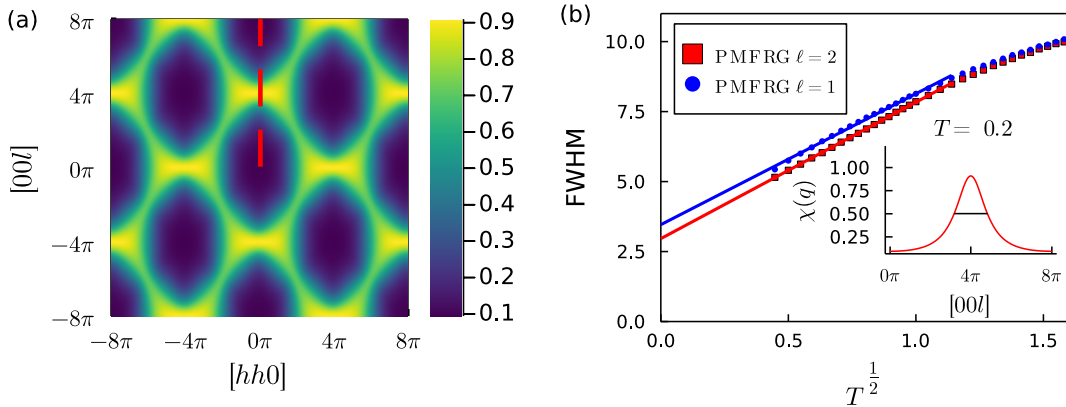


Figure 5.3.: (a) Two-loop static susceptibility of the antiferromagnetic Heisenberg model on the pyrochlore lattice in the  $[hh0]$ -plane ( $q_x = q_y = h$ ) at  $T = 0.2$  and (b) full-width at half maximum along of the pinch point as a function of temperature. The inset shows the cut along the  $[00l]$  line of the susceptibility from (a).

The results in Sec. 4 demonstrate that one-loop PMFRG allows one to accurately determine critical temperatures and scaling behavior for second order magnetic phase transitions in 3D quantum magnets. On the other hand, in strongly frustrated systems that remain magnetically disordered at low temperatures such as the pyrochlore model investigated in the last section, one-loop results are less accurate but two-loop corrections yield substantial improvements. What remains to be discussed is how two-loop PMFRG performs when applied to magnetically ordered systems.

To demonstrate the two-loop flow behavior in this case, we specifically consider the ferromagnetic ( $J_1 = -1$ ) nearest neighbor pyrochlore Heisenberg model but emphasize that the results below are typical for systems that order magnetically. While as usual the susceptibility flows smoothly as a function of the cutoff  $\Lambda$  (see Fig. 5.4), the one-loop susceptibility scales strongly with system size yielding a critical temperature  $T_c \simeq 0.685$  in good agreement to QMC ( $T_c^{\text{QMC}} = 0.7182$  [262]), see the crossing lines in Fig. 5.5. However, for  $\ell = 2$ , no such scaling and, hence, no magnetic order is found. The large quantitative difference between one-loop and two-loop in the magnetically ordered case suggests the necessity for higher loop order corrections, which is left for future work.

Initially, it may appear surprising that the detection of magnetic order is problematic at second loop order. However, a similar observation has been made in a recent multiloop PFFRG study [165], where magnetic ordering tendencies in the

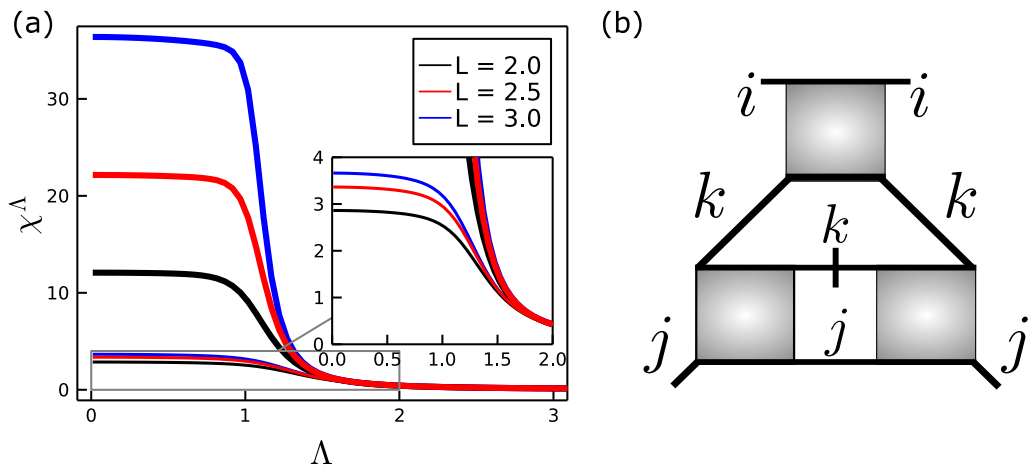


Figure 5.4.: (a) Ferromagnetic Heisenberg model on the pyrochlore lattice for  $T = 0.5$ , well below the critical temperature  $T_c = 0.685$  observed in Fig. 5.5: Flow of the uniform susceptibility  $\chi^\Lambda$  obtained in the one-loop (thick) and two-loop (thin) PMFRG as a function of the cutoff  $\Lambda$  for different maximum vertex lengths  $L$ . (b) Two-loop contribution to the right hand sides of the flow equation for  $\Gamma$  where a ladder diagram (with external site indices  $k, j$ ) is inserted into the RPA channel (with external site indices  $i, j$ ).

flow are found to be strongly suppressed at  $\ell = 2$  but recovered at  $\ell = 3$ .

A deeper understanding of this behavior can be obtained by inspecting the diagrammatic contributions in different loop orders. First recall that the four-point vertex flow is generated by different coupling channels with distinct physical meanings. Particularly, the random-phase approximation (RPA) terms enable the formation of magnetic long-range order, while all other channels (here, for simplicity referred to as “ladder channels”) induce quantum fluctuations. In multi-loop schemes these channels are inserted into each other, leading to a nested diagram structure, see Fig. 5.4(b) for an example. The nesting is subject to the rule that a contribution from a particular channel cannot be inserted into the same channel again, as this would yield an overcounting of diagrams.

With this multiloop construction in mind, the RPA diagrams which in magnetically ordered systems dominate the one-loop flow are dressed by ladder diagrams in two-loop. This strongly suppresses magnetic order and explains our observation in Fig. 5.4. In turn, the third loop order nesting can again be performed with RPA diagrams which would strengthen ordering effects. Overall, one may, hence, ex-

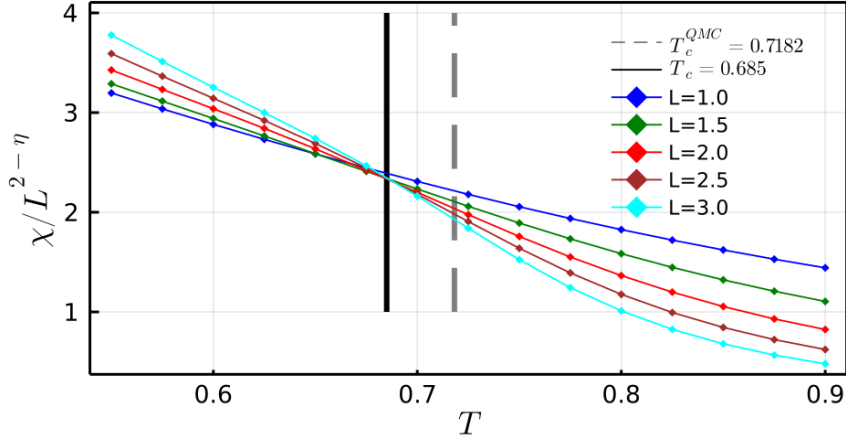


Figure 5.5.: PMFRG ( $\ell = 1$ ) results for the ferromagnetic Heisenberg model on the pyrochlore lattice indicating a phase transition at  $T_c \simeq 0.685$  in good agreement with the QMC value  $T_c^{\text{QMC}} = 0.7182$  from Ref. [262].

pect an even-odd-effect of magnetic ordering tendencies in loop order. It is possible that this type of behavior is characteristic for systems where one coupling channel (here, the RPA channel) dominates the physical behavior. The more systematic improvement upon increasing  $\ell$  observed for the magnetically disordered antiferromagnetic pyrochlore Heisenberg model can then be interpreted as a consequence of the fact that in this case *all* channels contribute more equally. However, as discussed in Chapter C, even the full parquet solution seems incapable of detecting order via a finite size scaling analysis. While the cause of this discrepancy is still an ongoing investigation [10], it is evident that the particular combination of diagrams in the one-loop truncations seems to include magnetic order and disorder in a more balanced fashion, while higher loop-orders, while more accurate from a purely perturbative perspective, may include a bias towards disordered states.

### 5.3. Spin 1 model

In this section, we address the finite-temperature properties of the nearest neighbor pyrochlore Heisenberg model, i.e., we set  $J_2 = 0$ . The ground state of this system was found to be non-magnetic in several previous works [150, 262, 265]. The investigation here also serves as a benchmark for the PMFRG method to check whether the level-repulsion term introduced in Eq. (3.40) can correctly eliminate

contributions from the unphysical states in thermodynamic quantities such as the specific heat and the susceptibility.

First, we determine the optimal value  $\gamma$  for the nearest neighbor pyrochlore model. To achieve this,  $\gamma$  is increased until convergence is found. As an additional verification of this procedure, after convergence density-matrix purification data is used to benchmark the PMFRG results [4]. Even though the density-matrix purification cannot access temperatures below  $T \sim 2$ , the regime  $T \gtrsim 2$  is still suitable for benchmarks, since the effects of unphysical states are more pronounced at higher temperatures. In Fig. 5.6 we show the specific heat capacity  $C_V$  and the uniform susceptibility  $\chi$  a function of temperature for varying values of  $\gamma$ . At the smallest level repulsion  $\gamma = 0.1$ , the effects of unphysical states are still clearly visible from the deviation between the PMFRG result (blue curve) and the density-matrix purification result (black curve). As the level repulsion is increased, the PMFRG results first undergo significant changes, in particular the specific heat. However, for  $\gamma \gtrsim 1$  the changes become smaller upon varying  $\gamma$  and we observe convergence around  $\gamma = 2$ . The agreement with the density-matrix purification is best at  $\gamma = 2.5$  (red curve). It is noted that for the conventional one-loop truncation, the specific heat and the susceptibility from PMFRG show a slightly enhanced deviation from the density-matrix purification results at the lowest temperatures  $T \sim 2$  accessible within the density-matrix purification. As discussed in Ref. [2], this can be remedied by a two-loop truncation of the vertex flow equations, which significantly decreases these deviations. In principle, the ideal choice of  $\gamma$  can change upon increasing  $J_2$ . However the excitation gap to unphysical states at constant  $\gamma$  and increasing  $J_2$  is expected to increase as a result of the decreasing frustration. Hence, the constant value  $\gamma = 2.5$  should also properly eliminate the impact of unphysical states for  $J_2 > 0$ .

As we approach  $T \sim 2$  a maximum seems to be formed in the heat capacity in agreement with the rotation-invariant Green function method [262]. Since the heat capacity peak occurs at temperatures on the order of the coupling  $J_1$ , the system turns into a strongly correlated quantum magnet in this temperature region. The PMFRG results are in remarkably good agreement with the ones from the purification approach, especially for the two-loop truncation scheme, which was previously found suitable for the  $S = 1/2$  nearest neighbor pyrochlore Heisenberg model [2]. Note that in PMFRG the specific heat is obtained via a numerical second derivative of the free energy, and thus requires a numerically accurate solution of the flow equations, making it prone to inaccuracies from error propagation. Due to such effects we find a slightly negative heat capacity at the highest temperatures  $T \sim 100$ , where the physical contribution of the interaction correction to the free

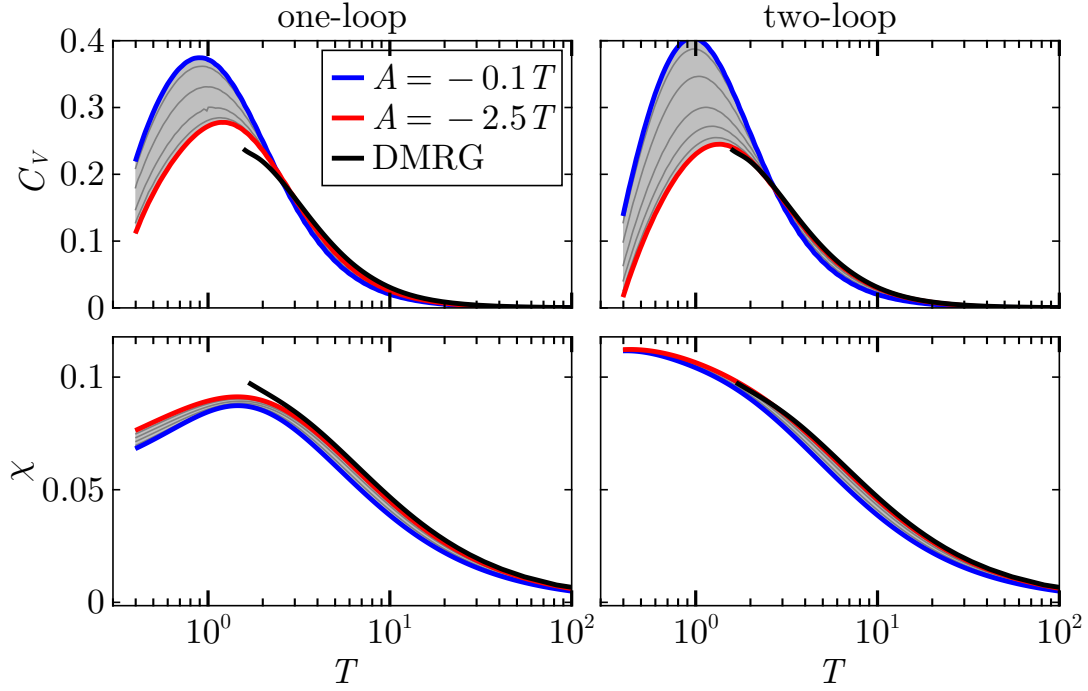


Figure 5.6.: Specific heat (top panel) and uniform susceptibility (bottom panel) obtained from PMFRG in the standard one-loop truncation (left) and two-loop truncation (right) as a function of temperature for different choices of the level repulsion  $A = -\gamma T$  ranging from  $\gamma = 0.1$  (blue lines) to  $\gamma = 2.5T$  (red lines). The values of  $\gamma$  for the thin gray lines in between are  $\gamma = 0.2, 0.5, 1, 1.5, 2$ . The black lines denote the density-matrix purification result.

energy is vanishingly small but the dominant interaction from the level repulsion  $A \sim T$  is still considerable. Likewise, at the lowest temperatures,  $T \lesssim 0.3$  errors from the truncation of PMFRG flow equations also lead to an unphysical heat capacity  $C_V < 0$ . We have omitted data at such low temperatures in Fig. 5.6. Nonetheless, the overall agreement between the two very different methods serves as an indication that even for spin magnitudes  $S > 1/2$ , PMFRG is a reliable approach to address finite-temperature properties.

## 5.4. Effect of the $J_2$ coupling

As mentioned before, an antiferromagnetic next-nearest neighbor coupling  $J_2$  enhances spin correlations of so-called  $\mathbf{k} = 0$  type [150]. The corresponding classical  $\mathbf{k} = 0$  order has ferromagnetic spin arrangements in each of the four sublattices of the pyrochlore lattice, individually. On the other hand, the relative orientations of the four spins in each tetrahedron fulfill the spin ice rule, which means that the sum of the four spins in each tetrahedron vanishes. The  $\mathbf{k} = 0$  order manifests in magnetic Bragg peaks in the spin structure factor at  $\mathbf{q} = (4\pi, 0, 0)$  and symmetry-equivalent points in the extended Brillouin zone. The main goal in this section is to identify and locate the phase boundary where  $J_2$  interactions drive  $\mathbf{k} = 0$  magnetic order in the  $S = 1$  system.

Figure 5.7 shows the equal-time spin structure factor  $S(\mathbf{q})$  in the non-magnetic phase at  $J_2 = 0.01875$  in comparison between PMFRG and DMRG. Since, by construction, all symmetries of the Hamiltonian remain intact within PMFRG, the DMRG data in Fig. 5.7 is symmetrized to enable a direct comparison between both approaches. Also note that the DMRG result corresponds to  $T = 0$  while the PMFRG data is taken at the lowest simulated temperature  $T = 0.25$ . Both methods agree well on their prediction of dominant wave vectors, however, in DMRG the peaks in  $S(\mathbf{q})$  (which indicate the proximity to the  $\mathbf{k} = 0$  ordered phase) are somewhat more pronounced. This is likely an effect of the different temperatures involved in the comparison, where the finite temperature  $T = 0.25$  used in PMFRG smears the signal. On the other hand, PMFRG can efficiently describe fully translationally invariant systems, restricting only the length of spin correlations (here,  $L = 10$ ). If  $L$  is chosen to be larger than the physical correlation length, this method provides a virtually infinite momentum resolution, which smoothes the more ‘grainy’ appearance of the spin structure factor from DMRG. As a consequence, remnants of the characteristic pinch-point pattern known from the  $J_1$ -only model become visible at  $\mathbf{q} = (4\pi, 0, 0)$  within PMFRG. However, due to the finite



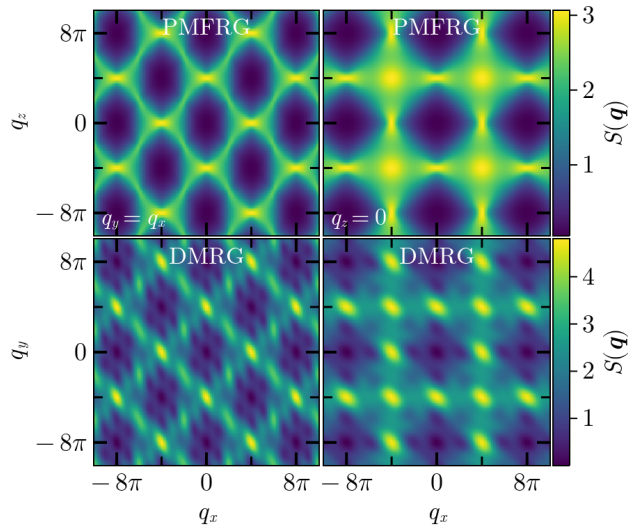


Figure 5.7.: Spin structure factor  $S(\mathbf{q})$  for  $J_2 = 0.01875$  from DMRG at  $T = 0$  with symmetrized wavefunction (bottom panel) and from PMFRG at  $T = 0.25$  (top panel) for  $L = 10$ . The left (right) plots show  $S(\mathbf{q})$  in the  $[hhl]$  ( $[hl0]$ ) plane.

$J_2$  coupling a peak starts to grow out of the pinch-point center [150].

Upon increasing  $J_2$  we observe growing intensities of the spin structure factor at the dominant wave vector  $\mathbf{q} = (4\pi, 0, 0)$  within PMFRG (not shown). In order to rigorously determine the transition to the  $\mathbf{k} = 0$  ordered phase in PMFRG we study the model for three different values of the maximal correlation length  $L = 6, 10, 14$  using the one-loop PMFRG scheme which was found to be more suitable for resolving magnetic order than higher loop-orders [2]. Critical temperatures of a second order phase transition are found via finite-size scaling of the correlation length  $\xi$  [see Eq. (1.10)] which, at the critical temperature  $T_c$ , scales as  $\xi/L = \text{const.}$ , i.e., linear in the numerically chosen maximum correlation distance  $L$ . The critical temperatures  $T_c$  determined this way are shown in Fig. 5.8 as a function of  $J_2$ . Although temperatures below  $T \lesssim 0.3$  cannot be resolved accurately due to the effects of neglecting higher order vertices in the flow equations,  $T_c$  shows a clear downward trend when lowering  $J_2$ . The phase boundary  $T_c(J_2)$  can be accurately fitted by a parabolic curve which we extrapolate to obtain an estimate for the phase boundary at  $T = 0$ , given by  $J_2 = 0.035(8)$ . The error bars for the data points in Fig. 5.8 are estimated from the maximal difference between pairwise crossing points of curves for different  $L$  (see inset). The error of the  $T = 0$  phase boundary is estimated through extrapolations of the errorbars as displayed in the

figure.

While the value  $J_2 = 0.035(8)$  from PMFRG is somewhat larger than the critical coupling  $J_2 \sim 0.02$  estimated with DMRG, taking into account the uncertainties of the extrapolation to  $T = 0$  in PMFRG and the fact that the DMRG result is obtained for a small spin cluster, both critical couplings can still be regarded as consistent. Particularly, the small critical  $J_2$  found in both approaches indicates a high fragility of the non-magnetic phase of the nearest neighbor model to second neighbor couplings.

## 5.5. Discussion of previous PFFRG results

The position of the zero-temperature phase transition at  $J_2 = 0.035(8)$  identified by PMFRG in the previous section differs considerably from the critical coupling  $J_2 = 0.09(2)$  found in Ref. [150] obtained by the similar PFFRG approach. This raises the question why these closely related approaches disagree so strongly in that result. The following discussion provides an explanation, points out precautions when using the PFFRG and describes how these methods should best be applied.

To start, it is worth explaining several properties of the PFFRG and how this method detects quantum phase transitions between magnetically ordered and disordered phases. The PFFRG, as detailed in Section 1.6, expresses spin operators in terms of *complex fermionic* auxiliary particles, so-called Abrikosov fermions, which introduce unphysical states. While at  $T = 0$ , the impact of unphysical states is usually found to be mild, at finite temperatures their contributions grow such that a meaningful application of the PFFRG is restricted to  $T = 0$  (unless a projection via the Popov-Fedotov method is applied [160]). Thus, a finite-temperature phase transition can never be directly observed in PFFRG but instead reveals itself at finite cutoff  $\Lambda > 0$  at  $T = 0$ . However, while  $\Lambda$  shares some properties with the temperature  $T$ , its artificial nature complicates the physical interpretation of results at finite  $\Lambda$ . For example, it is currently unclear whether critical scaling in the system size  $L$  is generally expected at finite  $\Lambda$ . Hence, the usual approach to nevertheless identify the onset of magnetic order for given coupling parameters at finite  $\Lambda$  and  $T = 0$  within PFFRG is to search for instability features of the susceptibility as a function of  $\Lambda$ , such as kinks or peaks. This identification of long-range order, however, gets increasingly difficult if one approaches a quantum critical point from the ordered side, since kinks get less pronounced, shift to lower  $\Lambda$  and continuously disappear. Furthermore, at low  $\Lambda$  the PFFRG becomes increasingly

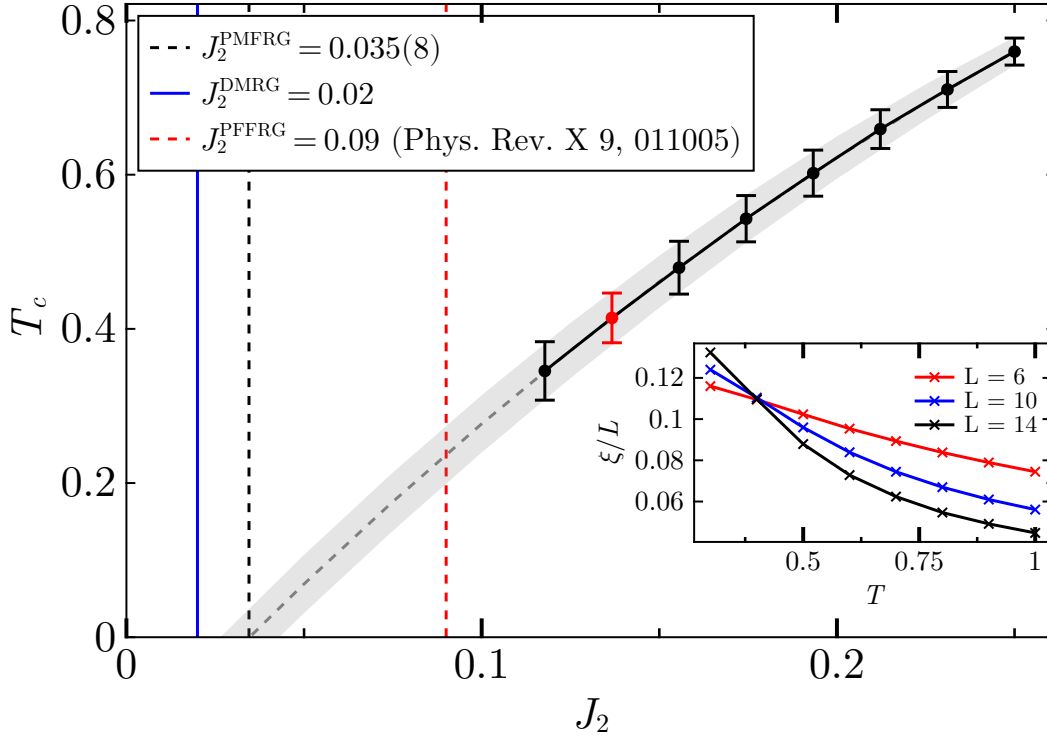


Figure 5.8.:  $J_2$  dependence of the critical temperature  $T_c$ , obtained via a scaling collapse of the correlation length  $\xi \sim L$  calculated with one-loop PMFRG. As an example, the inset shows the scaling collapse for the red data point in the main panel for maximal correlation distances  $L = 6, 10, 14$ . Error bars are estimated from the maximum deviation between crossing points of different curves. The gray dashed line is an extrapolation of the phase transition to  $T = 0$  using a parabolic fit, where the vertical black dashed line highlights the  $T = 0$  critical  $J_2$  coupling obtained this way. The vertical blue line indicates the critical  $J_2$  coupling from DMRG and the vertical red dashed line is the result from Ref. [150].

inaccurate (for the same intrinsic methodological reason why PMFRG becomes uncontrolled at low  $T$ ) and the existence or absence of weak instability features may sensitively depend on details of the implementation such as the chosen frequency mesh. As an example, Fig. 13 of Ref. [150] illustrates these difficulties in precisely locating zero-temperature phase boundaries in PFFRG, where a kink in the susceptibility flow of the nearest neighbor pyrochlore Heisenberg model continuously disappears when the spin magnitude  $S$  is decreased. Usually, in PFFRG the extent of a magnetically ordered zero-temperature phase is determined by the coupling parameter regime in which kinks in the  $\Lambda$  flow of the susceptibility are explicitly visible (although sometimes only faintly visible). The phase boundaries obtained this way (such as the critical second neighbor coupling  $J_2 = 0.09(2)$  of the  $S = 1$   $J_1$ - $J_2$  pyrochlore Heisenberg model obtained in Ref. [150]), might, however, underestimate the extent of ordered phases because there could be a parameter window where magnetic order exists, but the instability features are too faint to be visible in the susceptibility or the methodological limitations at small  $\Lambda$ , coarse frequency meshes and finite system sizes prevent their observation.

Let us compare this situation with the more quantitative method of locating a  $T = 0$  phase transition in PMFRG where a finite size scaling and an extrapolation to  $T = 0$  is employed. The phase diagram in Fig. 5.8 shows that a phase transition into a  $\mathbf{k} = 0$  magnetic regime is only explicitly observed via critical scaling for  $J_2 \gtrsim 0.12$ , while for smaller  $J_2$  the methodological limitations at low  $T$  or the actual absence of order prevent a direct detection of a phase transition. If the extent of the  $\mathbf{k} = 0$  ordered phase is only determined from the  $J_2$  regime where a transition is directly visible (via a susceptibility kink in PFFRG or via critical scaling in PMFRG) the two values  $J_2 = 0.09(2)$  in PFFRG and  $J_2 = 0.12$  in PMFRG are actually not so different. This indicates that the competition between magnetic order phenomena and magnetic disorder fluctuations might be described quite similarly in both approaches. A crucial difference, however, is that the more quantitative approach of detecting phase transitions in PMFRG allows an extrapolation to  $T = 0$ , and thus provides access to actual quantum phase transitions. Note that an analogous procedure in PFFRG, i.e., an extrapolation of kink-like instability features to  $\Lambda = 0$  would be considerably harder, since the  $\Lambda$  positions of weak kinks often depend sensitively on details of the implementation (precise choice of the frequency grid).

To summarize this discussion, the much larger zero-temperature critical  $J_2$  coupling from PFFRG compared to PMFRG does not necessarily indicate that PFFRG intrinsically underestimates magnetic order. Rather, the usual approach of identifying a quantum phase transition from PFFRG susceptibility data is in-

accurate and can make magnetically ordered phases appear smaller than they actually are. Therefore, zero-temperature phase boundaries from PFFRG are only rough estimates and the obtained sizes of magnetically ordered regimes can be understood as lower bounds for the actual extents of these phases. The results in this paper also show how PMFRG solves this problem via extrapolations of phase boundaries to  $T = 0$ , giving rise to more accurate positions of quantum phase transitions.



## Quantum Effects on Unconventional Pinch Point Singularities

### 6.1. Introduction

A particularly fascinating physical situation arises when a system of interacting spins realizes an emergent gauge theory, which is one of the defining properties of a quantum spin liquid [55]. Various different types of gauge theories may be realized in such phases. For example, quantum spin ice represents a variant of a quantum spin liquid, where an emergent U(1) gauge theory on a pyrochlore lattice establishes an astonishing analogy to three-dimensional electromagnetism including emergent photons and an effective fine-structure constant [12, 73]. The key ingredient enabling these non-trivial properties is the gauge constraint which, in the charge-free sector of a U(1) gauge theory, takes the form of a Gauss law  $\nabla \cdot \mathbf{E}(\mathbf{r}) = 0$ .

Meanwhile, generalizations of the standard U(1) gauge theories have become a new focus of theoretical investigations where the vector form of the Gauss-law is replaced by a tensor structure [89, 103, 117, 266], e.g.  $\sum_{\mu\nu} \partial_\mu \partial_\nu E_{\mu\nu}(\mathbf{r}) = 0$ , known as tensor gauge theories describing so-called fracton spin liquids [105, 106]. The most remarkable consequence of this generalization is that, besides the effective charge of a quasiparticle, multipole moments of charges become conserved quantities giving rise to excitations with fractionalized mobility [103]. Two cases can be distinguished [102]: In type-I fracton phases [116, 267, 268], described by symmetric tensor gauge theories, the quasiparticles are either completely immobile or have a residual mobility along subdimensional manifolds. Otherwise, in type-II fracton phases [118, 269, 270] all quasiparticles are completely immobile. In the associated multipolar gauge theories the Gauss law contains derivatives of different orders restricting charge configurations to certain fractal patterns [109, 111, 271, 272]. Remarkably, fracton phases also attract interest in fields such as quantum information [107, 273] and high energy physics [108, 112, 266, 274].

Recently, important steps have been undertaken to bring the rather abstract theoretical research on fracton phases closer to the established field of quantum magnetism and to experiments. For example, it has been found that type-I frac-

ton phases manifest themselves in multifold pinch-points [117] in the spin structure factor [Fig. 6.2(a)], generalizing the famous twofold pinch points known from conventional U(1) spin liquids [Fig. 6.1(c)]. Likewise, type-II fracton phases have been argued to be associated with quadratic pinch points [Fig. 6.3(d)] where contour lines exhibit a characteristic parabolic shape [113]. On a different front, a class of simple classical spin models have been identified [51] which give straightforward access to classical spin liquids described by tensor gauge theories and to unconventional pinch points in the spin structure factor. However, it is an open but experimentally relevant question how stable these phases are under modification from the ideal situations in which they are defined, e.g., by allowing for quantum fluctuations.

In the following, we consider the effects of quantum fluctuations on the ground state and finite-temperature phases of the classical spin model in Ref. [51]– the so-called octochlore model – whose three dimensional octahedral lattice is realized in rare-earth antiperovskites [275, 276]. This model represents a showcase example for exotic classical spin liquids: Apart from known twofold and multifold pinch points we identify exact realizations of quadratic pinch points [113] as well as unconventional pinch line singularities [277]. We add quantum fluctuations to the system by promoting it from a classical ( $S \rightarrow \infty$ ) to a quantum  $S = 1/2$  Heisenberg model which is then numerically treated via two powerful quantum many-body techniques, the pseudo fermion and the pseudo Majorana functional renormalization group. Overall, we find that exotic pinch point features are drastically affected by quantum fluctuations and appear more fragile compared to conventional twofold pinch points.

## 6.2. Unconventional gauge theories from an octochlore model.

The octahedral lattice consists of corner-sharing octahedra and is defined by simple cubic lattice vectors  $\mathbf{a}_m \in \{(1, 0, 0), (0, 1, 0), (0, 0, 1)\}$  together with a three site basis  $\mathbf{b}_m = \mathbf{a}_m/2$ . The Hamiltonian of the octochlore model [51] is constructed as the sum of squared vectors  $\mathbf{M}_{\text{oct},\alpha\beta}$  over all elementary octahedra

$$H = \frac{J}{2} \sum_{\text{oct}} \mathbf{M}_{\text{oct},\alpha\beta}^2, \quad (6.1)$$



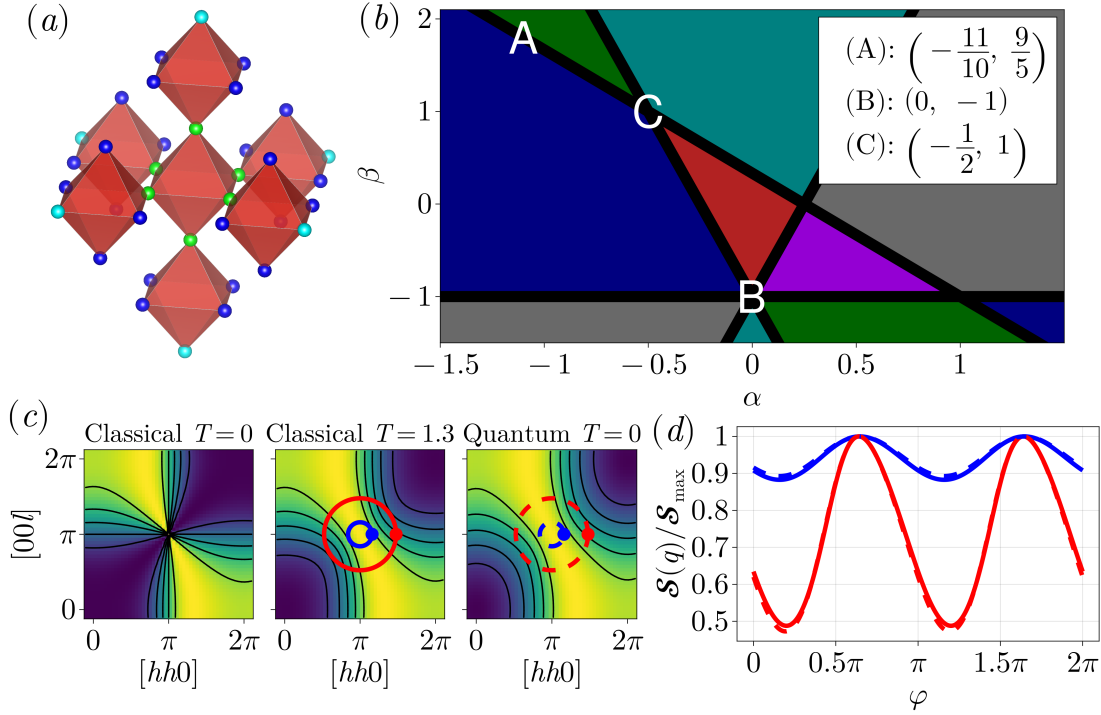


Figure 6.1.: (a) Octochlore model: Differently weighted sites in Eq. (6.2) are indicated by different colors. (b) Phase diagram of the model from Ref. [51]. The labels A, B, C [with parameters  $(\alpha, \beta)$  given in the inset] indicate the locations of multifold pinch points, quadratic pinch points and pinch lines as shown in Figs. 6.2, 6.3 and 6.5, respectively. (c) Spin structure factor of a twofold pinch point at  $\alpha = \beta = 0$  for the classical and quantum model. (d) Spin structure factor  $\mathcal{S}(\mathbf{q})$  along circular paths indicated in (c) normalized to their maxima.

where  $\mathbf{M}_{\text{oct},\alpha\beta}$  is the sum of spins in a cluster, weighted by dimensionless parameters  $\alpha, \beta$ ,

$$\mathbf{M}_{\text{oct},\alpha\beta} = \sum_{i \in \text{oct}} \mathbf{S}_i + \alpha \sum_{i \in \langle \text{oct} \rangle} \mathbf{S}_i + \beta \sum_{i \in \langle\langle \text{oct} \rangle\rangle} \mathbf{S}_i. \quad (6.2)$$

Here, a reference octahedron “oct” is given by the green sites in Fig. 6.1(a), while its closest surrounding sites “ $\langle \text{oct} \rangle$ ” and further distant sites “ $\langle\langle \text{oct} \rangle\rangle$ ” are colored blue and cyan, respectively. Henceforth, we set the energy scale such that the maximal Heisenberg coupling between two spins is equal to one.

For classical spins  $\mathbf{S}_i$ , the system’s extensively degenerate ground states follow from the constraints  $\mathbf{M}_{\text{oct},\alpha\beta} = 0$  which constitute discrete versions of Gauss’s law. These constraints can be expressed in reciprocal space as  $\sum_m L_m(\mathbf{q}) \mathbf{S}_m(\mathbf{q}) = 0$  [51], where  $m = 1, 2, 3$  label the sublattices,  $\mathbf{S}_m(\mathbf{q})$  is the Fourier-transformed spin on sublattice  $m$  and  $L_m(\mathbf{q})$  is the  $m$ -th component of the so-called constraint vector. Normalized constraint vectors  $\tilde{L}_m(\mathbf{q}) = L_m(\mathbf{q}) / \sqrt{\sum_n (L_n(\mathbf{q}))^2}$  can be defined over the entire  $\mathbf{q}$  space except at singular points  $\mathbf{q}^*$  where  $L_m(\mathbf{q}^*) = 0$  for all  $m$ . For isolated points  $\mathbf{q}^*$  in momentum space and with  $\tilde{L}_m(\mathbf{q})$  defined on the unit sphere  $S^2$  one can assign a topological index to the defect configuration  $\tilde{L}_m(\mathbf{q})$  around  $\mathbf{q}^*$  defined by the second homotopy group of  $S^2$ , which is the Skyrmion number  $Q$  [278, 279]. As demonstrated in Ref. [51] non-trivial  $Q \neq 0$  give rise to pinch points at  $\mathbf{q} = \mathbf{q}^*$  in the equal-time spin structure factor  $\mathcal{S}(\mathbf{q}) \equiv \langle \mathbf{S}(-\mathbf{q}) \cdot \mathbf{S}(\mathbf{q}) \rangle$ , where  $|Q| = 1$  is associated with twofold pinch points. Furthermore, expanding  $L_m(\mathbf{q})$  in powers of  $\mathbf{q}$  around  $\mathbf{q}^*$  reveals the underlying continuum gauge theory.

The number of such defects and their arrangement in the Brillouin zone yields a phase diagram spanned by  $\alpha$  and  $\beta$  featuring 10 distinct classical spin liquids, see Fig. 6.1(b). In particular, at points along the boundary [i.e., point A in Fig. 6.1(b)] multiple defects with  $Q = \pm 1$  merge, leading to a higher  $|Q| > 1$  associated with a tensor gauge theory and multifold pinch points, see Ref. [51]. In addition, we have identified even richer phenomena at crossing points of several phase boundaries: Point B in Fig. 6.1(b) displays a pinch point with purely parabolic contours, recently predicted to be a hallmark signature of type-II fracton phases [113], while point C features unusual, one-dimensional manifolds of pinch points, so-called pinch-lines [277].

### 6.3. Emergent gauge theories

As discussed in Ref. [51], the classical ground state constraint of the octochlore model can be written as

$$\sum_{i \in c} \eta_i \mathbf{S}_i = 0 \quad \forall c, \quad (6.3)$$

$$\eta_i = \begin{cases} 1, & i \in \text{oct} \\ \alpha, & i \in \langle \text{oct} \rangle \\ \beta, & i \in \langle \langle \text{oct} \rangle \rangle \end{cases}, \quad (6.4)$$

where  $c$  is the cluster of octahedra shown in Fig. 6.1(a). In reciprocal space, the constraint can be expressed using a constraint vector  $L_m(\mathbf{q})$

$$L_m(\mathbf{q}) = \sum_{i \in m \in c} \eta_i e^{i\mathbf{q}(\mathbf{r}_c - \mathbf{r}_i)} \quad (6.5)$$

$$\sum_{m=1}^{n_u} L_m^*(\mathbf{q}) \mathbf{S}_m(\mathbf{q}) = 0 \quad \forall \mathbf{q}, \quad (6.6)$$

where  $n_u = 3$  is the number of sites per unit cell,  $\mathbf{r}_c$  indicates the position of the center of the cluster  $c$  and  $\mathbf{r}_i$  the position of site  $i$ . As all spin components are equivalent, henceforth, we only consider the  $z$ -component. Even though the dimension of  $L_m$  is given by the number of sublattices and can in principle be of arbitrary dimension, here we shall label its three components as  $L_x, L_y, L_z$  for notational convenience. Equation (6.6) implies that the vector  $S_m^z$  is orthogonal to the constraint vector  $L_m(\mathbf{q})$ . Hence, the spin structure factor  $\mathcal{S}(\mathbf{q}) \equiv \frac{1}{n_u} \sum_{m,n} \langle S_m^z(-\mathbf{q}) S_n^z(\mathbf{q}) \rangle$  can be approximated at zero temperature by summing over all elements of the matrix projecting out  $\tilde{L}_m(\mathbf{q})$  [42, 51]. This explains the appearance of pinch points whenever  $L_m(\mathbf{q}) = \mathbf{0}$  and the projector becomes singular. The effective gauge theory is then given by expanding  $L_m(\mathbf{q})$  to leading order around the location of a pinch point  $\mathbf{q}^*$ , corresponding to a coarse graining of the system. If the lowest non-vanishing contribution is of first order, we obtain

$$\sum_m \sum_{\mu} \left. \frac{\partial L_m^*}{\partial \tilde{q}_{\mu}} \right|_{\tilde{\mathbf{q}}=0} \tilde{q}_{\mu} S_m^z(\tilde{\mathbf{q}}) \equiv \sum_{\mu} \tilde{q}_{\mu} E_{\mu}(\tilde{\mathbf{q}}) = 0, \quad (6.7)$$

where  $\tilde{\mathbf{q}} = \mathbf{q} - \mathbf{q}^*$ . This is a simple Gauss' law  $\nabla \cdot \mathbf{E} = 0$  in reciprocal space. The emergent gauge field  $E_{\mu}(\tilde{\mathbf{q}}) = \sum_m \left. \frac{\partial L_m^*}{\partial \tilde{q}_{\mu}} \right|_{\tilde{\mathbf{q}}=0} S_m^z(\tilde{\mathbf{q}})$  in this example is of rank-1 U(1) type. An interesting special case emerges when the gradient of the constraint vector also vanishes. In this case, the effective gauge field becomes a higher rank tensor which may depend on terms such as  $\frac{\partial^2 L_m^*}{\partial q_{\mu} \partial q_{\nu}}$ . We now consider more explicit

examples found on the octochlore model, for which the constraint vector can be written as

$$\mathbf{L}(\mathbf{q}) = \begin{pmatrix} 2 \cos\left(\frac{q_x}{2}\right) [2\alpha(\cos(q_y) + \cos(q_z)) + 2\beta \cos(q_x) + 1 - \beta] \\ 2 \cos\left(\frac{q_y}{2}\right) [2\alpha(\cos(q_x) + \cos(q_z)) + 2\beta \cos(q_y) + 1 - \beta] \\ 2 \cos\left(\frac{q_z}{2}\right) [2\alpha(\cos(q_x) + \cos(q_y)) + 2\beta \cos(q_z) + 1 - \beta] \end{pmatrix}. \quad (6.8)$$

## 6.4. Twofold pinch points

We start with a brief discussion of more conventional twofold pinch points with  $|Q| = 1$ , occurring in the bulk of every phase of Fig. 6.1(b) and previously featured in Chapter 5. At the pinch point positions  $\mathbf{q} = \mathbf{q}^*$ , the lowest non-vanishing term in an expansion of  $L_m(\mathbf{q})$  is the linear one, and hence, the emergent continuum Gauss law has the linear form  $\nabla \cdot \mathbf{E}(\mathbf{r}) = \mathbf{q} \cdot \mathbf{E}(\mathbf{q}) = 0$  where  $\mathbf{E}(\mathbf{q}) = \sum_m S_m^z(\mathbf{q}) \partial_{\mathbf{q}} L_m(\mathbf{q})$ <sup>1</sup>. First, consider the simple special case  $\alpha = \beta = 0$ . In this case we have  $\mathbf{L} = 2(\cos(q_x/2), \cos(q_y/2), \cos(q_z/2))$  which vanishes only at the pinch point  $q^* = (\pi, \pi, \pi)$  (and equivalent positions). Here, we find  $\partial_{q_\mu} L_m(\mathbf{q}^*) = -\delta_{\mu m}$ , i.e., the underlying gauge structure can be described by an emergent rank-1 gauge field, as expected.

Under the influence of quantum fluctuations at  $T = 0$  in the  $S = 1/2$  case treated with PFFRG, twofold pinch points show the typical broadening illustrated in Fig. 6.1(c) for the case  $\alpha = \beta = 0$ , while the overall pinch point shape stays rather intact. In particular, we observe the effects of quantum fluctuations to be analogous to those at a finite temperature  $T \sim 1.3$ . This broadening indicates violations of the ice rule constraint, and is expected as the absolute spin magnitudes  $\mathbf{M}_{\text{oct},\alpha\beta}^2$  of neighboring octahedra do not mutually commute and thus fluctuate, i.e.,  $\langle \mathbf{M}_{\text{oct},\alpha\beta}^2 \rangle \neq 0$ . Importantly, the signal at  $\mathbf{q} = \mathbf{q}^*$  remains strong and no indications for magnetic long-range order are observed in the full  $\alpha$ - $\beta$  plane [42]. We find these observations to be in direct analogy with past studies of the closely related nearest neighbor pyrochlore Heisenberg model [2, 8, 150, 165, 257, 260, 262, 263, 280].

---

<sup>1</sup>Derivatives here are taken at  $\mathbf{q} = \mathbf{q}^*$  and  $\mathbf{q}$  is meant to be the momentum relative to  $\mathbf{q}^*$ . Furthermore, since the different spin components  $\mu = x, y, z$  do not couple in the spin constraint, one may restrict to the  $z$ -component without loss of generality.

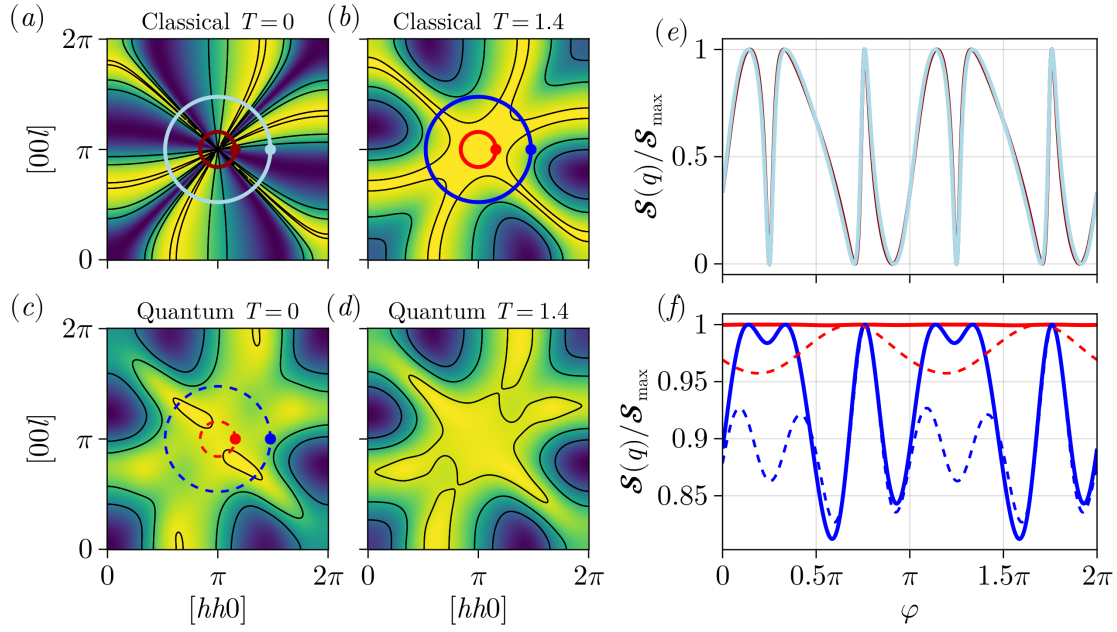


Figure 6.2.: (a-d): Spin structure factor  $\mathcal{S}(\mathbf{q})$  in the  $hhl$ -plane for a multifold  $Q = -7$  pinch point found at location A ( $\alpha = -\frac{11}{10}$ ,  $\beta = \frac{9}{5}$ ) in the phase diagram of Fig. 6.1. (e):  $\mathcal{S}(\mathbf{q})$  for the two paths indicated in (a), normalized to its maximum value along each path. (f): As in (e) but comparing classical thermal and quantum fluctuations along the paths in (b) and (c). The paths are counterclockwise and the start point  $\varphi = 0$  is indicated by a marker.

## 6.5. Multifold pinch points

A vanishing linear term in an expansion of  $L_m(\mathbf{q})$  around  $\mathbf{q} = \mathbf{q}^*$  is associated with multifold pinch points [51, 117, 266]. An instructive example occurs at  $\alpha = -11/10$ ,  $\beta = 9/5$  and  $\mathbf{q}^* = (\pi, \pi, \pi)$ , with a topological index  $Q = -7$  and six lobes of large intensity in the  $hhl$  plane, see Fig. 6.2(a) and Ref. [51]. We identify a gauge constraint of third rank  $\sum_{\mu\nu\sigma} q_\mu q_\nu q_\sigma E_{\mu\nu\sigma}(\mathbf{q}) = 0$  where  $E_{\mu\nu\rho}(\mathbf{q}) = \sum_m S_m^z(\mathbf{q}) \partial_{q_\mu} \partial_{q_\nu} \partial_{q_\rho} L_m(\mathbf{q})$ , implying conserved scalar charge, dipole and quadrupole moments.

### Fourfold pinch points

For  $\alpha = 0, \beta = -1$ ,  $\mathbf{L}(\mathbf{q})$  simplifies to

$$\mathbf{L}(\mathbf{q}) = \begin{pmatrix} 4 \cos\left(\frac{q_x}{2}\right) (1 - \cos(q_x)) \\ 4 \cos\left(\frac{q_y}{2}\right) (1 - \cos(q_y)) \\ 4 \cos\left(\frac{q_z}{2}\right) (1 - \cos(q_z)) \end{pmatrix}. \quad (6.9)$$

We find that all components of  $\mathbf{L}(\mathbf{q})$  and its first derivatives vanish at  $\mathbf{q}^* = (0, 0, 0)$ . The first nonzero contributions are all of second order

$$\partial_{q_\mu} \partial_{q_\nu} L_m \Big|_{\mathbf{q}=\mathbf{q}^*} = 4\delta_{\mu\nu} \delta_{\mu m} \quad (6.10)$$

As the underlying gauge field is a rank-2 tensor  $E_{\mu\nu}(\mathbf{q}) = 4\delta_{\mu\nu} S_\mu^z(\mathbf{q})$ , the structure factor displays a fourfold pinch point. A gauge theory of this form  $\partial_\mu \partial_\nu E_{\mu\nu} = 0$  implies the existence of quasiparticle excitations with conserved dipole moment [103, 117]. so-called *fractons* are thus immobile unless grouped together to form pairs or larger clusters. The effect of quantum fluctuations is seen to be rather similar to multifold pinch points, and shall be discussed in the following<sup>2</sup>.

---

<sup>2</sup>A more detailed discussion of fracton spin liquids in relation to fourfold pinch points will follow in Chapter 7.

## Multifold pinch point

At  $\alpha = -11/10, \beta = 9/5$ , an even higher rank gauge theory of the form  $\partial_\mu \partial_\nu \partial_\rho E_{\mu\nu\rho} = 0$  emerges, since both the first and the second order derivatives of the constraint vector vanish at the pinch point  $\mathbf{q}^* = (\pi, \pi, \pi)$ . Explicitly, we find for the first component of the constraint vector

$$\begin{aligned}\partial_{q_x}^3 L_x(\mathbf{q}^*) &= -54/5, \\ \partial_{q_x} \partial_{q_y}^2 L_x(\mathbf{q}^*) &= \partial_{q_x} \partial_{q_z}^2 L_x(\mathbf{q}^*) = 11/5,\end{aligned}\tag{6.11}$$

while other derivatives such as  $\partial_{q_x}^2 \partial_{q_y} L_x(\mathbf{q}^*)$  are zero. Consequently, not only monopole and dipole moments, but also the quadrupole moment are conserved. This feature is characterized by a skyrmion winding number of  $Q = -7$  and displays a sixfold pinch point when cut through the  $hhl$  plane. Figure 6.2 shows the impact of both quantum and thermal fluctuations on this multifold pinch point. The value of  $\mathcal{S}(\mathbf{q})$  along circular paths around the pinch point illustrates the presence of the singularity: For the exact gauge theory in the classical  $T = 0$  model, it retains the same strong angular dependence for arbitrarily small radii, see Fig. 6.2(e). Thermal fluctuations induce a rather featureless broadening and the angular dependence of the signal vanishes at small distances from the pinch point, see full red line in Fig. 6.2(f). Interestingly, the effects of quantum fluctuations are very different. In addition to a broadening, quantum fluctuations add a shift of spectral weight away from the pinch point origin in favor of soft maxima at incommensurate positions, effectively tearing apart the pinch point. It is noted that this observation stands in stark contrast to the case of twofold pinch points shown in Fig. 6.1(c), for which quantum fluctuations appear to act similarly to thermal ones.

In order to physically interpret the data in Fig. 6.2, two types of quantum effects need to be distinguished. First, the aforementioned broadening of pinch points rather indicates the destruction of the underlying gauge theory. However, a second well-known quantum effect consistent with a gauge theory is the formation of gapless photon modes with dispersion  $\omega(\mathbf{q})$ , resulting from an emergent conjugate vector potential  $A(\mathbf{r})$ . These photon modes give rise to an extra factor  $\omega(\mathbf{q})$  in the spin structure factor (i.e.,  $\mathcal{S}(\mathbf{q}) \rightarrow \omega(\mathbf{q})\mathcal{S}(\mathbf{q})$ ) suppressing the signal at the singularity due to  $\omega(\mathbf{q}^*) = 0$  [68, 113, 117]. To test whether the weight distribution in Fig. 6.2(c) contains possible signatures of such a modulation, we note that the mere multiplication of an exact pinch point with an isotropic factor  $\omega(\mathbf{q}) \sim |\mathbf{q} - \mathbf{q}^*|^\gamma$  (or, for that matter, **any** function  $\omega(|\mathbf{q} - \mathbf{q}^*|)$ )<sup>3</sup> leaves the sin-

<sup>3</sup>In the most common types of  $U(1)$  gauge theories including rank-1 and rank-2 versions the

gularity intact such that  $\mathcal{S}(\mathbf{q})$  along rings around the pinch point, normalized to its maximum on each path, would remain unchanged upon decreasing the radius of the rings. However, the dashed red and blue graphs in Fig. 6.2(f) illustrating the normalized signal along the ring-like paths in Fig. 6.2(c) are qualitatively very different and, hence, these results seem incompatible with an emergent photon mode. While it is possible that the ground state is described by a different gauge theory (i.e., with an emergent electric field given by a more complex function of spin operators), it is questionable whether fractonic phenomena that have been associated with these spectroscopic features still occur in the  $S = 1/2$  limit of the Heisenberg model.

## 6.6. Quadratic pinch points

A further generalization occurs if the gauge constraint contains derivatives of different orders as is characteristic for multipolar gauge theories describing type-II fracton phases. This gives rise to quadratic pinch points in the spin structure factor where lobes of strong intensity follow contour lines of the form  $q_{\parallel} \propto a q_{\perp}^2$  with  $q_{\parallel}$  and  $q_{\perp}$  being two perpendicular momentum space directions and  $a$  is the lattice constant (which is set to one here). The mixing of derivatives causes the lattice constant to explicitly appear in these spectroscopic patterns which is a direct manifestation of the ultraviolet-infrared mixing described in recent literature [113].

At  $(\alpha = 0, \beta = -1)$ , a pinch point with purely parabolic contours can be found at  $\mathbf{q}^* = (0, 0, \pi)$ . As pointed out by Hart et. al. in Ref. [113], such a pinch point can be a signature of a type-II fractonic phase. Indeed, we verify that for the present case,  $\mathbf{L}$  has a nonzero first derivative only in the  $q_z$  direction. For systems with emergent photon excitations, a similar suppression is also observed [68]. Here, the structure factor simply acquires a prefactor from the dispersion of a photon with the speed of light  $c$ .  $\omega(\tilde{\mathbf{q}}) = c\sqrt{\tilde{q}_z^2 + (\tilde{q}_x^2 + \tilde{q}_y^2)^2}$ , where [68]

$$\mathcal{S}(\tilde{\mathbf{q}}) \rightarrow \omega(\tilde{\mathbf{q}}) \coth\left(\frac{\omega(\tilde{\mathbf{q}})}{2T}\right) \mathcal{S}(\tilde{\mathbf{q}}). \quad (6.12)$$

In Fig. 6.4, the effect of such a modification is considered in comparison to the findings from PFFRG. The resulting structure factors are clearly qualitatively

---

photon dispersion is linear, i.e.,  $\gamma = 1$ , as long as charges are scalar [117].



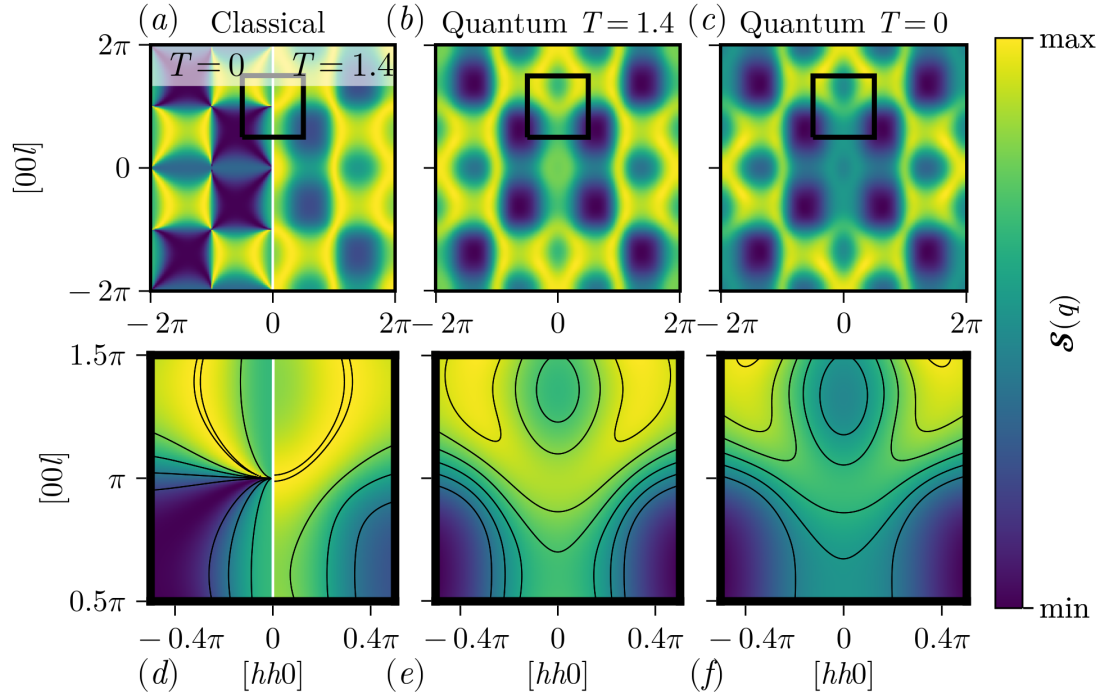


Figure 6.3.: Pinch point with parabolic contours in the  $hhl$ -plane found at point B ( $\alpha = 0, \beta = -1$ ). (a): Classical large- $N$  result for temperatures  $T = 0$  (left half) and  $T = 1.4$  (right half). (b) Quantum model at  $T = 1.4$  and (c) at  $T = 0$  obtained from PMFRG and PFRG in the low cutoff limit, respectively. (d-f): Magnifications of the regions indicated by black squares in the upper panel together with black contour lines.

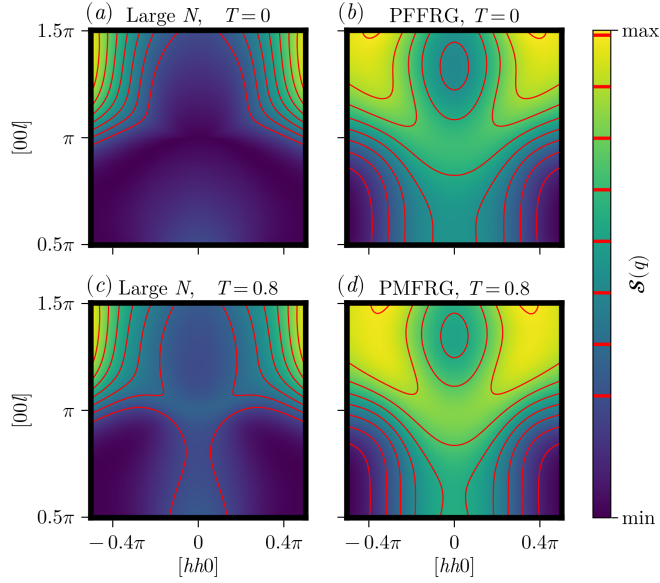


Figure 6.4.: **Quadratic pinch point at  $T = 0$  and  $T = 0.8$ .** Dispersion-corrected structure factor  $\mathcal{S}(\mathbf{q})$  obtained from large  $N$  and Eq. (6.12) in (a) and (c) in comparison of to PFFRG (b) and PMFRG (d).

distinct. While PFFRG is formally employed at zero temperature, the influence of its finite cutoff is often similar to a finite temperature. To investigate this possibility, a rough estimate of the structure factor can be obtained from large  $N$  at finite temperature by applying the correction from the photon dispersion in Eq. (6.12). Assuming that  $c = 1$  (in units of the normalized lattice constant and energy scale), the result is shown in panel (c) of Fig. 6.4. As in the case of quantum spin ice, this returns some spectral weight back to the pinch point. Although the intensity at the pinch point depends on microscopic details such as the value of  $c$ , we notice that the position of the maxima remains indifferent, following the original parabolic contour. This contrasts our numerical observations so that the presence of emergent photons remains unlikely.

Strikingly, such quadratic pinch points can be found in the classical octochlore model at  $\alpha = 0$ ,  $\beta = -1$  and  $\mathbf{q}^* = (0, 0, \pi)$ . The effective gauge theory in this case contains first derivatives along the  $z$ -direction, as  $\partial_{q_z} L_3(\mathbf{q}) \neq 0$ , while for the perpendicular  $x, y$  directions  $\partial_{q_x} L_m(\mathbf{q}) = \partial_{q_y} L_m(\mathbf{q}) = 0$  for  $m = 1, 2, 3$  and the lowest non-vanishing contribution comes from second derivatives. Indeed, it can be verified that for the present case,  $\mathbf{L}$  has a nonzero first derivative only in the  $q_z$

direction:

$$\partial_{q_\mu} L_m(\mathbf{q}) \Big|_{\mathbf{q}=\mathbf{q}^*} = \begin{cases} -4 & \mu = m = z \\ 0 & \text{else} \end{cases} \quad (6.13)$$

$$\partial_{q_\mu} \partial_{q_\nu} L_m(\mathbf{q}) \Big|_{\mathbf{q}=\mathbf{q}^*} = \begin{cases} 4 & \mu = \nu = m \text{ and } m = x, y \\ 0 & \text{else} \end{cases} . \quad (6.14)$$

The resulting quadratic pinch point in classical large- $N$  [Fig. 6.3(d)] has a shape which is similar to predictions from the U(1) Haah code [113]. The effect of finite temperatures in large- $N$  only amounts to a broadening near  $\mathbf{q}^*$  while retaining the quadratic shape and the strong signal around  $\mathbf{q}^*$ . This is to be contrasted with PMFRG at the same temperature where the signal is reduced near  $\mathbf{q}^*$  and quadratic contours are no longer discernible. This trend continues down to  $T = 0$  where the spin-structure factor appears even more strongly reduced around  $\mathbf{q}^*$ . Again however, this result seems incompatible with emergent photons, see Fig. 6.4.

## 6.7. Pinch-lines

As mentioned before, singularities in the structure factor are present at points  $\mathbf{q}^*$  where  $L_m(\mathbf{q}^*) = 0$ . Inspecting Eq. (6.8), we immediately observe that a pinch point can always be found at  $(\pi, \pi, \pi)$ , where the prefactors  $\cos(q_\mu/2)$  vanish. Other pinch points emerge at more complicated positions determined by a delicate balance between the parameters  $\alpha, \beta$  and the wavevector  $\mathbf{q}$ . This situation has previously been studied in Ref. [277] where the phenomenon has been dubbed a pinch line. Such patterns exhibit conventional twofold pinch points in all planar cuts through the pinch line. For the classical pyrochlore model investigated in Ref. [277] an underlying gauge constraint linear in the derivatives but with a tensor structure has been identified and a possible relevance for the pyrochlore material  $\text{Tb}_2\text{Ti}_2\text{O}_7$  [71] has been pointed out.

An analogous feature is found in the octochlore model at  $\alpha = -\frac{1}{2}$  and  $\beta = 1$  where pinch lines run along [111] and symmetry related directions in momentum space. The lowest non-vanishing derivatives of  $L_m(\mathbf{q})$  at  $\mathbf{q}^*$  are first order derivatives perpendicular to the pinch lines, in agreement with the pyrochlore model of Ref. [277]. Since the topological defect is now line-like and observing that the normalized constraint vector  $\tilde{L}_m(\mathbf{q})$  avoids two opposite points on the unit sphere  $S^2$ ,

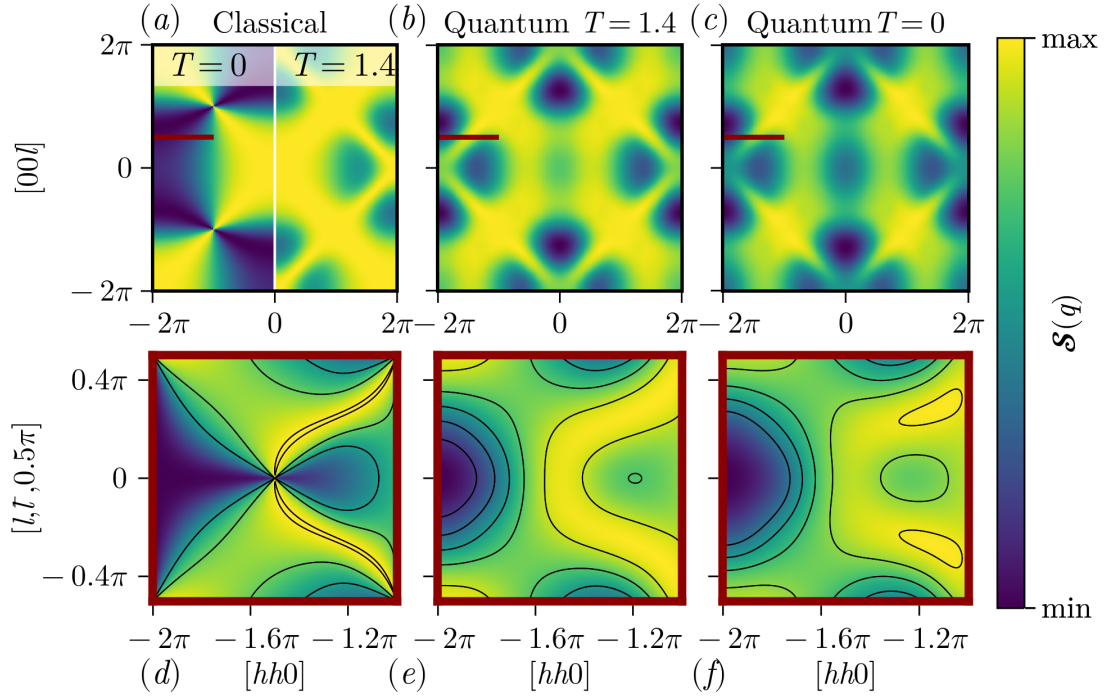


Figure 6.5.: (a-c): Temperature dependent spin structure factor for a pinch line at  $\alpha = -\frac{1}{2}$ ,  $\beta = 1$  [C in Fig. 6.1(b)] in the [111] direction. Panels (d-f) show a cut through the pinch line, here given by  $q_z = 0.5\pi$  as indicated by the solid dark red line in panels (a-c).

see Fig. 6.6, the topological index is given by the integer vortex winding number  $w$ . We find  $|w| = 1$  and consequently, twofold pinch points in planar cuts through the line defect, see bottom panel of Fig. 6.5 depicting cuts at  $q_z = 0.5\pi$ . Thermal fluctuations in the classical model [Fig. 6.5(a), right] shift spectral weight towards the pinch lines such that they become visible in the  $hhl$  plane as well defined, broadened lines of constant strong signal. In the generic case, for a fixed set of  $\alpha, \beta$ , the requirement that all three components of  $\mathbf{L}$  have to vanish leads to three equations, determining the positions of the pinch points  $\mathbf{q}^*$  uniquely (up to point group symmetries). However, for appropriate  $\alpha$  and  $\beta$ , one or more components can become equivalent, leading to a line-like manifold of singularities.

The location of the pinch point feature can be found by setting  $q_z = \pi$ , such that  $L_z = 0$ . One can see that whenever  $q_x = q_y$ , the first two components of  $L_m$  become equivalent:

$$\mathbf{L} = \begin{pmatrix} 2 \cos\left(\frac{q_x}{2}\right) [\cos(q_x)(2\alpha + 2\beta) + 1 - 2\alpha - \beta] \\ 2 \cos\left(\frac{q_x}{2}\right) [\cos(q_x)(2\alpha + 2\beta) + 1 - 2\alpha - \beta] \\ 0 \end{pmatrix} \quad (6.15)$$

These two components vanish for all  $q_x = q_y$  for  $\alpha = -\beta = 1$ , resulting in a line of pinch points, or pinch-line. This pinch line can be characterized by a topological, winding number. Here,  $\tilde{L}_m(\mathbf{q}) = L_m(\mathbf{q})/\sqrt{\sum_n L_n^2(\mathbf{q})}$  is traced on the unit sphere as one moves along a closed loop around the pinch line. Since the corresponding paths on the unit sphere avoid two opposite poles (see Fig. 6.6), the topological index can be defined as the corresponding winding number. For each point on the pinch line, the winding number takes the same integer value as long as the loop does not contain or intersect any other pinch point (where  $\tilde{L}(\mathbf{q})$  is singular).

## 6.8. Discussion

The classical octochlore model is identified as an exquisite physical platform for studying exotic spectroscopic features, such as multifold and quadratic pinch points as well as pinch lines, all associated with unconventional gauge theories. Numerical studies which systematically investigate the impact of quantum fluctuations on the corresponding classical spin liquids are, however, lacking so far. In the endeavor to fill this gap, the quantum spin  $S = 1/2$  model is treated by employing state-of-the-art PFFRG and PMFRG methods. A recurring theme is found in these results: Multifold pinch points, quadratic pinch points and pinch lines all undergo

a significantly different modification under quantum fluctuations than conventional twofold pinch points, showing a reduction of  $\mathcal{S}(\mathbf{q})$  at  $\mathbf{q}^*$  that is also at variance compared to the effects of pure thermal fluctuations in the classical case. This also implies that the absence of unconventional pinch points in an experimentally measured spin structure factor does not necessarily exclude the realization of a higher-rank  $U(1)$  gauge theory in the corresponding classical system.

From a methodological perspective, here, we benefit from the fact that the octochlore model has  $SU(2)$  spin symmetry which simplifies the application of PFFRG and PMFRG enormously. A (numerically more challenging) continuation of the present work could be to lift the  $SU(2)$  symmetry by considering an Ising version of the octochlore model supplemented with small transverse couplings, thus realizing an analogous situation as in quantum spin ice models. This will help identifying the fate of exotic pinch point singularities along a continuous classical-to-quantum interpolation. These results strongly motivate new avenues in the investigations of these exotic pinch points under quantum fluctuations, which appear to have a more significant impact compared to twofold-pinch points. Furthermore, this work sets the stage for determining the microscopic wave functions describing these resulting quantum phases, and whose correlation functions give rise to the static structure factors obtained here [198].

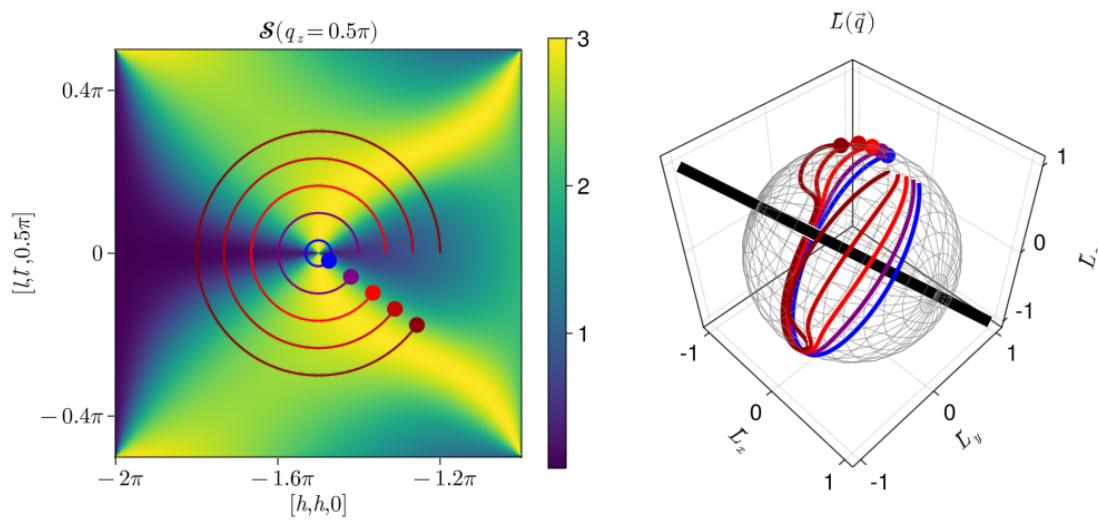


Figure 6.6.: **Vortex winding number for pinch line.** Left: Spin structure factor from large- $N$  at  $T = 0$  in a cut through the pinch line, with loops of different radius. Right: For each loop, the normalized constraint vector describes a path winding once around the same axis. Sufficiently close to the pinch point, this path is of circular shape.





## Fracton phase in a square lattice model

In the previous chapter, we explored how quantum fluctuations behave in a model known to exhibit a variety of exotic emergent gauge fields, including two types of fracton phases. In all cases, it was found that little remains of the features known to herald fractonic behavior, instead giving rise to rather complicated physics certainly out of scope for most approaches. This is not entirely surprising given the rather drastic differences between the classical and quantum Heisenberg models: Due to the noncommuting nature of spin operators, ice rule states, posing as classical ground states, are no longer a valid starting point for finding the quantum ground state as the charges  $\mathbf{M}_{\text{oct},\alpha\beta}^2$  are no longer well-defined quantum numbers.

On the other hand, one may want to consider a more gentle and controlled way to introduce quantum fluctuations into the classically degenerate ground state manifold by starting from a classical Ising model in which the charge excitations are gapped. In this case, small quantum fluctuations, e.g. introduced by couplings between transverse spin components  $S^{x,y}$ , will not be able to destroy this gap, while allowing fluctuations between the classically degenerate ground states. While this is certainly possible, the rather complicated nature of the interactions in the previously introduced octochlore model poses some challenges to this approach. In this chapter, we will therefore begin by constructing a more minimal model to aid our analysis.

### 7.1. Construction of a classical fracton model

While the model presented in Chapter 6 follows a very general construction that can be applied to other geometries such as the two-dimensional Honeycomb lattice [51], the constraints constructed in this way will typically involve many sites imposing additional restrictions on the dynamics of fractons and posing challenges to the study of even classical models [101]. As a result, here we consider a different approach which is to start directly from the desired gauge theory and discretize it on a square lattice to arrive at a spin model. The simplest model which nonetheless will classically exhibit a fracton phase will be a gauge theory with a rank-2

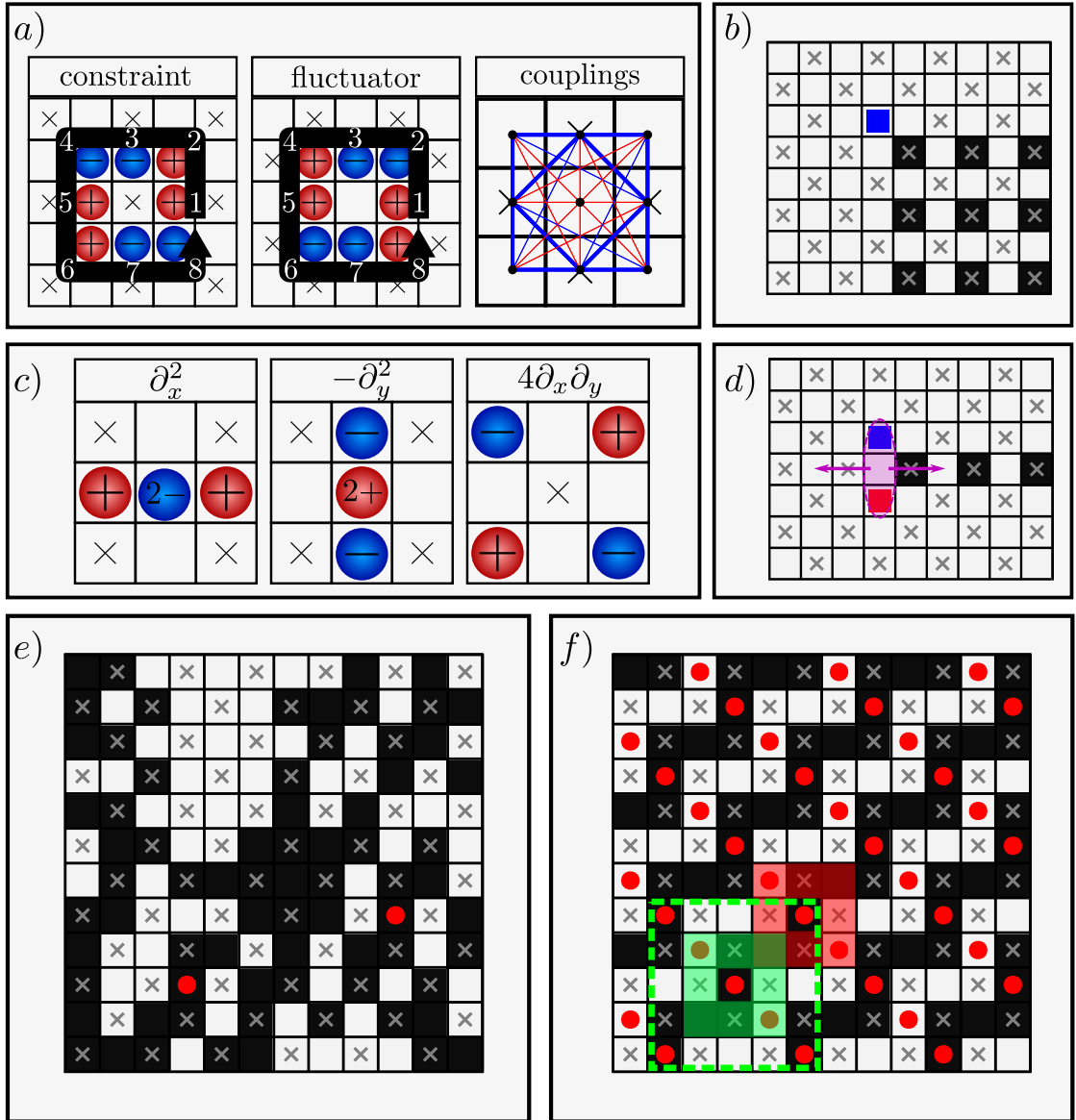


Figure 7.1.: Spiderweb model and its elementary excitations. a): The ground state constraint and the fluctuator are only defined on separate  $\times$  sublattices. The couplings for the model are obtained by squaring the constraint. Red (blue) couplings are  $J_{ij} = -1$  ( $J_{ij} = +1$ ), while thick lines correspond to an interaction  $|J_{ij}| = 2$ . b): Isolated, immobile fracton occurring on a domain between two different ground state patterns. c): Derivative operators discretized on the lattice from a). d): A Lineon, a pair of fractons, which can move along a single dimension. e): A generic ground state with two plaquettes where the fluctuator can be applied, indicated by red dots. f): The periodic *staircase state*, featuring the highest density of flippable plaquettes. Flipping the plaquette highlighted in green renders all other plaquettes in its vicinity (dashed green line) *unflippable*, such as the one highlighted in red.

tensor gauge field  $E^{\mu\nu}$ , where  $\mu, \nu = x, y$  such that  $E^{\mu\nu}$  is traceless ( $E^{xx} = -E^{yy}$ ) and symmetric ( $E^{xy} = E^{yx}$ ) [105]

$$\partial_\mu \partial_\nu E^{\mu\nu} = (\partial_x^2 - \partial_y^2) E^{xx} + 2\partial_x \partial_y E^{xy} = \rho. \quad (7.1)$$

Ultimately, we will replace the gauge field by localized spin degrees of freedom  $E^{\mu\nu}(\mathbf{r}) \rightarrow S_i^z$ , such that the derivatives are replaced by finite differences. On a square lattice with unit vectors of length 1, the derivatives in Eq. (7.1) acting on an arbitrary scalar field  $f(y)$  are discretized as

$$\begin{aligned} \partial_x^2 f(y) &\rightarrow f\left(\frac{x-1}{y}\right) - 2f\left(\frac{x}{y}\right) + f\left(\frac{x+1}{y}\right) \\ \partial_y^2 f(x) &\rightarrow f\left(\frac{x}{y-1}\right) - 2f\left(\frac{x}{y}\right) + f\left(\frac{x}{y+1}\right) \\ \partial_x \partial_y f(x) &\rightarrow \frac{f\left(\frac{x+1}{y+1}\right) - f\left(\frac{x-1}{y+1}\right) - f\left(\frac{x+1}{y-1}\right) + f\left(\frac{x-1}{y-1}\right)}{4}. \end{aligned} \quad (7.2)$$

Further, we need to associate each of the two independent components of the tensor with its own sublattice, absorbing the factor of 2 in Eq. (7.1) for convenience.

$$S_2^z(\mathbf{q}) = E^{xx}(\mathbf{q}) \quad (7.3)$$

$$2S_1^z(\mathbf{q}) = E^{xy}(\mathbf{q}). \quad (7.4)$$

Combining Eqs. (7.1), (7.2) and (7.4), we obtain a constraint corresponding to a discrete form of the desired gauge theory

$$S_{\boxplus_1}^z + S_{\boxplus_2}^z - S_{\boxplus_3}^z - S_{\boxplus_4}^z + S_{\boxplus_5}^z + S_{\boxplus_6}^z - S_{\boxplus_7}^z - S_{\boxplus_8}^z = 0, \quad (7.5)$$

where  $\boxplus$  corresponds to a cluster of sites centered around a sublattice 1 site, and the labels 1, . . . 8 enumerate its sites in counterclockwise fashion as shown in Fig. 7.1(a). We can easily define a classical Ising Hamiltonian whose ground states fulfill Eq. (7.5), by squaring over all constraints

$$\mathcal{H}_1 = \frac{J}{2} \sum_{\boxplus} \mathcal{C}_{\boxplus}^2 \quad (7.6)$$

$$\mathcal{C}_{\boxplus} = S_{\boxplus_1}^z + S_{\boxplus_2}^z - S_{\boxplus_3}^z - S_{\boxplus_4}^z + S_{\boxplus_5}^z + S_{\boxplus_6}^z - S_{\boxplus_7}^z - S_{\boxplus_8}^z. \quad (7.7)$$

Expanding the squares in  $\mathcal{H}_1$  leads to a network of spin interactions up to 5th neighbors on the square lattice, which, on each cluster  $\boxplus$ , resembles a spiderweb, see Fig. 7.1a). Henceforth, this model will thus be referred to as the *spiderweb model*. Before we move on to consider the effects of quantum fluctuations, we will first discuss the properties of the classical model.

## 7.2. Gaussian approximation of the classical model

We start by writing the ground state constraint defined in Eq. (7.5) as  $\mathcal{C}_{\boxplus} = \sum_{a=1}^8 \sigma_{\boxplus_a} S_{\boxplus_a}^z = 0$ , where  $\sigma_{\boxplus_a} \in \{+1, -1\}$  [see Fig. 7.1(a)]. In momentum space, this becomes

$$\sum_{m=1}^2 L_m^*(\mathbf{q}) S_m^z(\mathbf{q}) = 0, \quad (7.8)$$

where

$$\begin{aligned} L_1(\mathbf{q}) &= \sum_{a=2,4,6,8} \sigma_{\boxplus_a} e^{i\mathbf{q} \cdot \mathbf{r}_{\boxplus_a}} = -4 \sin q_x \sin q_y, \\ L_2(\mathbf{q}) &= \sum_{a=1,3,5,7} \sigma_{\boxplus_a} e^{i\mathbf{q} \cdot \mathbf{r}_{\boxplus_a}} = 2(\cos q_x - \cos q_y). \end{aligned} \quad (7.9)$$

Here,  $\mathbf{r}_{\boxplus_a}$  is the real space position of a site  $i$ , located relative to the center of a cluster  $\boxplus$  in the direction specified by the number  $a = 1, \dots, 8$  as shown in Fig. 7.1(a).

The constraint in the form of Eq. (7.8) implies that the Fourier components  $(S_1^z(\mathbf{q}), S_2^z(\mathbf{q}))$  of the ground state spin configurations must be ‘perpendicular’ to the vector  $(L_1(\mathbf{q}), L_2(\mathbf{q}))$  at each point in reciprocal space. The spin normalization constraint  $(S_i^z)^2 = 1/4$  is in practice difficult to enforce in this momentum space description and is instead approximated by an averaged one

$$\sum_i (S_i^z)^2 = 2 \sum_{\mathbf{q}, m} S_m^z(\mathbf{q}) S_m^z(-\mathbf{q}) / N_{\text{sites}} = N_{\text{sites}} / 4. \quad (7.10)$$

With this approximation, the model becomes a classical Gaussian theory subject to a single (global) constraint, in particular fully equivalent to the formalism outlined in Section 1.3. The spin structure factor  $\mathcal{S}(\mathbf{q})$  can then be obtained by projecting out all Fourier components ‘parallel’ to  $(L_1(\mathbf{q}), L_2(\mathbf{q}))$ :

$$\begin{aligned} \mathcal{S}(\mathbf{q}) &\equiv \sum_{mn} \langle S_m^z(-\mathbf{q}) S_n^z(\mathbf{q}) \rangle \\ &= \sum_{mn} \left( \delta_{mn} - \frac{L_m(\mathbf{q}) L_n(\mathbf{q})}{L_1^2(\mathbf{q}) + L_2^2(\mathbf{q})} \right) \\ &= \frac{(c_x - c_y + 2s_x s_y)^2}{(c_x - c_y)^2 + 4s_x^2 s_y^2} \end{aligned} \quad (7.11)$$

where we use the shorthand notation  $c_\mu = \cos q_\mu$ ,  $s_\mu = \sin q_\mu$  with  $\mu = x, y$ . The resulting structure factor is shown in panel a) of Fig. 7.3. Note that the average spin constraint in Eq. (7.10) simply amounts to a normalization of the

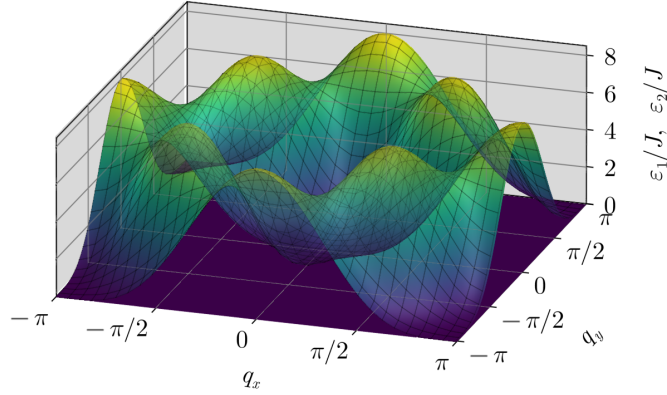


Figure 7.2.: Band structure of  $\mathcal{H}_1$  in Gaussian approximation with a flat lower band, dispersive upper band, and quartic band touching points at  $\mathbf{q} = (0, 0)$  and  $\mathbf{q} = (\pi, \pi)$ .

spin structure factor by the size of the Brillouin zone, i.e.,  $4/N_{\text{sites}}$ . A known property of this description is that the spin structure factor is non-analytic at points in momentum space where  $(L_1(\mathbf{q}), L_2(\mathbf{q})) = 0$ , giving rise to pinch points indicating an emergent gauge theory [51]. In this case,  $(L_1(\mathbf{q}), L_2(\mathbf{q})) = 0$  for  $\mathbf{q} = (0, 0)$  and  $\mathbf{q} = (\pi, \pi)$ . Especially, since also the *linear* terms in  $\mathbf{q}$  vanish at these two points, i.e.,  $\partial_\mu(L_1(\mathbf{q}), L_2(\mathbf{q})) = 0$  for  $\mu = x, y$ , the pinch points are four-fold [see Fig. 7.3(a)], as is characteristic for a rank-2 gauge theory [117].

An alternative way of discussing these properties is by diagonalizing  $\mathcal{H}_1$  in the space of the Fourier components  $S_1^z(\mathbf{q})$  and  $S_2^z(\mathbf{q})$ . Using that  $\mathcal{H}_1$  can be written as

$$\mathcal{H}_1 = \frac{J}{2} \sum_{\mathbf{q}, m, n} S_m^z(-\mathbf{q}) L_m(-\mathbf{q}) L_n(\mathbf{q}) S_n^z(\mathbf{q}), \quad (7.12)$$

this amounts to diagonalizing the  $2 \times 2$  matrix

$$H_{mn} = \frac{J}{2} L_m(-\mathbf{q}) L_n(\mathbf{q}), \quad (7.13)$$

which, due to its simple projector-like form, has eigenvalues  $\epsilon_1 = 0$  and  $\epsilon_2 = J(L_1^2(\mathbf{q}) + L_2^2(\mathbf{q}))/2$ . These eigenvalues, shown in Fig. 7.2, form a bottom flat band and a higher dispersive band with a band touching point at  $\mathbf{q} = (0, 0)$  and  $\mathbf{q} = (\pi, \pi)$ . Particularly, as a consequence of the quadratic behavior of  $L_1(\mathbf{q})$  and  $L_2(\mathbf{q})$  around these points, the band touching is of *quartic* type.

Crucially, expanding the constraint in momentum space around  $\mathbf{q} = 0$ , the lowest non-vanishing contribution arises in *quadratic* order  $\mathbf{q}$ . With this property,  $\mathcal{H}_1$  describes an *algebraic* classical spin liquid according to the classification principle in Ref. [52]. Setting  $2S_1^z(\mathbf{q}) = E^{xy}(\mathbf{q})$  and  $S_2^z(\mathbf{q}) = E^{xx}(\mathbf{q})$ , the constraint in Eq. (7.8) in lowest non-vanishing order in  $\mathbf{q}$  becomes

$$q_\mu q_\nu E^{\mu\nu}(\mathbf{q}) = 0 \text{ or } \partial_\mu \partial_\nu E^{\mu\nu}(\mathbf{r}) = 0. \quad (7.14)$$

Here, the right equation is the real-space continuum version of the left equation. This is the generalized charge-free Gauss law of a 2D electrostatic trace-less rank-2 U(1) gauge theory with an emergent matrix-valued electric field  $E^{\mu\nu}$  [103–106, 117]. The spectrum in Gaussian approximation depicted in Fig. 7.2, consists of a completely flat bottom band that corresponds to the charge-free subspace and a dispersive upper band that characterizes the charges  $\rho$ . In accordance with a quadratically vanishing constraint vector  $(L_1(\mathbf{q}), L_2(\mathbf{q}))$  at  $\mathbf{q} = 0$ , the spectrum features *quartic* band touching points at this momentum.

As outlined in the previous chapter, the generalized charge-free Gauss law in Eq. (7.14) is associated with four-fold pinch points in the spin structure factor  $\mathcal{S}(\mathbf{q}) = \sum_{mn} \langle S_m^z(-\mathbf{q}) S_n^z(\mathbf{q}) \rangle$  at  $T = 0$  [117]. These characteristic features are also revealed in the spiderweb model in self-consistent Gaussian approximation, see Fig. 7.3(a). In addition to the expected four-fold pinch point at  $\mathbf{q} = 0$  the same type of singularity is also obtained at  $\mathbf{q} = (\pi, \pi)$  which represents another quartic band touching point in Fig. 7.2 and where an expansion of the constraint vector in quadratic order in  $\mathbf{q}$  yields the same higher-rank Gauss law as in Eq. (7.14) (but with  $E^{xx} \rightarrow -E^{xx}$ ). The existence of two singular momenta with identical physical properties follows from a symmetry of  $\mathcal{H}$  which is invariant under a  $\pi$  rotation of spins around the  $x$ -axis on *one* sublattice, combined with mirror reflection  $x \rightarrow -x$  in real space. For the spin structure factor this symmetry implies  $\mathcal{S}(q_x, q_y) = \mathcal{S}(-q_x + \pi, q_y + \pi)$  mapping both pinch points onto each other.

The term  $\mathcal{H}_1$  can be considered as a special case in a wider class of Hamiltonians that are obtained by weighting spins  $S_i^z$  on sublattice 1 with a factor  $\lambda \in \mathbb{R}$  in Eq. (7.6), i.e.,  $S_{\square_a}^z \rightarrow \lambda S_{\square_a}^z$  for  $a = 2, 4, 6, 8$ . In Gaussian approximation, this modification preserves the bottom flat band in Fig. 7.2, the form of the Gauss law in Eq. (7.14), and the four-fold pinch points in the spin structure factor. It only changes the factor in the relation between  $S_1^z(\mathbf{q})$  and  $E^{xy}(\mathbf{q})$  to  $2\lambda S_1^z(\mathbf{q}) = E^{xy}(\mathbf{q})$ . This shows that a fully rotation symmetric higher-rank Gauss law in the spin variables and an associated rotation symmetric band touching point at the singular momenta requires  $\lambda = 1/2$ . However, the rotation invariance at long wavelengths obtained at  $\lambda = 1/2$  comes at the price of an imbalance of weighting of spins in the

constraint: While the four spins on sublattice 1 in each cluster  $\boxtimes$  carry a prefactor  $\lambda = 1/2$  in  $\mathcal{C}_{\boxtimes}$ , the four spins on sublattice 2 carry a prefactor 1. When considering actual discrete spin variables beyond the Gaussian approximation, this imbalance reduces the number of possibilities for the contributions from both sublattices to cancel each other to yield  $\mathcal{C}_{\boxtimes} = 0$ . To avoid such additional restrictions, here and in the following, we only focus on the model as given in Eq. (7.6) with  $\lambda = 1$ , despite its lack of rotation invariance at long wavelengths.

It should be noted that the recently proposed *honeycomb snowflake model* [52, 101, 277] is a similar 2D spin model featuring an effective rank-2 gauge constraint as in Eq. (7.14). However, the spiderweb model can be considered somewhat simpler since its constraint only requires eight spins, compared to twelve spins in the honeycomb snowflake model.

### 7.3. Classical Ising model

While it was demonstrated that  $\mathcal{H}_1$  realizes a classical spin liquid with an emergent rank-2 gauge constraint on the Gaussian level, whether these properties survive in the spin-1/2 Ising case of  $\mathcal{H}_1$  is highly non-trivial. An analogous question for the classical Ising honeycomb snowflake model was recently answered in the affirmative [101]. Allowing for charges  $\rho \neq 0$ , it can be seen that fractonic excitations, as implied by Eq. (7.14), remain for  $S_i^z = \pm 1/2$  spins: An isolated fracton (i.e., a single violated constraint  $\mathcal{C}_{\boxtimes} \neq 0$ ) can be constructed as the corner of a rectangular domain wall between a ferromagnetic  $S_i^z = 1/2$  state and a regular pattern of three quarter  $S_i^z = 1/2$  and one quarter  $S_i^z = -1/2$  spins, see Fig. 7.1(c). Moving such an excitation requires flipping a number of spins proportional to the linear size of the rectangular domain, which suppresses their motion for large domain sizes. It should be emphasized that isolated fractons can also be constructed in less regular spin patterns. Similarly, a lineon can be formed as a dipole of fractons at the ends of a semi-infinite string of alternating  $S_i^z = \pm 1/2$  spins [Fig. 7.1(d)] which retains mobility in the direction perpendicular to its dipole moment.

A second key property required for classical spin liquid behavior is that  $\mathcal{H}_1$  features exponentially many degenerate ground states with  $\rho = 0$ . This can best be verified by identifying local operations that may be performed on a ground state to lead to another ground state, which will be detailed further in the next section. Third, to show that these ground states also give rise to the emergent charge-free rank-2 Gauss law in Eq. (7.14), one must calculate  $\mathcal{S}(\mathbf{q})$  by equal-weight sampling

over a large number of such ground state configurations.

A natural approach to this problem is to use a classical Monte Carlo simulation, cooling a system down to temperatures near zero until a true ground state is found (whose validity may be verified quickly). While theoretically possible, this approach is severely limited due to the extremely limited mobility of fractons: Since a single fracton cannot be moved without creating even more fractons, traditional Monte Carlo update schemes involving single spin flips are inapplicable, as the acceptance rate of any Monte Carlo update vanishes at low temperatures, leading to glassy dynamics. This problem was explored in more detail in Ref. [263], where advanced update schemes have been proposed that make use of local moves similar to the one shown in Fig. 7.1a), as well as lineon-like propagations similar to Fig. 7.1d). While such an approach was shown to reach zero-charge ground states, it remains numerically challenging to sample ground states as legal lineon moves become less probable with increasing system size. Instead, here we attempt to construct valid ground states directly.

Another intuitive idea is to employ a tiling approach: One may find all  $3 \times 3$  tiles that satisfy the constraint on a single plaquette. Then, on each site of sublattice  $\boxtimes$ , we place another random tile, ensuring that they share the same spins on all overlapping sites. For larger system sizes, it frequently occurs that the configuration is stuck, i.e., no matching tile can be found that correctly overlaps with its surrounding tiles. In this case, it is necessary to backtrack and reset the configuration to an earlier step. While this approach efficiently generates many feasible ground states, the bias introduced by backtracking is impossible to control and grows with increasing system size. As we will see below, one can introduce additional random constraints to alleviate this problem, but this drastically increases the computational cost.

In order to employ state-of-the-art techniques, we may rephrase this problem in the domain of integer programming, a field that aims to find integer-valued solutions to problems. The ground state constraints can be posed as a linear system of equations for the spins  $S_1^z, \dots, S_{L^2}^z$ :

$$\sum_j \mathcal{C}_{ij} S_j^z = 0. \tag{7.15}$$

Here,  $\mathcal{C}_{ij}$  is a constraint matrix of dimension  $L^2 \times L^2/2$ . For continuous spins, this can be algebraically solved, however, enforcing the spin length constraint  $(S_i^z)^2 = 1$  makes the problem NP-complete [281] and requires more sophisticated tools such as *mixed integer programming* solvers. To employ these techniques, we only need to provide the set of constraints as well as an empty objective function (as here we



do not intend to optimize anything). It is evident that this approach will still be highly biased, as the constraint solver certainly does not choose uniformly among the feasible solutions.

This bias is overcome by systematically adding additional random constraints with the goal of restricting the solution space to a few, or even a single solution. These random constraints can be arbitrary. Here, we randomly select a fraction of all spins and initialize them with a random value. The size of this fraction controls the bias: If we place too many constraints, there will be no solution, if too few spins are chosen then there are many solutions and the sampling will not be unbiased. Ideally, we want to choose this fraction such that the system only has a single solution. Here, we chose a large fraction of  $L^2/6$  randomly initialized spins, which in most cases produces an infeasible problem, but may occasionally give rise to a solution<sup>1</sup> By repeating this process many times, we eventually accumulate enough solutions that are virtually uncorrelated with each other. The result is shown in Fig. 7.3b) and shows a structure factor surprisingly close to the one found in the Gaussian approximation.

## 7.4. Fluctuator and symmetry properties

Next, we will introduce quantum fluctuations to this model with the goal of stabilizing a massively entangled ground state with fractonic excitations. If these fluctuations are perturbatively small, they will not be able to create charge excitations, but instead will allow for fluctuations between the different ground states. The effective dynamics of the model will thus be governed by the fluctuator  $\mathcal{F}_\square$ , which we define to be the lowest order operator that enables tunneling from one ground state to another, in analogy to the ring exchange term in quantum spin ice shown in Fig. 1.2 [68, 72, 80, 84]. Alternatively, and equivalently, we can also define the fluctuator by discretizing the gauge transformations of Eq. (7.1)

$$\begin{aligned} E^{xx} &\rightarrow E^{xx} - \partial_x \partial_y h, & E^{xy} &\rightarrow E^{xy} + (\partial_x^2 - \partial_y^2) h \\ \mathcal{F}_\square &= S_1^+ S_2^- S_3^- S_4^+ S_5^+ S_6^- S_7^- S_8^+, \end{aligned} \quad (7.16)$$

with a similar sign structure as the constraint defined in Eq. (7.5), but shifted by one as shown in Fig. 7.1(a). In the following, a plaquette  $\square$  in a spin configuration

---

<sup>1</sup>We find this solution using the commercial software *Gurobi* [282], which we find to be significantly faster (though otherwise equally applicable) than non-commercial alternatives, such as SCP [283].

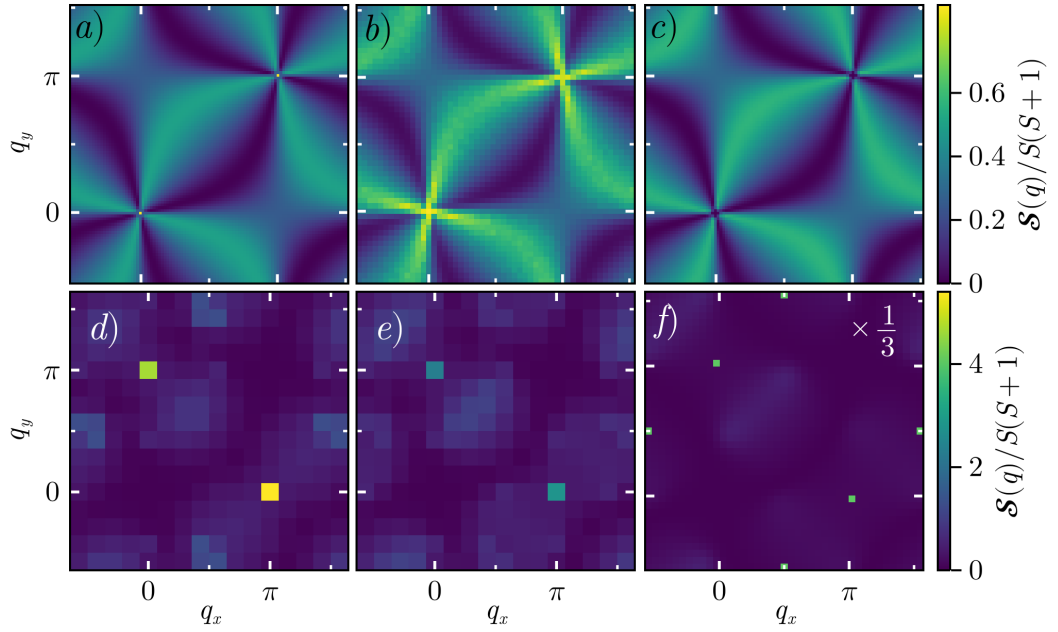


Figure 7.3.: (a-c) Classical structure factor in Gaussian approximation (a), and stochastic sampling of spin-1/2 (b) and spin 1 (c) ground states connected via loop moves to the uniform  $S^z = 0$  state. Quantum structure factor in the spin-1/2 staircase sector at  $\mu = 0$  (d) and the RK point  $\mu = 1$  from ED (e), and from GFMC (f). The color scale in (f) is rescaled by a factor of 1/3 for better visibility of the other plots.

$x = (S_1^z, \dots, S_{N_{\text{sites}}}^z)$  is referred to as *flippable* if the state  $|x\rangle$  is not annihilated by both  $\mathcal{F}_{\square}$  and  $\mathcal{F}_{\square}^{\dagger}$ . Panel e) of Fig. 7.1 shows an exemplary spin configuration satisfying all constraints and its flippable plaquettes. The fluctuating part of the Hamiltonian then becomes

$$\begin{aligned} \mathcal{H} &= \mathcal{H}_2 + \mathcal{H}_3 \\ &= -J' \sum_{\square} (\mathcal{F}_{\square} + \mathcal{F}_{\square}^{\dagger}) + \mu \sum_{\square} (\mathcal{F}_{\square}^{\dagger} \mathcal{F}_{\square} + \mathcal{F}_{\square} \mathcal{F}_{\square}^{\dagger}). \end{aligned} \quad (7.17)$$

Note that while the first term proportional to  $J'$  in Eq. (7.17) allows for fluctuations, it also favors states with many flippable plaquettes. The second term proportional to  $\mu$  is a Rokhsar-Kivelson potential, with a special point at  $\mu = J$  where the ground state becomes an exact, equal-weight superposition of all classical spin configurations. The eight-site spin flip terms  $\mathcal{F}_{\square}$  may seem artificial at first; however, they arise naturally for small perturbations around  $\mathcal{H}_1$ . For example,  $\mathcal{F}_{\square}$  is generated in fourth order perturbation theory in transverse nearest-neighbor interactions  $S_i^x S_j^x + S_i^y S_j^y$ , similar to the quantum dynamics generated by hexagon ring exchange terms in third order in pyrochlore quantum spin ice [68, 73], also detailed in Section 1.4. Alternatively,  $\mathcal{H}$  is generated in eighth-order perturbation theory in a transverse magnetic field  $\sim S_i^x$ . It should be noted that this eight-site fluctuator  $\mathcal{F}_{\square}$  is considerably simpler than the 24-site spin flip term of the honeycomb snowflake model [101]. In the following, we shall see that this is also a significant advantage for the realization of a quantum fracton phase.

## 7.5. Spin-1/2 spiderweb model

Next, we add quantum dynamics by setting  $J = 1$ ,  $\mu = 0$  and again assume  $T = 0$ , where  $\mathcal{H}$  acts on charge-free states  $\rho = 0$ . We find that this quantum spin-1/2 spiderweb model is an instance of extreme Hilbert space fragmentation, where  $\mathcal{H}$  splits up the Hilbert space into many sectors disconnected under the action of  $\mathcal{F}_{\square}$  and  $\mathcal{F}_{\square}^{\dagger}$ . In most cases of randomly generated charge-free states [see Fig. 7.1(e) for an example], the flippable eight-site clusters  $\square$  are sparse and non-overlapping, such that flipping one cluster neither enables nor disables other flippable clusters. Quantum dynamics is trivial in such sectors. Systematically, it was found that the charge-free state with the largest density of flippable clusters, which we identified as the ‘staircase state’ in Fig. 7.1(f), where half of all clusters  $\square$  are flippable. Due to its maximal density of flippable clusters, we find that the overall ground state of  $\mathcal{H}$  lies in the sector of the staircase state. The existence of this state with a finite density of flippable clusters also proves the extensive ground

state degeneracy in the classical  $J' = 0$  case mentioned above, since the number of classical configurations that can be generated starting from the staircase state is already extensive itself.

Despite the large density of flippable clusters, the quantum dynamics in the staircase sector is still relatively simple. As shown in Fig. 7.1(f), the action of  $\mathcal{F}_\square$  or  $\mathcal{F}_\square^\dagger$  disables flippable clusters in a  $5 \times 5$  square area around it, but its repeated action across the lattice cannot drive the system further away from the staircase parent state. By exhaustively generating all classical configurations within a given system size and bookkeeping which states are connected via single spin flips, the Hamiltonian can be constructed and exactly diagonalized (ED) to obtain the ground state. As this procedure considers each block in the Hamiltonian separately, this approach allows for considerably larger system sizes than naive ED approaches. In the staircase sector, systems with around  $\sim 14 \times 14$  sites can be solved exactly, while for larger sizes, the exponential growth of the Hilbert space becomes prohibitive. Section F.1 contains further details regarding the ED implementation. Fortunately, as the matrix elements of the Hamiltonian are strictly negative, larger system sizes can still be treated using the numerically exact Green function Monte Carlo (GFMC) method. Here, instead of performing an exhaustive search of all possible classical configurations, observables are sampled probabilistically by performing a random walk in the space of configurations. This method is further described in Section F.2.

In Fig. 7.3(d), it can be seen that  $\mathcal{S}(\mathbf{q})$  obtained in the staircase sector features a large ordering peak, inherited from the staircase order, with only a faint fluctuating background. This shows that, despite the classical spin liquid at  $J' = 0$ , the quantum dynamics at  $J' > 0$  is too restricted for spin-1/2 and leads to too much Hilbert space fragmentation to generate a quantum spin liquid.

While the existence of long-range order in the presence of only ring-exchange terms is a common observation also in other models [284], a possibility to still generate a quantum spin liquid is to add a potential term  $\mu \neq 0$  for flippable clusters in Eq. (7.17) and tune it to the Rokhsar-Kivelson (RK) point  $\mu = J'$  [76], see also Section 1.4. At this point, each classical spin configuration contributes equally to the ground state, since the kinetic  $\mathcal{H}_2$  and potential term  $\mathcal{H}_3$  in Eq. (7.17) cancel each other. The exact ground state wavefunction must then have an energy of  $E_0 = 0$  and can be constructed in *each* sector by an equal weight superposition of all states in that sector. While this implies that the equal weight superposition of *all* charge-free states [that gives rise to the four-fold pinch points in Fig. 7.3(b)] is also a *quantum* ground state at the RK point, the quantum dynamics still suffers

from the same restriction and fragmentation as for  $\mu = 0$ . To show this,  $\mathcal{S}(\mathbf{q})$  is displayed at the RK point in the staircase sector in Fig. 7.3(e,f), which still features sharp peaks that grow with system size, indicating long-range staircase order at variance with a quantum spin liquid.

At first glance, this prediction of a magnetically ordered ground state at the RK point may seem highly paradoxical, since the exact solution  $|\psi\rangle_{\text{RK}} = \sum_{\mathbf{x}} |x\rangle$  suggests a spin liquid. However, it should be emphasized that at the RK-point all Hilbert space sectors contribute equally to the ground state. On the other hand, since quantum fluctuations cannot tunnel between different sectors, this state shares more similarities with the classical spin liquid discussed in the previous section than with a true quantum spin liquid. It is thus evident that an actual realization of a quantum spin liquid in the spiderweb model needs to overcome the severe Hilbert space fragmentation.

## 7.6. Spin-1 spiderweb model

A natural way to reduce Hilbert space fractionalization and hopefully generate non-trivial quantum dynamics in the spiderweb model is to move on to the corresponding spin-1 model where the availability of more local spin states  $S_i^z = -1, 0, 1$  increases the possibilities for quantum fluctuations. A first important observation is that the charge-free spin-1 state with the largest density of flippable clusters is simply the homogeneous state with  $S_i^z = 0$  for all  $i$ . This state has the unique property that *all* clusters  $\square$  are flippable by  $\mathcal{F}_{\square}$  and by  $\mathcal{F}_{\square}^{\dagger}$ . Notably, computing  $\mathcal{S}(\mathbf{q})$  via a uniform sampling of all ground states in the  $S_i^z = 0$  sector yields intact four-fold pinch points [Fig. 7.3(c)] in excellent agreement with the Gaussian approximation<sup>2</sup>. This implies that even at  $J' = 0$ , the  $S_i^z = 0$  sector of the spin-1 spiderweb model is a classical spin liquid with an emergent rank-2 Gauss law. Both properties justify investigating the quantum dynamics of the spin-1 spiderweb model.

If indeed the spin system realizes an emergent quantum higher rank U(1) gauge theory [68, 73, 285], the properties of this liquid can be derived by expressing the spin flip operators as  $S_i^{\pm} = \sqrt{2}e^{\pm iA_i^{\alpha}}$  where  $A_i^{\alpha} \in [0, 2\pi]$  is a component of

<sup>2</sup>Note that a uniform sampling of configurations can be efficiently implemented by performing GFMC at the RK point using the exact solution as a guiding wavefunction, see Section F.2. However, a fully unguided random walk while less efficient will also yield the result shown in Fig. 7.3(c)

a compact matrix-valued field (generalized ‘vector’ potential) on site  $i$  with the convention that  $\alpha = xy$  ( $\alpha = xx$ ) when  $i$  is on sublattice 1 (2). Furthermore,  $S_i^z$  is identified with a conjugate integer-valued matrix electric field  $S_i^z = E_i^\alpha$  where  $[A_i^\alpha, E_i^\alpha] = i$  with the same convention for  $i$  and  $\alpha$ <sup>3</sup>. This allows us to define a gauge invariant emergent magnetic field  $B_\square$  for each cluster  $\square$  via

$$B_\square = A_{\square_1}^{xy} - A_{\square_2}^{xx} - A_{\square_3}^{xy} + A_{\square_4}^{xx} + A_{\square_5}^{xy} - A_{\square_6}^{xx} - A_{\square_7}^{xy} + A_{\square_8}^{xx}, \quad (7.18)$$

where the sign pattern follows that of the fluctuator [Fig. 7.1(a)], and the notation for sites  $i = \square_a$  is the same as in Eq. (7.17). It follows that  $\mathcal{H} \sim -\sum_\square \cos B_\square$ , which gives an energy density of the magnetic field  $\sim B_\square^2$  when expanded to quadratic order, as in a Maxwellian field theory. Thus, by collecting all the relevant terms, we can formulate an effective field theory for the spiderweb model, given by

$$\mathcal{H}_{\text{eff}} = \frac{U}{2} \sum_i (E_i^\alpha)^2 + \frac{K}{2} \sum_\square B_\square^2 + \frac{W}{2} \sum_\square \mathcal{N}_\square^2, \quad (7.19)$$

with

$$\mathcal{N}_\square = E_{\square_1}^{xy} - E_{\square_2}^{xx} - E_{\square_3}^{xy} + E_{\square_4}^{xx} + E_{\square_5}^{xy} - E_{\square_6}^{xx} - E_{\square_7}^{xy} + E_{\square_8}^{xx}. \quad (7.20)$$

The first term  $\sim U$ , not directly contained in  $\mathcal{H}$ , is introduced to energetically suppress high values of  $|E_i^\alpha|$  which mimics the hard constraint  $|S_i^z| \leq 1$ . It describes the energy density of the electric field and has the same form as the corresponding term in a usual Maxwellian field theory. The last term  $\sim W$  mimics the RK potential  $\mu$ , where the exact RK point is realized in the limit  $U/K \rightarrow 0$  [68]. Following the construction principle of Refs. [68, 73],  $\mathcal{N}_\square$  is obtained from  $B_\square$  by replacing  $A^{xy} \rightarrow E^{xy}$  and  $A^{xx} \rightarrow E^{xx}$  in Eq. (7.18). An effective field theory can generally contain further gauge invariant terms, however, as we will see below, Eq. (7.19) is sufficient to explain the numerical results. Note that, in contrast to the spin-1/2 quantum spin ice where the effective U(1) field theory is ‘frustrated’ [73] due to the impossibility of vanishing local electric fields, the mapping of the spin-1 system has the advantage of a well-defined vacuum  $S_i^z = 0$  of electric fields.

In order to find a solution to Eq. (7.19), we express the fields  $E, A$  in Fourier space defining in analogy to Eq. (1.11)

$$E^a(\mathbf{q}) = \frac{1}{\sqrt{N_{\text{cells}}}} \sum_{i \in \mathbf{a}} e^{-i\mathbf{q}\mathbf{r}_i} E_i^a, \quad E_i^a = \frac{1}{\sqrt{N_{\text{cells}}}} \sum_{\mathbf{q}} e^{i\mathbf{q}\mathbf{r}_i} E^a(\mathbf{q}) \quad (7.21)$$

<sup>3</sup>Note that this definition for the relation between  $S_i^z$  and  $E_i^{xy}$  differs slightly from the one above Eq. (7.14) where an additional factor 2 appears. This redefinition is necessary to ensure that  $E_i^{xy}$  takes the integer values  $E_i^{xy} = \pm 1$  expected in the field theory. The consequence for the continuum rank-2 Gauss law for  $E^{\mu\nu}$  is that it no longer has the simple form of Eq. (7.14) but becomes  $(\partial_x^2 - \partial_y^2)E^{xx} + \partial_x \partial_y E^{xy} = 0$  without rotation symmetry. This symmetry can only be restored in a model with  $\lambda = 1/2$ .

with equivalent expressions for  $A$ . Noting that the sum  $\sum_{\square}$  by definition iterates only the sites of one sublattice, we may write Eq. (7.18) more simply as

$$B_{\square} = \sum_{\mathbf{q}} e^{i\mathbf{q}\cdot\mathbf{r}_{\square}} B(\mathbf{q}) = \sum_{\mathbf{q}} e^{i\mathbf{q}\cdot\mathbf{r}_{\square}} [2A^{xy}(\mathbf{q})(\cos q_x - \cos q_y) + 4A^{xx}(\mathbf{q}) \sin q_x \sin q_y]. \quad (7.22)$$

A quadratic bosonic Hamiltonian that may be diagonalized using a Bogoliubov transform is then found by expressing the canonically conjugate fields  $E, A$  by a single bosonic field  $[(a^a(\mathbf{q}))^{\dagger}, a^a(\mathbf{q}')] = \delta(\mathbf{q} - \mathbf{q}')$  as

$$\begin{aligned} A_i^a &= \frac{1}{\sqrt{2}} [a_i^a + (a_i^a)^{\dagger}] , & A(\mathbf{q})^a &= \frac{1}{\sqrt{2}} [a^a(\mathbf{q}) + (a_i^a(-\mathbf{q}))^{\dagger}] , \\ E_i^a &= \frac{1}{\sqrt{2i}} [a_i^a - (a_i^a)^{\dagger}] , & E(\mathbf{q})^a &= \frac{1}{\sqrt{2i}} [a^a(\mathbf{q}) - (a_i^a(-\mathbf{q}))^{\dagger}] \end{aligned} \quad (7.23)$$

After these transformations, the model in Eq. (7.19) is a simple bosonic Hamiltonian with only quadratic terms that can be written as

$$\mathcal{H}_{\text{eff}} = \sum_{\mathbf{q}} \mathcal{A}^{\dagger}(\mathbf{q}) H_{\text{eff}} \mathcal{A}(\mathbf{q}) , \quad (7.24)$$

where  $\mathcal{A}(\mathbf{q})$  is a four-component operator

$$\mathcal{A}(\mathbf{q}) = (a^{xy}(\mathbf{q}), a^{xx}(\mathbf{q}), [a^{xy}(-\mathbf{q})]^{\dagger}, [a^{xx}(-\mathbf{q})]^{\dagger}) \quad (7.25)$$

and the  $4 \times 4$  matrix  $H_{\text{eff}}$  is given by

$$H_{\text{eff}} = KV_+^T V_+ + WV_-^T V_- + \frac{U}{4} \begin{pmatrix} 1 & 0 & -1 & 0 \\ 0 & 1 & 0 & -1 \\ -1 & 0 & 1 & 0 \\ 0 & -1 & 0 & 1 \end{pmatrix} \quad (7.26)$$

with

$$V_{\pm} = (c_x - c_y, 2s_x s_y, \pm(c_x - c_y), \pm 2s_x s_y) \quad (7.27)$$

and  $c_{\mu} = \cos q_{\mu}$ ,  $s_{\mu} = \sin q_{\mu}$  with  $\mu = x, y$ .

As it does not feature any interactions, Equation (7.24) can be solved exactly by using a Bogoliubov transform [286, 287], further detailed in Section F.3. The elementary excitations are given by a photon mode with the dispersion

$$\omega(\mathbf{q}) = 2\sqrt{K [(c_x - c_y)^2 + 4s_x^2 s_y^2]} \sqrt{\frac{U}{4} + W [(c_x - c_y)^2 + 4s_x^2 s_y^2]}. \quad (7.28)$$

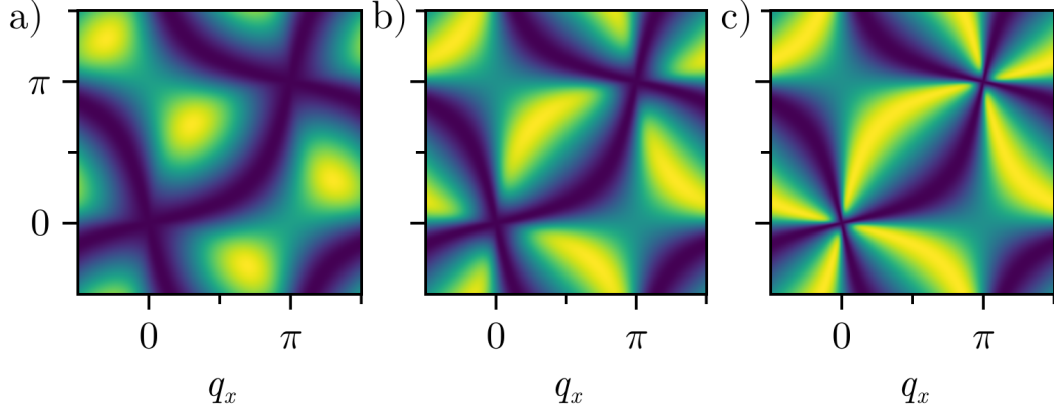


Figure 7.4.: (a-c) Structure factor obtained from the U(1) field theory in Eq. (7.31) for the ratios  $U/W = 100$  (a),  $U/W = 1$  (b) and  $U/W = 1/100$  (c).

It can be seen that  $\omega(\mathbf{q})$  is gapless with nodal points at the pinch point locations. An expansion of  $\omega(\mathbf{q})$  around these two points yields for  $U \neq 0$  in the lowest non-vanishing order

$$\omega(\mathbf{q}) \approx \sqrt{\frac{KU}{4}} \sqrt{q_x^4 + 14q_x^2q_y^2 + q_y^4}. \quad (7.29)$$

This function is quadratic in any radial direction away from the gapless points, however, it is not rotationally symmetric. On the other hand, exactly at the RK-point  $U = 0$ , the photon dispersion becomes quartic,

$$\omega(\mathbf{q}) \approx \sqrt{\frac{KW}{4}} (q_x^4 + 14q_x^2q_y^2 + q_y^4). \quad (7.30)$$

From this solution the structure factor can be computed through the electric field correlator

$$\begin{aligned} \mathcal{S}(\mathbf{q}) &= \langle (E^{xx}(-\mathbf{q}) + E^{xy}(-\mathbf{q})) (E^{xx}(\mathbf{q}) + E^{xy}(\mathbf{q})) \rangle \\ &= C \frac{(c_x - c_y + 2s_x s_y)^2}{\sqrt{(c_x - c_y)^2 + 4s_x^2 s_y^2} \sqrt{\frac{U}{W} + 4[(c_x - c_y)^2 + 4s_x^2 s_y^2]}}, \end{aligned} \quad (7.31)$$

defining the dimensionless constant  $C = \sqrt{\frac{K}{4W}}$  and the ratio  $U/W$ . While the effect of  $C$  is only a rescaling of  $\mathcal{S}(\mathbf{q})$ ,  $U/W$  determines the modulation of the structure factor around the pinch point, as shown in Fig. 7.4. It interpolates between the RK point at  $U/W = 0$ , which becomes analogous to the classical Gaussian theory



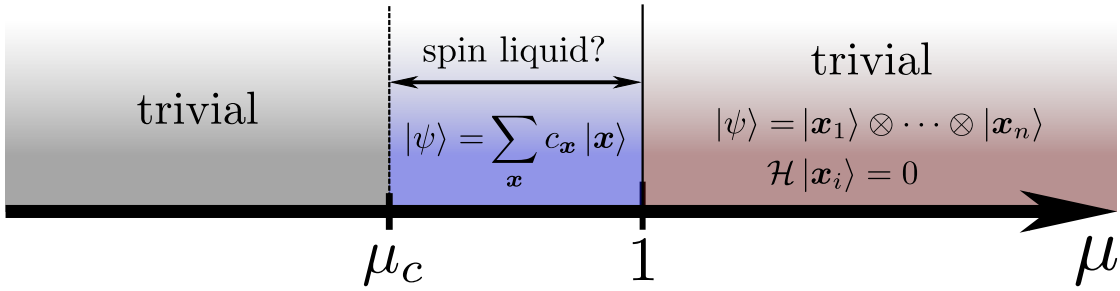


Figure 7.5.: Expected phases in the spin 1 spiderweb model as a function of  $\mu$ . The trivial phase for  $\mu \rightarrow \infty$  is a product state of all configurations with zero flippable plaquettes. The coefficients of the wavefunction  $|\psi\rangle$  depend on  $\mu$  but are real and positive. At the RK point  $\mu = 1$  all  $c_{\mathbf{x}}$  all equal.

Eq. (7.11) and sharp pinch points are visible, and  $U/W \rightarrow \infty$ , where the structure factor is modulated by the quadratic photon dispersion  $\mathcal{S}(\mathbf{q}) = \omega(\mathbf{q})\mathcal{S}_{\text{cl}}(\mathbf{q})$ , where  $\mathcal{S}_{\text{cl}}(\mathbf{q})$  is the classical spin structure factor in the Gaussian approximation from Fig. 7.3(a). This modulation of the classical result by the photon dispersion, has already been noted in previous works [68, 113, 117].

The structure factor obtained from the field theory will allow for a direct comparison to numerical results. However, it is useful to first discuss the expectations for varying values of  $\mu$ , setting  $J' = 1$ . A sketch of the expected phase diagram is shown in Section 7.6. Setting  $\mu = \infty$  in Eq. (7.17), it is evident that the ground state must be an eigenstate of  $\mathcal{H}_3$ . Since  $\mathcal{H}_3$  commutes with  $S_i^z$ , it follows directly that the ground state is a trivial state, consisting only of classical spin configurations that minimize the number of flippable plaquettes. Of course, there are states with no flippable plaquettes, for example, the ferromagnetic  $S_i^z = 1$  state. While there can be many such states, they cannot fluctuate into each other, leading to a trivial state with no quantum dynamics. This phase extends until the RK point<sup>4</sup>. Precisely at  $\mu = 1$ , the ground state realizes an equal weight superposition of all configurations. It is worth noting that in the  $S_i^z = 0$  sector, the spin structure factor will be equivalent to Fig. 7.3(c), as a uniform sampling over ground states converges to the exact sum over all classical configurations. On the other side of

<sup>4</sup>States with zero flippable plaquettes remain eigenstates with zero energy for all  $\mu \geq 1$ , since they are annihilated by the fluctuator. As the Hamiltonian is positive semi-definite, the ground state energy must be zero. The definiteness follows from the Gershgorin circle theorem, according to which eigenvalues must lie within a distance  $\sum_{\mathbf{x}' \neq \mathbf{x}} |\mathcal{H}_{\mathbf{x}\mathbf{x}'}|$  from  $\mathcal{H}_{\mathbf{x}\mathbf{x}}$ . For  $\mu \geq 1$ , the diagonal elements become larger than the sum of off-diagonal elements, so no eigenvalue can be negative.

the phase diagram towards  $\mu \rightarrow -\infty$  another trivial phase is expected. Although no classical configuration can be an eigenstate of  $\mathcal{H}_2$ , the ground state will generally featuring only small fluctuations around the classical configuration with the largest number of flippable plaquettes. The behavior for  $\mu < 1$  remains to be determined. An expectation from quantum dimer models on bipartite lattices is a symmetry-broken ground state [77]. Similarly, from a field theory perspective, one might expect a confining phase transition: The second assumption of small  $B_\square$  fluctuations is known to be non-trivial in two spatial dimensions since phase-slip events  $B_\square \rightarrow B_\square + 2\pi$  in 2+1 dimensional spacetime, so-called *instantons* [288], can proliferate, gap out the photons, and drive a system into an ordered phase.

While a numerical study of the spin-1 spiderweb model in the  $S_i^z = 0$  sector shows no sign of magnetic order even at  $\mu = 0$ , simulations initialized in different sectors of Hilbert space can have lower ground state energies. On the other hand, initializing the Hilbert space containing the state shown in Fig. 7.6(a) will lower the energy. Here, for small values of  $\mu \lesssim 0.4$ , sharp peaks at moments  $\mathbf{q} = (\pi/2, \pi/2)$  are found instead, a clear signature for a symmetry-broken phase. On the other hand, for larger values of  $0.4 \lesssim \mu \leq 1$  the structure factor becomes increasingly similar to the field theory prediction in Fig. 7.4. Moreover, the structure factor smoothly transitions into the expected result of sharp fourfold pinch points at the RK point, indicating no further phase transition in this regime. At  $\mu = 1.05$ , the pinch point pattern gets disrupted in favor of several sparsely distributed peaks. While this clearly signals a breakdown of the spin liquid phase, there are evidently several disconnected states which minimize the number of flippable plaquettes leading to highly non-ergodic behavior. While it is likely that other, magnetically ordered sectors with lower energy can be found, we shall first consider the possibility of realizing a quantum spin liquid in an excited sector.

The absence of magnetic order at  $\mu \gtrsim 0.4$  and the smooth transition into the RK point is a highly promising sign for a realization of a quantum spin liquid. This is further investigated in Fig. 7.7 where the spin structure factor for  $\mu = 0.7$  is compared against the field theoretical prediction. The free parameters  $C$  and  $U/W$  for the analytical result have been obtained via the best fit to the GFMC data at moderate values of  $\mu$  away from the RK point shown in Fig. 7.7(b). Visually, both results are in excellent agreement and in particular, the suppression of the structure factor at the pinch point location can be seen as a indication of emergent photon excitations. Figure 7.7(c) compares a cuts along a path of high-symmetry points which shows a truly astonishing degree of agreement between the numerical and analytical results to further evidence the realization of an emergent rank-2 U(1) gauge theory. It should be emphasized that the fit was obtained

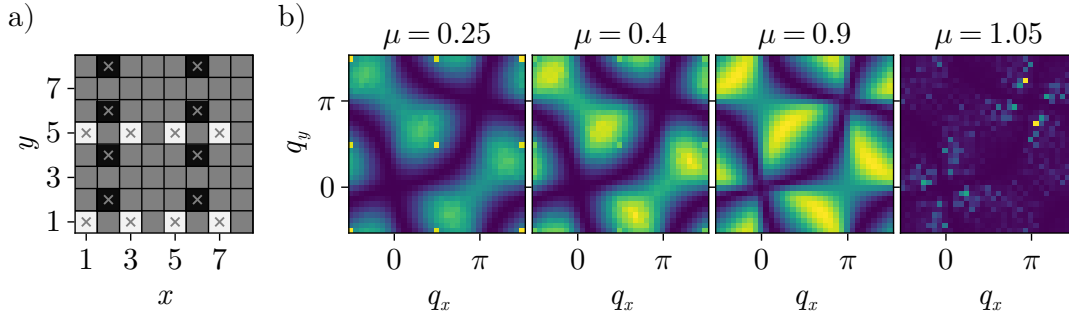


Figure 7.6.: (a): Spin-1 configuration where the maximally flippable state realizes magnetic order with a  $4 \times 4$  unit cell. The colors of squares indicate the spin value in  $S^z$  basis: black, grey and white correspond to  $\downarrow, 0 \uparrow$ , respectively. (b): Spin structure factor of the spin-1 model obtained from GFMC starting in the sector containing the spin configuration from panel (a) for a system of  $32 \times 32$  spins. The result is shown for different values of  $\mu$  as indicated above each plot.

using only two coefficients for the entire Brillouin zone, where the effect of the constant  $C$  only corresponds to a global rescaling of the structure factor which is a natural expectation as the electric field correlator obtained in the field theory is not subjected to any sum rules.

## 7.7. Discussion

This chapter introduces a new construction of a fracton model, named the spiderweb model, by explicitly discretizing a rank-2 U(1) gauge theory. Using a numerical construction of valid ground states, it is confirmed that, even in the spin-1/2 Ising case, the spiderweb model realizes a classical spin liquid described by an electrostatic rank-2 U(1) theory. However, it is found that when quantum dynamics are introduced, the lowest order spin flip terms are not sufficient to induce a quantum spin liquid. This is because the quantum ground state occurs in a magnetically ordering sector of a strongly fragmented Hilbert space. The origin of the observed Hilbert space fragmentation is the restrictive nature of the lowest-order operator, which can induce fluctuations that require a specific pattern of 8 spins, which is seldom realized for spin-1/2. This restriction is somewhat relaxed at higher spin quantum numbers, where the larger number of local spin

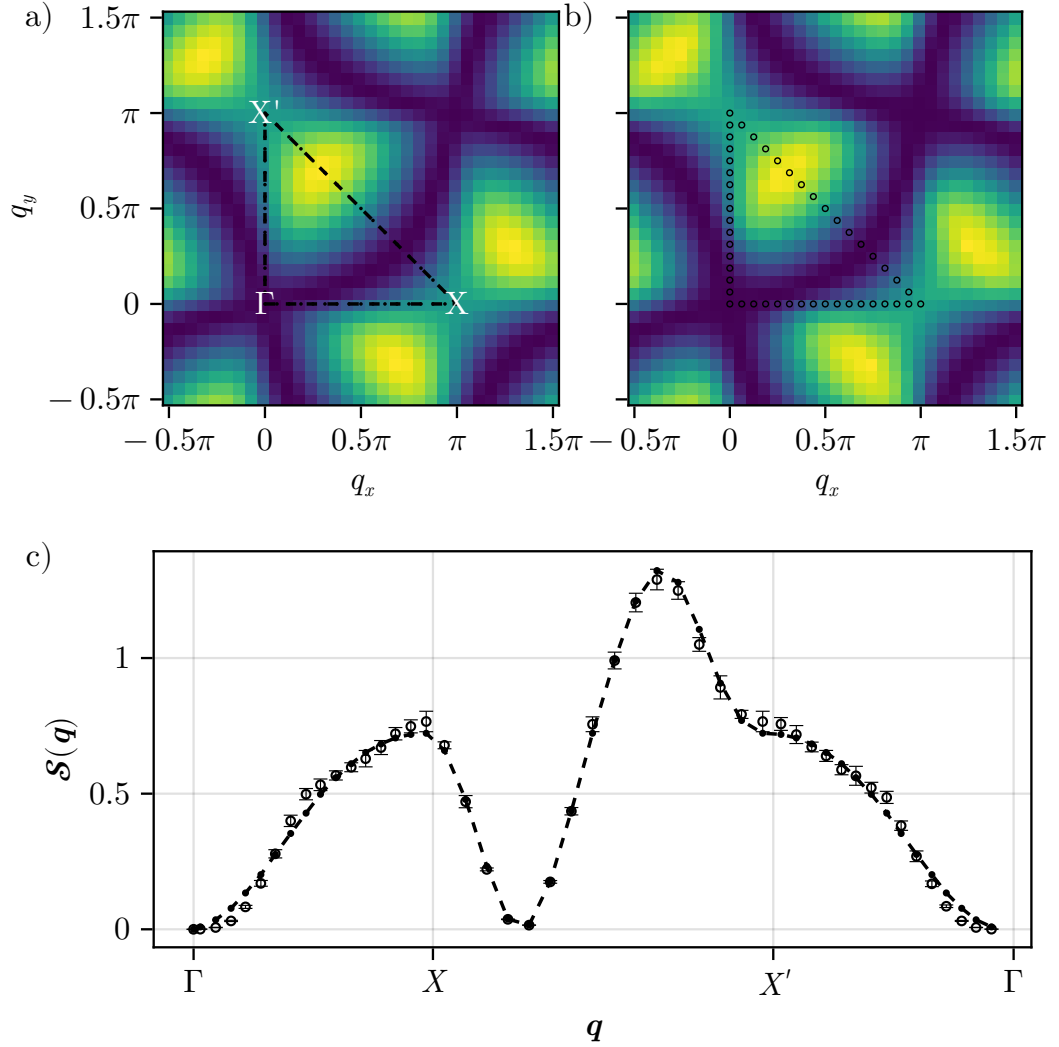


Figure 7.7.: Spin structure factor in the Maxwellian field theory (a) fitted for  $U/W = 25.66$ ,  $C = 2.33$ . (b) Spin structure factor of the spin - 1 model obtained from Monte Carlo simulation for  $\mu = 0.7$ . (c) Cut of the  $E$ -correlators and structure factor along the paths through high-symmetry points indicated in panels (a,b).

degrees of freedom allows for more fluctuations. As a result, the model is further investigated at spin 1 using numerically exact quantum Monte Carlo simulations initialized in an excited sector of the Hilbert space. Depending on the value of a model parameter  $\mu$ , three extended phases are identified, where one is found to be a magnetically disordered phase. This phase is adiabatically connected to a fine-tuned Rokhsar-Kivelson point at  $\mu = 1$ , for which the model realizes an exactly solvable quantum spin liquid ground state. Using the analytical solution of the compact rank-2 U(1) lattice gauge theory in comparison with numerical results in the spin model, an excellent agreement in the spin structure factor is found, further supporting the claim that the magnetically disordered phase is the realization of a quantum fracton spin liquid in an extended region of the parameter space. This agreement also includes the field theoretical expectation of a vanishing intensity of the spin structure factor at the pinch point due to the emergent photon excitations with gapless dispersion relations [68].

In the language of field theory, the spiderweb model becomes a gapless compact 2+1 dimensional field theory, which would typically be expected to exhibit confinement via instanton proliferation [288]. However, the only known mechanism to circumvent this, a duality between the electric and magnetic fields, is not realized in this model. It is therefore likely that the true ground state, taking into account all sectors of Hilbert space, may exhibit magnetic order throughout the phase diagram. Practically, the search for this sector is extremely challenging, as it would require an exhaustive analysis of the large number of Hilbert space sectors. On the other hand, if the assumption of an ordered ground state is correct, the presented finding of a stable quantum spin liquid surviving in an excited sector would be a remarkable result, as it represents another rare mechanism for escaping instanton confinement in a compact U(1) gauge theory. Moreover, the observation of a quantum fracton spin liquid phase makes the quantum spiderweb model an intriguing candidate for possible realizations in Rydberg systems, which have shown great promise in the realization of two-dimensional quantum spin liquids [90–93, 289–293]. In conclusion, the spiderweb model represents a significant advancement in the theoretical study of emergent fracton spin liquids and towards the realization of fracton phases in experimental platforms.



## Conclusion

Solving the quantum many-body problem, while certainly of immense interest, remains one of the most notorious problems in contemporary physics. Hence, approaches to improve our understanding of strongly interacting many-body systems have to choose between two primary strategies. The first strategy is to advance our methodological toolkit by inventing new techniques or significantly improving existing ones (i). The second strategy is to identify new problems with intriguing many-body properties to which the existing methodology can be applied (ii). This dissertation contains instances of both of these crucial approaches.

The first part of this dissertation has been devoted to addressing (i) via the development of the PMFRG, a new and powerful method for studying quantum many-body systems. The PMFRG's applicability at finite temperatures has enabled predictions that can be quantitatively compared to numerically exact methods. This is in stark contrast to many other diagrammatic approaches, including the PFFRG, whose results are often of qualitative nature. The ability to make quantitative comparisons also provides accountability and serves as an immensely useful aid in the process of formalism improvements. In Chapter 4, we came to the remarkable conclusion that critical scaling phenomena can be resolved accurately with PMFRG, allowing for an unbiased way to detect and map out magnetic phases determining their critical temperature in good agreement with numerically exact quantum Monte Carlo, wherever applicable. The only initial disadvantage of the PMFRG, its inaccuracies in resolving phase transitions at low temperatures, as well as the practical need for many expensive calculations at different temperatures, have been drastically improved by utilizing the temperature as a fully physical renormalization flow parameter. In addition, it was shown in Chapter 5 that the PMFRG can be applied to spins  $S > 1/2$ , rigorously demonstrating that unphysical states can be treated even at finite temperature. The PMFRG can thus be considered a true successor to its methodological ancestor, the PFFRG [294]. It retains the major strengths of flexibility and numerical efficiency while significantly improving its quantitative predictiveness.

It is interesting to point out other noteworthy avenues of further research that these developments in the PMFRG have opened up. One of the most important challenges to address is the loss of accuracy at low temperatures. Attempts to include higher loop orders or even to solve the full parquet equations have shown

somewhat limited improvements, except in some rare cases such as the Heisenberg pyrochlore model. It remains an open question whether the drawbacks, such as the lack of critical scaling, can be mitigated.

These questions raised by the preceding work have motivated an increasing number of related efforts in the community to improve diagrammatic methods for spin systems [10, 160, 236, 295, 296]. It is currently unknown whether improvements can be made by attempting to fix ward identities [158, 225], exploring other approximations for solving the Bethe-Salpeter equations [296–298], or even entirely new formulations of the FRG formalism based on spin operators [157, 158, 299]. Another drawback of spin-FRG methods is the limited access to measurable observables beyond spin-spin correlation functions. While this is partially addressed by the PMFRG through its capabilities in computing thermodynamic observables such as entropy and the specific heat, many observables which are in direct relation to spin liquid properties, such as the entanglement entropy, are currently inaccessible. However, there are promising developments underway to improve the number of accessible observables. One such development is the employment of the Keldysh formalism for the FRG, which allows access to dynamical correlators. These correlators are useful for comparison to experiments and can provide insights into low-energy excitations [300–303].

Regarding goal (ii), the final Chapters 6 and 7 provides important contributions to the study of emergent gauge theories in spin systems. These chapters investigate a variety of models with two-body spin interactions featuring emergent higher-rank gauge theories in the presence of quantum fluctuations. In the Heisenberg Octochlore model, strong quantum fluctuations lead to significant deviations in the structure factor, potentially disrupting the emergent gauge theory. However, in the presence of a perturbative inclusion of quantum effects, cooperative fluctuations between classically degenerate ground states may be supported without closing the excitation gap of electric charges. This allows for the existence of well-defined fracton and photon quasiparticles.

To test this hypothesis, a new spin model is constructed by explicitly discretizing a rank-2  $U(1)$  gauge theory on a square lattice. This model is first verified to exhibit a Fracton spin liquid in the classical Ising limit. Notably, this recipe offers a much simpler description compared to other classical fracton models and allows for more tunneling events between classical ground states via successive spin flips [101].

Introducing quantum effects, it is shown how local fluctuations lead to an



---

effective description of a ring-exchange Hamiltonian with a large number of disconnected Hilbert space blocks. For spin-1/2, this Hilbert-space fragmentation does not leave any blocks large enough to support a massively entangled ground state. However, by increasing the spin quantum number to 1, this obstacle is mitigated considerably. Furthermore, this model can be fine-tuned to a special Rokhsar-Kivelson point that exhibits an exact solution with a quantum spin liquid ground state. The strong agreement between Quantum Monte Carlo and the exact solution of the emergent rank-2 lattice gauge theory is a testimony that the spin-liquid phase has a finite stability region away from this point for spin-1 systems at least in some of the disconnected Hilbert space sectors.

In summary, this dissertation establishes that the PMFRG can be used as a particularly powerful extension for the PFFRG, capable of providing accurate estimates for the finite-temperature magnetic phase diagram of generic frustrated two-body spin models. Moreover, this dissertation investigates concrete examples of emergent higher-rank gauge theories and introduces the first model with two-body spin interactions to realize a quantum fracton spin liquid.



## Acknowledgements

In arguably one of the most important chapters of a thesis, I finally have the opportunity to express my sincere gratitude to all of those who have accompanied, guided, helped, and supported me. It cannot be overstated how lucky and grateful I feel to have been under the guidance of my supervisor, Johannes Reuther, who has been an immense source of knowledge, inspiration, but also common sense and empathy. I have never regretted staying for a PhD as I cannot imagine a better boss and, quite possibly, will carry unrealistic expectations for all my future supervisors. I would also like to thank my second advisor, Piet Brouwer, who has likewise inspired me to learn ever since he taught me the very basics of Physics and was always helpful with sound advice. Throughout the course of my PhD, I have profited enormously from the fantastic ideas, suggestions, mentorship, and collaboration of Björn Sbierski, who not only has my sincere gratitude but also my deepest respect for his enormous dedication and rigor in advancing the boundaries of method development.

The list of collaborators and friends whom I am grateful towards is long: I am grateful to Yasir Iqbal, who has enriched my initially rather method-development driven research with great physical intuition and further sparked my motivation to collect every Indian visa that can be obtained in my passport. I hope I can add more in the future! I also thank Dominik Kiese, who originally inspired me to embrace the joy of programming in Julia, as well as Benedikt Schneider, with whom it was a joy to work together on the PMFRG. I also thank my other long-term collaborators Francesco Ferrari, Michel Gingras, Nikita Astrakhantsev, Harald Jeschke, Tobias Müller, Simon Trebst, Ronny Thomale, and Arnaud Ralko, who have been amazing to work with on several projects.

I thank all my friends from the Dahlem Chamber for Charming Quirks Scholarship (or something) who have made it a joy to come there every single day, those whom I have distracted while I was stuck and those who distracted me when they were stuck (I am sure these sets have considerable overlap) and with whom I have shared a fantastic time during and off work hours. I thank Elies Gil-Fuster who never runs out of interesting topics to share and my habibis, Yanis Chaou, Miad Mansouri and Yussuf for their wisdom. There is much to be said, but I believe Yussuf's words summarize it best: "Your mind may be the spark that ignites the fire but the wise man knows that habibis are the fuel that keeps it burning". In

this sense thanks to those in my group, Yannik Schaden, Matías Gonzales, Anna Fancelli and Vincent Noculak and all members in the DCCQS: Harry Schmid, Oliver Franke, Zhiyang Tan, Kryštof Kolář, Vatsal Dwivedi, Gal Lehmüt, Jörg Behrmann, Jacob Steiner and Max Hering as well as Felix von Oppen, whose lectures I greatly enjoyed. In a broader sense, also a big thanks to my “GP-Ehen” and “Ü-Gruppenmitglieder” Nele Stetzuhn, Benjamin Sauer and Vincent Stegmaier for our time together learning physics and everything that comes along with it, as well as my friends from outside physics who gave me perspective.

Finally, my greatest thanks belong to Megha and the rest of my family for being there for me, helping me throughout past and future times and supporting my passion in physics.

## Inclusion of the RPA

In order to investigate the PMFRG's behaviour regarding a magnetic phase transition, we consider the contributions of the RPA channel in the (one-loop) PMFRG flow equations. We can do this mostly in analogy to Ref. [120], except that we now explicitly consider finite temperatures. In the RPA approximation for PMFRG, we restrict ourselves to diagrams with internal Majorana bubbles, i.e. site summations. As a result, the flow equations for the three types of vertices as presented in Ref. [1] decouple from each other. As seen in Eq. (E.1) the only vertex which is nonzero initially is the spin vertex  $\Gamma_c = \Gamma_{xyxy}$ ,

$$\begin{aligned} \frac{d}{d\Lambda} \Gamma_{c\ ij}^\Lambda(s, t, u) = T \sum_{\omega} \dot{g}^\Lambda(\omega) g^\Lambda(\omega + s) \sum_k \left[ \right. \\ \left. \Gamma_{c,ki}^\Lambda(s, \omega + \omega_1, \omega + \omega_2) \Gamma_{c,kj}^\Lambda(s, \omega - \omega_3, \omega - \omega_4) \right. \\ \left. + (\omega_1 \leftrightarrow \omega_2, \omega_3 \leftrightarrow \omega_4) \right]. \end{aligned} \quad (\text{A.1})$$

Since the vertices of type  $\Gamma_a$  and  $\Gamma_b$  are vanishing, it follows that the self energy must be zero as well and thus

$$\begin{aligned} g^\Lambda(i\omega_n) &= \frac{\omega_n}{\omega_n^2 + \Lambda^2}, \\ \dot{g}^\Lambda(i\omega_n) &= -\frac{2\Lambda}{\omega_n} g^2(i\omega_n). \end{aligned} \quad (\text{A.2})$$

Using that  $\Gamma_{c\ ij}^{\Lambda \rightarrow \infty} = -J_{ij}$  does not depend on any frequencies, we note that no dependence on  $t$  and  $u$  is generated from Eq. (A.1). The dominant contribution is the static component  $\Gamma_{c\ ij}^\Lambda(s=0) \equiv \Gamma_{c\ ij}^\Lambda$  for which

$$\begin{aligned} \frac{d}{d\Lambda} \Gamma_{c\ ij}^\Lambda &= -4\Lambda \sum_k \Gamma_{c,ki}^\Lambda \Gamma_{c,kj}^\Lambda T \sum_{\omega} \frac{(g^\Lambda(\omega))^3}{\omega}, \\ \frac{d}{d\Lambda} \Gamma_c^\Lambda(\mathbf{k}) &= -4\Lambda \Gamma_c^\Lambda(\mathbf{k})^2 T \sum_n \frac{\omega_n^2}{(\omega_n^2 + \Lambda^2)^3}, \end{aligned} \quad (\text{A.3})$$

where in the second step a Fourier transform to momentum space has been performed. The Matsubara sum may be evaluated exactly using the poles  $z_p \equiv i\omega_n =$

$\pm\Lambda$  to obtain

$$\begin{aligned} T \sum_n \frac{\omega_n^2}{(\omega_n^2 + \Lambda^2)^3} &= \sum_{z_p = \pm\Lambda} \text{Res} \left( \frac{z^2}{(z^2 - \Lambda^2)^3} n_F(z) \right) \Big|_{z=z_p} \\ &= \frac{\text{sech}^2\left(\frac{\beta\Lambda}{2}\right) \left( \sinh(\beta\Lambda) + \beta\Lambda \left( \beta\Lambda \tanh\left(\frac{\beta\Lambda}{2}\right) - 1 \right) \right)}{32\Lambda^3}. \end{aligned} \quad (\text{A.4})$$

Inserting this result into Eq. (A.3), the differential equation with  $\Gamma_c^{\Lambda \rightarrow \infty}(\mathbf{k}) = -J(\mathbf{k})$  has the exact solution

$$\begin{aligned} \Gamma_c^\Lambda(\mathbf{k}) &= -\frac{8J(\mathbf{k})\Lambda}{2J(\mathbf{k}) \tanh\left(\frac{\beta\Lambda}{2}\right) + \beta J(\mathbf{k})\Lambda \text{sech}^2\left(\frac{\beta\Lambda}{2}\right) + 8\Lambda}, \\ [\Gamma^{\Lambda=0}(\mathbf{k})]^{-1} &= -\frac{1}{4T} - \frac{1}{J(\mathbf{k})}, \end{aligned} \quad (\text{A.5})$$

in the simplified case of a single site per unit cell.

Below a critical temperature  $T_c^{\text{RPA}} = \frac{1}{4}J(\mathbf{k})$ , the RPA-vertex from Eq. (A.5) diverges before the end of the flow at  $\Lambda = 0$  is reached. This result exactly equals the one derived in Ref. [120], except here, no identification of  $\Lambda_c$  with  $T_c$  is necessary as Eq. (A.5) has been derived directly for arbitrary temperatures. Figure A.1 shows the flow of the RPA vertex in a nearest-neighbor cubic lattice where  $T_c^{\text{RPA}} = 1.5$ .

Interestingly, the full PMFRG solution is in stark contrast to bare RPA: While we could show here that the RPA's individually diverging contributions are contained in the PMFRG, no divergence at finite  $\Lambda$  is observed, in favor of a finite and smoothly flowing susceptibility as shown in Fig. 5.4. This beyond mean-field nature of the PMFRG, a result of the additional contributions from other channels, is quite surprising: In the closely related PFFRG formalism, a divergence of the RPA channel is often observed and, in particular, serves as the main indicator for the onset of magnetic order. In Chapter 4, we demonstrated that the absence of such an RPA-like divergence is extremely beneficial: The finite susceptibility which becomes physical at  $\Lambda = 0$  can be used in combination with a finite-size scaling analysis to obtain a more accurate estimate of critical temperatures.

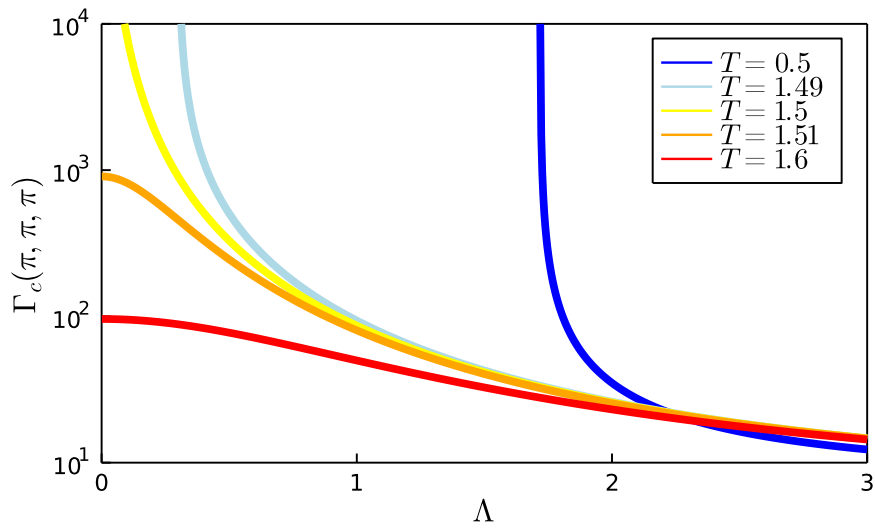


Figure A.1.: RPA solutions as a function of the cutoff  $\Lambda$  from Eq. (A.5) for the nearest-neighbor cubic lattice for different temperatures. The solution for the critical temperature  $T_c^{\text{RPA}} = \frac{6}{4} = 1.5$  (yellow) diverges exactly at  $\Lambda = 0$ , while at lower temperatures, the divergence is shifted to finite cutoffs.





# B

## Two-loop contributions within PMFRG

As detailed in previous works [195, 221], the one-loop FRG truncation can be extended by the inclusion of two-loop corrections using approximations based on the flow equation of the six-point vertex.

We start from the general form of the FRG flow equations, as found in Eq. (7.71) of Ref. [123] and expand the summations, neglecting all contributions from vertices with an odd number of legs as well as the eight-point vertex. For Majorana systems, the exchange statistics implies  $\mathbf{Z} = -1$  so that

$$\begin{aligned} \frac{d}{d\Lambda} \Gamma_{1,2,3,4,5,6}^{6,\Lambda} &= \frac{1}{2} \text{Tr} \left[ S_{1,2,3,4|5,6} \dot{\mathbf{G}}^{\Lambda} \mathbf{\Gamma}_{5,6}^{4,\Lambda} \mathbf{G}^{\Lambda} \mathbf{\Gamma}_{1,2,3,4}^{6,\Lambda} \right. & (a) \\ &+ S_{1,2|3,4,5,6} \dot{\mathbf{G}}^{\Lambda} \mathbf{\Gamma}_{3,4,5,6}^{6,\Lambda} \mathbf{G}^{\Lambda} \mathbf{\Gamma}_{1,2}^{4,\Lambda} & (b) \\ &+ S_{1,2|3,4|5,6} \dot{\mathbf{G}}^{\Lambda} \mathbf{\Gamma}_{5,6}^{4,\Lambda} \mathbf{G}^{\Lambda} \mathbf{\Gamma}_{3,4}^{4,\Lambda} \mathbf{G}^{\Lambda} \mathbf{\Gamma}_{1,2}^{4,\Lambda} & (c) \\ &+ \mathcal{O}(V_{\text{int}}^4). & (B.1) \end{aligned}$$

Bold quantities are matrices defined as  $[\mathbf{\Gamma}_{1,2,3,4}^{6,\Lambda}]_{5,6} = \Gamma_{5,6,1,2,3,4}^{6,\Lambda}$ .

This expression further contains the symmetrization operator  $S$  which ensures that the derivative of the six-point vertex is fully antisymmetric. Formally, it can be written as a sum over all permutations of indices with the appropriate sign together with a prefactor to prevent overcounting of already antisymmetric terms. For instance, the symmetrization  $S_{1,2,3,4|5,6}$  in term (a) of Eq. (B.1) contains a summation over all permutations of the numbers 1 to 6 as well as a prefactor  $\frac{1}{4!2!}$  since the expression is already antisymmetric in the first four and the last two indices. If we define the *outer* derivative  $\partial_{\Lambda}$  which only acts on the explicit  $\Lambda$ -dependence of two-point Green functions (treating  $\Sigma_{\Lambda}$  as a constant), we may write this as

$$\begin{aligned} \frac{d}{d\Lambda} \Gamma_{1,2,3,4,5,6}^{6,\Lambda} &= \frac{1}{2} \sum_{1', \dots, 4'} \left[ \partial_{\Lambda} \left( G_{1'2'}^{\Lambda} G_{3'4'}^{\Lambda} \right) S_{1,2|3,4,5,6} \Gamma_{2',3',3,4,5,6}^{6,\Lambda} \Gamma_{4',1',1,2}^{4,\Lambda} \right] \\ &+ \frac{1}{6} \sum_{1', \dots, 6'} \left[ \partial_{\Lambda} \left( G_{1'2'}^{\Lambda} G_{3'4'}^{\Lambda} G_{5'6'}^{\Lambda} \right) S_{1,2|3,4|5,6} \Gamma_{2',3',1,2}^{4,\Lambda} \Gamma_{4',5',3,4}^{4,\Lambda} \Gamma_{6',1',5,6}^{4,\Lambda} \right] \\ &+ \mathcal{O}(V_{\text{int}}^4) & (B.2) \end{aligned}$$

The defining step of the two-loop scheme is to promote the partial derivative to a full one which, in particular, also acts on vertex functions. The error generated by this step is of order  $\mathcal{O}(V^4)$  in the interaction and thus no larger than the error already present [195, 221]. The resulting equation can be integrated as a function of  $\Lambda$  and leads to a self-consistent equation for  $\Gamma^6$  for which in first iteration, we get

$$\begin{aligned}
 \Gamma_{1,2,3,4,5,6}^{6\ \Lambda} &= \frac{1}{12} \sum_{1',\dots,4'} \sum_{\beta_1,\dots,\beta_6} \left[ G_{1'2'}^\Lambda G_{3'4'}^\Lambda S_{1,2|3,4,5,6} \Gamma_{4',1',1,2}^{4,\ \Lambda} \right. \\
 &\quad \times \left( G_{\beta_1\beta_2}^\Lambda G_{\beta_3\beta_4}^\Lambda G_{\beta_5\beta_6}^\Lambda S_{1',2'|3,4|5,6} \Gamma_{\beta_2,\beta_3,2',3'}^{4,\ \Lambda} \Gamma_{\beta_4,\beta_5,3,4}^{4,\ \Lambda} \Gamma_{\beta_6,\beta_1,5,6}^{4,\ \Lambda} \right) \\
 &\quad \left. + \frac{1}{6} \sum_{1',\dots,6'} \left[ \left( G_{1'2'}^\Lambda G_{3'4'}^\Lambda G_{5'6'}^\Lambda \right) S_{1,2|3,4|5,6} \Gamma_{2',3',1,2}^{4,\ \Lambda} \Gamma_{4',5',3,4}^{4,\ \Lambda} \Gamma_{6',1',5,6}^{4,\ \Lambda} \right] + \mathcal{O}(V_{\text{int}}^4) \right].
 \end{aligned} \tag{B.3}$$

Figure 3.1 shows the diagrammatic form of this equation. While the first term is of fourth order in the interaction and will not be considered explicitly, we note that some of its contributions are precisely those generated by the Katanin substitution as detailed in Ref. [195].

In the same way, some of the derived two-loop contributions are equivalent to Katanin corrections of the one-loop flow equations. Naturally, the next step will be to identify these terms and omit them to prevent overcounting. Doing so requires explicitly evaluating all permutations generated by the symmetrization operator  $S$ . Initially, now using the shorthand notation  $\Gamma^4 \rightarrow \Gamma$ , we thus have

$$\begin{aligned}
 \frac{d}{d\Lambda} \Gamma_{1,2,3,4}^\Lambda &\equiv \dot{\Gamma}_{1,2,3,4}^{\Lambda\ 1L} + \dot{\Gamma}_{1,2,3,4}^{\Lambda\ 2L} \\
 \dot{\Gamma}_{1,2,3,4}^{\Lambda\ 2L} &= -\frac{1}{12} \sum_{1',2'} \dot{G}_{1',2'}^\Lambda \sum_{\beta_1,\dots,\beta_6} \left[ \right. \\
 &\quad \left. \left( G_{\beta_1\beta_2}^\Lambda G_{\beta_3\beta_4}^\Lambda G_{\beta_5\beta_6}^\Lambda \right) S_{1',2'|1,2|3,4} \Gamma_{\beta_2,\beta_3,1',2'}^\Lambda \Gamma_{\beta_4,\beta_5,1,2}^\Lambda \Gamma_{\beta_6,\beta_1,3,4}^\Lambda \right].
 \end{aligned} \tag{B.4}$$

Here,  $\dot{\Gamma}_{1,2,3,4}^{\Lambda\ 1L}$  refers to the three one-loop terms in Eq. (2.18c), which do not originate from the six-point vertex.

Expanding the symmetrization naïvely generates  $6! = 720$  permutations, however many of these are equivalent. Most importantly, all trivial permutations that exchange two indices on the same vertex are divided out by definition of  $S$ . This means we only need to consider  $\frac{720}{2! \cdot 2! \cdot 2!} = 90$  terms. Since we do not want to include terms which are given by the Katanin correction to the one-loop procedure, we will then neglect all diagrams in which a single vertex is contracted by the single-scale

---


$$\begin{aligned}
X_{1,2|3,4}^\Lambda &= \begin{array}{c} \text{Diagram 1} \\ \text{Diagram 2} \end{array} \equiv \begin{array}{c} \text{Diagram 3} \\ \text{Diagram 4} \end{array} \\
Y_{1,2|3,4}^\Lambda &= - \begin{array}{c} \text{Diagram 5} \\ \text{Diagram 6} \end{array} - \begin{array}{c} \text{Diagram 7} \\ \text{Diagram 8} \end{array}
\end{aligned}$$

Figure B.1.: One-loop and two-loop bubble functions from Eqs. (B.6) and (2.18d).

propagator, i.e. those where  $1'$  and  $2'$  appear on the same vertex. Hence, only 72 diagrams remain, 24 for each the  $s$ ,  $t$  and  $u$  channel.

It is helpful to note that  $t$  and  $u$  channels are given by re-labeling external indices of the  $s$ -channel, i.e. the first of the terms in Eq. (2.18c). Thus, we only need to consider the  $s$ -channel, which is defined by a pairing of either the indices 1 and 2 on one of the vertices or 3 and 4. Using the freedom to relabel internal site indices in the summation, only two distinct diagrams remain, one where 1 and 2 appear together on a vertex and the other two appear separately on the other two vertices and vice versa. In close analogy to the previous one-loop notation, we may then define

$$\dot{\Gamma}_{1,2,3,4}^{\Lambda, 2L} = Y_{1,2|3,4}^\Lambda - Y_{1,3|2,4}^\Lambda + Y_{1,4|2,3}^\Lambda \quad (\text{B.5})$$

$$Y_{1,2|3,4}^\Lambda = - \sum_{1', \dots, 4'} G_{1', 2'}^\Lambda G_{3', 4'}^\Lambda \left( \Gamma_{1, 2, 4', 2'}^\Lambda X_{3, 3'|4, 1'}^\Lambda + \Gamma_{1', 3', 3, 4}^\Lambda X_{2', 1|4', 2}^\Lambda \right), \quad (\text{B.6})$$

where  $Y_{1,2|3,4}^\Lambda$  defines the  $s$ -channel of the two-loop bubble function and is anti-symmetric under permutations of the first and last two indices as visible from Fig. B.1. Since Eq. (B.6) takes an analogous expression as the one-loop equations, using pre-computed one-loop bubble functions, computing the two-loop contributions amounts the same numerical complexity as the one-loop terms and thus approximately doubles the numerical effort.

## B.1. Parametrization

As usual, an efficient implementation requires the explicit parametrization of vertices in analogy to Ref. [1]. This parametrization is equivalent for both the one-loop ( $X$ ) and the two-loop bubble-functions  $Y$  so that for brevity we shall only write the results for  $X$  explicitly. It is evident from their definitions that the bilocal property of vertices carries over to  $X$  and  $Y$  due to the local nature of propagators. In the case of vertices, it is possible to re-arrange indices such that they are always of the form  $\Gamma_{ii'jj'}^\Lambda$ , however, for  $X$  and  $Y$  only the first and last two indices may be interchanged and hence we need to distinguish two distinct types of bubble-functions upon real-space parametrization

$$\begin{aligned} X_{ij}^\Lambda &\equiv X_{ii'jj'}^\Lambda \\ \tilde{X}_{i\neq j}^\Lambda &\equiv X_{ij|ij}^\Lambda, \quad \tilde{X}_{ii}^\Lambda = X_{ii}^\Lambda. \end{aligned} \quad (\text{B.7})$$

Physically,  $X_{ij}^\Lambda$  corresponds to an RPA-type contribution in which a summation over all sites occurs. This can be seen from Fig. B.1, where after external site indices are inserted, the propagators carry an internal site index  $k$  which may differ from both  $i$  and  $j$  in contrast to  $\tilde{X}_{ij}$ . Furthermore, energy conservation implies  $X(\omega_1, \omega_2 | \omega_3, \omega_4) \propto \delta_{\omega_1 + \omega_2 + \omega_3 + \omega_4, 0}$  and equally for  $Y$  which allows the usual definition via only three exchange frequencies  $s, t, u$ . Subsequently, summations over flavors may be computed explicitly by making use of the global  $SO(3)$  symmetry to distinguish three  $X$ -types  $X_a, X_b, X_c$  and four  $\tilde{X}$ -type vertices  $\tilde{X}_a, \tilde{X}_b, \tilde{X}_c, \tilde{X}_d$ . Here, the labels  $a \dots d$  are defined as sets of flavor indices:

$$a \equiv xx|xx \quad b \equiv xx|yy \quad c \equiv xy|xy \quad d \equiv xy|yx. \quad (\text{B.8})$$

All other combinations of flavors are either zero (e.g. the types  $xx|yz$ ), or may be transformed into the ones above via global  $SO(3)$  rotations (e.g.  $zz|xx \rightarrow xx|yy$ ). The  $d$  type channels need to be defined since the first and last two indices may no longer be permuted separately for  $\tilde{X}$  type vertices. This finally allows us to write Eq. (B.6) as:

$$\dot{\Gamma}_a^{\Lambda \text{ 2L}}(s, t, u) = Y_a^\Lambda(s, t, u) - \tilde{Y}_a^\Lambda(t, s, u) + \tilde{Y}_a^\Lambda(u, s, t) \quad (\text{B.9a})$$

$$\dot{\Gamma}_b^{\Lambda \text{ 2L}}(s, t, u) = Y_b^\Lambda(s, t, u) - \tilde{Y}_c^\Lambda(t, s, u) + \tilde{Y}_c^\Lambda(u, s, t) \quad (\text{B.9b})$$

$$\dot{\Gamma}_c^{\Lambda \text{ 2L}}(s, t, u) = Y_c^\Lambda(s, t, u) - \tilde{Y}_b^\Lambda(t, s, u) + \tilde{Y}_d^\Lambda(u, s, t) \quad (\text{B.9c})$$

where  $\tilde{Y}_d^{\Lambda \text{ 2L}}(s, t, u) = -\tilde{Y}_c^{\Lambda \text{ 2L}}(s, u, t) = -Y_c^\Lambda(s, u, t)$  and the definitions of  $Y_a$  etc. are given in Section B.2.

## B.2. Symmetries

For the numerical implementation of the  $X$ ,  $\tilde{X}$ ,  $Y$  and  $\tilde{Y}$ -terms, symmetries of the transfer frequencies  $s, t$  and  $u$  are crucial. In analogy to Ref. [1], the identities summarized in Table B.1 can be proven.

Operation	$X_{\mu, ij}^{\Lambda}(s, t, u)$	$\tilde{X}_{\mu, ij}^{\Lambda}(s, t, u)$
$1 \leftrightarrow 2$	$X_{a/b}(s, t, u)$ $\leftrightarrow -X_{a/b}(s, u, t)$	not allowed
$T \circ (1, 3) \leftrightarrow (2, 4)$	$s \leftrightarrow -s$	$s \leftrightarrow -s, i \leftrightarrow j$
$T \circ (1, 2) \leftrightarrow (3, 4)$	$t \leftrightarrow -t, i \leftrightarrow j$	$t \leftrightarrow -t$
$T \circ (1, 2) \leftrightarrow (4, 3)$	$u \leftrightarrow -u, i \leftrightarrow j$	$u \leftrightarrow -u, i \leftrightarrow j$

Table B.1.: Transformations of the frequency arguments under time reversal  $T$  and specific permutations of indices in  $X_{1,2|3,4}^{\Lambda ij}$  and  $\tilde{X}_{1,2|3,4}^{\Lambda ij}$ . The exchange  $1 \leftrightarrow 2$  would change  $X_c$  to the form  $X_{xyyx}$  and  $\tilde{X}$  to  $X_{ji|ij}$ . Hence, the resulting symmetries take the slightly different form in Eq. (B.13). Equivalent relations hold for  $X^{\Lambda} \rightarrow Y^{\Lambda}$  and  $\tilde{X}^{\Lambda} \rightarrow \tilde{Y}^{\Lambda}$ .

Finally, we prove an identity which eliminates the need of implementing a flow equation for the  $d$ -type-bubble functions. With the starting equation Eq. (B.10a) being a result of global  $SO(3)$  symmetry as proven in Ref. [1] we have:

$$\Gamma_{xxxx}^{\Lambda, \mu} = \Gamma_{xxyy}^{\Lambda, \mu} + \Gamma_{xyxy}^{\Lambda, \mu} + \Gamma_{xyyx}^{\Lambda, \mu} \quad (\text{B.10a})$$

$$\Rightarrow X_{xx|xx}^{\Lambda, \mu} = X_{xx|yy}^{\Lambda, \mu} + X_{xy|xy}^{\Lambda, \mu} + X_{xy|yx}^{\Lambda, \mu} \quad (\text{B.10b})$$

$$\Rightarrow Y_{xx|xx}^{\Lambda, \mu} = Y_{xx|yy}^{\Lambda, \mu} + Y_{xy|xy}^{\Lambda, \mu} + Y_{xy|yx}^{\Lambda, \mu}, \quad (\text{B.10c})$$

where  $\mu \equiv (i_1, i_2, i_3, i_4, \omega_1, \omega_2, \omega_3, \omega_4)$  refers to an arbitrary fixed set of site and frequencies, noting that no use of permutation symmetry is made in the following. To demonstrate that Eqs. (B.10b) and (B.10c) follow from Eq. (B.10a), the latter is inserted into the definitions of the one-loop and two-loop channel functions Eqs. (B.6) and (2.18d). Using that propagators are diagonal and computing the flavor summation first before any site or frequency parametrization is applied, we obtain

$$X_{\alpha_1 \alpha_2 | \alpha_3 \alpha_4}^{\Lambda, \mu} \sim \sum_{\beta_1, \beta_3} \Gamma_{\alpha_1 \alpha_2 | \beta_3 \beta_1}^{\Lambda, \nu} \Gamma_{\beta_1 \beta_3 | \alpha_3 \alpha_4}^{\Lambda, \rho}. \quad (\text{B.11})$$

Here, for convenience of notation, the propagators are kept only implicitly. After inserting external flavor labels on the left, the summation can be carried out so

that

$$\begin{aligned}
 X_{xx|xx}^{\Lambda, \mu} &\sim \Gamma_{xxx}^{\Lambda, \nu} \Gamma_{xxx}^{\Lambda, \rho} + 2\Gamma_{xxy}^{\Lambda, \nu} \Gamma_{xxy}^{\Lambda, \rho} \\
 X_{xx|yy}^{\Lambda, \mu} &\sim \Gamma_{xxy}^{\Lambda, \nu} \Gamma_{xxx}^{\Lambda, \rho} + \Gamma_{xxx}^{\Lambda, \nu} \Gamma_{xxy}^{\Lambda, \rho} + \Gamma_{xxy}^{\Lambda, \nu} \Gamma_{xxy}^{\Lambda, \rho} \\
 X_{xy|xy}^{\Lambda, \mu} &\sim \Gamma_{xyx}^{\Lambda, \nu} \Gamma_{xxy}^{\Lambda, \rho} + \Gamma_{xxy}^{\Lambda, \nu} \Gamma_{xyx}^{\Lambda, \rho} \\
 X_{xy|yx}^{\Lambda, \mu} &\sim \Gamma_{xyx}^{\Lambda, \nu} \Gamma_{xyx}^{\Lambda, \rho} + \Gamma_{xyx}^{\Lambda, \nu} \Gamma_{xyx}^{\Lambda, \rho}.
 \end{aligned} \tag{B.12}$$

Equation (B.10b) may then be proven by inserting these expressions into it and subsequently using Eq. (B.10a) on all occurring instances of  $\Gamma^\nu$  and  $\Gamma^\rho$  to verify the equivalence of the left and right hand side. This procedure may be repeated for the definition of the two-loop contributions to finally prove Eq. (B.10c).

As a result of this symmetry, we do not need to compute  $X_c^\Lambda(s, u, t)$  and  $Y_c^\Lambda(s, u, t)$  for  $t > u$  and in particular no flow equation is required for  $\tilde{X}_d^\Lambda$  and  $\tilde{Y}_d^\Lambda$  since Eq. (B.10b) can be written as

$$X_c^\Lambda(s, u, t) = \left( -X_a^\Lambda + X_b^\Lambda + X_c^\Lambda \right) (s, t, u) \tag{B.13a}$$

$$\tilde{X}_d^\Lambda(s, t, u) = \left( \tilde{X}_a^\Lambda - \tilde{X}_b^\Lambda - \tilde{X}_c^\Lambda \right) (s, t, u). \tag{B.13b}$$

### Explicit parametrization of bubble functions

Using the one-loop bubble functions  $X$  and  $\tilde{X}$  from Ref. [1], the two-loop bubble functions can be given explicitly. In the equations below, the propagator is  $i\mathcal{G}_i^\Lambda(\omega) = \frac{\omega}{\omega^2 + \omega\gamma_i(\omega) + \Lambda^2}$ , with  $\gamma_i(\omega) = i\Sigma_i(\omega)$ . While the site index is kept here for generality, it can be dropped in the case of lattices consisting of equivalent sites

only.

$$\begin{aligned}
 Y_a^\Lambda{}_{ij} = -T \sum_\omega \sum_k \mathcal{G}_k(\omega) \mathcal{G}_k(s + \omega) [ & \\
 & \left( \Gamma_{a\ ki}^\Lambda(s, \omega + \omega_1, \omega + \omega_2) \tilde{X}_{a\ kj}^\Lambda(\omega - \omega_4, s, \omega - \omega_3) \right. \\
 & \left. + \Gamma_{a\ kj}^\Lambda(s, \omega - \omega_3, \omega - \omega_4) \tilde{X}_{a\ ki}^\Lambda(\omega + \omega_2, s, \omega + \omega_1) \right) \\
 & \left. + 2(\Gamma_a^\Lambda \rightarrow \Gamma_b^\Lambda, \tilde{X}_a^\Lambda \rightarrow \tilde{X}_c^\Lambda) \right] \quad (\text{B.14a})
 \end{aligned}$$

$$\begin{aligned}
 Y_b^\Lambda{}_{ij} = -T \sum_\omega \sum_k \mathcal{G}_k(\omega) \mathcal{G}_k(s + \omega) [ & \\
 & \left( \Gamma_{b\ ki}^\Lambda(s, \omega + \omega_1, \omega + \omega_2) \tilde{X}_{a\ kj}^\Lambda(\omega - \omega_4, s, \omega - \omega_3) \right. \\
 & \left. + \Gamma_{b\ kj}^\Lambda(s, \omega - \omega_3, \omega - \omega_4) \tilde{X}_{a\ ki}^\Lambda(\omega + \omega_2, s, \omega + \omega_1) \right) \\
 & \left. + (\Gamma_b^\Lambda \rightarrow \Gamma_a^\Lambda, \tilde{X}_a^\Lambda \rightarrow \tilde{X}_c^\Lambda) + (\tilde{X}_a^\Lambda \rightarrow \tilde{X}_c^\Lambda) \right] \quad (\text{B.14b})
 \end{aligned}$$

$$\begin{aligned}
 Y_c^\Lambda{}_{ij} = -T \sum_\omega \sum_k \mathcal{G}_k(\omega) \mathcal{G}_k(s + \omega) [ & \\
 & \Gamma_{c\ ki}^\Lambda(s, \omega + \omega_2, \omega + \omega_1) \tilde{X}_{b\ kj}^\Lambda(\omega - \omega_4, s, \omega - \omega_3) \\
 & + \Gamma_{c\ kj}^\Lambda(s, \omega - \omega_4, \omega - \omega_3) \tilde{X}_{b\ ki}^\Lambda(\omega + \omega_2, s, \omega + \omega_1) \\
 & - \Gamma_{c\ ki}^\Lambda(s, \omega + \omega_1, \omega + \omega_2) \tilde{X}_{d\ kj}^\Lambda(\omega - \omega_4, s, \omega - \omega_3) \\
 & \left. - \Gamma_{c\ kj}^\Lambda(s, \omega - \omega_3, \omega - \omega_4) \tilde{X}_{d\ ki}^\Lambda(\omega + \omega_2, s, \omega + \omega_1) \right] \quad (\text{B.14c})
 \end{aligned}$$

$$\begin{aligned}
 \tilde{Y}_a^\Lambda{}_{ij} = -T \sum_\omega \mathcal{G}_i(\omega) \mathcal{G}_j(s + \omega) [ & \\
 & \left( \Gamma_{a\ ji}^\Lambda(\omega - \omega_3, s, \omega - \omega_4) \tilde{X}_{a\ ji}^\Lambda(\omega + \omega_2, \omega + \omega_1, s) \right. \\
 & \left. + \Gamma_{a\ ji}^\Lambda(\omega + \omega_1, s, \omega + \omega_2) \tilde{X}_{a\ ji}^\Lambda(\omega - \omega_4, \omega - \omega_3, s) \right) \\
 & \left. + 2(\Gamma_a^\Lambda \rightarrow \Gamma_c^\Lambda, \tilde{X}_a^\Lambda \rightarrow \tilde{X}_d^\Lambda) \right] \\
 -T \sum_\omega \mathcal{G}_j(\omega) \mathcal{G}_i(s + \omega) [ & \\
 & \left( \Gamma_{a\ ij}^\Lambda(\omega + \omega_2, s, \omega + \omega_1) X_{a\ ij}^\Lambda(\omega - \omega_4, s, \omega - \omega_3) \right. \\
 & \left. + \Gamma_{a\ ij}^\Lambda(\omega - \omega_4, s, \omega - \omega_3) X_{a\ ij}^\Lambda(\omega + \omega_2, s, \omega + \omega_1) \right) \\
 & \left. + 2(\Gamma_a^\Lambda \rightarrow \Gamma_c^\Lambda, X_a^\Lambda \rightarrow X_c^\Lambda) \right] \quad (\text{B.15a})
 \end{aligned}$$

$$\begin{aligned}
 \tilde{Y}_b^\Lambda{}_{ij} = & -T \sum_{\omega} \mathcal{G}_i(\omega) \mathcal{G}_j(s + \omega) \left[ \right. \\
 & \left( \Gamma_c^\Lambda{}_{ji}(\omega + \omega_1, s, \omega + \omega_2) \tilde{X}_a^\Lambda{}_{ji}(\omega - \omega_4, \omega - \omega_3, s) \right. \\
 & \left. + \Gamma_c^\Lambda{}_{ji}(\omega - \omega_3, s, \omega - \omega_4) \tilde{X}_a^\Lambda{}_{ji}(\omega + \omega_2, \omega + \omega_1, s) \right) \\
 & \left. + (\Gamma_c^\Lambda \rightarrow \Gamma_a^\Lambda, \tilde{X}_a^\Lambda \rightarrow \tilde{X}_d^\Lambda) + (\tilde{X}_a^\Lambda \rightarrow \tilde{X}_d^\Lambda) \right] \\
 & -T \sum_{\omega} \mathcal{G}_j(\omega) \mathcal{G}_i(s + \omega) \left[ \right. \\
 & \left( \Gamma_a^\Lambda{}_{ij}(\omega + \omega_2, s, \omega + \omega_1) X_c^\Lambda{}_{ij}(\omega - \omega_4, s, \omega - \omega_3) \right. \\
 & \left. + \Gamma_a^\Lambda{}_{ij}(\omega - \omega_4, s, \omega - \omega_3) X_c^\Lambda{}_{ij}(\omega + \omega_2, s, \omega + \omega_1) \right) \\
 & \left. + (\Gamma_a^\Lambda \rightarrow \Gamma_c^\Lambda, X_c^\Lambda \rightarrow X_a^\Lambda) + (\Gamma_a^\Lambda \rightarrow \Gamma_c^\Lambda) \right] \quad (\text{B.15b})
 \end{aligned}$$

$$\begin{aligned}
 \tilde{Y}_c^\Lambda{}_{ij} = & T \sum_{\omega} \mathcal{G}_i(\omega) \mathcal{G}_j(s + \omega) \left[ \right. \\
 & \left( \Gamma_c^\Lambda{}_{ji}(\omega + \omega_1, \omega + \omega_2, s) \tilde{X}_b^\Lambda{}_{ji}(\omega - \omega_4, \omega - \omega_3, s) \right. \\
 & \left. + \Gamma_c^\Lambda{}_{ji}(\omega - \omega_3, \omega - \omega_4, s) \tilde{X}_b^\Lambda{}_{ji}(\omega + \omega_2, \omega + \omega_1, s) \right) \\
 & \left. + (\Gamma_c^\Lambda \rightarrow \Gamma_b^\Lambda, \tilde{X}_b^\Lambda \rightarrow \tilde{X}_c^\Lambda) \right] \\
 & -T \sum_{\omega} \mathcal{G}_j(\omega) \mathcal{G}_i(s + \omega) \left[ \right. \\
 & \left( \Gamma_b^\Lambda{}_{ij}(\omega + \omega_2, \omega + \omega_1, s) X_b^\Lambda{}_{ij}(\omega - \omega_4, \omega - \omega_3, s) \right. \\
 & \left. + \Gamma_b^\Lambda{}_{ij}(\omega - \omega_4, \omega - \omega_3, s) X_b^\Lambda{}_{ij}(\omega + \omega_2, \omega + \omega_1, s) \right) \\
 & \left. + (\Gamma_b^\Lambda \rightarrow \Gamma_c^\Lambda, X_b^\Lambda \rightarrow X_c^\Lambda) \right] \quad (\text{B.15c})
 \end{aligned}$$

and as a consequence of Eq. (B.10c)

$$\tilde{Y}_d^\Lambda{}_{ij} = \tilde{Y}_a^\Lambda{}_{ij}(s, t, u) - \tilde{Y}_b^\Lambda{}_{ij}(s, t, u) - \tilde{Y}_c^\Lambda{}_{ij}(s, t, u). \quad (\text{B.15d})$$



## Parquet formalism for Majorana fermions

In this section, parquet equations for interacting Majorana fermions are derived from first principles. We proceed in close analogy to Ref. [222], where the complementary calculation for complex fermions has been carried out. To begin with, let us introduce the basic objects relevant for the derivation, namely, generating functionals and their derivatives. We consider the Majorana action

$$S[\eta] = -\frac{1}{2}(\eta, g_0^{-1}\eta) + \frac{1}{4!}\Gamma_{0,a_1a_2a_3a_4}\eta_{a_1}\eta_{a_2}\eta_{a_3}\eta_{a_4}, \quad (\text{C.1})$$

where equal indices are summed over. Here,  $\eta_a$  is a Grassmann valued field with the multi-index  $\alpha$  encompassing its relevant quantum numbers and  $(\eta, g_0^{-1}\eta) \equiv \eta_{a_1}g_{0,a_1a_2}^{-1}\eta_{a_2}$ . The matrix  $g_0$  is closely related to the bare propagator  $G_0$  via

$$G_{0,a_1a_2} = \langle \eta_{a_2}\eta_{a_1} \rangle_0 = -g_{0,a_2a_1}, \quad (\text{C.2})$$

where  $\langle \cdot \rangle_0$  denotes the Gaussian average. To set up the diagrammatic formalism, we define the partition function in the presence of external (Majorana) source fields  $h$  as

$$Z[h] = \int D[\eta] e^{-S[\eta]+(h,\eta)}, \quad (\text{C.3})$$

where  $Z_0$  denotes the partition function for the Gaussian action. We can now introduce the generating functional

$$\mathcal{G}_c[h] = \ln \left( \frac{Z[h]}{Z_0} \right), \quad (\text{C.4})$$

from which the  $n$ -point connected correlation function  $G_c^{(n)}$  is obtained as

$$G_{c,a_1\dots a_n}^{(n)} = \frac{\delta^n \mathcal{G}_c[h]}{\delta h_{a_n} \dots \delta h_{a_1}} \Big|_{h \rightarrow 0}. \quad (\text{C.5})$$

Here and in the following,  $\frac{\delta}{\delta f} = \overleftarrow{\frac{\delta}{\delta f}}$  for an arbitrary Grassmann field  $f$  is to be understood as a left-derivative. For our purposes, the one- and two-particle correlators  $G_c^{(2)}$  and  $G_c^{(4)}$  are most relevant. Using Eq. (C.4), they can be straightforwardly computed and evaluate to

$$\begin{aligned} G_{c,a_1a_2}^{(2)} &= G_{a_1a_2}^{(2)} = G_{a_1a_2} \\ G_{c,a_1a_2a_3a_4}^{(4)} &= G_{a_1a_2a_3a_4}^{(4)} - G_{a_1a_2}G_{a_3a_4} + G_{a_1a_3}G_{a_2a_4} - G_{a_1a_4}G_{a_2a_3}, \end{aligned} \quad (\text{C.6})$$

where  $G^{(2)}$  and  $G^{(4)}$  denote the disconnected one- and two-particle Green functions generated by  $\mathcal{G}[h] = \frac{Z[h]}{Z[h=0]}$ . Note that we have assumed vanishing Majorana-odd correlators in order to derive these identities. This is because they are generally not invariant under local  $\mathbb{Z}_2$  gauge transformations, which becomes important for the Majorana representation of spin operators discussed in Chapter 2. Finally, we can amputate propagators from the connected four-point correlator to obtain the one-particle irreducible (1PI) vertex  $\Gamma$  as

$$\Gamma_{b_1 b_2 b_3 b_4} = -G_{b_1 a_1}^{-1} G_{b_2 a_2}^{-1} G_{b_3 a_3}^{-1} G_{b_4 a_4}^{-1} G_{c, a_1 a_2 a_3 a_4}^{(4)}. \quad (\text{C.7})$$

The remainder of this section is divided into two parts. In the first part, the derivation of the Schwinger-Dyson equation, which expresses the self-energy  $\Sigma$  in terms of the Majorana vertex  $\Gamma$ , is presented. In a subsequent step, we derive a self-consistent decomposition of  $\Gamma$  itself, allowing us to group its contributions in terms of their two-particle reducibility.

## C.1. Schwinger-Dyson equation

We begin by noting that  $Z[h]$  can alternatively be written as

$$Z[h] = \int D[\eta] e^{-S[\eta-\epsilon] + (h, \eta-\epsilon)}, \quad (\text{C.8})$$

where we performed the substitution  $\eta \rightarrow \eta - \epsilon$ , for which the increment  $D[\eta]$  is invariant. Recall that for complex fermions, where conjugate fields also need to be included, one has to consider the employed shift separately in both the original and the conjugate field and prove that the final results are equivalent. This complication is, however, absent here. Expanding the integrand to linear order in  $\epsilon$ , we obtain (up to  $\mathcal{O}(\epsilon^2)$  corrections)

$$e^{-S[\eta-\epsilon] + (h, \eta-\epsilon)} = e^{-S[\eta] + (h, \eta)} + \left[ \left( h_b - \frac{\delta S[\eta - \epsilon]}{\delta \epsilon_b} \right) e^{-S[\eta-\epsilon] + (h, \eta-\epsilon)} \right]_{\epsilon=0} \epsilon_b, \quad (\text{C.9})$$

and by counting powers in  $\epsilon$ , it can be shown that

$$\left[ \frac{\delta S[\eta - \epsilon]}{\delta \epsilon_b} \right]_{\epsilon=0} = g_{0, b a_2}^{-1} \eta_{a_2} - \frac{1}{6} \Gamma_{0, b a_2 a_3 a_4} \eta_{a_2} \eta_{a_3} \eta_{a_4} = -\frac{\delta S[\eta]}{\delta \eta_b}. \quad (\text{C.10})$$

Combining Eqs. (C.8), (C.9) & (C.10) we thus find the identity

$$0 = \int D[\eta] \left( h_b + \frac{\delta S[\eta]}{\delta \eta_b} \right) e^{-S[\eta] + (h, \eta)}. \quad (\text{C.11})$$

Taking the derivative  $\frac{\delta}{\delta h_{b'}}$  and pursuing the limit  $h \rightarrow 0$  yields

$$0 = \int D[\eta] \left( \delta_{bb'} - \frac{\delta S[\eta]}{\delta \eta_b} \eta_{b'} \right) e^{-S[\eta]} = \delta_{bb'} Z - \int D[\eta] \frac{\delta S[\eta]}{\delta \eta_b} \eta_{b'} e^{-S[\eta]}, \quad (\text{C.12})$$

and by multiplying with  $\frac{1}{Z}$  we thus obtain

$$\begin{aligned} 0 &= \delta_{bb'} + g_{0,ba_2}^{-1} G_{b'a_2} - \frac{1}{6} \Gamma_{0,ba_2a_3a_4} G_{b'a_4a_3a_2}^{(4)} \\ &= \delta_{bb'} - G_{b'a_2} G_{0,a_2b}^{-1} - \frac{1}{6} \Gamma_{0,ba_2a_3a_4} G_{b'a_4a_3a_2}^{(4)}. \end{aligned} \quad (\text{C.13})$$

As a last step, we add a factor  $G_{ab'}^{-1}$  to both sides, which yields

$$\Sigma_{ab} = -\frac{1}{6} \Gamma_{0,ba_2a_3a_4} G_{ab'}^{-1} G_{b'a_4a_3a_2}^{(4)}, \quad (\text{C.14})$$

where we identified  $G_{ab}^{-1} - G_{0,ab}^{-1} = -\Sigma_{ab}$  via the Dyson identity. Using Eqs. (C.6) & (C.7) the disconnected four-point correlator  $G^{(4)}$  can be expressed by another 1PI vertex, which yields

$$\Sigma_{ab} = -\frac{1}{2} \Gamma_{0,baa_3a_4} G_{a_4a_3} + \frac{1}{6} \Gamma_{0,ba_2a_3a_4} G_{a_4c_4} G_{a_3c_3} G_{a_2c_2} \Gamma_{ac_4c_3c_2}. \quad (\text{C.15})$$

Using the antisymmetry of  $G$  and  $\Gamma$  under pairwise permutations of their respective indices, we have finally obtained the Schwinger-Dyson equation

$$\Sigma_{ab} = -\frac{1}{2} \Gamma_{0,aba_3a_4} G_{a_3a_4} + \frac{1}{6} \Gamma_{0,aa_2a_3a_4} G_{a_4c_4} G_{a_3c_3} G_{a_2c_2} \Gamma_{bc_2c_3c_4}, \quad (\text{C.16})$$

which is diagrammatically displayed in Fig. 3.2(b).

### Vertex decomposition and Bethe-Salpeter equations

Similar to the derivation of the Schwinger-Dyson equation, we first introduce a modified partition function

$$Z[H] = \int D[\eta] e^{-S[\eta] + \frac{1}{2}(\eta, H\eta)}, \quad (\text{C.17})$$

where  $(\eta, H\eta) = \eta_a H_{ab} \eta_b$ . The source field  $H$  is understood as a product of two Grassmann fields (e.g.,  $H_{ab} = h_a h_b$ ) and is therefore Grassmann-even and antisymmetric with respect to its indices, i.e.,  $H_{ab} = -H_{ba}$ . Consequently, we

can define the generating functional  $\tilde{\mathcal{G}}[H] = \ln\left(\frac{Z[H]}{Z_0}\right)$ , whose first and second functional derivatives evaluate to

$$\left.\frac{\delta\tilde{\mathcal{G}}[H]}{\delta H_{a_1a_2}}\right|_{H\rightarrow 0} = G_{a_1a_2}, \quad (\text{C.18})$$

and

$$\left.\frac{\delta^2\tilde{\mathcal{G}}[H]}{\delta H_{a_3a_4}\delta H_{a_1a_2}}\right|_{H\rightarrow 0} = G_{a_1a_2a_3a_4}^{(4)} - G_{a_1a_2}G_{a_3a_4} \equiv \chi_{a_1a_2|a_3a_4}. \quad (\text{C.19})$$

The horizontal line in the subscripts of  $\chi$  indicates that this vertex is antisymmetric under permutations within either the first or second set of indices. Our goal is to find an independent expression involving  $\chi$  to determine it self-consistently. We begin with the trivial identity.

$$G_{a_1b}[H]G_{ba_2}^{-1}[H] = \delta_{a_1a_2}, \quad (\text{C.20})$$

where  $G_{a_1a_2}[H]$  is defined by Eq. (C.18) without the limit  $H \rightarrow 0$ . Computing the derivative  $\frac{\delta}{\delta H_{a_3a_4}}$  using the Leibniz rule, we find

$$\frac{\delta G_{a_1a_2}[H]}{\delta H_{a_3a_4}} = -G_{a_1b_1}[H]\frac{\delta G_{b_1b_2}^{-1}[H]}{\delta H_{a_3a_4}}G_{b_2a_2}[H]. \quad (\text{C.21})$$

The derivative on the right hand side can also be expressed via the Dyson identity

$$\frac{\delta G_{a_1a_2}^{-1}[H]}{\delta H_{a_3a_4}} = \frac{\delta G_{0,a_1a_2}^{-1}[H]}{\delta H_{a_3a_4}} - \frac{\delta \Sigma_{a_1a_2}[H]}{\delta H_{a_3a_4}}. \quad (\text{C.22})$$

To continue, we recall that the self energy has a skeleton expansion  $\Sigma[H] = \Sigma[G[H], \Gamma_0]$  allowing us to rephrase

$$\frac{\delta \Sigma_{a_1a_2}[H]}{\delta H_{a_3a_4}} = \frac{\delta G_{b_1b_2}[H]}{\delta H_{a_3a_4}} \frac{\delta \Sigma_{a_1a_2}[H]}{\delta G_{b_1b_2}[H]}. \quad (\text{C.23})$$

Combining this result with Eqs. (C.21) & (C.22) we find

$$\frac{\delta G_{a_1a_2}[H]}{\delta H_{a_3a_4}} = -G_{a_1b_1}[H] \left( \frac{\delta G_{0,b_1b_2}^{-1}[H]}{\delta H_{a_3a_4}} - \frac{\delta G_{b_3b_4}[H]}{\delta H_{a_3a_4}} \frac{\delta \Sigma_{b_1b_2}[H]}{\delta G_{b_3b_4}[H]} \right) G_{b_2a_2}[H]. \quad (\text{C.24})$$

Taking the limit  $H \rightarrow 0$  and identifying

$$\left.\frac{\delta G_{a_1a_2}[H]}{\delta H_{a_3a_4}}\right|_{H\rightarrow 0} = \left.\frac{\delta^2\tilde{\mathcal{G}}[H]}{\delta H_{a_3a_4}\delta H_{a_1a_2}}\right|_{H\rightarrow 0} = \chi_{a_1a_2|a_3a_4} \quad (\text{C.25})$$

we finally obtain a self-consistent equation for  $\chi$

$$\chi_{a_1 a_2 | a_3 a_4} = -G_{a_1 b_1} \left( \frac{\delta G_{0, b_1 b_2}^{-1}[H]}{\delta H_{a_3 a_4}} \Big|_{H \rightarrow 0} - \chi_{b_3 b_4 | a_3 a_4} \frac{\delta \Sigma_{b_1 b_2}[H]}{\delta G_{b_3 b_4}[H]} \Big|_{H \rightarrow 0} \right) G_{b_2 a_2}. \quad (\text{C.26})$$

To determine the two leftover derivatives, we first recall, that  $G_{0, b_1 b_2}[H]$  corresponds to the propagator in the Gaussian approximation, i.e.  $\langle \eta_{b_2} \eta_{b_1} \rangle_0[H]$ , which, from the definition of the Majorana action Eq. (C.1) directly implies that

$$G_{0, a_1 a_2}^{-1}[H] = G_{0, a_1 a_2}^{-1} + H_{a_1 a_2} \quad (\text{C.27})$$

For the derivative of the self energy, we, at least for now, simply note that the resulting object is a two-particle vertex

$$Q_{a_1 a_2 | a_3 a_4} = \frac{\delta \Sigma_{a_1 a_2}[H]}{\delta G_{a_3 a_4}[H]} \Big|_{H \rightarrow 0}, \quad (\text{C.28})$$

since removing a propagator from a self energy (i.e. a two-point diagram), generates two more external legs. We will come back to the explicit discussion of this term once we have obtained our final result. Plugging everything into the equation for  $\chi$  yields

$$\begin{aligned} \chi_{a_1 a_2 | a_3 a_4} &= -G_{a_1 b_1} \left( \delta_{b_1 a_4} \delta_{b_2 a_3} - \delta_{b_1 a_3} \delta_{b_2 a_4} - \chi_{b_3 b_4 | a_3 a_4} Q_{b_1 b_2 | b_3 b_4} \right) G_{b_2 a_2} \\ &= -G_{a_1 a_4} G_{a_3 a_2} + G_{a_1 a_3} G_{a_4 a_2} + G_{a_1 b_1} \chi_{b_3 b_4 | a_3 a_4} Q_{b_1 b_2 | b_3 b_4} G_{b_2 a_2} \\ &= +G_{a_1 a_4} G_{a_2 a_3} - G_{a_1 a_3} G_{a_2 a_4} + G_{a_1 b_1} \chi_{b_3 b_4 | a_3 a_4} Q_{b_1 b_2 | b_3 b_4} G_{b_2 a_2}. \end{aligned} \quad (\text{C.29})$$

The remainder of the calculation revolves around converting this equation into a self-consistent relation for the two-particle vertex instead of one for  $\chi$ . Plugging in the definition of  $\chi$ , Eq. (C.19), one finds

$$\begin{aligned} G_{c, a_1 a_2 a_3 a_4}^{(4)} &= G_{a_1 b_1} G_{c, b_3 b_4 a_3 a_4}^{(4)} Q_{b_1 b_2 | b_3 b_4} G_{b_2 a_2} \\ &\quad - G_{a_1 b_1} G_{b_3 a_3} G_{b_4 a_4} Q_{b_1 b_2 | b_3 b_4} G_{b_2 a_2} + G_{a_1 b_1} G_{b_3 a_4} G_{b_4 a_3} Q_{b_1 b_2 | b_3 b_4} G_{b_2 a_2}, \end{aligned} \quad (\text{C.30})$$

and subsequently, using Eq. (C.7)

$$\Gamma_{a_1 a_2 a_3 a_4} = Q_{a_1 a_2 | b_3 b_4} G_{b_3 c_3} G_{b_4 c_4} \Gamma_{c_3 c_4 a_3 a_4} - 2Q_{a_1 a_2 | a_3 a_4}. \quad (\text{C.31})$$

Employing the definitions

$$\begin{aligned} I_{a_1 a_2 | a_3 a_4} &= -2Q_{a_1 a_2 | a_3 a_4} \\ \gamma_{a_1 a_2 | a_3 a_4} &= -\frac{1}{2} I_{a_1 a_2 | b_3 b_4} G_{b_3 c_3} G_{b_4 c_4} \Gamma_{c_3 c_4 a_3 a_4}, \end{aligned} \quad (\text{C.32})$$

we thus have the relation

$$\Gamma_{a_1 a_2 a_3 a_4} = I_{a_1 a_2 | a_3 a_4} + \gamma_{a_1 a_2 | a_3 a_4}, \quad (\text{C.33})$$

which is shown diagrammatically in Fig. 3.2(a). Using the antisymmetry of the vertex Eq. (C.33) can be written in three equivalent ways

$$\Gamma_{a_1 a_2 a_3 a_4} = I_{a_1 a_2 | a_3 a_4} + \gamma_{a_1 a_2 | a_3 a_4} = -I_{a_1 a_3 | a_2 a_4} - \gamma_{a_1 a_3 | a_2 a_4} = -I_{a_1 a_4 | a_3 a_2} - \gamma_{a_1 a_4 | a_3 a_2}. \quad (\text{C.34})$$

Defining

$$\begin{aligned} \gamma_{s, a_1 a_2 | a_3 a_4} &= +\gamma_{a_1 a_2 | a_3 a_4} \\ \gamma_{t, a_1 a_2 | a_3 a_4} &= -\gamma_{a_1 a_3 | a_2 a_4} \\ \gamma_{u, a_1 a_2 | a_3 a_4} &= -\gamma_{a_1 a_4 | a_3 a_2}, \end{aligned} \quad (\text{C.35})$$

and concomitantly

$$\begin{aligned} I_{s, a_1 a_2 | a_3 a_4} &= +I_{a_1 a_2 | a_3 a_4} \\ I_{t, a_1 a_2 | a_3 a_4} &= -I_{a_1 a_3 | a_2 a_4} \\ I_{u, a_1 a_2 | a_3 a_4} &= -I_{a_1 a_4 | a_3 a_2}, \end{aligned} \quad (\text{C.36})$$

we can write Eq. (C.34) in the more compact form

$$\Gamma = I_s + \gamma_s = I_t + \gamma_t = I_u + \gamma_u, \quad (\text{C.37})$$

which resembles the widely employed parquet decomposition of the two-particle vertex for complex fermions. This motivates the following definitions:

1. A diagram is called two-particle reducible in the  $s$ -channel if it can be disconnected by cutting two propagator lines, such that one disconnected part is antisymmetric under  $(a_1 \leftrightarrow a_2)$  and the other one under  $(a_3 \leftrightarrow a_4)$ . Diagrams that do not possess this property are consequently called two-particle irreducible in the  $s$ -channel.
2. A diagram is called two-particle reducible in the  $t$ -channel if it can be disconnected by cutting two propagator lines, such that one disconnected part is antisymmetric under  $(a_1 \leftrightarrow a_3)$  and the other one under  $(a_2 \leftrightarrow a_4)$ . Diagrams that do not possess this property are consequently called two-particle irreducible in the  $t$ -channel.
3. A diagram is called two-particle reducible in the  $u$ -channel if it can be disconnected by cutting two propagator lines, such that one disconnected part

is antisymmetric under  $(a_1 \leftrightarrow a_4)$  and the other one under  $(a_3 \leftrightarrow a_2)$ . Diagrams that do not possess this property are consequently called two-particle irreducible in the  $u$ -channel.

4. Diagrams that are not reducible in any channel are called fully irreducible.

Note that diagrams cannot be reducible in more than one channel. The contributions  $\gamma_c$  are  $c$ -reducible, which follows directly from their definition Eq. (C.32).  $I_c \sim \frac{\delta \Sigma}{\delta G}$ , on the other hand, contains only  $c$ -irreducible contributions. This can be seen by considering the Skeleton expansion of  $\Sigma$  in which  $c$ -reducible diagrams, after removing a fermionic propagator line, are absent. As a last step, we introduce the fully irreducible vertex  $R = I_c - \sum_{\bar{c} \neq c} \gamma_c$ , such that the vertex decomposition finally reads

$$\Gamma = R + \sum_c \gamma_c. \quad (\text{C.38})$$

## C.2. Multiloop Flow equations

Although we find that it is possible to directly obtain the solution to the parquet approximation, from a methodological perspective, it is useful to demonstrate that the previously employed one- and two-loop schemes follow from the first two orders of a multiloop expansion of the parquet approximation.

We start from the Bethe-Salpeter equation

$$\begin{aligned} \gamma_{1,2|3,4} &= -\frac{1}{2} I_{1,2|1',3'} G_{1',2'} G_{3',4'} \Gamma_{4',2',3,4} \\ &\equiv [I \circ \Pi \circ \Gamma]_{1,2,3,4} \end{aligned} \quad (\text{C.39})$$

Assuming the sum convention for repeated indices (e.g., indicated as  $1'$ ), this self-consistent equation relates the  $s$ -reducible parts  $\gamma$ , the full vertex  $\Gamma$ , and the  $s$ -irreducible vertex  $I$ . The tensor contraction  $\circ \Pi \circ$ , as defined by Eq. (C.39), connects the outer two indices of the left vertex with the inner two indices of the right one. Note that the prefactor  $-\frac{1}{2}$  is also included in the definition of  $\Pi$ . From this form, it immediately follows that the considerations made for complex fermions [164, 165, 167] in the derivation of the flow equations directly carry over to the present case of Majorana fermions. The only exception is that we only need to consider the  $s$ -reducible channel, as the others are given by permutations of

indices. By definition, the vertex is given by the sum of an  $s$ -reducible part  $\gamma$  and the  $s$ -irreducible part  $I$ .

$$\Gamma = I + \gamma = I + I \circ \Pi \circ \Gamma \quad (\text{C.40})$$

$$= I + I \circ \Pi \circ I + I \circ \Pi \circ I + I \circ \Pi \circ I \circ \Pi \circ I + \dots \quad (\text{C.41})$$

Taking a derivative with respect to the cutoff  $\Lambda$  of Eq. (C.38) and using the parquet approximation  $R = \Gamma_0$ , it follows that  $\dot{\Gamma} = \dot{\gamma} + \dot{\gamma}$ . Using Eq. (C.39) and Eq. (C.41), we then have

$$\dot{\gamma} = \partial_\Lambda [I \circ \Pi \circ I + I \circ \Pi \circ I \circ \Pi \circ I + \dots]. \quad (\text{C.42})$$

Using the product rule, we can distinguish two cases: The derivative can act on a double-propagator  $\Pi$  at any position in the expansion. One can see that all these contributions are given by expanding

$$\dot{\gamma}^{(1)} \equiv \Gamma \circ \dot{\Pi} \circ \Gamma \quad (\text{C.43})$$

via Eq. (C.41). As this diagram contains only a single internal loop connecting the two vertices, it is commonly referred to as the *one-loop* contribution. All the other diagrams contain derivatives of the  $s$ -irreducible part  $I$  instead. Similar to the previous case, the infinite series can be replaced by the full vertex so that we may write altogether

$$\dot{\gamma} = \dot{\gamma}^{(1)} + \dot{I} \circ \Pi \circ \Gamma + \Gamma \circ \Pi \circ \dot{I} \circ \Pi \circ \Gamma + \dot{I} \circ \Pi \circ \Gamma. \quad (\text{C.44})$$

In the parquet approximation, the derivative of the  $s$ -irreducible vertex is readily determined as  $\dot{I} = \partial_\Lambda [\Gamma_0 + \bar{\gamma}] = \dot{\bar{\gamma}}$ . To finally obtain an expression in terms of quantities that may be computed in the FRG scheme, we may formally expand Eq. (C.44) in loop orders, i.e., in orders of the double-propagator  $\Pi$ , so that  $\dot{\gamma} = \sum_\ell \dot{\gamma}^{(\ell)}$ . The full one-loop contribution, which is also computed in the Katanin truncated one-loop FRG scheme, has already been identified in Eq. (C.43). The second part of Eq. (C.44) generates all higher orders upon inserting  $\dot{\bar{\gamma}} = \sum_\ell \dot{\bar{\gamma}}^{(\ell)}$ . As a result, we may write the multiloop flow equations as

$$\begin{aligned} \dot{\gamma}^{(1)} &= \Gamma \circ \dot{\Pi} \circ \Gamma \\ \dot{\gamma}^{(2)} &= \dot{\bar{\gamma}}^{(1)} \circ \Pi \circ \Gamma + \Gamma \circ \Pi \circ \dot{\bar{\gamma}}^{(1)} \equiv \dot{\gamma}^{(2,L)} + \dot{\gamma}^{(2,R)} \\ \dot{\gamma}^{(\ell \geq 3)} &= \dot{\bar{\gamma}}^{(\ell-1)} \circ \Pi \circ \Gamma + \Gamma \circ \Pi \circ \dot{\bar{\gamma}}^{(\ell-2)} \circ \Pi \circ \Gamma + \Gamma \circ \Pi \circ \dot{\bar{\gamma}}^{(\ell-1)} \\ &= \dot{\bar{\gamma}}^{(\ell-1)} \circ \Pi \circ \Gamma + \dot{\bar{\gamma}}^{(\ell-1,R)} \circ \Pi \circ \Gamma + \Gamma \circ \Pi \circ \dot{\bar{\gamma}}^{(\ell-1)} \equiv \dot{\gamma}^{(\ell,L)} + \dot{\gamma}^{(\ell,C)} + \dot{\gamma}^{(\ell,R)}. \end{aligned} \quad (\text{C.45})$$

We will make further simplifications by re-inserting the explicit definitions of  $\Pi$  and  $\dot{\bar{\gamma}}$ . Starting with the one-loop equation, we have

$$\dot{\gamma}_{1,2|3,4}^{(1)} = -\frac{1}{2} \Gamma_{1,2,1',3'} (\dot{G}_{1',2'} G_{3',4'} + G_{1',2'} \dot{G}_{3',4'}) \Gamma_{4',2',3,4}. \quad (\text{C.46})$$



In the second term, we may re-label the indices  $(1'2') \leftrightarrow (3', 4')$  and use the antisymmetry of propagators and vertices to find it equal to the first one, canceling the pre-factor of  $\frac{1}{2}$ . For the higher-loop contributions, we may do similar simplifications, e.g:

$$\begin{aligned}
 \dot{\gamma}_{1,2|3,4}^{(\ell,L)} &= -\frac{1}{2} G_{1',2'} G_{3',4'} \dot{\gamma}_{1,2|1',3'}^{(\ell-1)} \Gamma_{4',2',3,4} \\
 &= -\frac{1}{2} G_{1',2'} G_{3',4'} \left( -\dot{\gamma}_{1,1'|2,3'}^{(\ell-1)} + \dot{\gamma}_{1,3'|2,1'}^{(\ell-1)} \right) \Gamma_{4',2',3,4} \\
 &= G_{1',2'} G_{3',4'} \dot{\gamma}_{1,1'|2,3'}^{(\ell-1)} \Gamma_{4',2',3,4} \equiv \mathcal{B}^2 \left( \dot{\gamma}^{(\ell-1)}, \Gamma \right)_{1,2|3,4}, \quad (C.47)
 \end{aligned}$$

where we have defined the four-point bubble  $\mathcal{B}_2$  as a shorthand notation. In addition, we may use the fact that the central part takes the form of the left one, and the right part must be equal to the left one after exchanging the first and last two indices with each other. Altogether, the general multiloop flow equations for Majorana fermions are thus

$$\dot{\gamma}_{1,2|3,4}^{(1)} = \dot{G}_{1',2'} G_{3',4'} \Gamma_{1,2,1',3'} \Gamma_{2',4',3,4}. \quad (C.48a)$$

$$\dot{\gamma}_{1,2|3,4}^{(2)} = \dot{\gamma}_{1,2||3,4}^{(2,L)} + \dot{\gamma}_{1,2||3,4}^{(2,R)} \quad (C.48b)$$

$$\dot{\gamma}_{1,2|3,4}^{(\ell \geq 3)} = \dot{\gamma}_{1,2||3,4}^{(\ell,L)} + \dot{\gamma}_{1,2|3,4}^{(\ell,C)} + \dot{\gamma}_{1,2||3,4}^{(\ell,R)} \quad (C.48c)$$

$$\dot{\gamma}_{1,2||3,4}^{(\ell,L)} = \mathcal{B}^2 \left( \dot{\gamma}^{(\ell-1)}, \Gamma \right)_{1,2||3,4} \quad (C.48d)$$

$$\dot{\gamma}_{1,2|3,4}^{(\ell,C)} = \mathcal{B}^2 \left( \dot{\gamma}^{(\ell-1,R)}, \Gamma \right)_{1,2|3,4} \quad (C.48e)$$

$$\dot{\gamma}_{1,2||3,4}^{(\ell,R)} = \mathcal{B}^2 \left( \dot{\gamma}^{(\ell-1)}, \Gamma \right)_{3,4||1,2}, \quad (C.48f)$$

where it can be seen that the one- and two-loop contributions are equivalent to the equations derived previously. [2].

## Parametrization of bubble functions

This section will employ the usual symmetry-based parametrization, in close analogy to previous works [1, 2]. Defining generic *bubble functions*, the special cases of one- or multiloop flow equations, and in particular the Parquet formalism are contained.

Most symmetries previously proven for the one- and two-loop bubble functions immediately generalize to higher loop orders. For instance, the antisymmetry

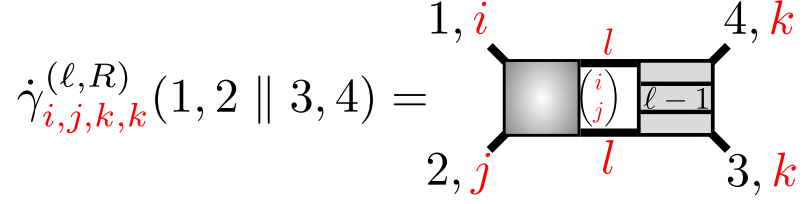


Figure C.1.: Right part of  $\dot{\gamma}^{(\ell)}$  with site indices made explicit. The internal propagators are local, while the vertex and  $\dot{\gamma}^{(\ell-1)}$  are bilocal.

$\dot{\gamma}_{1,2||3,4}^{(\ell,R)}$  under the exchange of the first and second two indices can be extended straightforwardly to arbitrary loop orders via induction. It is important to point out that while each bubble function  $\dot{\gamma}^{(\ell)}$  and even  $\dot{\gamma}^{(\ell,C)}$  are symmetric under  $(1,2) \leftrightarrow (3,4)$ , this is not the case for the left and right channels individually, which instead transform into each other as in Eq. (C.48f). While this special case requires attention in the derivation of final flow equations, we can prove all other symmetries directly on the level of  $\dot{\gamma}^{(\ell)}$ . Figure C.1 shows how a bilocal vertex and a bilocal bubble function of loop order  $\ell-1$  imply that the left part (and thus also  $\dot{\gamma}^{(\ell)}$ ) must be bilocal as well. After the external indices are specified, the indices of the internal propagators are determined. In the present example, the internal propagators take the form  $G_{i_i}G_{l_j} = 0$ , so the diagram must vanish (assuming that  $i \neq j$ ). This way, it can be seen that external sites of  $\dot{\gamma}^{(\ell,L)}$  must always be in pairs for a nonzero contribution.

It can be immediately seen that this argument can be made analogous to the flavor structure. Furthermore, global  $SO(3)$  rotations still allow for transformations  $zz|zz \rightarrow xx|xx$ . As a result, we may parametrize  $\dot{\gamma}^{(\ell,R)}$  (and thus also  $\dot{\gamma}^{(\ell)}$ ) analogous to the one and two-loop bubble functions. We thus identify three  $\dot{\gamma}^{(\ell,R)}$ -types  $X_a, X_b, X_c$  and four  $\dot{\gamma}^{(\ell,R)}$ -type vertices  $\dot{\gamma}_a^{(\ell,R)}, \dot{\gamma}_b^{(\ell,R)}, \dot{\gamma}_c^{(\ell,R)}, \dot{\gamma}_d^{(\ell,R)}$ . where the labels  $a, \dots, d$  are short for

$$a \equiv xx|xx \quad b \equiv xx|yy \quad c \equiv xy|xy \quad d \equiv xy|yx. \quad (\text{C.49})$$

Finally, there is the slightly more involved symmetry

$$\dot{\gamma}_{xx|xx}^{(\ell,R)} = \dot{\gamma}_{xx||yy}^{(\ell,R)} + \dot{\gamma}_{xy||xy}^{(\ell,R)} + \dot{\gamma}_{xy|yx}^{(\ell,R)}, \quad (\text{C.50})$$

which again follows inductively through all loop orders. The proof is equivalent to the procedure outlined in Ref. [2], i.e., starting from Eq. (C.48e), the identity can be inserted on both sides of the equation to derive a trivial equality. **Frequencies**

Energy conservation allows specification of  $\dot{\gamma}^{(\ell,R)}$  using the usual three exchange frequencies  $s = \omega_1 + \omega_2, t = \omega_1 + \omega_3, u = \omega_1 + \omega_4$ . The symmetries regarding

Operation	$\dot{\gamma}_{\mu, ij}^{(\ell, R)}(s, t, u)$	$\dot{\gamma}_{\mu, ij}^{(\ell, R)}(s, t, u)$
$1 \leftrightarrow 2$	$\dot{\gamma}_{a/b}^{(\ell)}(s, t, u)$ $\leftrightarrow -\dot{\gamma}_{a/b}^{(\ell)}(s, u, t)$	not allowed
$T \circ (1, 3) \leftrightarrow (2, 4)$	$s \leftrightarrow -s$	$s \leftrightarrow -s, i \leftrightarrow j$
$T \circ (1, 2) \leftrightarrow (3, 4)$	$t \leftrightarrow -t, i \leftrightarrow j, L \leftrightarrow R$	$t \leftrightarrow -t, L \leftrightarrow R$
$T \circ (1, 2) \leftrightarrow (4, 3)$	$u \leftrightarrow -u, i \leftrightarrow j, L \leftrightarrow R$	$u \leftrightarrow -u, i \leftrightarrow j, L \leftrightarrow R$

Table C.1.: Transformations of the frequency arguments under time reversal  $T$  and specific permutations of indices in the left part of bubble functions. The corresponding identities for the full bubble functions  $\dot{\gamma}^{(\ell, L)} + \dot{\gamma}^{(\ell, R)}$  are equivalent, while swaps of  $L$  and  $R$  may be ignored.

these exchange frequencies pointed out in Ref. [2] naturally apply to higher loop bubble functions too, since they are based on permutations of indices. However, as changing the sign of  $t$  and  $u$  frequencies requires exchanges of the left and right parts of a diagram, we need to keep track of all such changes to ensure that all flow equations are still valid when computing the central part. The frequency symmetries are summarized in Table C.1.

As the left, right, and central parts are very similar in form, we need only explicitly consider the central channel and derive the others from there: The left part is essentially equal to the central one, and one simply needs to replace all occurrences of  $\dot{\gamma}^{(\ell-1, R)}$  and  $\dot{\gamma}^{(\ell-1, L)}$  with a full bubble function  $\dot{\gamma}^{(\ell-1)}$ . The right part can be obtained from the left one after swapping the left and right pairs of indices. In the explicit parametrization, this means

$$\dot{\gamma}_{\mu, ij}^{(\ell, R)}(s, t, u) = \dot{\gamma}_{\mu, ji}^{(\ell, L)}(-s, t, -u) = \dot{\gamma}_{\mu, ji}^{(\ell, L)}(s, -t, u) \quad (\text{C.51})$$

$$\dot{\gamma}_{\mu, ij}^{(\ell, R)}(s, t, u) = \dot{\gamma}_{\mu, ij}^{(\ell, L)}(-s, t, -u) = \dot{\gamma}_{\mu, ij}^{(\ell, L)}(s, -t, u), \quad (\text{C.52})$$

since the flavor structure never changes under this transformation (i.e.  $(xy \parallel yx) \rightarrow (yx \parallel xy)$  still corresponds to the  $d$ -type vertex by virtue of the global  $SO(3)$  symmetry). Note, however, that the site indices will generally be affected by this transformation. With these considerations in mind, we may proceed to derive the final form of the flow equations as usual by starting from Eq. (C.48e) and eliminating site, frequency, and flavor summations using the (anti-)diagonality of Green functions initially:

$$G_{1', 2'} = G_{\beta_1, \beta_2}^{i_1'}(-\omega_{1'}) \beta \delta_{\omega_{1'}, -\omega_{2'}} \delta_{i_1', i_2'}. \quad (\text{C.53})$$

This step leads to the form

$$\begin{aligned} \dot{\gamma}_{\alpha_1, \alpha_2 \| \alpha_3, \alpha_4}^{(\ell-1, C) i_1, i_2 \| i_3, i_4}(\omega_1, \omega_2 \| \omega_3, \omega_4) &= -T \sum_{\omega} \sum_{\beta_1, \dots, \beta_4} \sum_{k, l} G_{\beta_1, \beta_2}^k(\omega) G_{\beta_3, \beta_4}^l(\omega + s) \\ &\times \dot{\gamma}_{\alpha_1, \beta_3 \| \beta_2, \alpha_2}^{(\ell-1, R) i_1 \| l, k, i_2}(\omega_1, -\omega - s \| \omega, \omega_2) \Gamma_{\alpha_3, \alpha_4, \beta_4, \beta_1}^{i_3, i_4, l, k}(\omega_3, \omega_4, \omega + s, -\omega). \end{aligned} \quad (\text{C.54})$$

Note that to arrive here, we re-labeled internal indices as  $(1', 2', 3', 4') \rightarrow (3', 4', 2', 1')$  and defined  $\omega = -\omega'_1$  in order to keep the frequency arguments in both Green functions positive. Then, upon specifying external indices corresponding to the parametrized bubble functions, i.e.,

$$\dot{\gamma}_{c, ij}^{(\ell, R)}(s, t, u) = \dot{\gamma}_{xi, yi \| xj, yj}^{(\ell, R)}(\omega_1, \omega_2 \| \omega_3, \omega_4) \beta \delta_{\omega_1 + \omega_2 + \omega_3 + \omega_4, 0} \quad (\text{C.55})$$

, the remaining sums are evaluated and occurring vertices and bubble functions are replaced by their parametrized versions, making use of their allowed permutations. This leads to the final equations:

$$\dot{\Gamma}_a{}_{ij}(s, t, u) = \sum_{\ell} \dot{\gamma}_a{}^{(\ell)}{}_{ij}(s, t, u) - \dot{\tilde{\gamma}}_a{}^{(\ell)}{}_{ij}(t, s, u) + \dot{\tilde{\gamma}}_a{}^{(\ell)}{}_{ij}(u, s, t) \quad (\text{C.56a})$$

$$\dot{\Gamma}_b{}_{ij}(s, t, u) = \sum_{\ell} \dot{\gamma}_b{}^{(\ell)}{}_{ij}(s, t, u) - \dot{\tilde{\gamma}}_b{}^{(\ell)}{}_{ij}(t, s, u) + \dot{\tilde{\gamma}}_b{}^{(\ell)}{}_{ij}(u, s, t) \quad (\text{C.56b})$$

$$\dot{\Gamma}_c{}_{ij}(s, t, u) = \sum_{\ell} \dot{\gamma}_c{}^{(\ell)}{}_{ij}(s, t, u) - \dot{\tilde{\gamma}}_c{}^{(\ell)}{}_{ij}(t, s, u) + \dot{\tilde{\gamma}}_c{}^{(\ell)}{}_{ij}(u, s, t) \quad (\text{C.56c})$$

where the one-loop versions are found in Ref. [1] and bubble functions for higher loop orders can be computed via the expressions in Section C.2.

Finally, we note that although the particular form of the flow equations appears highly symmetric, a separate evaluation of all three contributions ( $L, R, C$ ) is still necessary. For the left part, this is easy to see since it requires insertion of a completely different object on the right-hand side of the flow equations and thus will not be equal to the central part. The right part  $\dot{\gamma}^{(\ell, R)}$  is equivalent to the left one upon inversion of the  $t$  (or  $u$ ) frequency, which essentially requires us to compute the left part for a negative transfer frequency. Here, we chose to restrict ourselves to positive frequencies only and instead treat  $\dot{\gamma}^{(\ell, R)}$  as an individual contribution.

### Bethe-Salpeter and Schwinger-Dyson equations

Instead of using the Multiloop-FRG approach, one can also try to iteratively solve the Bethe-Salpeter equations in the parquet approximation and the Schwinger Dyson equation. As it turns out, this can be done numerically efficiently using our

previously gained knowledge on the parametrization. We start with Eq. (C.39) and insert  $I = \Gamma^0 + \bar{\gamma}$ , which we can then simplify to

$$\gamma_{1,2|3,4} = \frac{1}{2} \mathcal{B}^2(\Gamma^0, \Gamma) + \mathcal{B}^2(\gamma, \Gamma). \quad (\text{C.57})$$

The relative factor of 2 between both terms originates from the elimination of  $\bar{\gamma}$  in favor of two equivalent terms with  $\gamma$  analogous to Eq. (C.47). Writing the equation in this form allows us to find the parametrized version from the parametrized bubble functions in Section C.2. To realize this, we note that all properties of  $\gamma^\ell$  carry over to the irreducible vertex  $\gamma$  inductively. For the first term containing the bare interaction, the equation can be further simplified by noting that the parametrization allows us to simply permute indices to replace  $\tilde{\Gamma}$ -like expressions. In total, we may thus insert

$$\Gamma_{c, ij}^0 = -J_{ij} \quad (\text{C.58})$$

$$\tilde{\Gamma}_{b, ij}^0 \equiv \Gamma_{xi,xj,yi,yj}^0 = -\Gamma_{xi,yi,xj,yj}^0 = -\Gamma_{c, ij}^0 \quad (\text{C.59})$$

$$\tilde{\Gamma}_{d, ij}^0 = \Gamma_{c, ij}^0 \quad (\text{C.60})$$

$$\Gamma_a^0 = \Gamma_b^0 = 0 \quad (\text{C.61})$$

$$\tilde{\Gamma}_a^0 = \tilde{\Gamma}_c^0 = 0. \quad (\text{C.62})$$

Using the four-point bubble, the Schwinger-Dyson equation may also be iterated efficiently. Starting from its previously derived form

$$\Sigma_{1,2} = -\frac{1}{2} \Gamma_{1,2,1',2'}^0 G_{1',2'} + \frac{1}{6} G_{1',2'} G_{3',4'} G_{5',6'} \Gamma_{1,1',3',5'}^0 \Gamma_{2,2',4',6'} \quad (\text{C.63})$$

we may define a self-energy bubble as

$$\mathcal{B}^1(\Gamma)_{1,2} = G_{1',2'} \Gamma_{2',1,2,1'}, \quad (\text{C.64})$$

where we have chosen a permutation of indices that is most easily translated into diagrammatic form. The convention is to label indices on a vertex in a counter-clockwise direction starting from the top-left. In the second term we may then identify the one-and two-particle bubbles

$$\begin{aligned} G_{1',2'} \left( G_{3',4'} G_{5',6'} \Gamma_{1,1',3',5'}^0 \Gamma_{2,2',4',6'} \right) &= G_{1',2'} \left( G_{3',4'} G_{5',6'} \Gamma_{1,3',1',5'}^0 \Gamma_{6',4',2,2'} \right) \\ &= G_{1',2'} \mathcal{B}^2(\Gamma^0, \Gamma)_{1,1'|2,2'} \\ &= G_{1',2'} \mathcal{B}^2(\Gamma^0, \Gamma)_{2',1|2,1'} \\ &= \mathcal{B}^1 \left( \mathcal{B}^2(\Gamma^0, \Gamma) \right)_{1,2}. \end{aligned} \quad (\text{C.65})$$

Altogether, we have

$$\Sigma_{1,2} = \frac{1}{2} \mathcal{B}^1(\Gamma^0)_{1,2} + \frac{1}{6} \mathcal{B}^1(\mathcal{B}^2(\Gamma^0, \Gamma))_{1,2}. \quad (\text{C.66})$$

Again, to insert the explicit parametrization, we consider the more general case in which a two-particle bubble is inserted into a self-energy bubble:

$$\begin{aligned} \mathcal{B}^1(\mathcal{B}^2)_{1,2} &= G_{1',2'} \mathcal{B}_{2',1|2,1'}^2 \\ [\mathcal{B}^1(\mathcal{B}^2)]_{xi,xi}(\omega_1) &= T \sum_{\omega} \sum_{\beta} \sum_k \mathcal{G}_k(-\omega) \mathcal{B}_{\beta k, xi|xi, \beta k}^2(-\omega, \omega_1 | -\omega_1, \omega) \\ &= -T \sum_{\omega} \sum_k \mathcal{G}_k(-\omega) \left[ \tilde{\mathcal{B}}_{a, ki}^2(-\omega, \omega_1 | \omega, -\omega_1) \right. \\ &\quad \left. + 2\tilde{\mathcal{B}}_{c, ki}^2(-\omega, \omega_1 | \omega, -\omega_1) \right] \\ &= -T \sum_{\omega} \sum_k \mathcal{G}_k(\omega) \left[ \tilde{\mathcal{B}}_{a, ki}^2(\omega + \omega_1, 0, \omega - \omega_1) \right. \\ &\quad \left. + 2\tilde{\mathcal{B}}_{c, ki}^2(\omega + \omega_1, 0, \omega - \omega_1) \right]. \quad (\text{C.67}) \end{aligned}$$

This derivation is analogous if a vertex is inserted instead of a bubble. As in the previous case, we simply need to replace  $\tilde{\Gamma}_{a, ik}(s, t, u) = \Gamma_{a, ik}(t, u, s)$  and  $\tilde{\Gamma}_{c, ik}(s, t, u) = \Gamma_{b, ik}(t, u, s)$ . Note that this implies that in the current parametrization, the bubble containing only the bare vertex vanishes.

## Numerical procedure

To solve the Bethe-Salpeter and the Schwinger-Dyson equations self-consistently, we start from the parquet approximation  $I = \bar{\gamma} + \Gamma^0$  and further set the initial values as  $\Gamma = \Gamma^0$  and  $\Sigma = 0$ . As detailed in Fig. C.2, these values are inserted into the parquet formalism, which involves the following steps:

- Computing the bubble functions  $\mathcal{B}^2(\Gamma^0, \Gamma)$  and  $\mathcal{B}^2(\gamma, \Gamma)$  using the given vertex and self-energy.
- Obtaining the irreducible vertex  $\gamma$  from the bubble functions.
- Using the parquet approximation  $\Gamma = \Gamma^0 + \bar{\gamma}$ .
- Solving the Schwinger-Dyson equation using the current vertex and bubble functions. This is done self-consistently by re-evaluating the SDE using the updated self-energy in propagators until convergence is reached.

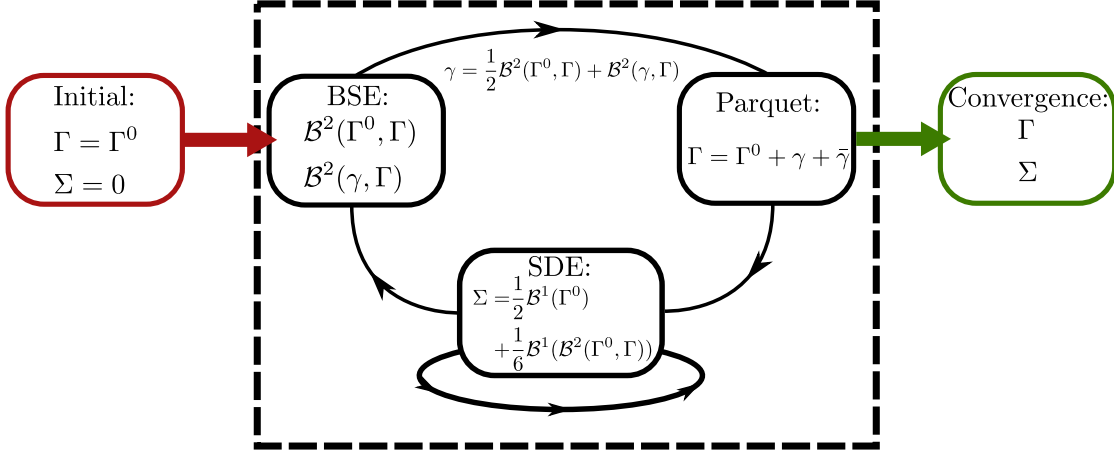


Figure C.2.: Iterative Parquet algorithm. Arrows indicate the input of data. The Schwinger-Dyson equation is solved self-consistently at each step until convergence is reached, which is numerically feasible if the bubble function  $\mathcal{B}^2$  is computed explicitly.

### Parametrization of Bubble functions

Finally, we can write the parametrized form of the flow equations concisely by using the parametrized version of four-point bubble functions.

$$\dot{\gamma}_{\mu, ij}^{\ell, L}(s, t, u) = \mathcal{B}^2 \left( \dot{\gamma}^{\ell-1}, \Gamma \right)_{\mu, ij}(s, t, u) \quad (\text{C.68a})$$

$$\dot{\gamma}_{\mu, ij}^{\ell, C}(s, t, u) = \mathcal{B}^2 \left( \dot{\gamma}^{\ell-1, R}, \Gamma \right)_{\mu, ij}(s, t, u) \quad (\text{C.68b})$$

$$\dot{\gamma}_{\mu, ij}^{(\ell, R)}(s, t, u) = \dot{\gamma}_{\mu, ij}^{(\ell, L)}(s, t, u) \Big|_{\omega_1 \leftrightarrow -\omega_3, \omega_2 \leftrightarrow -\omega_4, i \leftrightarrow j} \quad (\text{C.68c})$$

$$\dot{\check{\gamma}}_{\mu, ij}^{(\ell, R)}(s, t, u) = \dot{\check{\gamma}}_{\mu, ij}^{(\ell, L)}(s, t, u) \Big|_{\omega_1 \leftrightarrow -\omega_3, \omega_2 \leftrightarrow -\omega_4} \quad (\text{C.68d})$$

with expressions for  $\dot{\check{\gamma}}^{\ell, L}$  and  $\dot{\check{\gamma}}^{\ell, C}$  analogous to Eqs. (C.68a) and (C.68b)

$$\begin{aligned}
 \mathcal{B}^2 \left( \dot{\gamma}^{\ell-1,R}, \Gamma \right)_{a, ij} (s, t, u) &= -T \sum_{k\omega} \mathcal{G}_k(\omega) \mathcal{G}_k(\omega + s) \\
 &\quad \left( \Gamma_{a, kj} (s, \omega - \omega_3, \omega - \omega_4) \dot{\gamma}_{a, ki}^{(\ell-1,R)} (\omega + \omega_2, s, \omega + \omega_1) \right. \\
 &\quad \left. + 2\Gamma_{b, kj} (s, \omega - \omega_3, \omega - \omega_4) \dot{\gamma}_{c, ki}^{(\ell-1,R)} (\omega + \omega_2, s, \omega + \omega_1) \right)
 \end{aligned} \tag{C.69a}$$

$$\begin{aligned}
 \mathcal{B}^2 \left( \dot{\gamma}^{\ell-1,R}, \Gamma \right)_{b, ij} (s, t, u) &= -T \sum_{k\omega} \mathcal{G}_k(\omega) \mathcal{G}_k(\omega + s) \\
 &\quad \left( \Gamma_{b, kj} (s, \omega - \omega_3, \omega - \omega_4) \dot{\gamma}_{a, ki}^{(\ell-1,R)} (\omega + \omega_2, s, \omega + \omega_1) \right. \\
 &\quad + \Gamma_{a, kj} (s, \omega - \omega_3, \omega - \omega_4) \dot{\gamma}_{c, ki}^{(\ell-1,R)} (\omega + \omega_2, s, \omega + \omega_1) \\
 &\quad \left. + \Gamma_{b, kj} (s, \omega - \omega_3, \omega - \omega_4) \dot{\gamma}_{c, ki}^{(\ell-1,R)} (\omega + \omega_2, s, \omega + \omega_1) \right)
 \end{aligned} \tag{C.69b}$$

$$\begin{aligned}
 \mathcal{B}^2 \left( \dot{\gamma}^{\ell-1,R}, \Gamma \right)_{c, ij} (s, t, u) &= -T \sum_{k\omega} \mathcal{G}_k(\omega) \mathcal{G}_k(\omega + s) \\
 &\quad \left( -\Gamma_{c, kj} (s, \omega - \omega_4, \omega - \omega_3) \dot{\gamma}_{b, ki}^{(\ell-1,R)} (\omega + \omega_2, s, \omega + \omega_1) \right. \\
 &\quad \left. + \Gamma_{c, kj} (s, \omega - \omega_3, \omega - \omega_4) \dot{\gamma}_{d, ki}^{(\ell-1,R)} (\omega + \omega_2, s, \omega + \omega_1) \right)
 \end{aligned} \tag{C.69c}$$

$$\begin{aligned}
 \tilde{\mathcal{B}}^2 \left( \dot{\gamma}^{\ell-1,R}, \Gamma \right)_{a, ij} (s, t, u) &= -T \sum_{\omega} \mathcal{G}_i(\omega) \mathcal{G}_j(\omega + s) \\
 &\quad \left( \Gamma_{a, ji} (\omega - \omega_3, s, \omega - \omega_4) \dot{\gamma}_{a, ji}^{(\ell-1,R)} (\omega + \omega_2, \omega + \omega_1, s) \right. \\
 &\quad \left. + 2\Gamma_{c, ji} (\omega - \omega_3, s, \omega - \omega_4) \dot{\gamma}_{d, ji}^{(\ell-1,R)} (\omega + \omega_2, \omega + \omega_1, s) \right) \\
 &\quad \mathcal{G}_j(\omega) \mathcal{G}_i(\omega + s) \\
 &\quad \left( \dot{\gamma}_{a, ij}^{(\ell-1,L)} (\omega + \omega_2, s, \omega + \omega_1) \Gamma_{a, ij} (\omega - \omega_4, s, \omega - \omega_3) \right. \\
 &\quad \left. + 2\dot{\gamma}_{c, ij}^{(\ell-1,L)} (\omega + \omega_2, s, \omega + \omega_1) \Gamma_{c, ij} (\omega - \omega_4, s, \omega - \omega_3) \right)
 \end{aligned} \tag{C.70a}$$



$$\begin{aligned}
 \tilde{\mathcal{B}}^2 \left( \dot{\gamma}^{\ell-1,R}, \Gamma \right)_{b, ij} (s, t, u) = & -T \sum_{\omega} \mathcal{G}_i(\omega) \mathcal{G}_j(\omega + s) \\
 & \times \left[ \Gamma_{c, ji} (\omega - \omega_3, s, \omega - \omega_4) \left( \dot{\gamma}_{a, ji}^{(\ell-1,R)} (\omega + \omega_2, \omega + \omega_1, s) \right. \right. \\
 & \quad \left. \left. + \dot{\gamma}_{d, ji}^{(\ell-1,R)} (\omega + \omega_2, \omega + \omega_1, s) \right) \right. \\
 & \quad \left. + \Gamma_{a, ji} (\omega - \omega_3, s, \omega - \omega_4) \dot{\gamma}_{d, ji}^{(\ell-1,R)} (\omega + \omega_2, \omega + \omega_1, s) \right] \\
 & \quad + \mathcal{G}_j(\omega) \mathcal{G}_i(\omega + s) \\
 & \times \left[ \Gamma_{a, ij} (\omega - \omega_4, s, \omega - \omega_3) \dot{\gamma}_{c, ij}^{(\ell-1,L)} (\omega + \omega_2, s, \omega + \omega_1) \right. \\
 & \quad \left. + \Gamma_{c, ij} (\omega - \omega_4, s, \omega - \omega_3) \left( \dot{\gamma}_{a, ij}^{(\ell-1,L)} (\omega + \omega_2, s, \omega + \omega_1) \right. \right. \\
 & \quad \left. \left. + \dot{\gamma}_{c, ij}^{(\ell-1,L)} (\omega + \omega_2, s, \omega + \omega_1) \right) \right] \quad (C.70b)
 \end{aligned}$$

$$\begin{aligned}
 \tilde{\mathcal{B}}^2 \left( \dot{\gamma}^{\ell-1,R}, \Gamma \right)_{c, ij} (s, t, u) = & -T \sum_{\omega} -\mathcal{G}_i(\omega) \mathcal{G}_j(\omega + s) \\
 & \left[ \Gamma_{c, ji} (\omega - \omega_3, \omega - \omega_4, s) \dot{\gamma}_{b, ji}^{(\ell-1,R)} (\omega + \omega_2, \omega + \omega_1, s) \right. \\
 & \quad \left. + \Gamma_{b, ji} (\omega - \omega_3, \omega - \omega_4, s) \dot{\gamma}_{c, ji}^{(\ell-1,R)} (\omega + \omega_2, \omega + \omega_1, s) \right] \\
 & + \mathcal{G}_j(\omega) \mathcal{G}_i(\omega + s) \left[ \dot{\gamma}_{b, ij}^{(\ell-1,L)} (\omega + \omega_2, \omega + \omega_1, s) \Gamma_{b, ij} (\omega - \omega_4, \omega - \omega_3, s) \right. \\
 & \quad \left. + \dot{\gamma}_{c, ij}^{(\ell-1,L)} (\omega + \omega_2, \omega + \omega_1, s) \Gamma_{c, ij} (\omega - \omega_4, \omega - \omega_3, s) \right] \quad (C.70c)
 \end{aligned}$$

$$\begin{aligned}
 \tilde{\mathcal{B}}^2 \left( \dot{\gamma}^{\ell-1,R}, \Gamma \right)_{d, ij} (s, t, u) = & \tilde{\mathcal{B}}^2 \left( \dot{\gamma}^{\ell-1,R}, \Gamma \right)_{a, ij} (s, t, u) - \tilde{\mathcal{B}}^2 \left( \dot{\gamma}^{\ell-1,R}, \Gamma \right)_{b, ij} (s, t, u) \\
 & - \tilde{\mathcal{B}}^2 \left( \dot{\gamma}^{\ell-1,R}, \Gamma \right)_{c, ij} (s, t, u) \quad (C.70d)
 \end{aligned}$$

### C.3. Benchmarks

In this section, we shall review the performance of the Parquet algorithm for simple benchmark models with known solutions. A rigorous test of the correctness of FRG methods and their implementation is to observe whether the expected error scaling is reproduced. This is verified in Fig. C.3, which shows that at higher temperatures, the Parquet formalism indeed displays an error of the self-energy proportional to  $T^{-4}$ . This is more easily seen in the higher frequency components, as the error of the zero-frequency component has a sign change at intermediate temperatures. Despite this promising result, the Parquet formalism

fails to yield improvements for the more relevant magnetic susceptibility at lower temperatures. For the nearest neighbor cubic antiferromagnet, shown in Fig. C.4, it can be observed that the Parquet formalism, unlike the more simple one-loop FRG, fails to resolve magnetic ordering. This finding is in qualitative agreement with independent two-loop results shown for the pyrochlore FM in Fig. 5.5 and suggests that the Parquet formalism and the multiloop expansion are not suitable for the study of magnetic ordering in frustrated systems.

While this conclusion seems paradoxical, given the fact that the diagrams of the Parquet formalism form a strict superset of the one-loop diagrams, and thus reduce the approximation error in a perturbative sense, the application of FRG is typically done in a highly non-perturbative setting. In such cases, the validity of a given approximation can easily depend on other factors rather than the number of included diagrams. The unintuitive nature of these findings highlights the importance of performing quantitative benchmarks when comparing the efficiency of different diagrammatic methods.

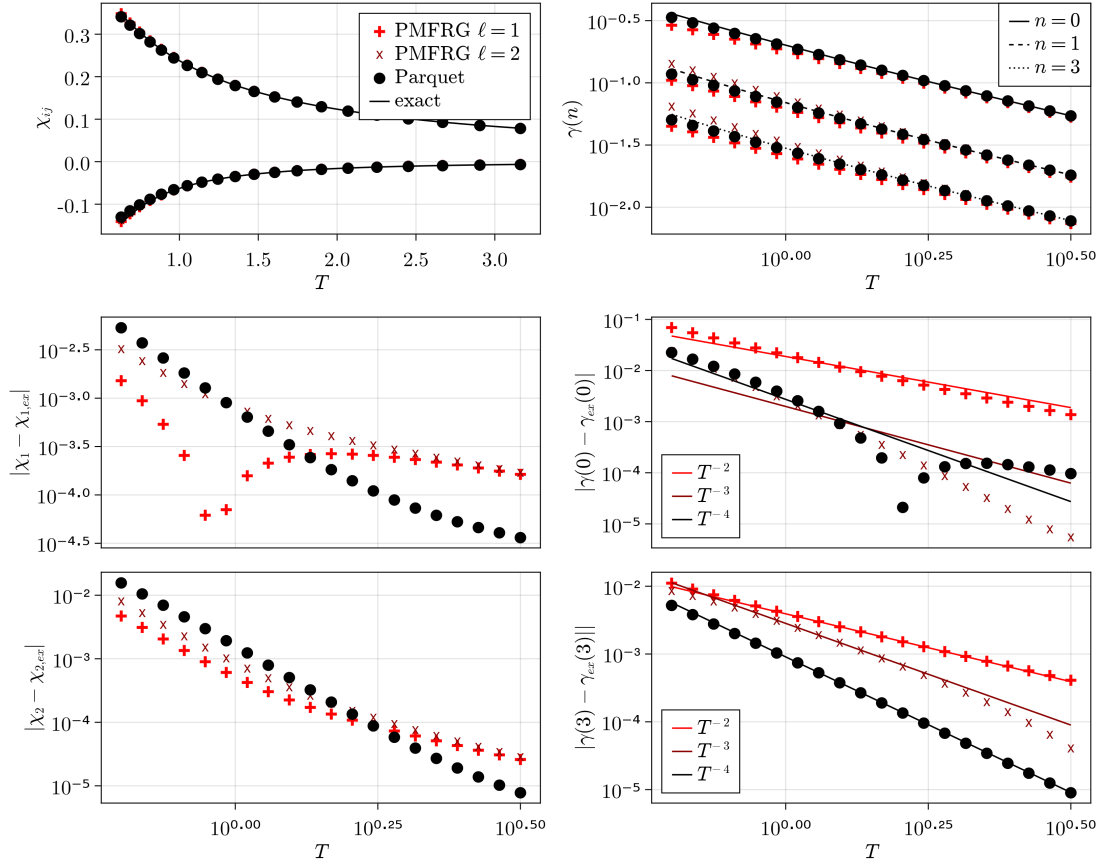


Figure C.3.: Benchmark of the Parquet algorithm for the spin-1/2 dimer. Shown are the asymptotic scalings of the two susceptibilities  $\chi_{11}$  and  $\chi_{12}$ , the self-energy  $\gamma(n)$ , and their respective absolute errors as a function of temperature. Symbols correspond to the one-loop  $\ell = 1$ , two-loop  $\ell = 2$ , and Parquet solutions. The expected error scaling of the self-energy compared to the exact solution is indicated by solid lines.

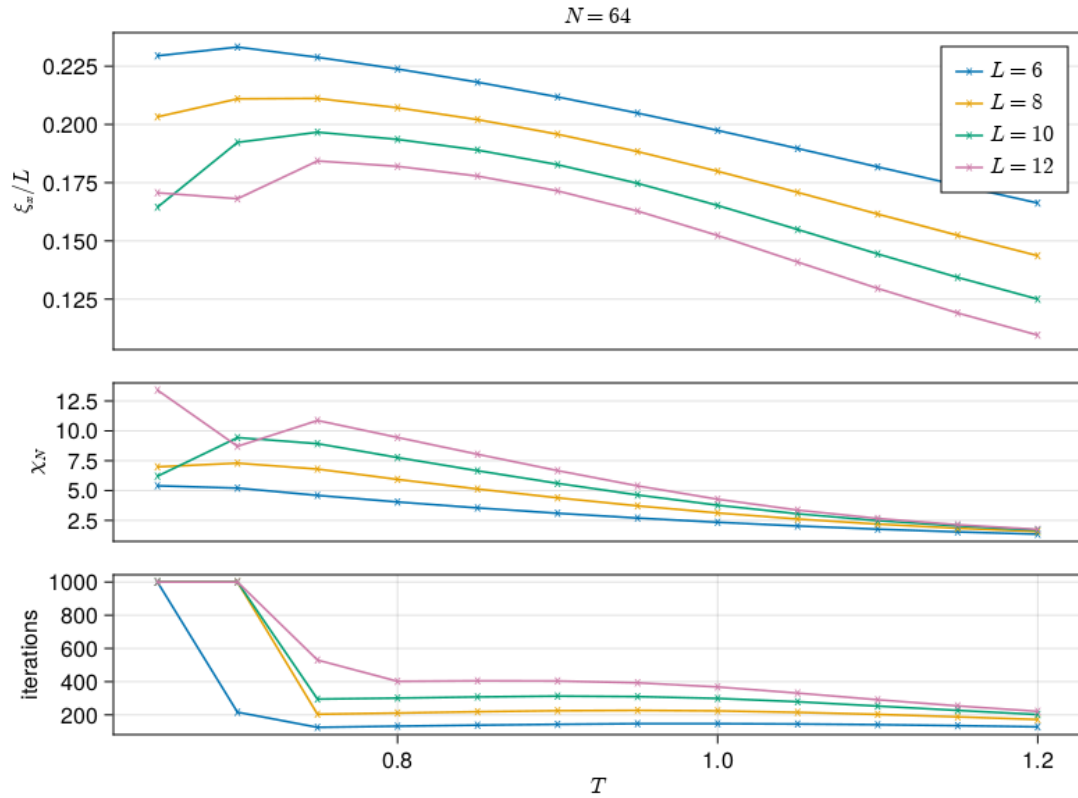


Figure C.4.: Susceptibility and rescaled correlation length obtained from the Parquet formalism. The expected ordering temperature  $T_c = 0.941$  from QMC is far surpassed without any indication of critical scaling. At lower temperatures, the Parquet equations fail to converge.

# D

## Spin-S flow equations and correlation functions

In PMFRG, we simulate the model in Eq. (3.39), i.e., a system of  $2S_{\text{eff}}N$  spin-1/2 degrees of freedom  $\mathbf{S}_{i_\mu}$  that are labelled by a site index  $i$  and a replica index  $\mu$ . At first glance treating this model may look like a considerable increase in numeric complexity since the number of bonds with a coupling  $J_{ij}$  increases by a factor  $(2S_{\text{eff}})^2$  relative to a genuine spin-1/2 model in which the replica index takes only a single value  $\mu = 1$  (i.e., no different replicas exist). However, below we will see that the introduction of replicas has virtually no impact on numerical performance due to a large number of symmetries in the replica index.

The central object to be calculated in PMFRG is the vertex function  $\Gamma_{f;i_\mu;j_\nu}(s, t, u)$  corresponding to the effective interaction between sites/replicas  $i_\mu$  and  $j_\nu$ , where  $f$  corresponds to the flavor combination, e.g.  $xyxy$  [1] and  $s, t, u$  are Matsubara frequencies. At the initial cutoff scale  $\Lambda \rightarrow \infty$  the vertex function is determined by the bare couplings  $J_{i_\mu;j_\nu}$ . Since an efficient PMFRG implementation only considers *symmetry-inequivalent* vertex functions  $\Gamma_{f;i_\mu;j_\nu}(s, t, u)$ , the first step is to determine all independent site/replica arguments  $(i_\mu, j_\nu)$  that have to be taken into account. As illustrated in Fig. 3.5, replicas  $\mu$ , positioned on the same site  $i$ , are equivalent, implying an invariance of the system under local permutations of replicas  $i_\mu \rightarrow i_{\mu'}$ . Thus, the site/replica arguments of vertex functions  $(i_\mu, j_\nu)$  can be divided into three equivalence classes of bonds denoted  $(i_1, j_1)$ ,  $(i_1, i_1)$ ,  $(i_1, i_2)$  where each of the three bonds corresponds to a representative element in each class. The three classes are defined by

$$(i_\mu, j_\nu) = \begin{cases} (i_1, j_1), & i \neq j \\ (i_1, i_1), & i = j \text{ and } \mu = \nu \\ (i_1, i_2), & i = j \text{ and } \mu \neq \nu \end{cases} . \quad (\text{D.1})$$

The first  $(i_1, j_1)$  and second bond  $(i_1, i_1)$  are the inter-site and onsite bonds already known from a genuine spin-1/2 model. On the other hand, the last bond  $(i_1, i_2)$  between two different replicas on the same physical site  $i$  does not exist in the genuine spin-1/2 case. Notably, apart from additional factors in the flow equation as discussed below, the introduction of replicas only amounts to the consideration of the additional symmetry-inequivalent bond  $(i_1, i_2)$  regardless of the value of  $S_{\text{eff}}$  which explains the negligible costs of the replica construction.

We now make use of the equivalence classes to determine the flow equations for arbitrary  $S_{\text{eff}}$ . To this end, we consider an exemplary term on the right hand side of the flow equation for  $d\Gamma_{f;ij}(s, t, u)/d\Lambda$  in Eq. (51) of Ref. [1] which, before the introduction of replicas, has the form

$$X_{ij} = \sum_k \Gamma_{ki}^{(L)} \Gamma_{kj}^{(R)} P_{kk}. \quad (\text{D.2})$$

Equation (D.2) is written in a strongly condensed form: As frequency indices and Majorana flavors  $x, y, z$  are irrelevant for our discussion, they are omitted in the bubble propagator  $P_{ii} \equiv -S_i^\Lambda(\omega)G_i^\Lambda(\omega')$  where  $S_i^\Lambda(\omega)$  is the single-scale propagator and  $G_i^\Lambda(\omega')$  is the fully dressed single-particle propagator. Likewise, to suppress frequency and flavor indices, we use dummy labels for vertices  $\Gamma_{ij}^{(L)}$  and  $\Gamma_{ij}^{(R)}$  to refer to arbitrary left and right vertices as appearing in each term of the flow equations in Eq. (51) of Ref. [1], for example  $\Gamma_{ij}^{(L)} = \Gamma_{a,ij}^\Lambda(s, \omega + \omega_1, \omega + \omega_2)$  in Eq. (51a) of Ref. [1].

Upon introducing the spin-1/2 replicas by splitting the sum over  $k$  as  $\sum_k \rightarrow \sum_k \sum_{\mu=1}^{2S_{\text{eff}}}$ , we reorganize and group the terms in the summation over  $\mu$  according to the equivalence classes in Eq. (D.1). It is noted that due to the aforementioned permutation symmetry in the replica index  $\mu$ , we may write the propagator as  $G_{i_\mu} = G_{i_1} \equiv G_i$  and thus  $P_{i_\mu, i_\mu} \equiv P_{i, i}$ . Hence, Eq. (D.2) in the class of bonds  $(i_1, j_1)$  becomes

$$\begin{aligned} X_{i_1 j_1} &= \sum_{k\mu} \Gamma_{k\mu, i_1}^{(L)} \Gamma_{k\mu, j_1}^{(R)} P_{k\mu, k\mu} \\ &= 2S_{\text{eff}} \sum_{k \neq i, j} \Gamma_{k_1, i_1}^{(L)} \Gamma_{k_1, j_1}^{(R)} P_{k, k} \\ &\quad + \Gamma_{i_1, i_1}^{(L)} \Gamma_{i_1, j_1}^{(R)} P_{i, i} + \Gamma_{j_1, i_1}^{(L)} \Gamma_{j_1, j_1}^{(R)} P_{j, j} \\ &\quad + (2S_{\text{eff}} - 1) \left( \Gamma_{i_1, i_2}^{(L)} \Gamma_{i_1, j_1}^{(R)} P_{i, i} + \Gamma_{j_1, i_1}^{(L)} \Gamma_{j_1, j_2}^{(R)} P_{j, j} \right). \end{aligned} \quad (\text{D.3})$$

The first term is equivalent to the non-local contributions in the genuine spin-1/2 case, rescaled by a factor  $2S_{\text{eff}}$  accounting for all replicas. On the other hand, the newly introduced bond  $(i_1, i_2)$  requires us to add the last line in Eq. (D.3). It can be seen that in the special case  $S_{\text{eff}} = 1/2$ , when no replicas are introduced, this expression reduces back to Eq. (D.2). In the same way we obtain for the bonds  $(i_1, i_1)$  and  $(i_1, i_2)$ :

$$\begin{aligned} X_{i_1, i_1} &= 2S_{\text{eff}} \sum_{k \neq i} \Gamma_{k_1, i_1}^{(L)} \Gamma_{k_1, i_1}^{(R)} P_{k, k} \\ &\quad + \Gamma_{i_1, i_1}^{(L)} \Gamma_{i_1, i_1}^{(R)} P_{i, i} + (2S_{\text{eff}} - 1) \left( \Gamma_{i_1, i_2}^{(L)} \Gamma_{i_1, i_2}^{(R)} P_{i, i} \right) \end{aligned} \quad (\text{D.4})$$

and

$$\begin{aligned}
X_{i_1, i_2} &= 2S_{\text{eff}} \sum_{k \neq i} \Gamma_{k_1, i_1}^{(\text{L})} \Gamma_{k_1, i_1}^{(\text{R})} P_{k, k} \\
&+ \left( \Gamma_{i_1, i_1}^{(\text{L})} \Gamma_{i_1, i_2}^{(\text{R})} + \Gamma_{i_1, i_2}^{(\text{L})} \Gamma_{i_1, i_1}^{(\text{R})} \right. \\
&\left. + (2S_{\text{eff}} - 2) \Gamma_{i_1, i_2}^{(\text{L})} \Gamma_{i_1, i_2}^{(\text{R})} \right) P_{i, i}.
\end{aligned} \tag{D.5}$$

The site summation for the self energy similarly changes through the introduction of replicas and its terms, are the same as found for  $X_{i_1, i_1}$ , see [1]. It is worth emphasizing again that the only additional terms compared to a genuine spin-1/2 model are those containing vertex functions on  $(i_1, i_2)$  bonds. Hence, for a PMFRG implementation of models with higher spins  $S > 1/2$  one can copy most terms from a spin-1/2 code while only the terms with  $(i_1, i_2)$  bonds need to be added manually <sup>1</sup>.

Ultimately, the object of interest are spin correlators  $\chi_{ij} \equiv \langle \mathbf{S}_{i, \text{eff}} \cdot \mathbf{S}_{j, \text{eff}} \rangle$ . Since the PMFRG only returns replica correlators  $\langle \mathbf{S}_{i_\mu} \cdot \mathbf{S}_{j_\nu} \rangle$ , we obtain  $\chi_{ij}$  via replacing  $\mathbf{S}_{i, \text{eff}}$  by its definition in Eq. (3.38) and expanding the replica summation. Again, we use the equivalence classes in Eq. (D.1) to simplify the expression. For non-local correlators  $i \neq j$ , all terms in the sum are equal and thus we obtain a simple prefactor  $(2S_{\text{eff}})^2$ . For local correlators  $i = j$  we distinguish between contributions from two different replicas  $\langle \mathbf{S}_{i_1} \cdot \mathbf{S}_{i_2} \rangle$  and contributions from identical replicas  $\langle \mathbf{S}_{i_1} \cdot \mathbf{S}_{i_2} \rangle$ :

$$\chi_{i, j \neq i} = (2S_{\text{eff}})^2 \langle \mathbf{S}_{i_1} \cdot \mathbf{S}_{j_1} \rangle \tag{D.6}$$

$$\chi_{i, i} = 2S_{\text{eff}} \langle \mathbf{S}_{i_1} \cdot \mathbf{S}_{i_1} \rangle + 2S_{\text{eff}}(2S_{\text{eff}} - 1) \langle \mathbf{S}_{i_1} \cdot \mathbf{S}_{i_2} \rangle \tag{D.7}$$

As the heat capacity is determined from PMFRG via derivatives of the interacting free energy, we also adjust this quantity to be

$$f_{\text{int}} \rightarrow 2S_{\text{eff}} f_{\text{int}}. \tag{D.8}$$

---

<sup>1</sup>This must only be implemented once for an arbitrary lattice. An exemplary code implementation can be found in the publicly available package SpinFRGLattices.jl, where a given lattice geometry may simply be modified to obtain the corresponding effective spin- $S$  model.





## Details on the numerical PMFRG implementation

This appendix will give a few general remarks regarding the numerical implementation of the PMFRG method featured in this thesis. Numerical results of the previous chapters are obtained using the self-developed package *PMFRG.jl* found under <https://github.com/NilsNiggemann/PMFRG.jl>.

The solution of the flow equations amounts to the numerical integration of a large system of coupled ordinary differential equations (ODE's). The initial conditions are given as

$$\begin{aligned}\Gamma_c^{\Lambda_0}(s, t, u) &= -J_{ij} \\ \gamma_i^{\Lambda_0}(\omega) &= \Gamma_a^{\Lambda_0}(s, t, u) = \Gamma_b^{\Lambda_0}(s, t, u) = 0,\end{aligned}\tag{E.1}$$

with  $\Lambda_0$  (or  $T_0$  in the case of the temperature flow method) at least two orders of magnitude above the largest exchange coupling. To obtain a finite system of equations, only the first  $N_\omega$  non-negative Matsubara frequencies are considered (negative frequencies are related by symmetries). Matsubara sums over  $i\omega_n$  are truncated for  $|n| > N_\omega$ . The error made in this approximation is controlled since the contribution of large frequencies is typically small due to the vanishing propagator  $\mathcal{G}(i\omega_n) \sim 1/i\omega_n$ . For four-point vertices, we must pay special attention to the fact that combinations of bosonic Matsubara integers  $n_s, n_t, n_u$  are (un-)physical if their sum  $n_s + n_t + n_u$  is odd (even) [1]. Vertices with unphysical frequency arguments will never appear in flow equations and are thus not computed. If one or more Matsubara integers are greater or equal to  $N_\omega$ , the vertex is approximated by setting the associated index to either  $N_\omega - 1$  or  $N_\omega - 2$  such that  $n_s + n_t + n_u$  is odd. This avoids the introduction of errors at the boundaries of the frequency range. For the same reason, we also refrain from the alternative of interpolating between frequencies and instead raise the number of positive frequencies until convergence is reached. Good results are typically obtained at  $N_\omega = 32$ , particularly, for temperatures  $T \gtrsim 0.5$ . For the lowest temperature treated, usually a larger number of frequencies,  $N_\omega = 64$ , or even more may be needed. While the latter is typically a good rule of thumb, it is useful to check convergence for each individual case.

Regarding the real space cutoff used here, no significant dependence on the

particular choice of the cutoff is reported. If the maximum vertex length is defined by the number of nearest-neighbor bonds instead of an (isotropic) distance  $L$ , the same scaling behaviour is observed.

Numerically, the flow equations were solved using adaptive, error-controlled methods provided in the Julia package “DifferentialEquations.jl” [304]. To allow for accurate numerical derivatives of the free energy, a relative tolerance  $\sim 10^{-8}$  is required in which case the Dormand-Prince(5) method was found to be most efficient.

## Implementation details regarding the spiderweb model

### F.1. Exact diagonalization in block diagonal Hilbert space

Due to the exponential growth of the Hilbert space with the number of sites, it is inefficient to work directly in the  $S^z$  basis. However, the large number of independent Hilbert space blocks simplifies this problem significantly. To determine the ground state of the Hamiltonian in Eq. (7.17), we must thus first identify all states within a given Hilbert space sector. We start with a classical spin configuration and find all flippable plaquettes to generate all other classical configurations that the state can tunnel into via application of  $\mathcal{H}_2$  defined in Eq. (7.17). As an example, consider the staircase state displayed in Fig. 7.1 f), which we shall here label as  $|x_0\rangle$ : A single plaquette flip can be applied in 36 different locations, indicated by red dots, resulting in 36 new configurations. We assign a *unique* label to each newly generated state  $|x_1\rangle \dots |x_{36}\rangle$  and record  $\mathcal{H}_{x_0, x_i} = -1, \forall i \in 1, 2, \dots, 36$  for the elements of the Hamiltonian of so-far unspecified dimension. This procedure is then repeated for each of the new states generated this way. It is evident that the labels  $|x_i\rangle$  of newly found states must be unique such that no single configuration may be mapped to two different labels. Numerically, this can be efficiently achieved by using a hash-map, usually implemented as a dictionary in many languages. While it is possible to use the entire spin configuration as a key to the dictionary, hashing an entire array is slow, so further compression is useful. In the case of spin-1/2, we may uniquely determine each state by a number of plaquette flips acting on the parent state, for example the stair case state. If we identify all position of flippable plaquettes, we may encode a single configuration within a single bitstring, i.e. the state "0000" corresponds the staircase state with no plaquettes flipped while the state "0100" differs by applying a single plaquette flip of plaquette number 2. A single UInt64 has 64 bits of information and may thus represent any state in a Hilbert sector with no more than 64 possible plaquette positions.

For finite system sizes, after a finite number of iterations, no new configurations

are found, i.e. all states that are found have already been assigned their label. The resulting sparse Hamiltonian matrix may then straight-forwardly be diagonalized with standard linear algebra routines and observables such as the spin structure factor can be evaluated by converting the unique bitstrings from found previously back into their corresponding spin configurations.

In the language of graph theory, we can also specify the above procedure as a breadth-first search algorithm of an undirected graph where the nodes are given by classical spin configurations and the edges are determined by the applicability of single plaquette flips. The Hamiltonian  $\mathcal{H}_{x_i, x_j} = 0, -1$  is then equivalent to the adjacency matrix of this network.

In this way, we can determine exact eigenvalues and eigenvectors in a given block of the Hamiltonian for systems up to  $\sim 14 \times 14$  sites. For larger systems, the exponential growth of the Hilbert space quickly leads to extreme memory requirements to store the classical spin configurations, even when represented as bitstrings. To investigate larger sizes at spin 1, we employ the Green function Monte Carlo method.

## **F.2. Green function Monte Carlo**

Quantum Monte Carlo methods are numerically exact ways to determine ground state properties of Hamiltonians that are free from the sign problem. Here, the Green Function Monte Carlo (GFMC) approach is implemented as in Ref. [305], which we find particularly useful for the given problem. See also References [125, 306, 307]. In essence, GFMC avoids the exhaustive computation of the entire Hilbert space in favor of a statistical sampling of observables by performing a random walk instead. The random walk is utilized to realize a projection approach, i.e. making use of the fact that repeated applications of the Hamiltonian to a trial state  $|\psi_T\rangle$  converge to the ground state exponentially, or, more precisely,  $(\Lambda - \mathcal{H})^{\mathcal{P}} |\psi_T\rangle \rightarrow |\psi_0\rangle$  for  $\mathcal{P} \rightarrow \infty$ . The constant  $\Lambda$  can be used to shift the spectrum such that the dominant eigenvector of  $\mathcal{G} \equiv \Lambda - \mathcal{H}$  corresponds to the ground state of  $\mathcal{H}$  as opposed to the maximally excited one. If the Hamiltonian has purely negative elements,  $\lambda = 0$  is sufficient as  $E_{\max} \leq |E_0|$  according to the Perron–Frobenius theorem. If  $\mathcal{H}$  has positive diagonal elements, we may choose a finite  $\Lambda \geq \max_x \mathcal{H}_{xx}$ . The only requirement for the trial wavefunction  $|\psi_T\rangle$  is that it has nonzero overlap with the ground state. This can be asserted by  $\psi_T(x) > 0$  for all configurations  $x$ .

As outlined in the previous section, the Hilbert space is represented by a graph with an adjacency matrix  $\mathcal{H}_{xx'}$ . Despite the exponential growth of the Hilbert space, there are at most  $L^2/2$  neighboring states for which  $\mathcal{H}_{xx'} \neq 0$  for a given configuration  $|x\rangle$ . Thus, starting from the initial configuration  $|x_0\rangle = (0, 0, \dots, 0)$ , we can perform a random walk by randomly selecting one of the neighboring states accessible by a single plaquette flip. To discuss how the formalism works, we first consider a special case in which the Hamiltonian is equivalent to a stochastic transition matrix  $p_{x'x} \geq 0$  that fulfills the property

$$\sum_{x'} p_{xx'} = 1. \quad (\text{F.1})$$

In a sector with  $N_{\square}$  non-overlapping plaquettes, none of the moves affect each other, and we can easily identify  $\mathcal{G}_{xx'} = p_{xx'} N_{\square}$ . We will discuss later how to treat the more general case.

Starting from an initial configuration  $|x\rangle$ , at each step of the random walk, we select one of the configurations  $|x'\rangle$  with a probability given by  $p_{xx'}$ , defining a Markov process. After a sufficiently long time, the probability amplitude  $\psi_x^{\text{Eq}}$  to be in any state  $x$  converges to an equilibrium [307]

$$\sum_{x'} p_{xx'} \psi_{x'}^{\text{Eq}} = \psi_x^{\text{Eq}}. \quad (\text{F.2})$$

Interpreting the above as an eigenvalue equation, we see that the equilibrium probability distribution  $\psi_x^{\text{Eq}}$  is an eigenvector of  $p_{xx'}$  and thus also of  $\mathcal{H}$  with eigenvalue 1. It can be easily seen that this is fulfilled by the eigenvector given as  $\psi^{\text{Eq}} = (1, 1, \dots, 1)$ . Moreover, due to Eq. (F.1), the spectrum of  $p_{xx'}$  is bounded such that all other eigenvalues  $\lambda_i \leq 1$  [307]. Since the largest eigenvalue of  $p_{xx'}$  corresponds to the minimum eigenvalue of  $\mathcal{H}_{xx'}$ , we can identify  $\psi_T(x) = \psi^{\text{Eq}}(x) = 1$ . As this trial wavefunction is exact, we can determine any observable  $\mathcal{O}$  in the ground state by sampling over a large enough number  $N$  of equilibrated configurations  $x_n$ :

$$\langle \mathcal{O} \rangle = \frac{\langle \psi_T | \mathcal{G}^P \mathcal{O} \mathcal{G}^P | \psi_T \rangle}{\langle \psi_T | \mathcal{G}^P \mathcal{G}^P | \psi_T \rangle} \quad (\text{F.3})$$

$$= \lim_{N \rightarrow \infty} \frac{1}{N} \sum_n^N \langle \psi_T | \mathcal{O} | x_n \rangle. \quad (\text{F.4})$$

In the second line, we used the fact that  $|\psi_T\rangle = |\psi^{\text{Eq}}\rangle$  and  $H^P |\psi^{\text{Eq}}\rangle \sim |\psi^{\text{Eq}}\rangle$ . We now discuss the more general case in which  $\mathcal{G}_{xx'} \approx p_{xx'}$ . In this case, we can still define a random walk by defining the probability as

$$p_{xx'} = \frac{\mathcal{G}_{xx'}}{\sum_{x'} \mathcal{G}_{xx'}} \equiv \frac{\mathcal{G}_{xx'}}{w_x}. \quad (\text{F.5})$$

Clearly, the ground state is no longer given by the equilibrium  $\psi_x^{\text{Eq}}$ , and the projection in Eq. (F.3) is nontrivial. To measure an observable  $\mathcal{O}$ , we must first apply  $\mathcal{G}$  for  $\mathcal{P}$  steps to a configuration  $|x_n\rangle$  and sample the value of  $\mathcal{O}$ . Averaged over many runs, this corresponds to an evolution of the walker of  $\mathcal{P}$  steps, with probability given by  $p_{xx'}$ . However, since  $\mathcal{G}_{x,x'} = p_{x,x'} w_x$ , we also need to multiply the weights  $w_x$  at each step. Any observable may thus be computed exactly as

$$\langle \mathcal{O} \rangle = \frac{\sum_{n=\mathcal{P}}^{N-\mathcal{P}} W_n^{\mathcal{P}} \mathcal{O}(x_n)}{\sum_{n=\mathcal{P}}^{N-\mathcal{P}} W_n^{\mathcal{P}}}. \quad (\text{F.6})$$

The weights of the projection before and after applying the operator  $\mathcal{O}$  to the trial state are accumulated as

$$W_n^{\mathcal{P}} = \prod_{n-\mathcal{P}}^{n+\mathcal{P}} w_{x_n}. \quad (\text{F.7})$$

If the operator  $\mathcal{O}$  in Eq. (F.6) is diagonal in  $x$ , i.e.  $\langle x' | \mathcal{O} | x \rangle \sim \delta_{xx'}$ , both the numerator and the denominator can be determined from the same Markov chain. This is because applying  $\mathcal{O}$  at any step does not alter the configuration and the weight at step  $n$  only needs to be rescaled by  $\langle x_n | \mathcal{O} | x_n \rangle$ . For off-diagonal observables, applying  $\mathcal{O}$  changes the configuration  $|x_n\rangle$ , so that a new simulation of length  $\mathcal{P}$  needs to be run starting from one of the possible configurations obtained from applying  $\mathcal{O} |x_n\rangle$  (chosen with weights given by  $\mathcal{O}_{x'x_n}$ <sup>1</sup>). The above procedure converges to the correct mean; however, the product in Eq. (F.7) leads to strong fluctuations that diverge exponentially in  $\mathcal{P}$ , rendering this basic approach extremely ineffective. In order to reduce the statistical fluctuations, two important additions to the formalism are necessary.

*Importance sampling* – A purely random walk is a rather inefficient way to sample the Hilbert space. Better convergence can be achieved by favoring classical states with a large overlap with the ground state wavefunction. Such a *guiding wavefunction* can be employed simply by rescaling  $\mathcal{G}_{xx'}$  by a factor of  $\psi_T(x')/\psi_T(x)$ . If the exact ground state wavefunction is chosen, as shown in the previous example, the variance of the energy is exactly zero and the projection converges at  $\mathcal{P} = 0$ . In the generic case, the exact solution is typically unattainable; however, the required number of projection steps and statistical fluctuations can still be greatly reduced by choosing an optimal variational function. Crucially, no bias is introduced provided that the guiding wavefunction is nonsingular, i.e.,  $\infty \neq \psi_T(x) \neq 0$  for any  $x$ . A good starting point is the relatively simple variational wavefunction  $\psi_T(x) = \exp(\alpha N_{\square}(x))$ , where a positive  $\alpha$  increases the contribution from states with a higher number of flippable plaquettes  $N_{\square}(x) = \mathcal{F}_{\square}^{\dagger} \mathcal{F}_{\square} + \mathcal{F}_{\square} \mathcal{F}_{\square}^{\dagger}$ . This choice

---

<sup>1</sup>Or, in the case of importance sampling introduced below,  $\mathcal{O}_{x'x_n} \psi_T(x')/\psi_T(x_n)$

will yield good results as it can be shown that it is equivalent to an imaginary time evolution of length  $\alpha$  of the RK wavefunction.

$$\langle x | e^{-\alpha H} | \psi_{RK} \rangle = e^{-\alpha \sum_{x'} H_{x',x}} = e^{\alpha N_{\square}(x)}. \quad (\text{F.8})$$

For larger system sizes, it is helpful to optimize a variational wavefunction with more parameters. A good choice is

$$\psi_T(x) = \exp \left\{ \sum_i \alpha_i n_{\square_i}(x) + \sum_{i < j} \beta_{i,j} n_{\square_i}(x) n_{\square_j}(x) \right\}, \quad (\text{F.9})$$

where the index  $i$  iterates over all plaquettes. The variational parameters  $\alpha_i$  and  $\beta_{i,j}$  are optimized using the stochastic reconfiguration method [308]. In principle, it is also possible to choose even more sophisticated variational approaches, such as neural network states or even results from tensor network methods [134, 309]. As the guiding wavefunction is evaluated many times in each Markov step, it is crucial that it is efficient to evaluate.

### *Many walker formalism–*

To reduce the amount of fluctuations at large values of  $\mathcal{P}$ , we employ the many-walker formalism. The procedure used here is the one introduced in Ref. [305], which is particularly useful as it does not introduce any systematic errors regardless of the number of walkers [307, 310]. The many-walker approach is used as follows: First,  $N_w$  walkers are initialized and evolve fully independently for  $n_{\text{branch}}$  steps, accumulating their weight  $w_\alpha = \prod_1^{n_{\text{branch}}} w_{\alpha n}$  for  $\alpha = 1, \dots, N_w$  as described before. Afterwards, we perform the reconfiguration in which each walker is given a new configuration from all walkers, sampled with probability  $w_\alpha / \sum_\alpha^{N_w} w_\alpha$ . This process is a single Markov step which will contribute an ensemble of configurations with a single weight  $w = \frac{1}{N_w} \sum_\alpha^{N_w} w_\alpha$ . This reconfiguration ensures that walkers with negligible weight are eliminated while those with large weight are multiplied, which explores the Hilbert space much more efficiently. It is noted that to measure observables with the forward walking method, the exact reconfiguration process has to be saved, as some of the walkers are eliminated during the reconfiguration steps following the application of  $\mathcal{O}$ . See [125, 305] for more details.

### **Ergodicity**

Although numerically exact, GFMC, like any Markov-based method, can potentially suffer from long correlation times, especially if the graph of the Hamiltonian features large, sparsely connected clusters [284, 311]. We have found that this

can be diagnosed by initializing a large fraction, approximately 9/10, of the walkers with a random configuration in the  $S^z = 0$  subsector (chosen by performing approximately 20,000 fully random plaquette flips) for several independent runs. If the equilibration times are too long, this may result in very large errors in the mean energy, even at  $\mathcal{P} = 0$ . By using a sufficiently large number of walkers and keeping the number of branching steps  $N_{\text{Bra}}$  high enough, the reconfiguration process drastically improves equilibration and keeps errors of all quantities low between several independent runs. As the accuracy of the simulation can be extremely high for smaller system sizes, it is also practical to verify that physical properties do not change upon increasing the system size. A demonstration of the application of GFMC in comparison with ED is given in Fig. F.1. A good indicator of the convergence of the projection is the ground state energy shown in panel (a). The data point at  $\mathcal{P} = 0$  for the single walker corresponds to a variational Monte Carlo (VMC) estimate using the trial wavefunction. The many-walker formalism can be seen to improve statistical errors at higher projection orders.

If the Hamiltonian features large positive diagonal elements, it is advisable to consider the *continuous-time* limit  $\Lambda \rightarrow \infty$ , in which the projector is equivalent to  $e^{-\mathcal{H}\Delta\tau}$  for a numerically chosen time step  $\tau$  [125]. Using the forward walking formalism, arbitrary observables in the  $S^z$  basis can be measured. All observables can be seen to converge to the exact result after 50 projection steps for  $N_w = 20$  walkers. The required number of projection steps usually depends on the system size  $L$  and the number of walkers. For example, for Fig. 7.3(c), an ensemble of 12,800 walkers was used that were evolved with a continuous-time step  $\Delta\tau = 0.2$  for 12,000 steps after equilibration. The mean and standard deviations (error bars) were estimated by performing 14 independent runs. The projection typically converged after  $\tau \gtrsim 15$ . For smaller system sizes, a much lesser number of steps and walkers is usually sufficient. It should be noted that the projection procedure requires the existence of a gapped spectrum. While a gapless spectrum is predicted in some cases in the thermodynamic limit, one can expect a finite size gap for all finite systems.

### F.3. Details on the rank-2 U(1) field theory

The Maxwellian field theory in Eq. (7.19) is derived by expressing the spin flip operators in  $\mathcal{H}_2$  in terms of rotor variables  $S_i^\pm = \sqrt{2}e^{\pm iA_i^\alpha}$ , where  $A_i^\alpha$  plays the role of a generalized ‘vector’ potential. The operators  $A_i^\alpha$  (which follow the convention that  $\alpha = xy$  when  $i$  is on sublattice 1 and  $\alpha = xx$  when  $i$  is on sublattice 2) are the



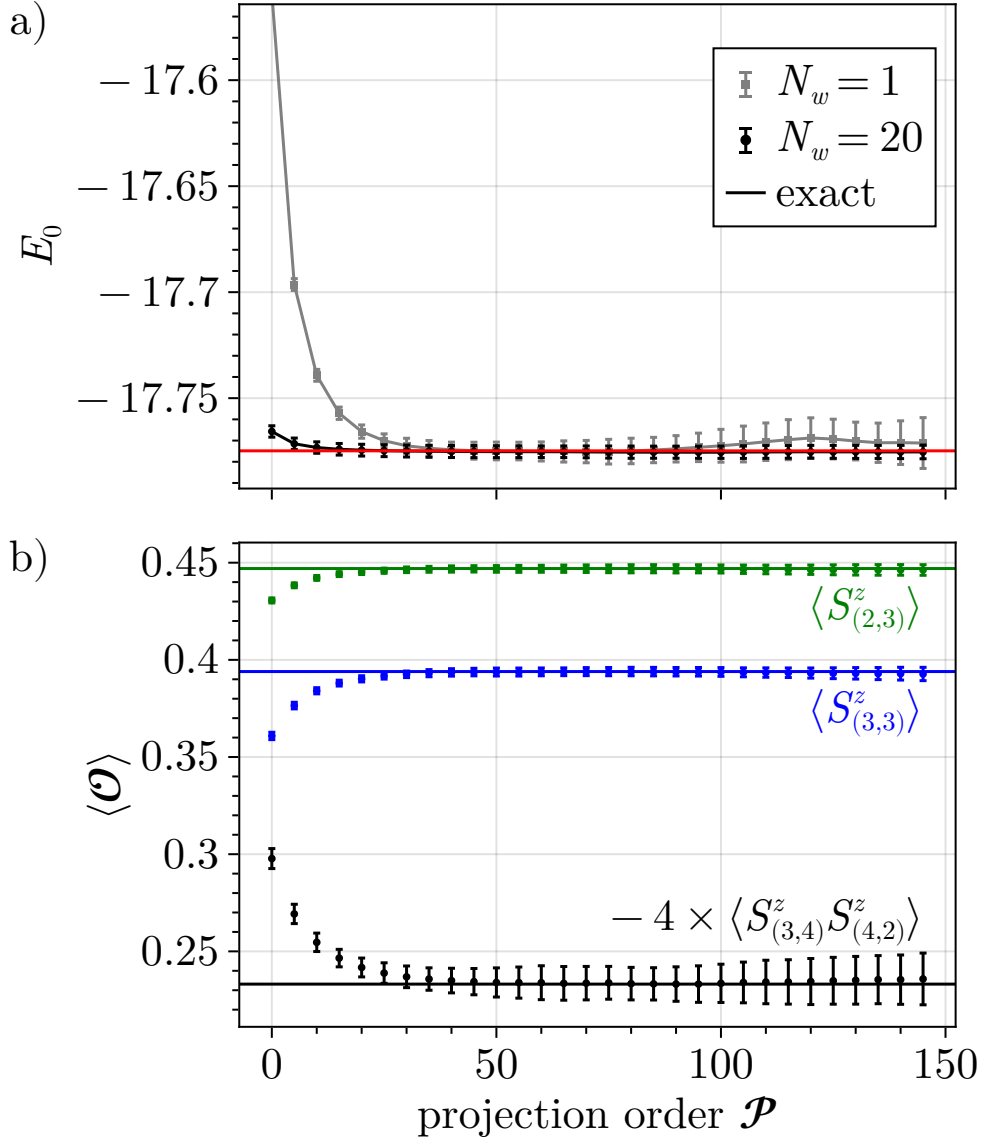


Figure F.1.: Comparison of GFMC in the spin-1/2 staircase sector with ED for  $L = 14$  with open boundary conditions. (a): Ground state energy as a function of the projection order for a single walker (grey) compared to an ensemble of 20 walkers (black) and the exact result (red horizontal line). (b): Different expectation values of different one- and two-point spin correlators each compared to the exact result in the same color.

components of a trace-free and symmetric matrix-valued field, i.e.,  $A_i^{xx} = -A_i^{yy}$  and  $A_i^{xy} = A_i^{yx}$ . Furthermore,  $A_i^\alpha$  is compact, i.e., its eigenvalues lie in the interval  $[0, 2\pi]$ . In addition to the notation  $A_i^\alpha$ , we will use the alternative notation  $A_{\square}^{xy}$  ( $A_{\square}^{xx}$ ) to indicate that  $A_i^{xy}$  ( $A_i^{xx}$ ) is defined for each site  $i$  that is the center of a  $\square$  cluster ( $\square$  cluster). The  $z$ -components of the spins  $S_i^z$  take the role of a conjugate integer-valued matrix electric field  $S_i^z = E_i^\alpha$  with  $[A_i^\alpha, E_i^\alpha] = i$ . We will also use the notation  $E_{\square}^{xy}$  and  $E_{\square}^{xx}$  for the electric field components, in analogy to  $A_{\square}^{xy}$  and  $A_{\square}^{xx}$ . With these definitions,  $\mathcal{H}_2$  takes the form

$$\mathcal{H}_2 \sim - \sum_{\square} \cos B_{\square} \sim + \sum_{\square} B_{\square}^2 \quad (\text{F.10})$$

where  $B_{\square}$  is defined for each cluster  $\square$  as given in Eq. (7.18), and the rightmost expression in Eq. (F.10) represents the expansion of  $\mathcal{H}_2$  in the lowest non-trivial order in  $B_{\square}$ . Together with the electric field term  $\sim (E_i^\alpha)^2$  and the RK potential  $\sim \mathcal{N}_{\square}^2$ , we obtain the effective field theory in Eq. (7.19). An important property of this theory that distinguishes it from conventional U(1) gauge theories is the absence of electromagnetic duality. This is already evident from the different properties of the electric and magnetic fields, where the former is a matrix while the latter is a scalar.

The field theory has a local gauge freedom that follows from the rank-2 Gauss law and amounts to the invariance under the operation [55]

$$U(f_{\square}) = \exp\left(i \sum_{\square} f_{\square} \mathcal{C}_{\square}\right) \quad (\text{F.11})$$

where  $f_{\square}$  is an arbitrary function defined for each cluster  $\square$  or, stated differently,  $f_{\square}$  is located on sublattice 1. Using

$$\mathcal{C}_{\square} = E_{\square_1}^{xx} + E_{\square_2}^{xy} - E_{\square_3}^{xx} - E_{\square_4}^{xy} + E_{\square_5}^{xx} + E_{\square_6}^{xy} - E_{\square_7}^{xx} - E_{\square_8}^{xy} \quad (\text{F.12})$$

the sum in the exponent of Eq. (F.11) can be rearranged yielding

$$U(f_{\square}) = \exp\left[i \sum_{\square} E_{\square}^{xy} (f_{\square_2} - f_{\square_4} + f_{\square_6} - f_{\square_8})\right] \times \exp\left[i \sum_{\square} E_{\square}^{xx} (f_{\square_1} - f_{\square_3} + f_{\square_5} - f_{\square_7})\right]. \quad (\text{F.13})$$

Here, the notation  $E_{\square_a}^{xy}$ ,  $f_{\square_a}$  with  $a = 2, 4, 6, 8$  and  $E_{\square_a}^{xx}$ ,  $f_{\square_a}$  with  $a = 1, 3, 5, 7$  makes use of the site labelling convention in Eq. (7.17) where, e.g.,  $f_{\square_1}$  is a site to the right of the center of a  $\square$  cluster, such that  $f_{\square_1}$  is still defined on sublattice

Sublattice 1	Sublattice 2
Center of $\boxtimes$ cluster	Center of $\square$ cluster
Quantities on sublattice 1: $\mathcal{C}$ (constraint) $\rho$ (fractons) $A^{xy}, E^{xy}$ (fields of U(1) theory) $f$ (gauge transformation)	Quantities on sublattice 2: $\mathcal{F}$ (fluctuator) $B$ (magnetic field) $A^{xx}, E^{xx}$ (fields of U(1) theory) $\mathcal{N}^2$ (RK potential) $h$ (height field)

Table F.1.: Definitions of the two sublattices of the spiderweb model and location of different quantities.

1 (center of a  $\boxtimes$  cluster). Since  $\exp(i\theta E_i^\alpha)$  with  $\theta \in \mathbb{R}$  shifts  $A_i^\alpha \rightarrow A_i^\alpha + \theta$  the operation in Eq. (F.13) can be written as

$$\begin{aligned} A_{\boxtimes}^{xy} &\rightarrow A_{\boxtimes}^{xy} + f_{\boxtimes_2} - f_{\boxtimes_4} + f_{\boxtimes_6} - f_{\boxtimes_8}, \\ A_{\square}^{xx} &\rightarrow A_{\square}^{xx} + f_{\square_1} - f_{\square_3} + f_{\square_5} - f_{\square_7}. \end{aligned} \quad (\text{F.14})$$

By simple bookkeeping of all terms it can be checked that Eq. (7.18) is indeed invariant under this transformation.

Table F.1 summarizes all the definitions related to the two sublattices and the quantities located on them. The gauge transformation in Eq. (F.14) becomes more transparent in a continuum description, where it can be written as:

$$\begin{aligned} A^{xy} &\rightarrow A^{xy} + 4\partial_x \partial_y f, \\ A^{xx} &\rightarrow A^{xx} + (\partial_x^2 - \partial_y^2) f. \end{aligned} \quad (\text{F.15})$$

Using the continuum definition of the magnetic field in Eq. (7.18):

$$B = -4\partial_x \partial_y A^{xx} + (\partial_x^2 - \partial_y^2) A^{xy}, \quad (\text{F.16})$$

it is immediately obvious that  $B$  is invariant under the gauge transformation in Eq. (F.15). The special property of Eq. (F.16) is that  $B$  is constructed from *second* derivatives of  $A^{xx}$  and  $A^{xy}$ . This is in contrast to a three-dimensional scalar charge rank-1 or rank-2 U(1) gauge theory, where one derivative is sufficient to construct a gauge-invariant magnetic field [103].

Returning to the lattice version of our rank-2 U(1) gauge theory [see Eq. (7.24)], this Hamiltonian can now be solved using a bosonic Bogoliubov transformation.

The naïve approach would be to diagonalize  $\mathcal{H}_{\text{eff}}$  using the usual unitary transformations, leading to a Hamiltonian

$$\mathcal{H}_{\text{eff}} = \sum_{\mathbf{q}\mathbf{a}} \varepsilon_{\mathbf{a}}(\mathbf{q}) \gamma_{\mathbf{a}}^{\dagger}(\mathbf{q}) \gamma_{\mathbf{a}}(\mathbf{q}). \quad (\text{F.17})$$

However, this transformation does not preserve the bosonic commutation relations and would thus lead to the wrong result. The solution is to use a paraunitary transformation, which can be shown to preserve the commutation relations [286, 287]. Put precisely, we need to rewrite  $\mathcal{H}_{\text{eff}}$  in terms of Bose operators  $C(\mathbf{q})$  for the eigenmodes:

$$C(\mathbf{q}) = (c_1(\mathbf{q}), c_2(\mathbf{q}), c_1^{\dagger}(\mathbf{q}), c_2^{\dagger}(\mathbf{q})) \quad (\text{F.18})$$

where  $C(\mathbf{q}) = \mathcal{J}(\mathbf{q})A(\mathbf{q})$ , such that  $(\mathcal{J}^{\dagger})^{-1}H_{\text{eff}}\mathcal{J}^{-1}$  is diagonal. The paraunitary  $4 \times 4$  matrix  $J(\mathbf{q})$  satisfies  $\mathcal{J}^{\dagger}g\mathcal{J} = g$  with  $g = \text{diag}(1, 1, -1, -1)$  [286]. A subtlety arises because of the gauge invariance of  $\mathcal{H}_{\text{eff}}$ , which manifests in a bosonic zero mode. While these zero modes are known not to contribute to gauge-invariant quantities, such as correlators [68], here they are dealt with via an additional term in the Hamiltonian of the form  $2d \sum_i (A_i^{\alpha})^2$ , which breaks gauge invariance and allows for an explicit calculation of  $\mathcal{J}(\mathbf{q})$ . The gauge-invariant limit  $d \rightarrow 0$  can then be recovered at the end of the calculation. The transformation matrix  $\mathcal{J}(\mathbf{q})$  is found to be:

$$\begin{aligned} \mathcal{J}(\mathbf{q}) &= \frac{1}{\sqrt{8(L_1^2 + L_2^2)}} \times \\ &\times \begin{pmatrix} L_1\xi_+ & L_2\xi_+ & -L_1\xi_- & -L_2\xi_- \\ -L_2\lambda_+ & L_1\lambda_+ & L_2\lambda_- & -L_1\lambda_- \\ -L_1\xi_- & -L_2\xi_- & L_1\xi_+ & L_2\xi_+ \\ L_2\lambda_- & -L_1\lambda_- & -L_2\lambda_+ & L_1\lambda_+ \end{pmatrix} \end{aligned} \quad (\text{F.19})$$

with

$$\xi_{\pm} = \left(\frac{U}{d}\right)^{1/4} \pm 2 \left(\frac{d}{U}\right)^{1/4}, \quad (\text{F.20})$$

$$\lambda_{\pm} = \sqrt{2} \left[ \left(\frac{\eta_2}{\eta_1}\right)^{1/4} \pm \left(\frac{\eta_1}{\eta_2}\right)^{1/4} \right], \quad (\text{F.21})$$

$$\eta_1 = d + K [(c_x - c_y)^2 + 4s_x^2 s_y^2], \quad (\text{F.22})$$

$$\eta_2 = \frac{U}{4} + W [(c_x - c_y)^2 + 4s_x^2 s_y^2], \quad (\text{F.23})$$

and  $L_1, L_2$  are defined in Eq. (7.9). Diagonalizing  $H_{\text{eff}}$  with  $\mathcal{J}$  leads in the limit  $d \rightarrow 0$  to a zero mode due to the systems gauge freedom and a single photon mode

with the dispersion

$$\begin{aligned}\omega(\mathbf{q}) &= 2\sqrt{\eta_1\eta_2} \\ &= 2\sqrt{K[(c_x - c_y)^2 + 4s_x^2s_y^2]} \times\end{aligned}\quad (\text{F.24})$$

$$\times \sqrt{\frac{U}{4} + W[(c_x - c_y)^2 + 4s_x^2s_y^2]}.\quad (\text{F.25})$$

This photon dispersion is gapless at  $\mathbf{q} = (0, 0)$  and  $\mathbf{q} = (\pi, \pi)$ . An expansion of  $\omega(\mathbf{q})$  around these two points yields for  $U \neq 0$  in lowest non-vanishing order

$$\omega(\mathbf{q}) \approx \sqrt{\frac{KU}{4}} \sqrt{q_x^4 + 14q_x^2q_y^2 + q_y^4}.\quad (\text{F.26})$$

This function is quadratic in any radial direction away from gapless points, however, it is not rotation symmetric. On the other hand, exactly at the RK-point  $U = 0$ , the photon dispersion becomes quartic,

$$\omega(\mathbf{q}) \approx \sqrt{\frac{KW}{4}} (q_x^4 + 14q_x^2q_y^2 + q_y^4).\quad (\text{F.27})$$

Another prediction of the field theory is the spin structure factor

$$\mathcal{S}(\mathbf{q}) = \langle (E^{xx}(-\mathbf{q}) + E^{xy}(-\mathbf{q})) (E^{xx}(\mathbf{q}) + E^{xy}(\mathbf{q})) \rangle,\quad (\text{F.28})$$

which can be obtained by expressing the electric fields in terms of  $a_i^\alpha$ ,  $(a_i^\alpha)^\dagger$  bosons via Eq. (7.23), transforming them into the eigenbasis of  $C$  bosons using the matrix  $\mathcal{J}$  and exploiting that the groundstate is free of any photon excitations. For  $d \rightarrow 0$  this yields

$$\begin{aligned}\mathcal{S}(\mathbf{q}) &= \sqrt{\frac{\eta_1}{\eta_2}} \frac{(L_1 - L_2)^2}{L_1^2 + L_2^2} \\ &= \frac{\sqrt{K}(c_x - c_y + 2s_x s_y)^2}{\sqrt{(c_x - c_y)^2 + 4s_x^2s_y^2} \sqrt{\frac{U}{4} + W[(c_x - c_y)^2 + 4s_x^2s_y^2]}}.\end{aligned}\quad (\text{F.29})$$

In the RK limit  $U \rightarrow 0$ , where  $\eta_1/\eta_2 = K/W$  is a constant, the expression in Eq. (F.29) becomes (up to a prefactor) identical to the classical spin structure factor in Eq. (7.11). This is expected because at the RK point, a ground state can be constructed by an equal weight superposition of all  $S_i^z$  basis states in a given Hilbert space sector, similar to a classical (non-coherent) superposition. Furthermore, at  $W = 0$ , when  $\eta_2 = U/4$  is a constant, the spin structure factor in Eq. (F.29) corresponds to the classical result, multiplied by the photon dispersion  $\omega(\mathbf{q})$ , which

suppresses the four-fold pinch points around their center. The interpolation between both limits is determined by the term  $\sqrt{U/4 + W [(c_x - c_y)^2 + 4s_x^2 s_y^2]}$  in the denominator of Eq. (F.29). For finite  $W > 0$ , there is a threshold momentum  $q_c$  (which decreases with increasing  $W$ ) above which the  $W$ -term dominates and the spin structure factor resembles the classical one. On the other hand, for  $q \lesssim q_c$ , the  $U$ -term dominates and the spin structure factor is suppressed.

## Bibliography

- [1] N. Niggemann, B. Sbierski, and J. Reuther, “Frustrated quantum spins at finite temperature: Pseudo-Majorana functional renormalization group approach”, *Physical Review B*, vol. 103, no. 10, p. 104431, Mar. 2021, ISSN: 2469-9950, 2469-9969. DOI: 10.1103/PhysRevB.103.104431.
- [2] N. Niggemann, J. Reuther, and B. Sbierski, “Quantitative functional renormalization for three-dimensional quantum Heisenberg models”, *SciPost Physics*, vol. 12, no. 5, p. 156, May 2022, ISSN: 2542-4653. DOI: 10.21468/SciPostPhys.12.5.156.
- [3] N. Niggemann, Y. Iqbal, and J. Reuther, “Quantum effects on unconventional pinch point singularities”, *Physical Review Letters*, vol. 130, no. 19, p. 196601, May 2023. DOI: 10.1103/PhysRevLett.130.196601.
- [4] I. Hagymási, N. Niggemann, and J. Reuther, “Phase diagram of the antiferromagnetic  $J_1$ – $J_2$  spin-1 pyrochlore Heisenberg model”, *Phys. Rev. B*, vol. 110, p. 224416, 22 Dec. 2024. DOI: 10.1103/PhysRevB.110.224416.
- [5] B. Schneider, J. Reuther, M. G. Gonzalez, B. Sbierski, and N. Niggemann, “Temperature flow in pseudo-Majorana functional renormalization for quantum spins”, *Physical Review B*, vol. 109, no. 19, p. 195109, May 2024. DOI: 10.1103/PhysRevB.109.195109.
- [6] N. Niggemann, M. Adhikary, Y. Schaden, and J. Reuther, *Exact fracton quantum spin liquid in a spin-1 square lattice model*.
- [7] N. Niggemann, M. Hering, and J. Reuther, “Classical spiral spin liquids as a possible route to quantum spin liquids”, *Journal of Physics: Condensed Matter*, vol. 32, no. 2, p. 024001, Oct. 2019. DOI: 10.1088/1361-648X/ab4480.
- [8] N. Astrakhantsev, F. Ferrari, N. Niggemann, T. Müller, A. Chauhan, A. Kshetrimayum, P. Ghosh, N. Regnault, R. Thomale, J. Reuther, T. Neupert, and Y. Iqbal, “Pinwheel valence bond crystal ground state of the spin- $\frac{1}{2}$  Heisenberg antiferromagnet on the shuriken lattice”, *Physical Review B*, vol. 104, no. 22, p. L220408, Dec. 2021. DOI: 10.1103/PhysRevB.104.L220408.

- [9] D. Kiese, F. Ferrari, N. Astrakhantsev, N. Niggemann, P. Ghosh, T. Müller, R. Thomale, T. Neupert, J. Reuther, M. J. P. Gingras, S. Trebst, and Y. Iqbal, “Pinch-points to half-moons and up in the stars: The kagome skymap”, vol. 5, no. 1, p. L012025, Feb. 2023. DOI: 10.1103/PhysRevResearch.5.L012025.
- [10] T. Müller, D. Kiese, N. Niggemann, B. Sbierski, J. Reuther, S. Trebst, R. Thomale, and Y. Iqbal, “Pseudo-fermion functional renormalization group for spin models”, *Reports on Progress in Physics*, vol. 87, no. 3, p. 036 501, Feb. 2024. DOI: 10.1088/1361-6633/ad208c.
- [11] N. Niggemann, N. Astrakhantsev, A. Ralko, F. Ferrari, A. Maity, T. Müller, J. Richter, R. Thomale, T. Neupert, J. Reuther, Y. Iqbal, and H. O. Jeschke, “Quantum paramagnetism in the decorated square-kagome antiferromagnet  $\text{Na}_6\text{Cu}_7\text{BiO}_4(\text{PO}_4)_4\text{Cl}_3$ ”, *Physical Review B*, vol. 108, no. 24, p. L241117, Dec. 2023. DOI: 10.1103/PhysRevB.108.L241117.
- [12] S. D. Pace, S. C. Morampudi, R. Moessner, and C. R. Laumann, “Emergent fine structure constant of quantum spin ice is large”, *Physical Review Letters*, vol. 127, no. 11, p. 117 205, Sep. 2021. DOI: 10.1103/PhysRevLett.127.117205.
- [13] A. Kitaev, “Anyons in an exactly solved model and beyond”, *Annals of Physics*, vol. 321, no. 1, pp. 2–111, 2006, ISSN: 0003-4916. DOI: 10.1016/j.aop.2005.10.005.
- [14] X. G. Wen, “Mean-field theory of spin-liquid states with finite energy gap and topological orders”, *Physical Review B*, vol. 44, no. 6, pp. 2664–2672, Aug. 1991. DOI: 10.1103/PhysRevB.44.2664.
- [15] E. Ising, “Beitrag zur Theorie des Ferromagnetismus”, *Zeitschrift für Physik*, vol. 31, no. 1, pp. 253–258, Feb. 1925, ISSN: 0044-3328. DOI: 10.1007/BF02980577.
- [16] L. Onsager, “Crystal Statistics. I. A Two-Dimensional Model with an Order-Disorder Transition”, *Physical Review*, vol. 65, no. 3-4, pp. 117–149, Feb. 1944, ISSN: 0031-899X. DOI: 10.1103/PhysRev.65.117.
- [17] G. Parisi, “Order Parameter for Spin-Glasses”, *Physical Review Letters*, vol. 50, no. 24, pp. 1946–1948, Jun. 1983, ISSN: 0031-9007. DOI: 10.1103/PhysRevLett.50.1946.
- [18] E. H. Lieb, “The classical limit of quantum spin systems”, *Communications in Mathematical Physics*, vol. 31, no. 4, pp. 327–340, Dec. 1, 1973, ISSN: 1432-0916. DOI: 10.1007/BF01646493.



- 
- [19] L. Engelhardt, M. Luban, and C. Schröder, “Finite quantum Heisenberg spin models and their approach to the classical limit”, *Physical Review B*, vol. 74, no. 5, p. 054413, Aug. 2006. DOI: 10.1103/PhysRevB.74.054413.
- [20] W. Nolting and A. Ramakanth, “Hubbard Model”, in *Quantum Theory of Magnetism*, W. Nolting and A. Ramakanth, Eds., Berlin, Heidelberg: Springer, 2009, pp. 387–490, ISBN: 978-3-540-85416-6. DOI: 10.1007/978-3-540-85416-6\_8.
- [21] D. Bergman, J. Alicea, E. Gull, S. Trebst, and L. Balents, “Order-by-disorder and spiral spin-liquid in frustrated diamond-lattice antiferromagnets”, *Nature Physics*, vol. 3, no. 7, pp. 487–491, 2007.
- [22] A. Mulder, R. Ganesh, L. Capriotti, and A. Paramekanti, “Spiral order by disorder and lattice nematic order in a frustrated Heisenberg antiferromagnet on the honeycomb lattice”, *Physical Review B*, vol. 81, no. 21, p. 214419, Jun. 2010. DOI: 10.1103/PhysRevB.81.214419.
- [23] J. Wen, S.-L. Yu, S. Li, W. Yu, and J.-X. Li, “Experimental identification of quantum spin liquids”, *npj Quantum Materials*, vol. 4, no. 1, p. 12, 2019.
- [24] B. S. Shastry and B. Sutherland, “Exact ground state of a quantum mechanical antiferromagnet”, *Physica B+C*, vol. 108, no. 1, pp. 1069–1070, 1981, ISSN: 0378-4363. DOI: 10.1016/0378-4363(81)90838-X.
- [25] R. Schäfer, B. Placke, O. Benton, and R. Moessner, “Abundance of hard-hexagon crystals in the quantum Pyrochlore antiferromagnet”, *Physical Review Letters*, vol. 131, no. 9, p. 096702, Aug. 2023. DOI: 10.1103/PhysRevLett.131.096702.
- [26] D. Lozano-Gómez, V. Noculak, J. Oitmaa, R. R. P. Singh, Y. Iqbal, J. Reuther, and M. J. P. Gingras, “Competing gauge fields and entropically driven spin liquid to spin liquid transition in non-Kramers Pyrochlores”, *Proceedings of the National Academy of Sciences*, vol. 121, no. 36, e2403487121, 2024. DOI: 10.1073/pnas.2403487121.
- [27] M. Adhikary, A. Ralko, and B. Kumar, “Quantum paramagnetism and magnetization plateaus in a kagome-honeycomb Heisenberg antiferromagnet”, *Physical Review B*, vol. 104, no. 9, p. 094416, Sep. 2021. DOI: 10.1103/PhysRevB.104.094416.
- [28] R. Pohle, Y. Yamaji, and M. Imada, *Ground state of the  $S=1/2$  Pyrochlore Heisenberg antiferromagnet: A quantum spin liquid emergent from dimensional reduction*, 2023.
- [29] L. Balents, “Spin liquids in frustrated magnets”, *Nature News*, vol. 464, no. 7286, pp. 199–208, Mar. 2010, ISSN: 1476-4687. DOI: 10.1038/nature08917.

- [30] P. M. Chaikin and T. C. Lubensky, *Principles of Condensed Matter Physics*. Cambridge: Cambridge University Press, 1995, ISBN: 978-0-521-79450-3. DOI: 10.1017/CB09780511813467.
- [31] S. Sachdev, *Quantum Phase Transitions*, 2nd ed. Cambridge Univ. Press, 2011.
- [32] A. W. Sandvik, “Computational studies of quantum spin systems”, *AIP Conference Proceedings*, vol. 1297, no. 1, pp. 135–338, Nov. 2010, ISSN: 0094-243X. DOI: 10.1063/1.3518900.
- [33] A. Lucas, “Ising formulations of many NP problems”, *Frontiers in Physics*, vol. 2, Feb. 2014, ISSN: 2296-424X. DOI: 10.3389/fphy.2014.00005.
- [34] G. Baskaran, Y. Fu, and P. W. Anderson, “On the statistical mechanics of the traveling salesman problem”, *Journal of Statistical Physics*, vol. 45, no. 1, pp. 1–25, Oct. 1986, ISSN: 1572-9613. DOI: 10.1007/BF01033073.
- [35] W. Janke, “Monte Carlo Simulations of Spin Systems”, in *Computational Physics: Selected Methods Simple Exercises Serious Applications*, K. H. Hoffmann and M. Schreiber, Eds., Berlin, Heidelberg: Springer, 1996, pp. 10–43, ISBN: 978-3-642-85238-1. DOI: 10.1007/978-3-642-85238-1\_3.
- [36] D. A. Garanin and B. Canals, “Classical spin liquid: Exact solution for the infinite-component antiferromagnetic model on the kagomé lattice”, *Physical Review B*, vol. 59, no. 1, pp. 443–456, Jan. 1999. DOI: 10.1103/PhysRevB.59.443.
- [37] C. Glittum and O. F. Syljuåsen, “Arc-shaped structure factor in the  $J_1$ - $J_2$ - $J_3$  classical Heisenberg model on the triangular lattice”, *Physical Review B*, vol. 104, no. 18, p. 184427, Nov. 2021. DOI: 10.1103/PhysRevB.104.184427.
- [38] S. Gao, M. A. McGuire, Y. Liu, D. L. Abernathy, C. dela Cruz, M. Frontzek, M. B. Stone, and A. D. Christianson, “Spiral spin liquid on a honeycomb lattice”, *Physical Review Letters*, vol. 128, no. 22, p. 227201, Jun. 2022. DOI: 10.1103/PhysRevLett.128.227201.
- [39] W. Yao, Q. Huang, T. Xie, A. Podlesnyak, A. Brassington, C. Xing, R. S. D. Mudiyansele, H. Wang, W. Xie, S. Zhang, M. Lee, V. S. Zapf, X. Bai, D. A. Tennant, J. Liu, and H. Zhou, “Continuous spin excitations in the three-dimensional frustrated magnet  $K_2Ni_2(SO_4)_3$ ”, *Physical Review Letters*, vol. 131, no. 14, p. 146701, Oct. 2023. DOI: 10.1103/PhysRevLett.131.146701.
- [40] B. Canals and C. Lacroix, “Quantum spin liquid: The Heisenberg antiferromagnet on the three-dimensional Pyrochlore lattice”, *Physical Review B*, vol. 61, no. 2, pp. 1149–1159, Jan. 2000. DOI: 10.1103/PhysRevB.61.1149.

- 
- [41] S. V. Isakov, K. Gregor, R. Moessner, and S. L. Sondhi, “Dipolar spin correlations in classical Pyrochlore magnets”, *Physical Review Letters*, vol. 93, no. 16, p. 167 204, Oct. 2004. DOI: 10.1103/PhysRevLett.93.167204.
- [42] C. L. Henley, “Power-law spin correlations in Pyrochlore antiferromagnets”, *Physical Review B*, vol. 71, no. 1, p. 014 424, Jan. 2005. DOI: 10.1103/PhysRevB.71.014424.
- [43] P. H. Conlon and J. T. Chalker, “Absent pinch points and emergent clusters: Further neighbor interactions in the Pyrochlore Heisenberg antiferromagnet”, *Physical Review B*, vol. 81, no. 22, p. 224 413, Jun. 2010. DOI: 10.1103/PhysRevB.81.224413.
- [44] M. Taillefumier, J. Robert, C. L. Henley, R. Moessner, and B. Canals, “Semiclassical spin dynamics of the antiferromagnetic Heisenberg model on the kagome lattice”, *Physical Review B*, vol. 90, no. 6, p. 064 419, Aug. 2014. DOI: 10.1103/PhysRevB.90.064419.
- [45] D. T. Liu, F. J. Burnell, L. D. C. Jaubert, and J. T. Chalker, “Classical spin liquids in stacked triangular-lattice Ising antiferromagnets”, *Physical Review B*, vol. 94, no. 22, p. 224 413, Dec. 2016. DOI: 10.1103/PhysRevB.94.224413.
- [46] M. Schechter, O. F. Syljuåsen, and J. Paaske, “Nematic bond theory of Heisenberg helimagnets”, *Physical Review Letters*, vol. 119, no. 15, p. 157 202, Oct. 2017. DOI: 10.1103/PhysRevLett.119.157202.
- [47] É. Lantagne-Hurtubise, J. G. Rau, and M. J. P. Gingras, “Spin-ice thin films: Large-N theory and monte carlo simulations”, *Physical Review X*, vol. 8, no. 2, p. 021 053, May 2018. DOI: 10.1103/PhysRevX.8.021053.
- [48] J. M. Luttinger and L. Tisza, “Theory of Dipole Interaction in Crystals”, *Physical Review*, vol. 70, no. 11-12, pp. 954–964, Dec. 1946. DOI: 10.1103/PhysRev.70.954.
- [49] J. W. Negele and H. Orland, “Quantum many-particle systems”, *Quantum Many-Particle Systems*, Jan. 2018. DOI: 10.1201/9780429497926.
- [50] C. L. Henley, “Order by disorder and gaugelike degeneracy in a quantum Pyrochlore antiferromagnet”, *Physical Review Letters*, vol. 96, no. 4, p. 047 201, Jan. 2006. DOI: 10.1103/PhysRevLett.96.047201.
- [51] O. Benton and R. Moessner, “Topological route to new and unusual coulomb spin liquids”, *Physical Review Letters*, vol. 127, no. 10, p. 107 202, Sep. 2021. DOI: 10.1103/PhysRevLett.127.107202.

- [52] H. Yan, O. Benton, A. H. Nevidomskyy, and R. Moessner, “Classification of classical spin liquids: Detailed formalism and suite of examples”, *Physical Review B*, vol. 109, no. 17, p. 174421, May 2024, ISSN: 2469-9950, 2469-9969. DOI: 10.1103/PhysRevB.109.174421.
- [53] H. Yan, O. Benton, R. Moessner, and A. H. Nevidomskyy, “Classification of classical spin liquids: Typology and resulting landscape”, *Physical Review B*, vol. 110, no. 2, p. L020402, Jul. 2024. DOI: 10.1103/PhysRevB.110.L020402.
- [54] Y. Fang, J. Cano, A. H. Nevidomskyy, and H. Yan, “Classification of classical spin liquids: Topological quantum chemistry and crystalline symmetry”, *Physical Review B*, vol. 110, no. 5, p. 054421, Aug. 2024. DOI: 10.1103/PhysRevB.110.054421.
- [55] L. Savary and L. Balents, “Quantum spin liquids: A review”, *Reports on Progress in Physics*, vol. 80, no. 1, p. 016502, 2016. DOI: 10.1088/0034-4885/80/1/016502.
- [56] P. A. Lee, “Quantum spin liquid: A tale of emergence from frustration”, *Journal of Physics: Conference Series*, vol. 529, p. 012001, Aug. 2014, ISSN: 1742-6588, 1742-6596. DOI: 10.1088/1742-6596/529/1/012001.
- [57] J. Knolle and R. Moessner, “A Field Guide to Spin Liquids”, *Annual Review of Condensed Matter Physics*, vol. 10, no. 1, pp. 451–472, Mar. 2019, ISSN: 1947-5454, 1947-5462. DOI: 10.1146/annurev-conmatphys-031218-013401.
- [58] X.-G. Wen, “Quantum orders and symmetric spin liquids”, *Physical Review B*, vol. 65, no. 16, p. 165113, Apr. 2002. DOI: 10.1103/PhysRevB.65.165113.
- [59] L. Pauling, “The Structure and Entropy of Ice and of Other Crystals with Some Randomness of Atomic Arrangement”, *Journal of the American Chemical Society*, vol. 57, no. 12, pp. 2680–2684, Dec. 1935, ISSN: 0002-7863. DOI: 10.1021/ja01315a102.
- [60] P. W. Anderson, “Ordering and Antiferromagnetism in Ferrites”, *Physical Review*, vol. 102, no. 4, pp. 1008–1013, May 1956, ISSN: 0031-899X. DOI: 10.1103/PhysRev.102.1008.
- [61] M. J. Harris, S. T. Bramwell, D. F. McMorrow, T. Zeiske, and K. W. Godfrey, “Geometrical frustration in the ferromagnetic Pyrochlore  $\text{Ho}_2\text{Ti}_2\text{O}_7$ ”, *Physical Review Letters*, vol. 79, no. 13, pp. 2554–2557, Sep. 1997. DOI: 10.1103/PhysRevLett.79.2554.

- 
- [62] S. T. Bramwell and M. J. Harris, “The history of spin ice”, *Journal of Physics: Condensed Matter*, vol. 32, no. 37, p. 374 010, Jun. 2020, ISSN: 0953-8984. DOI: 10.1088/1361-648X/ab8423.
- [63] S. T. Bramwell and M. J. P. Gingras, “Spin ice state in frustrated magnetic Pyrochlore materials”, *Science*, vol. 294, no. 5546, pp. 1495–1501, 2001. DOI: 10.1126/science.1064761.
- [64] T. Fennell, P. P. Deen, A. R. Wildes, K. Schmalzl, D. Prabhakaran, A. T. Boothroyd, R. J. Aldus, D. F. McMorrow, and S. T. Bramwell, “Magnetic coulomb phase in the spin ice  $\text{Ho}_2\text{Ti}_2\text{O}_7$ ”, *Science*, vol. 326, no. 5951, pp. 415–417, 2009. DOI: 10.1126/science.1177582.
- [65] A. P. Ramirez, A. Hayashi, R. J. Cava, R. Siddharthan, and B. S. Shastry, “Zero-point entropy in ‘spin ice’”, *Nature*, vol. 399, no. 6734, pp. 333–335, May 1999, ISSN: 1476-4687. DOI: 10.1038/20619.
- [66] L. D. C. Jaubert and P. C. W. Holdsworth, “Signature of magnetic monopole and Dirac string dynamics in spin ice”, *Nature Physics*, vol. 5, no. 4, pp. 258–261, Apr. 2009, ISSN: 1745-2481. DOI: 10.1038/nphys1227.
- [67] D. J. P. Morris, D. A. Tennant, S. A. Grigera, B. Klemke, C. Castelnovo, R. Moessner, C. Czternasty, M. Meissner, K. C. Rule, J.-U. Hoffmann, K. Kiefer, S. Gerischer, D. Slobinsky, and R. S. Perry, “Dirac strings and magnetic monopoles in the spin ice  $\text{Dy}_2\text{Ti}_2\text{O}_7$ ”, *Science*, vol. 326, no. 5951, pp. 411–414, 2009. DOI: 10.1126/science.1178868.
- [68] O. Benton, O. Sikora, and N. Shannon, “Seeing the light: Experimental signatures of emergent electromagnetism in a quantum spin ice”, *Phys. Rev. B*, vol. 86, no. 7, p. 075 154, Aug. 2012. DOI: 10.1103/PhysRevB.86.075154.
- [69] J. Knolle, D. L. Kovrizhin, J. T. Chalker, and R. Moessner, “Dynamics of a Two-Dimensional Quantum Spin Liquid: Signatures of Emergent Majorana Fermions and Fluxes”, *Physical Review Letters*, vol. 112, no. 20, p. 207 203, May 2014, ISSN: 0031-9007, 1079-7114. DOI: 10.1103/PhysRevLett.112.207203.
- [70] S. V. Isakov, R. Moessner, and S. L. Sondhi, “Why Spin Ice Obeys the Ice Rules”, *Physical Review Letters*, vol. 95, no. 21, p. 217 201, Nov. 2005. DOI: 10.1103/PhysRevLett.95.217201.
- [71] T. Fennell, M. Kenzelmann, B. Roessli, M. K. Haas, and R. J. Cava, “Power-law spin correlations in the Pyrochlore antiferromagnet  $\text{Tb}_2\text{Ti}_2\text{O}_7$ ”, *Physical Review Letters*, vol. 109, no. 1, p. 017 201, Jul. 2012. DOI: 10.1103/PhysRevLett.109.017201.

- [72] M. J. P. Gingras and P. A. McClarty, “Quantum spin ice: A search for gapless quantum spin liquids in Pyrochlore magnets”, *Reports on Progress in Physics*, vol. 77, no. 5, p. 056 501, May 2014, ISSN: 0034-4885. DOI: 10.1088/0034-4885/77/5/056501.
- [73] M. Hermele, M. P. A. Fisher, and L. Balents, “Pyrochlore photons: The U(1) spin liquid in a  $S=\frac{1}{2}$  three-dimensional frustrated magnet”, *Physical Review B*, vol. 69, no. 6, p. 064 404, Feb. 2004, ISSN: 1098-0121, 1550-235X. DOI: 10.1103/PhysRevB.69.064404.
- [74] Y. Kato and S. Onoda, “Numerical Evidence of Quantum Melting of Spin Ice: Quantum-to-Classical Crossover”, *Physical Review Letters*, vol. 115, no. 7, p. 077 202, Aug. 2015. DOI: 10.1103/PhysRevLett.115.077202.
- [75] A. Banerjee, S. V. Isakov, K. Damle, and Y. B. Kim, “Unusual Liquid State of Hard-Core Bosons on the Pyrochlore lattice”, *Physical Review Letters*, vol. 100, no. 4, p. 047 208, Jan. 2008. DOI: 10.1103/PhysRevLett.100.047208.
- [76] D. S. Rokhsar and S. A. Kivelson, “Superconductivity and the quantum hard-core dimer gas”, *Physical Review Letters*, vol. 61, no. 20, pp. 2376–2379, Nov. 1988. DOI: 10.1103/PhysRevLett.61.2376.
- [77] R. Moessner, S. L. Sondhi, and M. O. Goerbig, “Quantum dimer models and effective Hamiltonians on the Pyrochlore lattice”, *Physical Review B*, vol. 73, no. 9, Mar. 2006, ISSN: 1550-235X. DOI: 10.1103/physrevb.73.094430.
- [78] P. W. Anderson, “Resonating valence bonds: A new kind of insulator?”, *Materials Research Bulletin*, vol. 8, no. 2, pp. 153–160, Feb. 1973, ISSN: 0025-5408. DOI: 10.1016/0025-5408(73)90167-0.
- [79] A. Szabó and C. Castelnovo, “Seeing beyond the light: Vison and photon electrodynamics in quantum spin ice”, *Physical Review B*, vol. 100, no. 1, p. 014 417, Jul. 2019. DOI: 10.1103/PhysRevB.100.014417.
- [80] J. Gaudet, E. M. Smith, J. Dudemaine, J. Beare, C. R. C. Buhariwalla, N. P. Butch, M. B. Stone, A. I. Kolesnikov, G. Xu, D. R. Yahne, K. A. Ross, C. A. Marjerrison, J. D. Garrett, G. M. Luke, A. D. Bianchi, and B. D. Gaulin, “Quantum spin ice dynamics in the dipole-octupole Pyrochlore magnet  $Ce_2Zr_2O_7$ ”, *Physical Review Letters*, vol. 122, no. 18, p. 187 201, May 2019. DOI: 10.1103/PhysRevLett.122.187201.
- [81] E. M. Smith *et al.*, “Case for a  $U(1)_\pi$  quantum spin liquid ground state in the dipole-octupole Pyrochlore  $Ce_2Zr_2O_7$ ”, *Physical Review X*, vol. 12, no. 2, p. 021 015, Apr. 2022. DOI: 10.1103/PhysRevX.12.021015.

- 
- [82] L. E. Chern, F. Desrochers, Y. B. Kim, and C. Castelnovo, “Pseudofermion functional renormalization group study of dipolar-octupolar Pyrochlore magnets”, *Physical Review B*, vol. 109, no. 18, p. 184421, May 2024. DOI: 10.1103/PhysRevB.109.184421.
- [83] B. Gao *et al.*, “Experimental signatures of a three-dimensional quantum spin liquid in effective spin-1/2  $\text{Ce}_2\text{Zr}_2\text{O}_7$  Pyrochlore”, *Nature Physics*, vol. 15, no. 10, pp. 1052–1057, 2019. DOI: 10.1038/s41567-019-0577-6.
- [84] E. M. Smith, J. Dudemaine, B. Placke, R. Schäfer, D. R. Yahne, T. DeLazzer, A. Fitterman, J. Beare, J. Gaudet, C. R. C. Buhariwalla, A. Podlesnyak, G. Xu, J. P. Clancy, R. Movshovich, G. M. Luke, K. A. Ross, R. Moessner, O. Benton, A. D. Bianchi, and B. D. Gaulin, “Quantum spin ice response to a magnetic field in the dipole-octupole Pyrochlore  $\text{Ce}_2\text{Zr}_2\text{O}_7$ ”, *Physical Review B*, vol. 108, no. 5, p. 054438, Aug. 2023. DOI: 10.1103/PhysRevB.108.054438.
- [85] J. Beare, E. M. Smith, J. Dudemaine, R. Schäfer, M. R. Rutherford, S. Sharma, A. Fitterman, C. A. Marjerrison, T. J. Williams, A. A. Aczel, S. R. Dunsiger, A. D. Bianchi, B. D. Gaulin, and G. M. Luke, “ $\mu\text{SR}$  study of the dipole-octupole quantum spin ice candidate  $\text{Ce}_2\text{Zr}_2\text{O}_7$ ”, *Physical Review B*, vol. 108, no. 17, p. 174411, Nov. 2023. DOI: 10.1103/PhysRevB.108.174411.
- [86] R. Sibille, N. Gauthier, H. Yan, M. Ciomaga Hatnean, J. Ollivier, B. Winn, U. Filges, G. Balakrishnan, M. Kenzelmann, N. Shannon, and T. Fennell, “Experimental signatures of emergent quantum electrodynamics in  $\text{Pr}_2\text{Hf}_2\text{O}_7$ ”, *Nature Physics*, vol. 14, no. 7, pp. 711–715, 2018. DOI: 10.1038/s41567-018-0116-x.
- [87] R. Sibille, E. Lhotel, V. Pomjakushin, C. Baines, T. Fennell, and M. Kenzelmann, “Candidate quantum spin liquid in the  $\text{Ce}^{3+}$  Pyrochlore stannate  $\text{Ce}_2\text{Sn}_2\text{O}_7$ ”, *Physical Review Letters*, vol. 115, no. 9, p. 097202, Aug. 2015. DOI: 10.1103/PhysRevLett.115.097202.
- [88] A. Y. Kitaev, “Fault-tolerant quantum computation by anyons”, *Annals of Physics*, vol. 303, no. 1, pp. 2–30, Jan. 2003, ISSN: 0003-4916. DOI: 10.1016/S0003-4916(02)00018-0.
- [89] C. Xu, “Gapless bosonic excitation without symmetry breaking: An algebraic spin liquid with soft gravitons”, *Physical Review B*, vol. 74, no. 22, p. 224433, Dec. 2006. DOI: 10.1103/PhysRevB.74.224433.

- [90] A. Celi, B. Vermersch, O. Viyuela, H. Pichler, M. D. Lukin, and P. Zoller, “Emerging two-dimensional gauge theories in Rydberg configurable arrays”, *Physical Review X*, vol. 10, no. 2, p. 021057, Jun. 2020. DOI: 10.1103/PhysRevX.10.021057.
- [91] G. Giudici, M. D. Lukin, and H. Pichler, “Dynamical preparation of quantum spin liquids in Rydberg atom arrays”, *Physical Review Letters*, vol. 129, no. 9, p. 090401, Aug. 2022. DOI: 10.1103/PhysRevLett.129.090401.
- [92] R. Samajdar, W. W. Ho, H. Pichler, M. D. Lukin, and S. Sachdev, “Quantum phases of Rydberg atoms on a kagome lattice”, *Proceedings of the National Academy of Sciences*, vol. 118, no. 4, e2015785118, 2021. DOI: 10.1073/pnas.2015785118.
- [93] P. S. Tarabunga, F. M. Surace, R. Andreoni, A. Angelone, and M. Dalmonte, “Gauge-theoretic origin of Rydberg quantum spin liquids”, *Physical Review Letters*, vol. 129, no. 19, p. 195301, Nov. 2022. DOI: 10.1103/PhysRevLett.129.195301.
- [94] Z. Y. Meng, T. C. Lang, S. Wessel, F. F. Assaad, and A. Muramatsu, “Quantum spin liquid emerging in two-dimensional correlated Dirac fermions”, *Nature*, vol. 464, no. 7290, pp. 847–851, Apr. 2010, ISSN: 1476-4687. DOI: 10.1038/nature08942.
- [95] D. Wulferding, P. Lemmens, P. Scheib, J. Röder, P. Mendels, S. Chu, T. Han, and Y. S. Lee, “Interplay of thermal and quantum spin fluctuations in the kagome lattice compound herbertsmithite”, *Physical Review B*, vol. 82, no. 14, p. 144412, Oct. 2010. DOI: 10.1103/PhysRevB.82.144412.
- [96] S. Hu, W. Zhu, S. Eggert, and Y.-C. He, “Dirac spin liquid on the spin-1/2 triangular Heisenberg antiferromagnet”, *Physical Review Letters*, vol. 123, no. 20, p. 207203, Nov. 2019. DOI: 10.1103/PhysRevLett.123.207203.
- [97] Y. Iqbal, F. Becca, S. Sorella, and D. Poilblanc, “Gapless spin-liquid phase in the kagome spin- $\frac{1}{2}$  Heisenberg antiferromagnet”, *Physical Review B*, vol. 87, no. 6, p. 060405, Feb. 2013. DOI: 10.1103/PhysRevB.87.060405.
- [98] R. B. Laughlin and Z. Zou, “Properties of the chiral-spin-liquid state”, *Physical Review B*, vol. 41, no. 1, pp. 664–687, Jan. 1990. DOI: 10.1103/PhysRevB.41.664.
- [99] H. Yao and S. A. Kivelson, “Exact Chiral Spin Liquid with Non-Abelian Anyons”, *Physical Review Letters*, vol. 99, no. 24, p. 247203, Dec. 2007. DOI: 10.1103/PhysRevLett.99.247203.
- [100] L. Messio, B. Bernu, and C. Lhuillier, “Kagome antiferromagnet: A chiral topological spin liquid?”, *Physical Review Letters*, vol. 108, no. 20, p. 207204, May 2012. DOI: 10.1103/PhysRevLett.108.207204.



- 
- [101] B. Placke, O. Benton, and R. Moessner, *Ising fracton spin liquid on the honeycomb lattice*, 2023.
- [102] S. Vijay, J. Haah, and L. Fu, “Fracton topological order, generalized lattice gauge theory, and duality”, *Physical Review B*, vol. 94, no. 23, p. 235 157, Dec. 2016. DOI: 10.1103/PhysRevB.94.235157.
- [103] M. Pretko, “Subdimensional particle structure of higher rank  $U(1)$  spin liquids”, *Physical Review B*, vol. 95, no. 11, p. 115 139, Mar. 2017. DOI: 10.1103/PhysRevB.95.115139.
- [104] M. Pretko, “Generalized electromagnetism of subdimensional particles: A spin liquid story”, *Physical Review B*, vol. 96, no. 3, p. 035 119, Jul. 2017. DOI: 10.1103/PhysRevB.96.035119.
- [105] M. Pretko, X. Chen, and Y. You, “Fracton phases of matter”, *International Journal of Modern Physics A*, vol. 35, no. 06, p. 2030 003, 2020. DOI: 10.1142/S0217751X20300033.
- [106] R. M. Nandkishore and M. Hermele, “Fractons”, *Annual Review of Condensed Matter Physics*, vol. 10, no. 1, pp. 295–313, 2019. DOI: 10.1146/annurev-conmatphys-031218-013604.
- [107] A. T. Schmitz, H. Ma, R. M. Nandkishore, and S. A. Parameswaran, “Recoverable information and emergent conservation laws in fracton stabilizer codes”, *Physical Review B*, vol. 97, no. 13, p. 134 426, Apr. 2018. DOI: 10.1103/PhysRevB.97.134426.
- [108] P. Gorantla, H. T. Lam, N. Seiberg, and S.-H. Shao, “Fcc lattice, checkerboards, fractons, and quantum field theory”, *Physical Review B*, vol. 103, no. 20, p. 205 116, May 2021. DOI: 10.1103/PhysRevB.103.205116.
- [109] A. Gromov, “Towards classification of fracton phases: The multipole algebra”, *Physical Review X*, vol. 9, no. 3, p. 031 035, Aug. 2019. DOI: 10.1103/PhysRevX.9.031035.
- [110] A. Gromov and L. Radzihovsky, “Colloquium: Fracton matter”, *Reviews of Modern Physics*, vol. 96, no. 1, p. 011 001, Jan. 2024. DOI: 10.1103/RevModPhys.96.011001.
- [111] A. T. Schmitz, *Distilling fractons from layered subsystem-symmetry protected phases*, 2019. DOI: 10.48550/ARXIV.1910.04765.
- [112] N. Seiberg and S.-H. Shao, “Exotic  $U(1)$  symmetries, duality, and fractons in 3+1-dimensional quantum field theory”, *SciPost Physics*, vol. 9, p. 046, 2020. DOI: 10.21468/SciPostPhys.9.4.046.

- [113] O. Hart and R. Nandkishore, “Spectroscopic fingerprints of gapless type-II fracton phases”, *Physical Review B*, vol. 105, no. 18, p. L180416, May 2022. DOI: 10.1103/PhysRevB.105.L180416.
- [114] M. Pretko, “Emergent gravity of fractons: Mach’s principle revisited”, *Physical Review D: Particles and Fields*, vol. 96, no. 2, p. 024051, Jul. 2017. DOI: 10.1103/PhysRevD.96.024051.
- [115] M. Pretko and L. Radzihovsky, “Fracton-elasticity duality”, *Physical Review Letters*, vol. 120, no. 19, p. 195301, May 2018. DOI: 10.1103/PhysRevLett.120.195301.
- [116] C. Chamon, “Quantum glassiness in strongly correlated clean systems: An example of topological overprotection”, *Physical Review Letters*, vol. 94, no. 4, p. 040402, Jan. 2005. DOI: 10.1103/PhysRevLett.94.040402.
- [117] A. Prem, S. Vijay, Y.-Z. Chou, M. Pretko, and R. M. Nandkishore, “Pinch point singularities of tensor spin liquids”, *Physical Review B*, vol. 98, no. 16, p. 165140, Oct. 2018. DOI: 10.1103/PhysRevB.98.165140.
- [118] J. Haah, “Local stabilizer codes in three dimensions without string logical operators”, *Physical Review A: Atomic, Molecular, and Optical Physics*, vol. 83, no. 4, p. 042330, Apr. 2011. DOI: 10.1103/PhysRevA.83.042330.
- [119] J. Reuther and P. Wölfle, “ $J_1$ - $J_2$  frustrated two-dimensional Heisenberg model: Random phase approximation and functional renormalization group”, *Physical Review B*, vol. 81, no. 14, p. 144410, Apr. 2010. DOI: 10.1103/PhysRevB.81.144410.
- [120] M. L. Baez and J. Reuther, “Numerical treatment of spin systems with unrestricted spin length  $S$ : A functional renormalization group study”, *Physical Review B*, vol. 96, no. 4, p. 045144, Jul. 2017. DOI: 10.1103/PhysRevB.96.045144.
- [121] F. L. Buessen, D. Roscher, S. Diehl, and S. Trebst, “Functional renormalization group approach to  $SU(N)$  Heisenberg models: Real-space renormalization group at arbitrary  $N$ ”, *Physical Review B*, vol. 97, no. 6, p. 064415, Feb. 2018. DOI: 10.1103/PhysRevB.97.064415.
- [122] F. L. Buessen, V. Nocolak, S. Trebst, and J. Reuther, “Functional renormalization group for frustrated magnets with nondiagonal spin interactions”, *Physical Review B*, vol. 100, no. 12, p. 125164, Sep. 2019. DOI: 10.1103/PhysRevB.100.125164.
- [123] P. Kopietz, L. Bartosch, and F. Schütz, *Introduction to the Functional Renormalization Group* (Lecture Notes in Physics). Berlin, Heidelberg: Springer Berlin Heidelberg, 2010, vol. 798, ISBN: 978-3-642-05093-0 978-3-642-05094-7. DOI: 10.1007/978-3-642-05094-7.

- 
- [124] J. Gubernatis, N. Kawashima, and P. Werner, *Quantum Monte Carlo Methods: Algorithms for Lattice Models*. Cambridge: Cambridge University Press, 2016, ISBN: 978-1-107-00642-3. DOI: 10.1017/CB09780511902581.
- [125] F. Becca and S. Sorella, *Quantum Monte Carlo Approaches for Correlated Systems*. Cambridge: Cambridge University Press, 2017, ISBN: 978-1-107-12993-1. DOI: 10.1017/9781316417041.
- [126] J. Eisert, M. Cramer, and M. B. Plenio, “Colloquium : Area laws for the entanglement entropy”, *Reviews of Modern Physics*, vol. 82, no. 1, pp. 277–306, Feb. 2010, ISSN: 0034-6861, 1539-0756. DOI: 10.1103/RevModPhys.82.277.
- [127] R. B. Laughlin, “Anomalous quantum Hall effect: An incompressible quantum fluid with fractionally charged excitations”, *Physical Review Letters*, 1983, ISSN: 00319007. DOI: 10.1103/PhysRevLett.50.1395.
- [128] P. W. Anderson, “The resonating valence bond state in La<sub>2</sub>CuO<sub>4</sub> and superconductivity”, *Science*, 1987, ISSN: 00368075. DOI: 10.1126/science.235.4793.1196.
- [129] L. Balents, “Energy density of variational states”, *Physical Review B*, vol. 90, no. 24, p. 245 116, Dec. 2014, ISSN: 1098-0121, 1550-235X. DOI: 10.1103/PhysRevB.90.245116.
- [130] M. Capello, F. Becca, M. Fabrizio, S. Sorella, and E. Tosatti, “Variational description of mott insulators”, *Physical Review Letters*, vol. 94, no. 2, p. 026 406, Jan. 2005. DOI: 10.1103/PhysRevLett.94.026406.
- [131] G. Dev and J. K. Jain, “Jastrow-Slater trial wave functions for the fractional quantum Hall effect: Results for few-particle systems”, *Physical Review B*, vol. 45, no. 3, pp. 1223–1230, Jan. 1992. DOI: 10.1103/PhysRevB.45.1223.
- [132] W. L. McMillan, “Ground state of liquid He<sup>4</sup>”, *Physical Review*, vol. 138, A442–A451, 2A Apr. 1965. DOI: 10.1103/PhysRev.138.A442.
- [133] S. Sorella, “Wave function optimization in the variational Monte Carlo method”, *Physical Review B*, vol. 71, no. 24, p. 241 103, Jun. 2005. DOI: 10.1103/PhysRevB.71.241103.
- [134] G. Carleo and M. Troyer, “Solving the quantum many-body problem with artificial neural networks”, *Science*, vol. 355, no. 6325, pp. 602–606, 2017. DOI: 10.1126/science.aag2302.
- [135] L. Huang and L. Wang, “Accelerated monte carlo simulations with restricted boltzmann machines”, *Physical Review B*, vol. 95, no. 3, p. 035 105, Jan. 2017. DOI: 10.1103/PhysRevB.95.035105.

- [136] H. Lange, A. Van de Walle, A. Abedinnia, and A. Bohrdt, “From architectures to applications: A review of neural quantum states”, *Quantum Science and Technology*, 2024.
- [137] M. Reh, M. Schmitt, and M. Gärttner, “Optimizing design choices for neural quantum states”, *Physical Review B*, vol. 107, no. 19, p. 195 115, May 2023. DOI: 10.1103/PhysRevB.107.195115.
- [138] F. Vicentini, D. Hofmann, A. Szabó, D. Wu, C. Roth, C. Giuliani, G. Pescia, J. Nys, V. Vargas-Calderón, N. Astrakhantsev, and G. Carleo, “Codebase release 3.4 for NetKet”, *SciPost Phys. Codebases*, 7–r3.4, 2022. DOI: 10.21468/SciPostPhysCodeb.7–r3.4.
- [139] F. Vicentini, D. Hofmann, A. Szabó, D. Wu, C. Roth, C. Giuliani, G. Pescia, J. Nys, V. Vargas-Calderón, N. Astrakhantsev, and G. Carleo, “NetKet 3: Machine learning toolbox for many-body quantum systems”, *SciPost Phys. Codebases*, p. 7, 2022. DOI: 10.21468/SciPostPhysCodeb.7.
- [140] A. Altland and B. D. Simons, *Condensed Matter Field Theory*, 2nd ed. Cambridge: Cambridge University Press, 2010.
- [141] L. P. Kadanoff, “Scaling laws for ising models near  $T_c$ ”, *Physics Physique Fizika*, vol. 2, no. 6, pp. 263–272, Jun. 1966. DOI: 10.1103/PhysicsPhysiqueFizika.2.263.
- [142] K. G. Wilson, “Renormalization Group and Critical Phenomena. II. Phase-Space Cell Analysis of Critical Behavior”, *Physical Review B*, vol. 4, no. 9, pp. 3184–3205, Nov. 1971. DOI: 10.1103/PhysRevB.4.3184.
- [143] K. G. Wilson and J. Kogut, “The renormalization group and the  $\epsilon$  expansion”, *Physics Reports*, vol. 12, no. 2, pp. 75–199, Aug. 1974, ISSN: 0370-1573. DOI: 10.1016/0370-1573(74)90023-4.
- [144] K. G. Wilson, “The renormalization group: Critical phenomena and the Kondo problem”, *Reviews of Modern Physics*, vol. 47, no. 4, pp. 773–840, Oct. 1975. DOI: 10.1103/RevModPhys.47.773.
- [145] W. Metzner, M. Salmhofer, C. Honerkamp, V. Meden, and K. Schönhammer, “Functional renormalization group approach to correlated fermion systems”, *Reviews of Modern Physics*, vol. 84, no. 1, pp. 299–352, Mar. 2012, ISSN: 0034-6861, 1539-0756. DOI: 10.1103/RevModPhys.84.299.
- [146] W. Metzner, “Functional Renormalization Group Computation of Interacting Fermi Systems”, vol. 160, pp. 58–78, Jun. 2005. DOI: 10.1143/PTPS.160.58.

- 
- [147] M. Salmhofer, C. Honerkamp, W. Metzner, and O. Lauscher, “Renormalization group flows into phases with broken symmetry”, *Progress of theoretical physics*, vol. 112, no. 6, pp. 943–970, 2004. DOI: 10.1143/PTP.112.943.
- [148] C. Honerkamp, M. Salmhofer, N. Furukawa, and T. M. Rice, “Breakdown of the Landau-Fermi liquid in two dimensions due to umklapp scattering”, *Physical Review B*, vol. 63, no. 3, p. 035 109, Jan. 2001. DOI: 10.1103/PhysRevB.63.035109.
- [149] A. A. Katanin, “Fulfillment of Ward identities in the functional renormalization group approach”, *Physical Review B*, vol. 70, no. 11, p. 115 109, Sep. 2004. DOI: 10.1103/PhysRevB.70.115109.
- [150] Y. Iqbal, T. Müller, P. Ghosh, M. J. P. Gingras, H. O. Jeschke, S. Rachel, J. Reuther, and R. Thomale, “Quantum and classical phases of the Pyrochlore Heisenberg model with competing interactions”, *Physical Review X*, vol. 9, no. 1, p. 011 005, Jan. 2019. DOI: 10.1103/PhysRevX.9.011005.
- [151] M. Hering, V. Noculak, F. Ferrari, Y. Iqbal, and J. Reuther, “Dimerization tendencies of the Pyrochlore Heisenberg antiferromagnet: A functional renormalization group perspective”, *Phys. Rev. B*, vol. 105, no. 5, p. 054 426, Feb. 2022. DOI: 10.1103/PhysRevB.105.054426.
- [152] V. Noculak, D. Lozano-Gómez, J. Oitmaa, R. R. P. Singh, Y. Iqbal, M. J. P. Gingras, and J. Reuther, “Classical and quantum phases of the Pyrochlore  $S=\frac{1}{2}$  magnet with Heisenberg and Dzyaloshinskii-Moriya interactions”, *Physical Review B*, vol. 107, no. 21, p. 214 414, Jun. 2023. DOI: 10.1103/PhysRevB.107.214414.
- [153] A. Keleş and E. Zhao, “Rise and fall of plaquette order in the Shastry-Sutherland magnet revealed by pseudofermion functional renormalization group”, *Physical Review B*, vol. 105, no. 4, p. L041115, Jan. 2022. DOI: 10.1103/PhysRevB.105.L041115.
- [154] A. Keleş and E. Zhao, “Renormalization group analysis of dipolar Heisenberg model on square lattice”, *Physical Review B*, vol. 97, no. 24, p. 245 105, Jun. 2018. DOI: 10.1103/PhysRevB.97.245105.
- [155] D. Roscher, F. L. Buessen, M. M. Scherer, S. Trebst, and S. Diehl, “Functional renormalization group approach to  $SU(N)$  Heisenberg models: Momentum-space renormalization group for the large- $N$  limit”, *Physical Review B*, vol. 97, no. 6, p. 064 416, Feb. 2018. DOI: 10.1103/PhysRevB.97.064416.
- [156] D. Tarasevych and P. Kopietz, “Dissipative spin dynamics in hot quantum paramagnets”, *Physical Review B*, vol. 104, no. 2, p. 024 423, Jul. 2021. DOI: 10.1103/PhysRevB.104.024423.

- [157] D. Tarasevych and P. Kopietz, “Critical spin dynamics of Heisenberg ferromagnets revisited”, *Physical Review B*, vol. 105, no. 2, p. 024403, Jan. 2022. DOI: 10.1103/PhysRevB.105.024403.
- [158] A. Rückriegel, D. Tarasevych, and P. Kopietz, “Phase diagram of the  $J_1$ - $J_2$  quantum Heisenberg model for arbitrary spin”, *Physical Review B*, vol. 109, no. 18, p. 184410, May 2024. DOI: 10.1103/PhysRevB.109.184410.
- [159] A. A. Abrikosov, L. P. Gorkov, and I. E. Dzialoshinskii, *Methods of Quantum Field Theory in Statistical Physics*. New York: Dover Publications Inc., 1975, ISBN: 978-0-486-63228-5.
- [160] B. Schneider, D. Kiese, and B. Sbierski, “Taming pseudofermion functional renormalization for quantum spins: Finite temperatures and the Popov-Fedotov trick”, *Physical Review B*, vol. 106, no. 23, p. 235113, Dec. 2022. DOI: 10.1103/PhysRevB.106.235113.
- [161] J. L. Martin, “Generalized classical dynamics, and the ‘classical analogue’ of a Fermioscillator”, *Proc. R. Soc. London A*, vol. 251, no. 1267, pp. 536–542, 1959. DOI: 10.1098/rspa.1959.0126.
- [162] A. M. Tsvelik, “New fermionic description of quantum spin liquid state”, *Physical Review Letters*, vol. 69, no. 14, pp. 2142–2144, Oct. 1992, ISSN: 0031-9007. DOI: 10.1103/PhysRevLett.69.2142.
- [163] J. Fu, J. Knolle, and N. B. Perkins, “Three types of representation of spin in terms of Majorana fermions and an alternative solution of the Kitaev honeycomb model”, *Physical Review B*, vol. 97, no. 11, p. 115142, Mar. 2018. DOI: 10.1103/PhysRevB.97.115142.
- [164] J. Thoenniss, M. K. Ritter, F. B. Kugler, J. von Delft, and M. Punk, *Multiloop pseudofermion functional renormalization for quantum spin systems: Application to the spin-1/2 kagome Heisenberg model*, 2020. arXiv: 2011.01268.
- [165] D. Kiese, T. Müller, Y. Iqbal, R. Thomale, and S. Trebst, “Multiloop functional renormalization group approach to quantum spin systems”, *Physical Review Research*, vol. 4, no. 2, p. 023185, Jun. 2022. DOI: 10.1103/PhysRevResearch.4.023185.
- [166] F. B. Kugler and J. Von Delft, “Multiloop functional renormalization group for general models”, *Physical Review B*, vol. 97, no. 3, p. 35162, 2018. DOI: 10.1103/PhysRevB.97.035162.
- [167] F. B. Kugler and J. von Delft, “Derivation of exact flow equations from the self-consistent parquet relations”, *New Journal of Physics*, vol. 20, no. 12, p. 123029, Dec. 2018. DOI: 10.1088/1367-2630/aaf65f.

- 
- [168] C. Lacroix, P. Mendels, and F. Mila, *Introduction to Frustrated Magnetism: Materials, Experiments, Theory* (Springer Series in Solid-State Sciences). Springer Berlin Heidelberg, 2011.
- [169] M. Vojta, “Quantum phase transitions”, *Reports on Progress in Physics*, vol. 66, no. 12, pp. 2069–2110, Nov. 2003. DOI: 10.1088/0034-4885/66/12/r01.
- [170] X. G. Wen and Q. Niu, “Ground-state degeneracy of the fractional quantum Hall states in the presence of a random potential and on high-genus Riemann surfaces”, *Physical Review B*, vol. 41, no. 13, pp. 9377–9396, May 1990. DOI: 10.1103/PhysRevB.41.9377.
- [171] C. H. Bennett and D. P. DiVincenzo, “Quantum information and computation”, *Nature*, vol. 404, no. 6775, pp. 247–255, 2000. DOI: 10.1038/35005001.
- [172] A. W. Sandvik and J. Kurkijärvi, “Quantum Monte Carlo simulation method for spin systems”, *Physical Review B*, vol. 43, no. 7, pp. 5950–5961, Mar. 1991. DOI: 10.1103/PhysRevB.43.5950.
- [173] A. W. Sandvik, “Critical temperature and the transition from quantum to classical order parameter fluctuations in the three-dimensional Heisenberg antiferromagnet”, *Physical Review Letters*, vol. 80, no. 23, pp. 5196–5199, Jun. 1998. DOI: 10.1103/PhysRevLett.80.5196.
- [174] S. R. White, “Density matrix formulation for quantum renormalization groups”, *Phys. Rev. Lett.*, vol. 69, no. 19, pp. 2863–2866, Nov. 1992. DOI: 10.1103/PhysRevLett.69.2863.
- [175] U. Schollwöck, “The density-matrix renormalization group”, *Reviews of Modern Physics*, vol. 77, no. 1, pp. 259–315, Apr. 2005. DOI: 10.1103/RevModPhys.77.259.
- [176] U. Schollwöck, “The density-matrix renormalization group in the age of matrix product states”, *Annals of Physics*, vol. 326, no. 1, pp. 96–192, 2011, ISSN: 0003-4916. DOI: 10.1016/j.aop.2010.09.012.
- [177] F. Verstraete, V. Murg, and J. Cirac, “Matrix product states, projected entangled pair states, and variational renormalization group methods for quantum spin systems”, *Advances in Physics*, vol. 57, no. 2, pp. 143–224, 2008. DOI: 10.1080/14789940801912366.
- [178] R. Orús, “A practical introduction to tensor networks: Matrix product states and projected entangled pair states”, *Annals of Physics*, vol. 349, pp. 117–158, 2014, ISSN: 0003-4916. DOI: 10.1016/j.aop.2014.06.013.

- [179] C. Wetterich, “Exact evolution equation for the effective potential”, *Physics Letters B*, vol. 301, no. 1, pp. 90–94, 1993, ISSN: 0370-2693. DOI: 10.1016/0370-2693(93)90726-X.
- [180] J. Polchinski, “Renormalization and effective lagrangians”, *Nuclear Physics B*, vol. 231, no. 2, pp. 269–295, 1984, ISSN: 0550-3213. DOI: 10.1016/0550-3213(84)90287-6.
- [181] C. Platt, W. Hanke, and R. Thomale, “Functional renormalization group for multi-orbital Fermi surface instabilities”, *Advances in Physics*, vol. 62, no. 4-6, pp. 453–562, 2013. DOI: 10.1080/00018732.2013.862020.
- [182] C. J. Halboth and W. Metzner, “Renormalization-group analysis of the two-dimensional Hubbard model”, *Physical Review B*, vol. 61, no. 11, pp. 7364–7377, Mar. 2000. DOI: 10.1103/PhysRevB.61.7364.
- [183] A. A. Abrikosov, “Electron scattering on magnetic impurities in metals and anomalous resistivity effects”, *Physics Physique Fizika*, vol. 2, no. 1, pp. 5–20, Sep. 1965. DOI: 10.1103/PhysicsPhysiqueFizika.2.5.
- [184] J. Reuther and R. Thomale, “Cluster functional renormalization group”, *Physical Review B*, vol. 89, no. 2, p. 024412, Jan. 2014. DOI: 10.1103/PhysRevB.89.024412.
- [185] Y. Iqbal, H. O. Jeschke, J. Reuther, R. Valentí, I. I. Mazin, M. Greiter, and R. Thomale, “Paramagnetism in the kagome compounds  $(\text{Zn,Mg,Cd})\text{Cu}_3(\text{OH})_6\text{Cl}_2$ ”, *Physical Review B*, vol. 92, no. 22, p. 220404, Dec. 2015. DOI: 10.1103/PhysRevB.92.220404.
- [186] I. Rousochatzakis, J. Reuther, R. Thomale, S. Rachel, and N. B. Perkins, “Phase diagram and quantum order by disorder in the kitaev  $\text{K}_1\text{-K}_2$  honeycomb magnet”, *Physical Review X*, vol. 5, no. 4, p. 041035, Dec. 2015. DOI: 10.1103/PhysRevX.5.041035.
- [187] Y. Iqbal, R. Thomale, F. Parisen Toldin, S. Rachel, and J. Reuther, “Functional renormalization group for three-dimensional quantum magnetism”, *Physical Review B*, vol. 94, no. 14, p. 140408, Oct. 2016. DOI: 10.1103/PhysRevB.94.140408.
- [188] C. Balz, B. Lake, J. Reuther, H. Luetkens, R. Schönemann, T. Herrmannsdörfer, Y. Singh, A. T. M. Nazmul Islam, E. M. Wheeler, J. A. Rodriguez-Rivera, T. Guidi, G. G. Simeoni, C. Baines, and H. Ryll, “Physical realization of a quantum spin liquid based on a complex frustration mechanism”, *Nature Physics*, vol. 12, no. 10, pp. 942–949, Oct. 2016. DOI: 10.1038/nphys3826.



- 
- [189] Y. Iqbal, P. Ghosh, R. Narayanan, B. Kumar, J. Reuther, and R. Thomale, “Intertwined nematic orders in a frustrated ferromagnet”, *Physical Review B*, vol. 94, no. 22, p. 224 403, Dec. 2016. DOI: 10.1103/PhysRevB.94.224403.
- [190] F. L. Buessen and S. Trebst, “Competing magnetic orders and spin liquids in two- and three-dimensional kagome systems: Pseudofermion functional renormalization group perspective”, *Physical Review B*, vol. 94, no. 23, p. 235 138, Dec. 2016. DOI: 10.1103/PhysRevB.94.235138.
- [191] M. Hering and J. Reuther, “Functional renormalization group analysis of Dzyaloshinsky-Moriya and Heisenberg spin interactions on the kagome lattice”, *Physical Review B*, vol. 95, no. 5, p. 054 418, Feb. 2017. DOI: 10.1103/PhysRevB.95.054418.
- [192] Y. Iqbal, T. Müller, K. Riedl, J. Reuther, S. Rachel, R. Valentí, M. J. P. Gingras, R. Thomale, and H. O. Jeschke, “Signatures of a gearwheel quantum spin liquid in a spin- $\frac{1}{2}$  Pyrochlore molybdate Heisenberg antiferromagnet”, *Physical Review Materials*, vol. 1, no. 7, p. 071 201, Dec. 2017. DOI: 10.1103/PhysRevMaterials.1.071201.
- [193] J. Reuther, D. A. Abanin, and R. Thomale, “Magnetic order and paramagnetic phases in the quantum  $J_1$ - $J_2$ - $J_3$  honeycomb model”, *Physical Review B*, vol. 84, no. 1, p. 014 417, Jul. 2011. DOI: 10.1103/PhysRevB.84.014417.
- [194] F. L. Buessen, M. Hering, J. Reuther, and S. Trebst, “Quantum spin liquids in frustrated spin-1 diamond antiferromagnets”, *Physical Review Letters*, vol. 120, no. 5, p. 057 201, Jan. 2018. DOI: 10.1103/PhysRevLett.120.057201.
- [195] M. Rück and J. Reuther, “Effects of two-loop contributions in the pseudofermion functional renormalization group method for quantum spin systems”, *Physical Review B*, vol. 97, no. 14, p. 144 404, 2018. DOI: 10.1103/PhysRevB.97.144404.
- [196] Y. Iqbal, T. Müller, H. O. Jeschke, R. Thomale, and J. Reuther, “Stability of the spiral spin liquid in  $\text{MnSc}_2\text{S}_4$ ”, *Physical Review B*, vol. 98, no. 6, p. 064 427, Aug. 2018. DOI: 10.1103/PhysRevB.98.064427.
- [197] A. Keleş and E. Zhao, “Absence of Long-Range Order in a Triangular Spin System with Dipolar Interactions”, *Physical Review Letters*, vol. 120, no. 18, p. 187 202, May 2018. DOI: 10.1103/PhysRevLett.120.187202.
- [198] M. Hering, J. Sonnenschein, Y. Iqbal, and J. Reuther, “Characterization of quantum spin liquids and their spinon band structures via functional renormalization”, *Physical Review B*, vol. 99, no. 10, p. 100 405, Mar. 2019. DOI: 10.1103/PhysRevB.99.100405.

- [199] P. Ghosh, Y. Iqbal, T. Müller, R. T. Ponnaganti, R. Thomale, R. Narayanan, J. Reuther, M. J. P. Gingras, and H. O. Jeschke, “Breathing chromium spinels: A showcase for a variety of Pyrochlore Heisenberg Hamiltonians”, *npj Quantum Materials*, vol. 4, no. 1, p. 63, Dec. 2019. DOI: 10.1038/s41535-019-0202-z.
- [200] J. Reuther, R. Thomale, and S. Trebst, “Finite-temperature phase diagram of the Heisenberg-Kitaev model”, *Physical Review B*, vol. 84, no. 10, p. 100406, Sep. 2011. DOI: 10.1103/PhysRevB.84.100406.
- [201] P. Ghosh, T. Müller, F. P. Toldin, J. Richter, R. Narayanan, R. Thomale, J. Reuther, and Y. Iqbal, “Quantum paramagnetism and helimagnetic orders in the Heisenberg model on the body centered cubic lattice”, *Physical Review B*, vol. 100, no. 1, p. 014420, Jul. 2019. DOI: 10.1103/PhysRevB.100.014420.
- [202] A. Revelli, C. C. Loo, D. Kiese, P. Becker, T. Fröhlich, T. Lorenz, M. Moretti Sala, G. Monaco, F. L. Buessen, J. Attig, M. Hermanns, S. V. Streltsov, D. I. Khomskii, J. van den Brink, M. Braden, P. H. M. van Loosdrecht, S. Trebst, A. Paramekanti, and M. Grüninger, “Spin-orbit entangled  $j=\frac{1}{2}$  moments in  $\text{Ba}_2\text{CeIrO}_6$ : A frustrated fcc quantum magnet”, *Physical Review B*, vol. 100, no. 8, p. 085139, Aug. 2019. DOI: 10.1103/PhysRevB.100.085139.
- [203] D. Roscher, N. Gneist, M. M. Scherer, S. Trebst, and S. Diehl, “Cluster functional renormalization group and absence of a bilinear spin liquid in the  $J_1$ - $J_2$  Heisenberg model”, *Physical Review B*, vol. 100, no. 12, p. 125130, Sep. 2019. DOI: 10.1103/PhysRevB.100.125130.
- [204] S. Chillal, Y. Iqbal, H. O. Jeschke, J. A. Rodriguez-Rivera, R. Bewley, P. Manuel, D. Khalyavin, P. Steffens, R. Thomale, A. T. M. N. Islam, J. Reuther, and B. Lake, “Evidence for a three-dimensional quantum spin liquid in  $\text{PbCuTe}_2\text{O}_6$ ”, *Nature Communications*, vol. 11, no. 1, p. 2348, May 2020. DOI: 10.1038/s41467-020-15594-1.
- [205] A. Revelli, M. Moretti Sala, G. Monaco, C. Hickey, P. Becker, F. Freund, A. Jesche, P. Gegenwart, T. Eschmann, F. L. Buessen, S. Trebst, P. H. M. van Loosdrecht, J. van den Brink, and M. Grüninger, “Fingerprints of Kitaev physics in the magnetic excitations of honeycomb iridates”, *Physical Review Research*, vol. 2, no. 4, p. 043094, Oct. 2020. DOI: 10.1103/PhysRevResearch.2.043094.
- [206] D. Kiese, F. L. Buessen, C. Hickey, S. Trebst, and M. M. Scherer, “Emergence and stability of spin-valley entangled quantum liquids in moiré heterostructures”, vol. 2, no. 1, p. 013370, Mar. 2020. DOI: 10.1103/PhysRevResearch.2.013370.

- 
- [207] J. Reuther, P. Wölfle, R. Darradi, W. Brenig, M. Arlego, and J. Richter, “Quantum phases of the planar antiferromagnetic  $J_1$ - $J_2$ - $J_3$  Heisenberg model”, *Physical Review B*, vol. 83, no. 6, p. 064 416, Feb. 2011. DOI: 10.1103/PhysRevB.83.064416.
- [208] J. Reuther, R. Thomale, and S. Rachel, “Spiral order in the honeycomb iridate  $\text{Li}_2\text{IrO}_3$ ”, *Physical Review B*, vol. 90, no. 10, p. 100 405, Sep. 2014. DOI: 10.1103/PhysRevB.90.100405.
- [209] Y. Singh, S. Manni, J. Reuther, T. Berlijn, R. Thomale, W. Ku, S. Trebst, and P. Gegenwart, “Relevance of the Heisenberg-kitaev model for the honeycomb lattice iridates  $\text{A}_2\text{IrO}_3$ ”, *Physical Review Letters*, vol. 108, no. 12, p. 127 203, Mar. 2012. DOI: 10.1103/PhysRevLett.108.127203.
- [210] J. Reuther, R. Thomale, and S. Rachel, “Magnetic ordering phenomena of interacting quantum spin Hall models”, *Physical Review B*, vol. 86, no. 15, p. 155 127, Oct. 2012. DOI: 10.1103/PhysRevB.86.155127.
- [211] S. Göttel, S. Andergassen, C. Honerkamp, D. Schuricht, and S. Wessel, “Critical scales in anisotropic spin systems from functional renormalization”, *Physical Review B*, vol. 85, no. 21, p. 214 406, Jun. 2012. DOI: 10.1103/PhysRevB.85.214406.
- [212] R. Suttner, C. Platt, J. Reuther, and R. Thomale, “Renormalization group analysis of competing quantum phases in the  $J_1$ - $J_2$  Heisenberg model on the kagome lattice”, *Physical Review B*, vol. 89, no. 2, p. 020 408, Jan. 2014. DOI: 10.1103/PhysRevB.89.020408.
- [213] A. Shnirman and Y. Makhlin, “Spin-spin correlators in the Majorana representation”, *Physical Review Letters*, vol. 91, no. 20, p. 207 204, Nov. 2003. DOI: 10.1103/PhysRevLett.91.207204.
- [214] R. R. Biswas, L. Fu, C. R. Laumann, and S. Sachdev, “ $\text{SU}(2)$ -invariant spin liquids on the triangular lattice with spinful Majorana excitations”, *Physical Review B*, vol. 83, no. 24, p. 245 131, Jun. 2011. DOI: 10.1103/PhysRevB.83.245131.
- [215] P. Schad, Y. Makhlin, B. Narozhny, G. Schön, and A. Shnirman, “Majorana representation for dissipative spin systems”, *Annals of Physics*, vol. 361, pp. 401–422, 2015, ISSN: 0003-4916. DOI: 10.1016/j.aop.2015.07.006.
- [216] J. Nilsson and M. Bazzanella, “Majorana fermion description of the Kondo lattice: Variational and path integral approach”, *Physical Review B*, vol. 88, no. 4, p. 045 112, Jul. 2013. DOI: 10.1103/PhysRevB.88.045112.
- [217] J. Behrends, J. H. Bardarson, and B. Béri, “Tenfold way and many-body zero modes in the Sachdev-Ye-Kitaev model”, *Physical Review B*, vol. 99, no. 19, p. 195 123, May 2019. DOI: 10.1103/PhysRevB.99.195123.

- [218] T. R. Morris, “The exact renormalization group and approximate solutions”, *International Journal of Modern Physics A*, vol. 09, no. 14, pp. 2411–2449, 1994. DOI: 10.1142/S0217751X94000972.
- [219] C. Karrasch, R. Hedden, R. Peters, T. Pruschke, K. Schönhammer, and V. Meden, “A finite-frequency functional renormalization group approach to the single impurity Anderson model”, *Journal of Physics: Condensed Matter*, vol. 20, no. 34, p. 345 205, Aug. 2008. DOI: 10.1088/0953-8984/20/34/345205.
- [220] V. N. Popov and S. Fedotov, “The functional-integration method and diagram technique for spin systems”, *Soviet Physics-JETP [translation of Zhurnal Eksperimentalnoi i Teoreticheskoi Fiziki]*, vol. 67, no. 3, pp. 535–541, 1988.
- [221] A. Eberlein, “Fermionic two-loop functional renormalization group for correlated fermions: Method and application to the attractive Hubbard model”, *Physical Review B*, vol. 90, no. 11, p. 115 125, Sep. 2014. DOI: 10.1103/PhysRevB.90.115125.
- [222] F. B. Kugler, “Renormalization group approaches to strongly correlated electron systems”, *PhD thesis, Ludwig-Maximilians-Universität München*, 2019.
- [223] M. Gievers, E. Walter, A. Ge, J. von Delft, and F. B. Kugler, “Multi-loop flow equations for single-boson exchange fRG”, *The European Physical Journal B: Condensed Matter and Complex Systems*, vol. 95, no. 7, p. 108, Jul. 2022. DOI: 10.1140/epjb/s10051-022-00353-6.
- [224] A. Tagliavini, C. Hille, F. B. Kugler, S. Andergassen, A. Toschi, and C. Honerkamp, “Multiloop functional renormalization group for the two-dimensional Hubbard model: Loop convergence of the response functions”, *SciPost Physics*, vol. 6, no. 1, p. 9, 2019. DOI: 10.21468/SciPostPhys.6.1.009.
- [225] P. Chalupa-Gantner, F. B. Kugler, C. Hille, J. von Delft, S. Andergassen, and A. Toschi, “Fulfillment of sum rules and Ward identities in the multiloop functional renormalization group solution of the Anderson impurity model”, vol. 4, no. 2, p. 023 050, Apr. 2022. DOI: 10.1103/PhysRevResearch.4.023050.
- [226] C. Hille, F. B. Kugler, C. J. Eckhardt, Y.-Y. He, A. Kauch, C. Honerkamp, A. Toschi, and S. Andergassen, “Quantitative functional renormalization group description of the two-dimensional Hubbard model”, *Physical Review Research*, vol. 2, no. 3, p. 033 372, Sep. 2020. DOI: 10.1103/PhysRevResearch.2.033372.

- 
- [227] C. De Dominicis and P. C. Martin, “Stationary entropy principle and renormalization in normal and superfluid systems. II. Diagrammatic formulation”, *Journal of Mathematical Physics*, vol. 5, no. 1, pp. 31–59, Jan. 1964, ISSN: 0022-2488. DOI: 10.1063/1.1704064.
- [228] C. De Dominicis and P. C. Martin, “Stationary entropy principle and renormalization in normal and superfluid systems. I. Algebraic formulation”, *Journal of Mathematical Physics*, vol. 5, no. 1, pp. 14–30, Jan. 1964, ISSN: 0022-2488. DOI: 10.1063/1.1704062.
- [229] E. E. Salpeter and H. A. Bethe, “A relativistic equation for bound-state problems”, *Physical Review*, vol. 84, no. 6, pp. 1232–1242, Dec. 1951. DOI: 10.1103/PhysRev.84.1232.
- [230] C. Honerkamp and M. Salmhofer, “Temperature-flow renormalization group and the competition between superconductivity and ferromagnetism”, *Physical Review B*, vol. 64, no. 18, p. 184516, Oct. 2001. DOI: 10.1103/PhysRevB.64.184516.
- [231] C. Honerkamp, D. Rohe, S. Andergassen, and T. Enss, “Interaction flow method for many-fermion systems”, *Physical Review B*, vol. 70, no. 23, p. 235115, Dec. 2004. DOI: 10.1103/PhysRevB.70.235115.
- [232] B. Sbierski, M. Bintz, S. Chatterjee, M. Schuler, N. Y. Yao, and L. Pollet, “Magnetism in the two-dimensional dipolar XY model”, *Physical Review B*, vol. 109, no. 14, p. 144411, Apr. 2024. DOI: 10.1103/PhysRevB.109.144411.
- [233] Y. Schaden and J. Reuther, “Bilinear Majorana representations for spin operators with spin magnitudes  $S \geq 1/2$ ”, vol. 5, no. 2, p. 023067, Apr. 2023. DOI: 10.1103/PhysRevResearch.5.023067.
- [234] W. Heisenberg, “Zur Theorie des Ferromagnetismus”, *Zeitschrift fur Physik*, vol. 49, no. 9-10, pp. 619–636, Sep. 1928. DOI: 10.1007/BF01328601.
- [235] M. Suzuki, S. Miyashita, and A. Kuroda, “Monte carlo simulation of quantum spin systems. I”, *Progress of Theoretical Physics*, vol. 58, no. 5, pp. 1377–1387, Nov. 1977. DOI: 10.1143/PTP.58.1377.
- [236] J. Krieg and P. Kopietz, “Exact renormalization group for quantum spin systems”, *Physical Review B*, vol. 99, no. 6, p. 060403, Feb. 2019. DOI: 10.1103/PhysRevB.99.060403.
- [237] J. Cardy, P. Goddard, and J. Yeomans, *Scaling and Renormalization in Statistical Physics* (Cambridge Lecture Notes in Physics). Cambridge University Press, 1996, ISBN: 978-0-521-49959-0.

- [238] P. Peczak, A. M. Ferrenberg, and D. P. Landau, “High-accuracy Monte Carlo study of the three-dimensional classical Heisenberg ferromagnet”, *Physical Review B*, vol. 43, no. 7, pp. 6087–6093, Mar. 1991. DOI: 10.1103/PhysRevB.43.6087.
- [239] S. M. Chester, W. Landry, J. Liu, D. Poland, D. Simmons-Duffin, N. Su, and A. Vichi, “Bootstrapping Heisenberg magnets and their cubic instability”, *Physical Review D: Particles and Fields*, vol. 104, no. 10, p. 105 013, Nov. 2021. DOI: 10.1103/PhysRevD.104.105013.
- [240] B. Knorr, “Critical chiral Heisenberg model with the functional renormalization group”, *Physical Review B*, vol. 97, no. 7, p. 075 129, Feb. 2018. DOI: 10.1103/PhysRevB.97.075129.
- [241] J. Berges, N. Tetradis, and C. Wetterich, “Non-perturbative renormalization flow in quantum field theory and statistical physics”, *Physics Reports*, vol. 363, no. 4, pp. 223–386, 2002, ISSN: 0370-1573. DOI: 10.1016/S0370-1573(01)00098-9.
- [242] W. Mao, P. Coleman, C. Hooley, and D. Langreth, “Spin dynamics from Majorana fermions”, *Physical Review Letters*, vol. 91, no. 20, p. 207 203, Nov. 2003. DOI: 10.1103/PhysRevLett.91.207203.
- [243] Y. Iqbal, W.-J. Hu, R. Thomale, D. Poilblanc, and F. Becca, “Spin liquid nature in the Heisenberg  $J_1$ - $J_2$  triangular antiferromagnet”, *Physical Review B*, vol. 93, no. 14, p. 144 411, Apr. 2016. DOI: 10.1103/PhysRevB.93.144411.
- [244] C. Pinettes and H. T. Diep, “Phase transition and phase diagram of the  $J_1$ - $J_2$  Heisenberg model on a simple cubic lattice”, *Journal of Applied Physics*, vol. 83, no. 11, pp. 6317–6319, Jun. 1998, ISSN: 0021-8979, 1089-7550. DOI: 10.1063/1.367729.
- [245] K. Kubo and T. Kishi, “Ordering due to quantum fluctuations in the frustrated Heisenberg model”, *Journal of the Physical Society of Japan*, vol. 60, no. 2, pp. 567–572, 1991. DOI: 10.1143/JPSJ.60.567.
- [246] V. Y. Irkhin, A. A. Katanin, and M. I. Katsnelson, “On the self-consistent spin-wave theory of frustrated Heisenberg antiferromagnets”, *Journal of Physics: Condensed Matter*, vol. 4, no. 22, p. 5227, Jun. 1992, ISSN: 0953-8984. DOI: 10.1088/0953-8984/4/22/019.
- [247] A. F. Barabanov, V. M. Beresovsky, and E. Zasiwas, “Quantum phase transitions in a three-dimensional frustrated  $S=1/2$  Heisenberg antiferromagnet”, *Physical Review B*, vol. 52, no. 14, pp. 10 177–10 181, Oct. 1995. DOI: 10.1103/PhysRevB.52.10177.

- 
- [248] J. R. Viana, J. R. de Sousa, and M. A. Continentino, “Quantum phase transition in the three-dimensional anisotropic frustrated Heisenberg anti-ferromagnetic model”, *Physical Review B*, vol. 77, no. 17, p. 172412, May 2008. DOI: 10.1103/PhysRevB.77.172412.
- [249] D. J. J. Farnell, O. Götze, and J. Richter, “Ground-state ordering of the  $J_1$ - $J_2$  model on the simple cubic and body-centered cubic lattices”, *Physical Review B*, vol. 93, no. 23, p. 235123, Jun. 2016. DOI: 10.1103/PhysRevB.93.235123.
- [250] K. Majumdar and T. Datta, “Zero temperature phases of the frustrated  $J_1$ - $J_2$  antiferromagnetic spin-1/2 Heisenberg model on a simple cubic lattice”, *Journal of statistical physics*, vol. 139, no. 4, pp. 714–726, May 2010, ISSN: 1572-9613. DOI: 10.1007/s10955-010-9967-y.
- [251] M. Laubach, D. G. Joshi, J. Reuther, R. Thomale, M. Vojta, and S. Rachel, “Quantum disordered insulating phase in the frustrated cubic-lattice Hubbard model”, *Physical Review B*, vol. 93, no. 4, p. 041106, Jan. 2016, ISSN: 2469-9950, 2469-9969. DOI: 10.1103/PhysRevB.93.041106.
- [252] J. Reuther and P. Wölfle, “A diagrammatic theory of the antiferromagnetic frustrated 2d Heisenberg model”, *Journal of physics. Conference series*, vol. 200, no. 2, p. 022051, Jan. 2010. DOI: 10.1088/1742-6596/200/2/022051.
- [253] J. G. Rau and M. J. Gingras, “Frustrated quantum rare-earth Pyrochlores”, *Annual Review of Condensed Matter Physics*, vol. 10, no. 1, pp. 357–386, 2019. DOI: 10.1146/annurev-conmatphys-022317-110520.
- [254] C. Liu, G. B. Halász, and L. Balents, “Symmetric  $U(1)$  and  $Z_2$  spin liquids on the Pyrochlore lattice”, *Physical Review B*, vol. 104, no. 5, p. 054401, Aug. 2021. DOI: 10.1103/PhysRevB.104.054401.
- [255] R. Moessner and J. T. Chalker, “Properties of a classical spin liquid: The Heisenberg Pyrochlore antiferromagnet”, *Physical Review Letters*, vol. 80, no. 13, pp. 2929–2932, Mar. 1998. DOI: 10.1103/PhysRevLett.80.2929.
- [256] M. Hering, H. Yan, and J. Reuther, “Fracton excitations in classical frustrated kagome spin models”, *Physical Review B*, vol. 104, no. 6, p. 064406, Aug. 2021. DOI: 10.1103/PhysRevB.104.064406.
- [257] I. Hagymási, R. Schäfer, R. Moessner, and D. J. Luitz, “Possible inversion symmetry breaking in the  $S=1/2$  Pyrochlore Heisenberg magnet”, *Physical Review Letters*, vol. 126, no. 11, p. 117204, Mar. 2021. DOI: 10.1103/PhysRevLett.126.117204.

- [258] Y. Huang, K. Chen, Y. Deng, N. Prokof'ev, and B. Svistunov, "Spin-ice state of the quantum Heisenberg antiferromagnet on the Pyrochlore lattice", *Physical Review Letters*, vol. 116, no. 17, p. 177 203, Apr. 2016. DOI: 10.1103/PhysRevLett.116.177203.
- [259] A. Lohmann, H.-J. Schmidt, and J. Richter, "Tenth-order high-temperature expansion for the susceptibility and the specific heat of spin-s Heisenberg models with arbitrary exchange patterns: Application to Pyrochlore and kagome magnets", *Physical Review B*, vol. 89, no. 1, p. 014 415, Jan. 2014. DOI: 10.1103/PhysRevB.89.014415.
- [260] O. Derzhko, T. Hutak, T. Krokhmal'skii, J. Schnack, and J. Richter, "Adapting Planck's route to investigate the thermodynamics of the spin-half Pyrochlore Heisenberg antiferromagnet", *Physical Review B*, vol. 101, no. 17, p. 174 426, 2020. DOI: 10.1103/PhysRevB.101.174426.
- [261] S. Zhang, H. J. Changlani, K. W. Plumb, O. Tchernyshyov, and R. Moessner, "Dynamical structure factor of the three-dimensional quantum spin liquid candidate  $\text{NaCaNi}_2\text{F}_7$ ", *Physical Review Letters*, vol. 122, no. 16, p. 167 203, Apr. 2019. DOI: 10.1103/PhysRevLett.122.167203.
- [262] P. Müller, A. Lohmann, J. Richter, and O. Derzhko, "Thermodynamics of the Pyrochlore-lattice quantum Heisenberg antiferromagnet", *Physical Review B*, vol. 100, no. 2, p. 024 424, Jul. 2019. DOI: 10.1103/PhysRevB.100.024424.
- [263] R. Schäfer, I. Hagymási, R. Moessner, and D. J. Luitz, "Pyrochlore  $S=\frac{1}{2}$  Heisenberg antiferromagnet at finite temperature", *Physical Review B*, vol. 102, no. 5, p. 054 408, Aug. 2020. DOI: 10.1103/PhysRevB.102.054408.
- [264] C. Hille, D. Rohe, C. Honerkamp, and S. Andergassen, "Pseudogap opening in the two-dimensional Hubbard model: A functional renormalization group analysis", vol. 2, no. 3, p. 033 068, Jul. 2020. DOI: 10.1103/PhysRevResearch.2.033068.
- [265] I. Hagymási, V. Noculak, and J. Reuther, "Enhanced symmetry-breaking tendencies in the  $S=1$  Pyrochlore antiferromagnet", *Physical Review B*, vol. 106, no. 23, p. 235 137, Dec. 2022. DOI: 10.1103/PhysRevB.106.235137.
- [266] H. Yan, O. Benton, L. D. C. Jaubert, and N. Shannon, "Rank-2  $U(1)$  spin liquid on the breathing Pyrochlore lattice", *Physical Review Letters*, vol. 124, no. 12, p. 127 203, Mar. 2020. DOI: 10.1103/PhysRevLett.124.127203.



- 
- [267] S. Bravyi, B. Leemhuis, and B. M. Terhal, “Topological order in an exactly solvable 3D spin model”, *Annals of Physics (New York)*, vol. 326, no. 4, pp. 839–866, 2011, ISSN: 0003-4916. DOI: 10.1016/j.aop.2010.11.002.
- [268] S. Vijay, J. Haah, and L. Fu, “A new kind of topological quantum order: A dimensional hierarchy of quasiparticles built from stationary excitations”, *Physical Review B*, vol. 92, no. 23, p. 235136, Dec. 2015. DOI: 10.1103/PhysRevB.92.235136.
- [269] B. Yoshida, “Exotic topological order in fractal spin liquids”, *Physical Review B*, vol. 88, no. 12, p. 125122, Sep. 2013. DOI: 10.1103/PhysRevB.88.125122.
- [270] C. Castelnovo, R. Moessner, and S. Sondhi, “Spin Ice, Fractionalization, and Topological Order”, *Annual Review of Condensed Matter Physics*, vol. 3, no. 1, pp. 35–55, Mar. 2012, ISSN: 1947-5454, 1947-5462. DOI: 10.1146/annurev-conmatphys-020911-125058.
- [271] D. Bulmash and M. Barkeshli, *Generalized  $U(1)$  gauge field theories and fractal dynamics*, 2018. DOI: 10.48550/ARXIV.1806.01855.
- [272] A. Gromov, *A duality between  $U(1)$  haah code and 3D smectic a phase*, 2020. DOI: 10.48550/ARXIV.2002.11817.
- [273] B. M. Terhal, “Quantum error correction for quantum memories”, *Reviews of Modern Physics*, vol. 87, no. 2, pp. 307–346, Apr. 2015. DOI: 10.1103/RevModPhys.87.307.
- [274] H. Yan, “Hyperbolic fracton model, subsystem symmetry, and holography. II. The dual eight-vertex model”, *Physical Review B*, vol. 100, no. 24, p. 245138, Dec. 2019. DOI: 10.1103/PhysRevB.100.245138.
- [275] S. R. Sklan and C. L. Henley, “Nonplanar ground states of frustrated antiferromagnets on an octahedral lattice”, *Physical Review B*, vol. 88, no. 2, p. 024407, Jul. 2013. DOI: 10.1103/PhysRevB.88.024407.
- [276] A. Szabó, F. Orlandi, and P. Manuel, “Fragmented spin ice and multi-k ordering in rare-earth antiperovskites”, *Physical Review Letters*, vol. 129, no. 24, p. 247201, Dec. 2022. DOI: 10.1103/PhysRevLett.129.247201.
- [277] O. Benton, L. D. C. Jaubert, H. Yan, and N. Shannon, “A spin-liquid with pinch-line singularities on the Pyrochlore lattice”, *Nature Communications*, vol. 7, no. 1, p. 11572, 2016/05/26, 2016. DOI: 10.1038/ncomms11572.
- [278] N. D. Mermin, “The topological theory of defects in ordered media”, *Reviews of Modern Physics*, vol. 51, no. 3, pp. 591–648, Jul. 1979. DOI: 10.1103/RevModPhys.51.591.

- [279] M. Kléman, Ed., *Points, Lines and Walls in Liquid Crystals, Magnetic Systems and Various Ordered Media*. John Wiley & Sons Inc, 1983.
- [280] M. Hering, F. Ferrari, A. Razpopov, I. I. Mazin, R. Valenti, H. O. Jeschke, and J. Reuther, “Phase diagram of a distorted kagome antiferromagnet and application to Y-kapellasite”, *npj Computational Materials*, vol. 8, no. 1, p. 10, 2022. DOI: 10.1038/s41524-021-00689-0.
- [281] R. M. Karp, “Reducibility among Combinatorial Problems”, in *Complexity of Computer Computations: Proceedings of a Symposium on the Complexity of Computer Computations, Held March 20–22, 1972, at the IBM Thomas J. Watson Research Center, Yorktown Heights, New York, and Sponsored by the Office of Naval Research, Mathematics Program, IBM World Trade Corporation, and the IBM Research Mathematical Sciences Department*, R. E. Miller, J. W. Thatcher, and J. D. Bohlinger, Eds., Boston, MA: Springer US, 1972, pp. 85–103, ISBN: 978-1-4684-2001-2. DOI: 10.1007/978-1-4684-2001-2\_9.
- [282] Gurobi Optimization, LLC, *Gurobi optimizer reference manual*, 2023.
- [283] S. Bolusani *et al.*, “The SCIP optimization suite 9.0”, Optimization Online, Technical Report, Feb. 2024.
- [284] O. Sikora, N. Shannon, F. Pollmann, K. Penc, and P. Fulde, “Extended quantum U(1)-liquid phase in a three-dimensional quantum dimer model”, *Physical Review B*, vol. 84, no. 11, p. 115129, Sep. 2011. DOI: 10.1103/PhysRevB.84.115129.
- [285] D. A. Huse, W. Krauth, R. Moessner, and S. L. Sondhi, “Coulomb and liquid dimer models in three dimensions”, *Physical Review Letters*, vol. 91, no. 16, p. 167004, Oct. 2003. DOI: 10.1103/PhysRevLett.91.167004.
- [286] J. Colpa, “Diagonalization of the quadratic boson hamiltonian”, *Physica A: Statistical Mechanics and its Applications*, vol. 93, no. 3, pp. 327–353, 1978, ISSN: 0378-4371. DOI: 10.1016/0378-4371(78)90160-7.
- [287] S. Toth and B. Lake, “Linear spin wave theory for single-Q incommensurate magnetic structures”, *Journal of Physics: Condensed Matter*, vol. 27, no. 16, p. 166002, Mar. 2015. DOI: 10.1088/0953-8984/27/16/166002.
- [288] A. Polyakov, “Quark confinement and topology of gauge theories”, *Nuclear Physics B*, vol. 120, no. 3, pp. 429–458, 1977, ISSN: 0550-3213. DOI: 10.1016/0550-3213(77)90086-4.
- [289] A. Browaeys and T. Lahaye, “Many-body physics with individually controlled Rydberg atoms”, *Nature Physics*, vol. 16, no. 2, pp. 132–142, Feb. 1, 2020, ISSN: 1745-2481. DOI: 10.1038/s41567-019-0733-z.

- 
- [290] A. W. Glaetzle, M. Dalmonte, R. Nath, C. Gross, I. Bloch, and P. Zoller, “Designing frustrated quantum magnets with laser-dressed Rydberg atoms”, *Physical Review Letters*, vol. 114, no. 17, p. 173002, Apr. 2015. DOI: 10.1103/PhysRevLett.114.173002.
- [291] A. W. Glaetzle, M. Dalmonte, R. Nath, I. Rousochatzakis, R. Moessner, and P. Zoller, “Quantum spin-ice and dimer models with Rydberg atoms”, *Physical Review X*, vol. 4, no. 4, p. 041037, Nov. 2014. DOI: 10.1103/PhysRevX.4.041037.
- [292] A. M. Kaufman and K.-K. Ni, “Quantum science with optical tweezer arrays of ultracold atoms and molecules”, *Nature Physics*, vol. 17, no. 12, pp. 1324–1333, Dec. 1, 2021, ISSN: 1745-2481. DOI: 10.1038/s41567-021-01357-2.
- [293] I. Lesanovsky and H. Katsura, “Interacting fibonacci anyons in a Rydberg gas”, *Physical Review A: Atomic, Molecular, and Optical Physics*, vol. 86, no. 4, p. 041601, Oct. 2012. DOI: 10.1103/PhysRevA.86.041601.
- [294] J. Reuther, “Frustrated Quantum Heisenberg Antiferromagnets: Functional Renormalization-Group Approach in Auxiliary-Fermion Representation”, Ph.D. dissertation, Karlsruher Institut für Technologie (KIT), 2011.
- [295] B. Schneider and B. Sbierski, *Taming spin susceptibilities in frustrated quantum magnets: Mean-field form and approximate nature of the quantum-to-classical correspondence*, 2024.
- [296] D. Kiese, N. Wentzell, I. Krivenko, O. Parcollet, K. Held, and F. Krien, *Embedded multi-boson exchange: A step beyond quantum cluster theories*, 2024.
- [297] A. Toschi, A. A. Katanin, and K. Held, “Dynamical vertex approximation: A step beyond dynamical mean-field theory”, *Physical Review B*, vol. 75, no. 4, p. 045118, Jan. 2007. DOI: 10.1103/PhysRevB.75.045118.
- [298] K. Held, “Electronic structure calculations using dynamical mean field theory”, *Advances in Physics*, vol. 56, no. 6, pp. 829–926, 2007. DOI: 10.1080/00018730701619647.
- [299] D. Tarasevych, A. Rückriegel, S. Keupert, V. Mitsioannou, and P. Kopietz, “Spin-functional renormalization group for the  $J_1J_2J_3$  quantum Heisenberg model”, *Physical Review B*, vol. 106, no. 17, p. 174412, Nov. 2022. DOI: 10.1103/PhysRevB.106.174412.
- [300] S. G. Jakobs, V. Meden, and H. Schoeller, “Nonequilibrium functional renormalization group for interacting quantum systems”, vol. 99, no. 15, p. 150603, Oct. 2007. DOI: 10.1103/PhysRevLett.99.150603.

- [301] S. G. Jakobs, M. Pletyukhov, and H. Schoeller, “Nonequilibrium functional renormalization group with frequency-dependent vertex function: A study of the single-impurity Anderson model”, *Physical Review B*, vol. 81, no. 19, p. 195 109, May 2010. DOI: 10.1103/PhysRevB.81.195109.
- [302] C. Fräßdorf and J. E. M. Mosig, “Keldysh functional renormalization group for electronic properties of graphene”, vol. 95, no. 12, p. 125 412, Mar. 2017. DOI: 10.1103/PhysRevB.95.125412.
- [303] J. Potten, T. Mueller, and R. Thomale, “Frequency-resolved functional renormalization group for quantum magnetic systems”, in *APS March Meeting Abstracts*, ser. APS Meeting Abstracts, vol. 2023, Jan. 2023, W56.011.
- [304] C. Rackauckas and Q. Nie, “DifferentialEquations.jl – a performant and feature-rich ecosystem for solving differential equations in Julia”, *Journal of Open Research Software*, vol. 5, 2017. DOI: 10.5334/jors.151.
- [305] M. Calandra Buonauro and S. Sorella, “Numerical study of the two-dimensional Heisenberg model using a Green function Monte Carlo technique with a fixed number of walkers”, *Physical Review B*, vol. 57, no. 18, pp. 11 446–11 456, May 1998. DOI: 10.1103/PhysRevB.57.11446.
- [306] N. Trivedi and D. M. Ceperley, “Ground-state correlations of quantum antiferromagnets: A Green-function Monte Carlo study”, *Physical Review B*, vol. 41, no. 7, pp. 4552–4569, Mar. 1990. DOI: 10.1103/PhysRevB.41.4552.
- [307] J. H. Hetherington, “Observations on the statistical iteration of matrices”, *Physical Review A: Atomic, Molecular, and Optical Physics*, vol. 30, no. 5, pp. 2713–2719, Nov. 1984. DOI: 10.1103/PhysRevA.30.2713.
- [308] S. Sorella, “Green function Monte Carlo with stochastic reconfiguration”, *Physical Review Letters*, vol. 80, no. 20, pp. 4558–4561, May 1998. DOI: 10.1103/PhysRevLett.80.4558.
- [309] H.-Y. Lin, Y. Guo, R.-Q. He, Z. Y. Xie, and Z.-Y. Lu, “Green’s function Monte Carlo combined with projected entangled pair state approach to the frustrated  $J_1$ - $J_2$  Heisenberg model”, *Physical Review B*, vol. 109, no. 23, p. 235 133, Jun. 2024. DOI: 10.1103/PhysRevB.109.235133.
- [310] K. J. Runge, “Quantum Monte Carlo calculation of the long-range order in the Heisenberg antiferromagnet”, *Physical Review B*, vol. 45, no. 13, pp. 7229–7236, Apr. 1992. DOI: 10.1103/PhysRevB.45.7229.
- [311] A. Ralko, M. Ferrero, F. Becca, D. Ivanov, and F. Mila, “Zero-temperature properties of the quantum dimer model on the triangular lattice”, *Physical Review B*, vol. 71, no. 22, p. 224 109, Jun. 2005. DOI: 10.1103/PhysRevB.71.224109.